

Magazine of Civil Engineering

ISSN 2712-8172

100(8), 2020





ПОЛИТЕХ
Санкт-Петербургский
политехнический университет
Петра Великого

Инженерно-строительный институт
Центр дополнительных профессиональных программ
195251, г. Санкт-Петербург, Политехническая ул., 29,
тел/факс: 552-94-60, www.stroikursi.spbstu.ru,
stroikursi@mail.ru

**Приглашает специалистов организаций, вступающих в СРО,
на курсы повышения квалификации (72 часа)**

Код	Наименование программы	Виды работ*
Курсы по строительству		
БС-01-04	«Безопасность и качество выполнения общестроительных работ»	п.1,2, 3, 5, 6, 7, 9, 10, 11, 12, 13, 14
БС-01	«Безопасность и качество выполнения геодезических, подготовительных и земляных работ, устройства оснований и фундаментов»	1,2,3,5
БС-02	«Безопасность и качество возведения бетонных и железобетонных конструкций»	6,7
БС-03	«Безопасность и качество возведения металлических, каменных и деревянных конструкций»	9,10,11
БС-04	«Безопасность и качество выполнения фасадных работ, устройства кровель, защиты строительных конструкций, трубопроводов и оборудования»	12,13,14
БС-05	«Безопасность и качество устройства инженерных сетей и систем»	15,16,17,18,19
БС-06	«Безопасность и качество устройства электрических сетей и линий связи»	20,21
БС-08	«Безопасность и качество выполнения монтажных и пусконаладочных работ»	23,24
БС-12	«Безопасность и качество устройства мостов, эстакад и путепроводов»	29
БС-13	«Безопасность и качество выполнения гидротехнических, водолазных работ»	30
БС-14	«Безопасность и качество устройства промышленных печей и дымовых труб»	31
БС-15	«Осуществление строительного контроля»	32
БС-16	«Организация строительства, реконструкции и капитального ремонта. Выполнение функций технического заказчика и генерального подрядчика»	33
Курсы по проектированию		
БП-01	«Разработка схемы планировочной организации земельного участка, архитектурных решений, мероприятий по обеспечению доступа маломобильных групп населения»	1,2,11
БП-02	«Разработка конструктивных и объемно-планировочных решений зданий и сооружений»	3
БП-03	«Проектирование внутренних сетей инженерно-технического обеспечения»	4
БП-04	«Проектирование наружных сетей инженерно-технического обеспечения»	5
БП-05	«Разработка технологических решений при проектировании зданий и сооружений»	6
БП-06	«Разработка специальных разделов проектной документации»	7
БП-07	«Разработка проектов организации строительства»	8
БП-08	«Проектные решения по охране окружающей среды»	9
БП-09	«Проектные решения по обеспечению пожарной безопасности»	10
БП-10	«Обследование строительных конструкций и грунтов основания зданий и сооружений»	12
БП-11	«Организация проектных работ. Выполнение функций генерального проектировщика»	13
Э-01	«Проведение энергетических обследований с целью повышения энергетической эффективности и энергосбережения»	
Курсы по инженерным изысканиям		
И-01	«Инженерно-геодезические изыскания в строительстве»	1
И-02	«Инженерно-геологические изыскания в строительстве»	2,5
И-03	«Инженерно-гидрометеорологические изыскания в строительстве»	3
И-04	«Инженерно-экологические изыскания в строительстве»	4
И-05	«Организация работ по инженерным изысканиям»	7

*(согласно приказам Минрегионразвития РФ N 624 от 30 декабря 2009 г.)

**По окончании курса слушателю выдается удостоверение о краткосрочном повышении
квалификации установленного образца (72 ак. часа)**

Для регистрации на курс необходимо выслать заявку на участие, и копию диплома об образовании по телефону/факсу: 8(812) 552-94-60, 535-79-92, , e-mail: stroikursi@mail.ru.

Magazine of Civil Engineering

SCHOLAR JOURNAL

ISSN 2712-8172

Свидетельство о государственной регистрации:
Эл № ФС77-77906 от 19.02.2020,
выдано Роскомнадзором

Специализированный научный журнал. Выходит с
09.2008.

Включен в Перечень ВАК РФ

Индексируется в БД Scopus

Периодичность: 8 раз в год

Учредитель и издатель:

Санкт-Петербургский политехнический университет
Петра Великого

Адрес редакции:

195251, СПб, ул. Политехническая, д. 29

Главный редактор:

Екатерина Александровна Линник

Научный редактор:

Виталий Владимирович Сергеев

Заместитель главного научного редактора:

Галина Леонидовна Козинец

Редакционная коллегия:

PhD, проф. Т. Аввад;
д.т.н., проф. М.И. Бальзанников
д.т.н., проф. А.И. Белостоцкий;
к.т.н., проф. А.И. Боровков;
д.т.н., проф. А. Бородинец;
PhD, проф. М. Велькович;
PhD, проф. Р.Д. Гарг;
PhD, М.Р. Гарифуллин;
Dr.-Ing, проф. Т. Грис;
д.т.н., проф. Т.А. Дацюк;
д.т.н., проф. В.В. Елистратов;
Dr.-Ing., проф. Т. Кэрки;
д.т.н., проф. Д.В. Козлов;
д.т.н., доцент С.В. Корниенко;
д.т.н., проф. Ю.Г. Лазарев;
д.т.н., проф. М.М. Мухаммадиев;
Dr.-Ing. Habil., проф. Х. Пастернак;
Dr.-Ing., проф. Ф. Рёгинер;
д.т.н., проф. Т.З. Султанов;
д.т.н., проф. М.Г. Тягунов;
акад. РАН, д.т.н., проф. М.П. Федоров;
Dr.-Ing., проф. Д. Хецк;
д.г.-м.н. А.Г. Шашкин;
д.т.н. В.Б. Штильман

Дата выхода: 27.12.2020

© ФГАОУ ВО СПбПУ, 2020
© Иллюстрация на обложке: Илья Смагин

Magazine of Civil Engineering

SCHOLAR JOURNAL

ISSN 2712-8172

Peer-reviewed scientific journal

Start date: 2008/09

8 issues per year

Publisher:

Peter the Great St. Petersburg Polytechnic University

Indexing:

Scopus, Russian Science Citation Index (WoS),
Compendex, EBSCO, Google Academia, Index
Copernicus, ProQuest, Ulrich's Serials Analysis System,
CNKI

Corresponding address:

29 Polytechnicheskaya st., Saint-Petersburg, 195251,
Russia

Editor-in-chief:

Ekaterina A. Linnik

Science editor:

Vitaly V. Sergeev

Deputy chief science editor:

Galina L. Kozinetc

Editorial board:

T. Awwad, PhD, professor
M.I. Balzannikov, D.Sc., professor
A.I. Belostotsky, D.Sc., professor
A.I. Borovkov, PhD, professor
A. Borodinets, Dr.Sc.Ing., professor
M. Veljkovic, PhD, professor
R.D. Garg, PhD, professor
M. Garifullin, PhD, postdoctorant
T. Gries, Dr.-Ing., professor
T.A. Datsyuk, D.Sc., professor
V.V. Elistratov, D.Sc., professor
T. Kärki, Dr.-Ing., professor
D.V. Kozlov, D.Sc., professor
S.V. Korniyenko, D.Sc., professor
Yu.G. Lazarev, D.Sc., professor
M.M. Muhammadiev, D.Sc., professor
H. Pasternak, Dr.-Ing.habil., professor
F. Rögener, Dr.-Ing., professor
T.Z. Sultanov, D.Sc., professor
M.G. Tyagunov, D.Sc., professor
M.P. Fedorov, D.Sc., professor
D. Heck, Dr.-Ing., professor
A.G. Shashkin, D.Sc.
V.B. Shtilman, D.Sc.

Date of issue: 27.12.2020

© Peter the Great St. Petersburg Polytechnic University.
All rights reserved.
© Coverpicture – Ilya Smagin

Contacts:

E-mail: mce@spbstu.ru
Web: <http://www.engstroy.spbstu.ru>

Contents

Popov, A.N., Lovtsov, A.D. Frictional contact problem in building constructions analysis	10001
Al Rjoub, Y.S., Hamad, A.G. Free vibration of axially loaded multi-cracked Timoshenko beams	10002
Lesovik, V.S., Glagolev, E.S., Voronov, V.V., Zagorodnyuk, L.Kh., Fediuk, R.S., Baranov, A.V., Alaskhanov, A.Kh., Svintsov, A.P. Durability behaviors of foam concrete made of binder composites	10003
Rybakov, V.A., Zhuvak, O.V., Hoffmann, A., Sergeeva, F.A., Verigo, P.A. The influence of reinforcing joints on the fire resistance of reinforced concrete structures	10004
Abdulsada, S.A., Kristaly, F., Torok, T.I. Distribution of corrosion products at the steel-concrete interface of XD3 concrete samples	10005
Erofeev, V.T., Rodin, A.I., Bochkin, V.S., Ermakov, A.A. The formation mechanism of the porous structure of glass ceramics from siliceous rock	10006
Nazirov, R.A., Inzhutov, I.S., Dubrovskaya, O.G., Gunenko, E.D., Vede, P.Y. Effect of sorption moisture content of heavy concrete on radon emanation	10007
Iskakbayev, A., Teltayev, B.B., Rossi, C.O., Yensebayeva, G., Abu, B., Kutimov, K.S. Impact of loading rate on asphalt concrete deformation and failure	10008
Shepelenko, T.S., Vatin, N.I., Zubkova, O.A. Hydration and structure formation of Chloride-Activated Cement Paste	10009
Hasan, M.M., Pial, M.A., Arafat, M.S., Miah, M.J., Miah, M.S. Influence of raw greywater on compressive strength of concrete	10010
Teltayev, B.B., Loprencipe, G., Bonin, G., Suppes, E.A., Tileu, K. Temperature and moisture in highways in different climatic regions	10011
Kozinetc, K.G., Kaarki, T., Barabanshchikov, Yu.G., Lahtela, V., Zotov, D.K. Mechanical properties of sustainable wooden structures reinforced with Basalt Fiber Reinforced Polymer	10012

+



Magazine of Civil Engineering

ISSN
2712-8172

journal homepage: <http://engstroy.spbstu.ru/>

DOI: 10.18720/MCE.100.1

Frictional contact problem in building constructions analysis

A.N. Popov*, A.D. Lovtsov

Pacific National University, Khabarovsk, Russia

* *E-mail: sanyapov@mail.ru*

Keywords: building constructions, contact nonlinearity, frictional contact, unilateral constraints, linear complementarity problem, numerical models, finite element method

Abstract. The article discusses the contact interaction of deformable building constructions or their parts. Such interaction is realized for example at: hydraulic structures; suspension pile foundations, girder, raft, sheet piling; friction bearings and kinematic bearings of seismically insulated buildings, etc. The subject of the study is the formulation of the contact interaction problem as a linear complementarity problem. Such formulation of the problem allows the use of effective step-by-step algorithms and provides minimum qualification requirements to user. Expansion of existing formulations of the problems of frictionless contact and contact with the known friction bound in the form of linear complementarity problem to the formulation of the frictional contact is offered. Eventually, a heuristic formulation of the contact problem with friction is obtained in the form of a linear complementarity problem. The problem is solved by the Lemke step-type algorithm in the form of a displacement method. The results of the solutions obtained on test problems and on the Ansys software almost coincide with the results obtained by the proposed algorithm.

1. Introduction

The object of this study is the contact interaction of deformable building constructions or their parts (suspension pile foundations; girder; raft; sheet piling; friction bearings and kinematic bearings of seismically insulated buildings; pipelines with frictional contact on supports). One of the important problems of strength analysis in the calculation of buildings is the problem of determining the contact interaction forces between deformable bodies [1–9]. The new formulation of the frictional contact problem is proposed in the form of a linear complementarity problem. In the case of solving contact problems with Coulomb friction, three main statements can be distinguished:

1. Frictionless contact when contact zone and separation zone of the contacting parts of the structure are unknown. The problem is formulated as a conditional minimization of a differentiable functional [10–13].
2. A problem with known friction bound, when the contact zone is known, but the cohering zone and the slippage zone are unknown. In this case, the problem is posed as a variational inequality, which can be reduced to unconditional minimization of a non-differentiable functional [1, 2, 7, 14–18].
3. The general case is when the contact zone, and inside it is the zone of cohering and slip are unknown in advance. In this case, the problem is also put in the form of a variational inequality, but there is no formulation of the problem as a minimum of the energy functional.

In civil engineering the most commonly used numerical methods for solving contact problems in the form of variational inequalities are method of Lagrange Multipliers, the Penalty Function Method and their modifications [10, 11, 19–23]. These methods are implemented in most software tools for calculating buildings that can solve contact problems [24–26]. It is also important to mention alternative methods for solving contact problems: 1) group of methods using contact finite elements [27–30]; 2) group using algorithms [14, 15, 31–34] of linear complementarity problem (LCP); 3) other methods [8, 35, 36].

The purpose of this work is to set new formulation of the frictional contact problem of deformable bodies in the LCP form. The tasks can be divided:



1. To expand the formulations of frictionless contact and contact with friction bound obtained by the authors of this article for the general case of frictional contact;
2. To propose a method (algorithm) for calculating such problems;
3. Test Algorithm;
4. To compare solutions obtained using known and proposed algorithms.

2. Methods

In the following formulation of the calculation of contact problems with friction – contact “node to node” is used. These nodes will be referred to as the contact pair. It is assumed that in each contact pair the points are connected by unilateral joints. Joint, normal to the contact zone is turned on when these points are in contact and turned off otherwise. It is supposed that unilateral joints work only in compression in the normal direction. Joint, tangential to the contact zone is turned on if the interaction forces are less than the friction bound and turned off if the interaction forces are equal to the friction bound. That is, when the joint is turned on, the slipping of the points of the contact pair is impossible, and when it is off, it is possible.

The following signs` rule is accepted:

- For forces and displacements normal to the contact surface: the compressive force of interaction of points of a contact pair $x_{ni} > 0$; mutual removal of points of a contact pair $z_{ni} > 0$ (Fig. 1, a).
- For forces and displacements tangentially to the contact surface: if the points of the contact pair conditionally spread apart by normal to the contact zone, then interaction forces $x_{\tau i} > 0$ will create a couple of forces with the moment in the clockwise direction; mutual displacement $z_{\tau i} > 0$, if it coincides in direction with $x_{\tau i} > 0$ (Fig. 1, b).

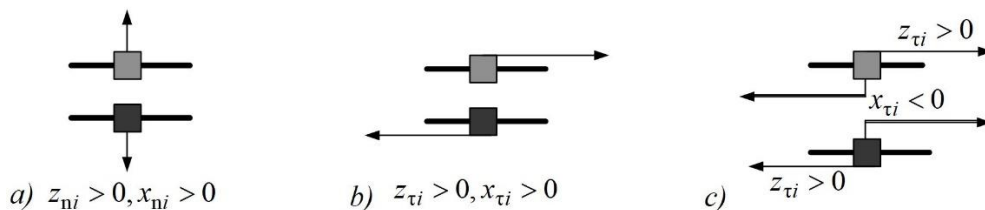


Figure 1. Unilateral constraints. The signs` rule for the interaction forces x and mutual displacements z .

In [14], cases of frictionless contact and contact with known friction bound are reduced to linear complementarity problems, and the displacement method (stiffness method) of their solution have been developed.

To implement the displacement method, it is necessary to form a contact stiffness matrix (CSM) and a contact load vector (CLV) in the main system of mentioned method. The main system of the displacement method is obtained from a given system by transformation of all unilateral joints (along the normal and tangential to the contact zone in each contact pair) into bilateral joints (Fig. 2, nodes are spaced for visibility). The component $R_{i,j}$ of the CSM is the effort in the main system of the displacement method in the entered joint i from a unit dislocation in the direction of the entered joint j . Component R_{Fi} of the CSM is an effort in the entered constraint i from external load.

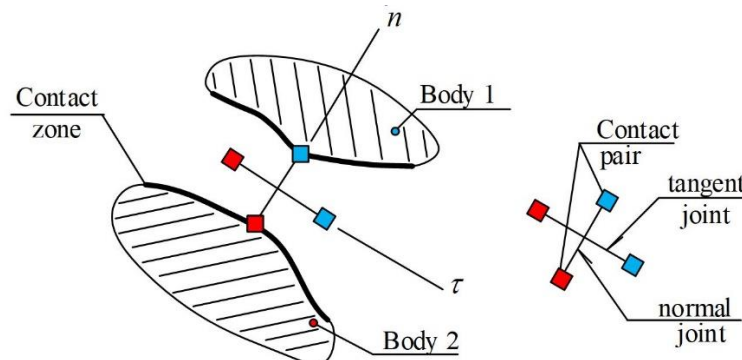


Figure 2. Constraints in the main system of the displacement method.

Frictionless contact. In this case, it is not necessary to enter joints tangentially to the contact zone. Thus, to form the main system, you should enter bilateral joints only normal to the contact zone in each contact pair. Therefore, to describe the stress-strain state (SSS) of the contact pair i of a given system, two non-negative variables are enough x_{ni}, z_{ni} . LCP for the unilateral frictionless contact has the form:

$$\begin{aligned} \mathbf{x}_n &= \mathbf{R}_{nn} \cdot \mathbf{z}_n + \mathbf{R}_{Fn}; \\ \mathbf{z}_n &\geq 0; \quad \mathbf{x}_n \geq 0; \quad \mathbf{z}_n^T \cdot \mathbf{x}_n = 0, \end{aligned} \tag{1}$$

where \mathbf{R}_{nn} is CSM $[m \times m]$ for joints in contact pairs along the normal to the contact zone from a unit dislocation of the nodes of contact pairs along the normal to the expected contact zone L (Fig. 3); $\mathbf{x}_n, \mathbf{z}_n$ are vectors $[m \times 1]$ of interaction forces and mutual displacements of contact pairs along the normal to the contact zone; \mathbf{R}_{Fn} is CLV $[m \times 1]$ for constraints normal to the contact zone; m is total number of contact pairs.

Frictional contact with known friction bound. In the works [16–18] the cases are considered for which contact with the known friction bound is realized. The calculation of such systems is reduced to the problem of unconditional optimization of a non-differentiable functional. In [14, 37], such problems, in turn, are reduced to the conditional optimization of a differentiable functional, conditions of Kuhn-Tucker which lead to LCP of the form:

$$\begin{aligned} \begin{bmatrix} \mathbf{x}_\tau^+ \\ \mathbf{x}_\tau^- \end{bmatrix} &= \begin{bmatrix} \mathbf{R}_{\tau\tau} & -\mathbf{R}_{\tau\tau} \\ -\mathbf{R}_{\tau\tau} & \mathbf{R}_{\tau\tau} \end{bmatrix} \cdot \begin{bmatrix} \mathbf{z}_\tau^+ \\ \mathbf{z}_\tau^- \end{bmatrix} + \begin{bmatrix} \mathbf{R}_{F\tau} \\ -\mathbf{R}_{F\tau} \end{bmatrix} + \begin{bmatrix} \mathbf{r}_f \\ \mathbf{r}_f \end{bmatrix}; \\ \mathbf{x}_\tau^+ &\geq 0; \quad \mathbf{x}_\tau^- \geq 0; \quad \mathbf{z}_\tau^+ \geq 0; \quad \mathbf{z}_\tau^- \geq 0; \quad \mathbf{z}_\tau^{+T} \cdot \mathbf{x}_\tau^+ = 0; \quad \mathbf{z}_\tau^{-T} \cdot \mathbf{x}_\tau^- = 0; \end{aligned} \tag{2}$$

where $\mathbf{R}_{\tau\tau}$ is CSM $[m \times m]$ for joints entered in contact pairs *tangentially* to the contact zone from a unit dislocation of contact pairs *tangential* to the contact zone. $\mathbf{R}_{F\tau}$ is CLV for the joints tangential to the contact zone; $\mathbf{x}_\tau = (\mathbf{x}_\tau^+ - \mathbf{x}_\tau^-) / 2$ is vector $[m \times 1]$ of efforts of interaction of contact pairs tangentially to the contact zone (Fig. 3, where q'', q' are external loads); $\mathbf{z}_\tau = \mathbf{z}_\tau^+ - \mathbf{z}_\tau^-$ is vector $[m \times 1]$ of mutual displacements of contact pairs tangentially to the contact zone; $\mathbf{r}_f = f \cdot \mathbf{x}_n$ is vector of friction bound; f is coefficient of friction between contact pairs; \mathbf{x}_n is pressing force vector.

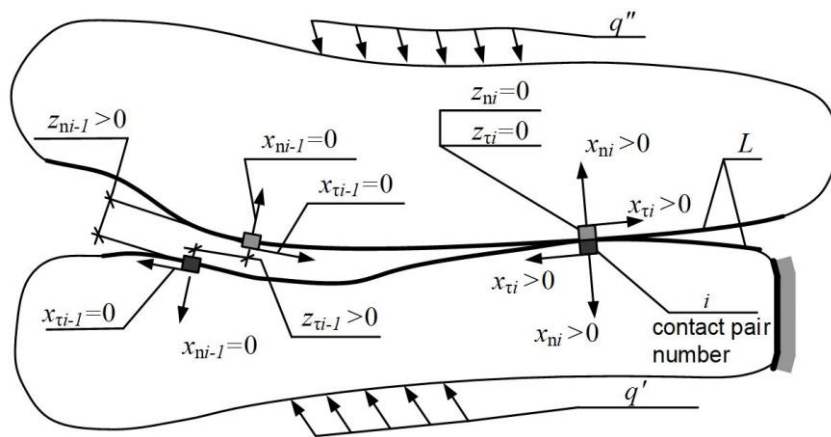


Figure 3. Contact of deformable bodies after deformation. Separation of $i-1$ contact pair and touch of i contact pair.

Note that to describe the SSS of a contact pair i of a given system, four non-negative variables are needed: $x_{ti}^+, x_{ti}^-, z_{ti}^+, z_{ti}^-$, since mutual displacements z_{ti} and forces x_{ti} have no sign limitation.

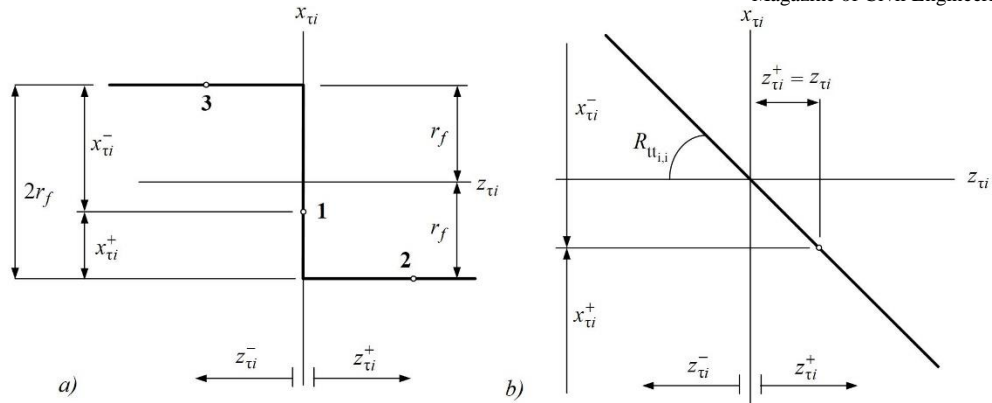


Figure 4. The dependence of the interaction forces and mutual displacements of the contact pair i : a) in a given system; b) in the main system.

The variable x_{ti}^+ can be understood as the “cohering reserve” of the contact pair i with the tendency (attempt) to shift from the catenation state in the direction $z_{ti} > 0$ (see sign` rule in Fig. 1). This case is shown in Fig. 4.

Fig. 4, a point 1. The variable x_{ti}^- is the “cohering reserve” of the contact pair i when attempting to shift from the catenation state towards $z_{ti} < 0$. The variables z_{ti}^+ and z_{ti}^- in turn are the mutual displacements of the points of the contact pair i in the positive and negative directions, respectively. That is, with a positive mutual displacement of $z_{ti} > 0$, we have $z_{ti}^+ > 0$, $z_{ti}^- = 0$ and $z_{ti} = z_{ti}^+$, and with a negative $z_{ti} < 0$ we have $z_{ti}^- > 0$, $z_{ti}^+ = 0$ and $z_{ti} = -z_{ti}^-$.

In this way, with exhaustion of the reserve $x_{ti}^+ = 0$ friction force in the contact pair is equal to friction bound $x_{ti}^+ = r_{fi}$ and slippage occurs in the direction $z_{ti} > 0$, i.e. variable $z_{ti}^+ > 0$ (point 2 on Fig. 4).

Fig. 4, a: when reserve x_{ti}^- is exhausted the situation is similar (point 3 on Fig. 4).

Let us turn further to the main system of the displacement method for the problem under consideration. It is not required to enter constraints normal to the contact zone. The main displacement method system is obtained by converting all unilateral friction constraints into bilateral. Thus, the slipping of points of a contact pair in the main system is excluded.

Vectors $\mathbf{x}_\tau, \mathbf{z}_\tau$ in the main system are connected by the ratio $\mathbf{x}_\tau = -\mathbf{R}_{\tau\tau} \cdot \mathbf{z}_\tau$ (taking into account accepted signs` rule Fig. 1, b and Fig. 1, c). Similar ratios are connecting the vectors $\mathbf{x}_\tau^+, \mathbf{x}_\tau^-, \mathbf{z}_\tau^+, \mathbf{z}_\tau^-$.

Figure 4, b, when z_{ti}^+ is increasing: x_{ti}^+ is decreasing and x_{ti}^- is increasing; when z_{ti}^- is increasing: x_{ti}^+ is increasing and x_{ti}^- is decreasing):

$$\begin{aligned} \mathbf{x}_\tau^+ &= -(-\mathbf{R}_{\tau\tau} \cdot \mathbf{z}_\tau^+) + (-\mathbf{R}_{\tau\tau} \cdot \mathbf{z}_\tau^-) = +\mathbf{R}_{\tau\tau} \cdot \mathbf{z}_\tau^+ - \mathbf{R}_{\tau\tau} \cdot \mathbf{z}_\tau^-; \\ \mathbf{x}_\tau^- &= +(-\mathbf{R}_{\tau\tau} \cdot \mathbf{z}_\tau^+) - (-\mathbf{R}_{\tau\tau} \cdot \mathbf{z}_\tau^-) = -\mathbf{R}_{\tau\tau} \cdot \mathbf{z}_\tau^+ + \mathbf{R}_{\tau\tau} \cdot \mathbf{z}_\tau^-. \end{aligned}$$

If we also take into account external load and friction bound, then:

$$\begin{aligned} \mathbf{x}_\tau^+ &= \mathbf{R}_{\tau\tau} \cdot \mathbf{z}_\tau^+ - \mathbf{R}_{\tau\tau} \cdot \mathbf{z}_\tau^- + \mathbf{R}_{F\tau} + \mathbf{r}_f, \\ \mathbf{x}_\tau^- &= -\mathbf{R}_{\tau\tau} \cdot \mathbf{z}_\tau^+ + \mathbf{R}_{\tau\tau} \cdot \mathbf{z}_\tau^- - \mathbf{R}_{F\tau} + \mathbf{r}_f, \end{aligned} \tag{3}$$

which coincides with the system of equations in (2).

Thus, in both cases considered above, the LCP can be formed directly using the main system of the displacement method. It is further proposed to use this approach.

General case of frictional contact. In the general case of friction contact, the formulation of the problem in form of conditional extremum of some functional is not gotten. Therefore, based on “plausible” reasoning, we propose further setting up a general case of friction contact in the form of a LCP, written for a discretized system. In this case, for the formation of the main system, you should enter bilateral joints along the normal and tangential to the contact zone for each contact pair.

In this case, for the formation of the main system, it is needed to enter bilateral joints along the normal and tangential to the contact zone for each contact pair. To describe the SSS of the contact pair i of a given system, we use six non-negative variables $x_{ni}, z_{ni}, x_{\tau i}^+, x_{\tau i}^-, z_{\tau i}^+, z_{\tau i}^-$. It is clear that in such a main system, the force \mathbf{x}_n depends not only on \mathbf{z}_n , but also on \mathbf{z}_τ :

$$\mathbf{x}_n = \mathbf{R}_{nn} \cdot \mathbf{z}_n + \mathbf{R}_{n\tau} \cdot \mathbf{z}_\tau + \mathbf{R}_{Fn},$$

where $\mathbf{R}_{n\tau}$ is CSM $[m \times m]$ for normal joints from unit dislocations tangential to the contact zone.

Or, given that: $\mathbf{z}_\tau = \mathbf{z}_\tau^+ - \mathbf{z}_\tau^-$:

$$\mathbf{x}_n = \mathbf{R}_{nn} \cdot \mathbf{z}_n + \mathbf{R}_{n\tau} \cdot \mathbf{z}_\tau^+ - \mathbf{R}_{n\tau} \cdot \mathbf{z}_\tau^- + \mathbf{R}_{Fn}, \quad (4)$$

In addition to (3), we take into account the dependence on $\mathbf{x}_\tau^+, \mathbf{x}_\tau^-$ and on \mathbf{z}_n :

$$\begin{aligned} \mathbf{x}_\tau^+ &= \mathbf{R}_{\tau n} \cdot \mathbf{z}_n + \mathbf{R}_{\tau\tau} \cdot \mathbf{z}_\tau^+ - \mathbf{R}_{\tau\tau} \cdot \mathbf{z}_\tau^- + \mathbf{R}_{F\tau} + \mathbf{r}_f, \\ \mathbf{x}_\tau^- &= -\mathbf{R}_{\tau n} \cdot \mathbf{z}_n - \mathbf{R}_{\tau\tau} \cdot \mathbf{z}_\tau^+ + \mathbf{R}_{\tau\tau} \cdot \mathbf{z}_\tau^- - \mathbf{R}_{F\tau} + \mathbf{r}_f, \end{aligned} \quad (5)$$

where $\mathbf{R}_{\tau n}$ is CSM $[m \times m]$ for tangential joints from unit dislocations normal to the contact zone (note that $\mathbf{R}_{\tau n} = \mathbf{R}_{n\tau}^T$), \mathbf{r}_f is friction bound depends on contact compressive interaction forces (4):

$$\mathbf{r}_f = f \cdot \mathbf{x}_n = f \cdot (\mathbf{R}_{nn} \cdot \mathbf{z}_n + \mathbf{R}_{n\tau} \cdot \mathbf{z}_\tau^+ - \mathbf{R}_{n\tau} \cdot \mathbf{z}_\tau^- + \mathbf{R}_{Fn}). \quad (6)$$

As a result of combining (4) and (5), taking into account (6), we have:

$$\begin{aligned} \mathbf{x}_n &= \mathbf{R}_{nn} \cdot \mathbf{z}_n + \mathbf{R}_{n\tau} \cdot \mathbf{z}_\tau^+ - \mathbf{R}_{n\tau} \cdot \mathbf{z}_\tau^- + \mathbf{R}_{Fn}; \\ \mathbf{x}_\tau^+ &= \mathbf{R}_{\tau n} \cdot \mathbf{z}_n + \mathbf{R}_{\tau\tau} \cdot \mathbf{z}_\tau^+ - \mathbf{R}_{\tau\tau} \cdot \mathbf{z}_\tau^- + \mathbf{R}_{F\tau} + f \cdot (\mathbf{R}_{nn} \cdot \mathbf{z}_n + \mathbf{R}_{n\tau} \cdot \mathbf{z}_\tau^+ - \mathbf{R}_{n\tau} \cdot \mathbf{z}_\tau^- + \mathbf{R}_{Fn}); \\ \mathbf{x}_\tau^- &= -\mathbf{R}_{\tau n} \cdot \mathbf{z}_n - \mathbf{R}_{\tau\tau} \cdot \mathbf{z}_\tau^+ + \mathbf{R}_{\tau\tau} \cdot \mathbf{z}_\tau^- - \mathbf{R}_{F\tau} + f \cdot (\mathbf{R}_{nn} \cdot \mathbf{z}_n + \mathbf{R}_{n\tau} \cdot \mathbf{z}_\tau^+ - \mathbf{R}_{n\tau} \cdot \mathbf{z}_\tau^- + \mathbf{R}_{Fn}). \end{aligned} \quad (7)$$

Adding to the system of equations (7) the conditions of non-negativity and complementarity non-rigidity from (1) and (2) we come to the LCP for frictional contact:

$$\begin{aligned} \begin{bmatrix} \mathbf{x}_n \\ \mathbf{x}_\tau^+ \\ \mathbf{x}_\tau^- \end{bmatrix} &= \begin{bmatrix} \mathbf{R}_{nn} & \mathbf{R}_{n\tau} & -\mathbf{R}_{n\tau} \\ \mathbf{R}_{\tau n} + f \cdot \mathbf{R}_{nn} & \mathbf{R}_{\tau\tau} + f \cdot \mathbf{R}_{n\tau} & -\mathbf{R}_{\tau\tau} - f \cdot \mathbf{R}_{n\tau} \\ -\mathbf{R}_{\tau n} + f \cdot \mathbf{R}_{nn} & -\mathbf{R}_{\tau\tau} + f \cdot \mathbf{R}_{n\tau} & \mathbf{R}_{\tau\tau} - f \cdot \mathbf{R}_{n\tau} \end{bmatrix} \cdot \begin{bmatrix} \mathbf{z}_n \\ \mathbf{z}_\tau^+ \\ \mathbf{z}_\tau^- \end{bmatrix} + \begin{bmatrix} \mathbf{R}_{Fn} \\ \mathbf{R}_{F\tau} + f \cdot \mathbf{R}_{Fn} \\ -\mathbf{R}_{F\tau} + f \cdot \mathbf{R}_{Fn} \end{bmatrix} \\ \mathbf{z}_n &\geq 0; \quad \mathbf{x}_n \geq 0; \quad \mathbf{z}_n^T \cdot \mathbf{x}_n = 0; \end{aligned} \quad (8)$$

$$\mathbf{x}_\tau^+ \geq 0; \quad \mathbf{x}_\tau^- \geq 0; \quad \mathbf{z}_\tau^+ \geq 0; \quad \mathbf{z}_\tau^- \geq 0; \quad \mathbf{z}_\tau^{+T} \cdot \mathbf{x}_\tau^+ = 0; \quad \mathbf{z}_\tau^{-T} \cdot \mathbf{x}_\tau^- = 0,$$

There are many methods for solving LCP. They can be divided into 2 groups: iterative methods (including using machine learning [38, 39]); step methods, that can obtain a solution in a finite number of steps. Lemke's algorithm and its modifications are step methods and allow you to physically interpret each step of the algorithm. And this interpretation does not contradict the physical nature of the problem.

To solve the LCP (7), we use the Lemke method with the extension parameter of the problem p [40, 41], which in our case takes on the physical meaning of an additional “tightening weight” (force bringing together nodes) of the contact pair [14, 42]. The steps of the Lemke algorithm are a change of work schemes with a sequential decrease in the “tightening weight”. Three types of LCP solutions are possible:

1. a trivial solution is a case when separation and slipping do not occur along the supposed contact zone (the main system is the solution to the problem);

2. a normal solution is when the value of the artificially entered “tightening weight” p becomes equal to zero;
3. a ray solution for which there are two interpretations:
 - $p > 0$ means that the given system is substatic structure (when the “tightening weight” is fully removed, the displacements become uncertain).
 - the p value is close to zero and small in comparison with the friction bound. This can be interpreted as a normal solution.

3. Results and Discussion

There are plenty of problems in the construction of buildings and structures that are connected with frictional unilateral contact, for example: contact seams [28]; kinematic foundations; constructions under the soil which interacting with that soil with separation and slippage [31, 33], multilayer structures; crack opening in concrete elements; slope stability [32], frictional supports of seismically insulated building. We show the features of the solution with a few simple examples. All results were rounded to 3 decimal places.

Example 1. We consider a freely supported multi-span beam on unilateral supports with friction (Fig. 5). The beam is approximated by frame rod elements with three degrees of freedom in the node. It is loaded with forces F that do not change during deformation, which ensures the constant friction bound $f \cdot F$ on supports. The solution to this problem is obvious:

1. with $F_2 \leq f \cdot F$ the cohering of the beam with all the supports is realized;
2. with $f \cdot F < F_2 < 6f \cdot F$, slippage is realized on the part of the supports, and on the other part – cohesion;
3. with $F_2 > 6f \cdot F$, slippage is realized on all six supports and the beam displacements become undefined;
4. when $F_2 = 6f \cdot F$, the friction bound is realized on all supports, while the displacements on the extreme left support are zero, and on all other supports – slippage. This case is the most difficult for the algorithms.

In the first case, according to the algorithm, we obtain a trivial solution (see (7)):

$$\mathbf{z}_n = 0, \mathbf{z}_\tau^+ = 0, \mathbf{z}_\tau^- = 0, \mathbf{x}_n = \mathbf{R}_{F_n}, \mathbf{x}_\tau^+ = \mathbf{R}_{F_\tau} + f \cdot \mathbf{R}_{F_n}, \mathbf{x}_\tau^- = -\mathbf{R}_{F_\tau} + f \cdot \mathbf{R}_{F_n},$$

$$\text{here: } \mathbf{x}_\tau = (\mathbf{x}_\tau^+ - \mathbf{x}_\tau^-) / 2 = \mathbf{R}_{F_\tau} \text{ and } \mathbf{z}_\tau = \mathbf{z}_\tau^+ - \mathbf{z}_\tau^- = 0.$$

In the second case, using the algorithm, we obtain a normal solution in which at least one support is cohering with the beam, or the beam is slipping on at least one support. The results of solving the LCP, with $F_2 = F = 100H$, for tangential mutual displacements (increased scale) and interaction forces (friction forces) on unilateral supports are presented in Fig. 5, a (in a black frame the values for the interaction forces are shown, and in grey frames – mutual displacements).

In the third case, as a result of using the algorithm, we obtain a “ray solution” with the parameter $p > 0$. This is interpreted as the destruction of the system: a further decrease in the “tightening weight” p will lead to undefined displacements. In the fourth case, the result of using the algorithm can be both specific interaction forces and mutual displacements in the contact area ($p = 0$, “normal solution”), as well as the “ray solution”, which is due to rounding errors, the “tightening weight” parameter is $p \ll f \cdot F$ (this situation should also be interpreted as a “normal solution”). The results of solving the LCP, with $F_2 = 6 \cdot f \cdot F = 100H$, for tangential mutual displacements (increased scale) and interaction forces (friction forces) on unilateral supports are presented in Fig. 5, b. In this case, the ratio of the applied external load to the “tightening weight” turned out:

$$F/p > 10^{13}.$$

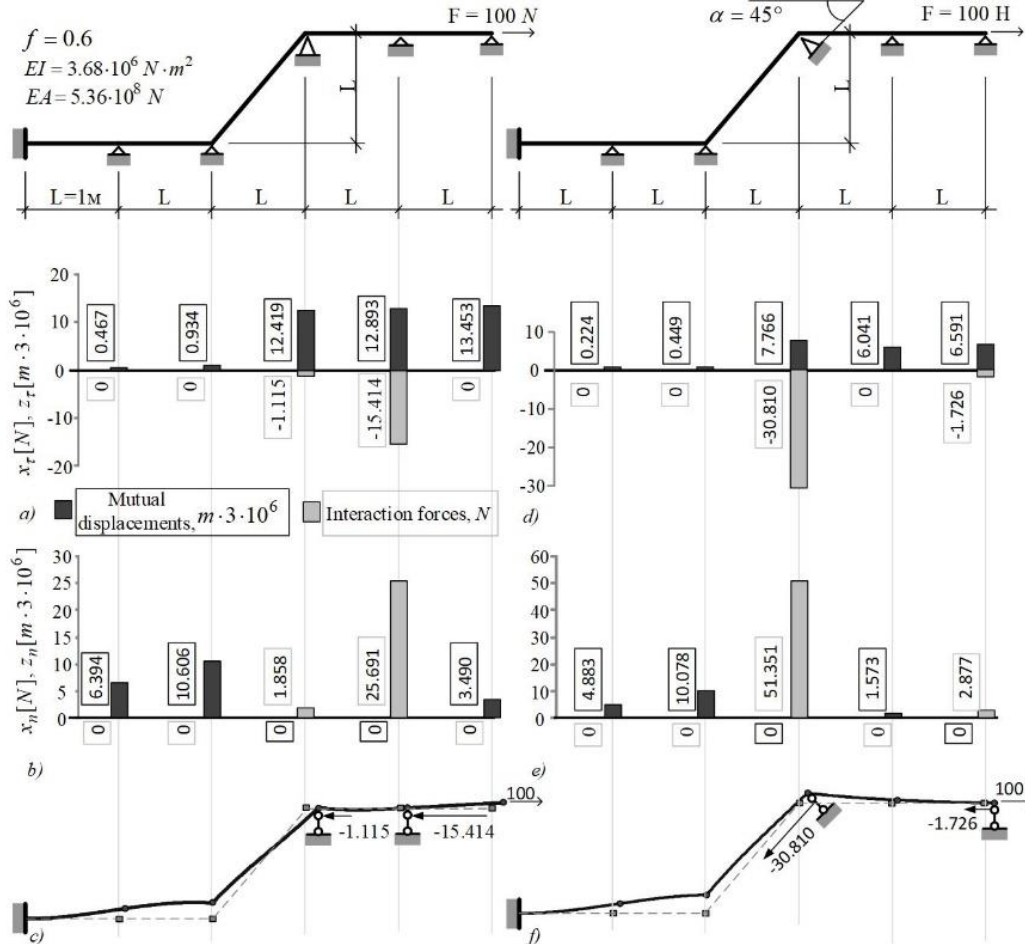


Figure 6. Scheme of the frame and calculation results: a-c) the frame with vertical supports, d-f) the frame with the third rotated support.

Example 3. The plane deformation problem for plates 0.1 m thick and 8m by 4m size (Fig. 7). For the plate approximation four-node finite element with two degrees of freedom in the node was used. Dimensions of square four-node finite elements 0.5x0.5 m. The expected contact zone considered to be fixed [26]. Two cases of support conditions of the left boundary with a rigidly pinched lower plate at the base are considered.

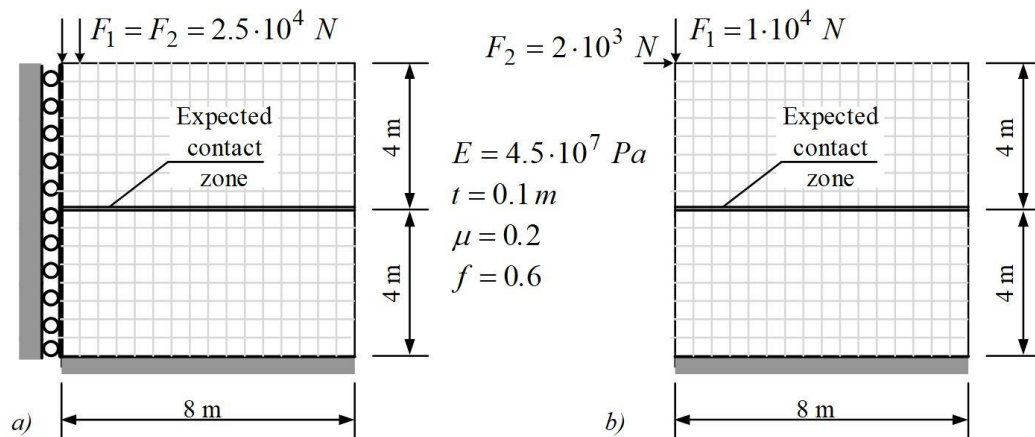


Figure 7. The design scheme of the plates for the calculation of the contact problem: a) with hinge support on the left, b) without supports on the left.

Use of CSM and CLV for a problem (at Fig. 7, a) with the total number of unknowns equal to 612, the contact problem (8) is formed using only 48 unknowns, and in [12], [26–29] and others the size of the problem is determined by the total number of degrees of freedom. The results of solving LCP for frictional unilateral contact of the plates with hinge supports on the left and deformation of the contact zone (S50:1) are shown in Fig. 8 (note that results are shown from the second node from left, because first one is fixed in horizontal direction and it is connecting plates). The results of solving LCP for plates without supports on the left (free boundary) with additional horizontal load and frictional unilateral contact along all bottom of the upper body (it can move as a rigid whole) are shown in Fig. 9. Note, that friction bound occurred on the leftmost contact pair, this case similar with situation 4 in example 1.

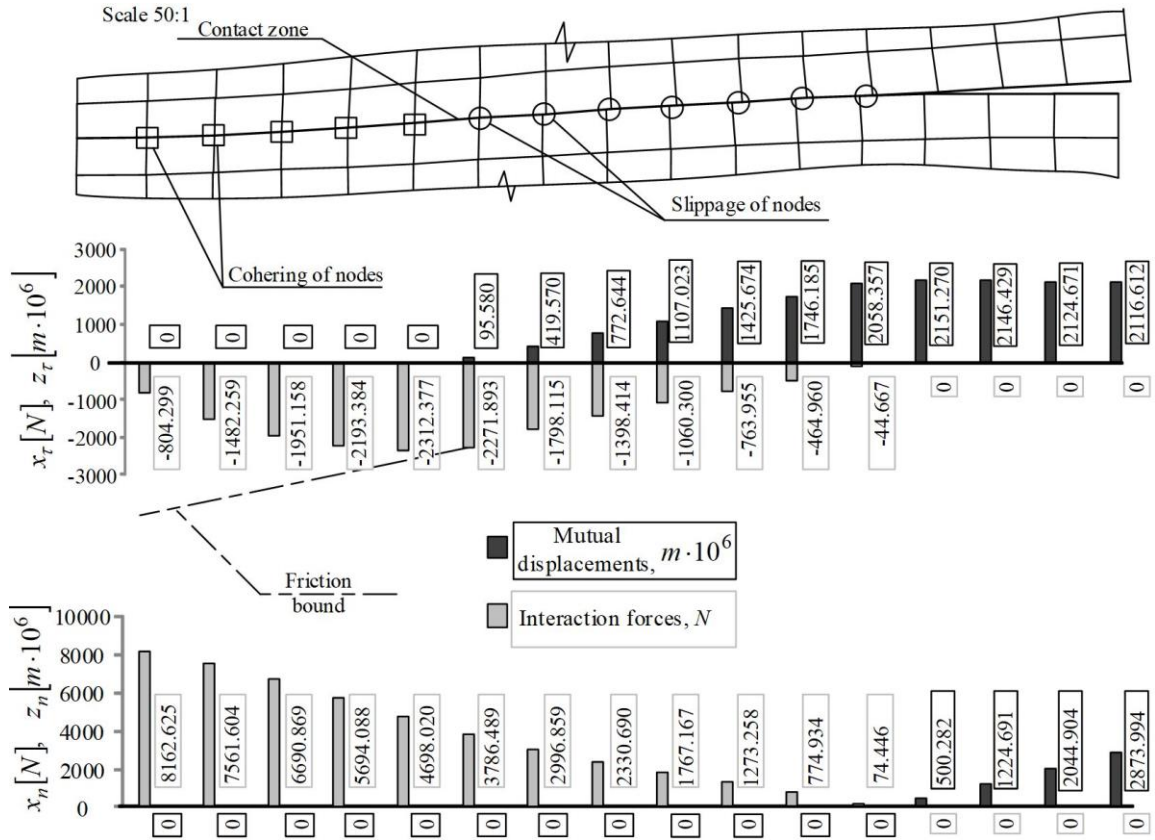


Figure 8. Plates calculation results of LCP with hinge supports on the left.

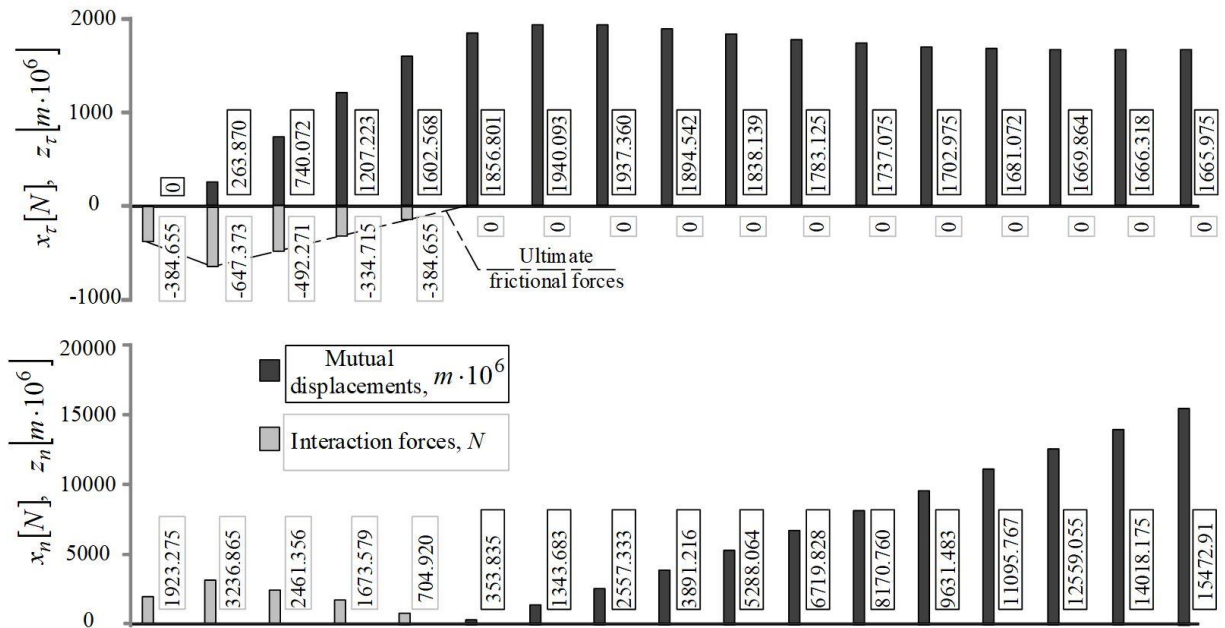


Figure 9. Plates calculation results of LCP with the free left boundary.

The problem (case with hinged left side Fig. 7, a) was calculated on Ansys 18.2 Academic. It's turned out that contact parameters that most strongly affecting the result are: Penetration Tolerance and Elastic Slip Tolerance. A decrease in the values of these parameters brought the Ansys solution closer to the solution obtained using the algorithm described in this paper. Getting a more precise solution in Ansys requires (thorough) fine-tuning the program. The second case showed on Fig. 7, b can't be solved strictly without adding boundary conditions (it have to be fixed from moving as a rigid whole) to the upper body in Ansys. Allowance of the penetration [26], [30] and requiring of fine-tuning [25], [29], [36] is normal to the existing most widespread unilateral contact solvers.

4. Conclusions

1. A heuristic formulation of the contact problem with friction is obtained in the form of a linear complementarity problem

2. To solve this problem, the displacement method has been developed as a modification of the Lemke step by step algorithm. For discretized problems, this method ensures the fulfillment of the non-interpenetration condition; does not use the artificial concept of “stiffness of contact joints”; is step by step, which removes the question of the user assigning parameters to exit the iterative process.

3. The algorithm has been tested on a large number of problems. The algorithm has proven its effectiveness by coinciding with exact solutions or solutions obtained by other algorithms.

4. Comparison of the results of solutions obtained using the proposed algorithm and the Ansys 18.2 Academic software showed their almost complete match. Adjustment of the contact parameters in Ansys brought the solution closer to the solution obtained using the proposed displacement method. Getting a more precise solution in Ansys requires (thorough) fine-tuning the program.

References

- Glowinski, R., Lions, J.-L., Trémolières, R. Numerical Analysis of Variational Inequalities Elsevier Science, 1981. DOI: 10.1016/S0168-2024(08)70201-7
- Duvaut, G., Lions, J.-L. Inequalities in Mechanics and Physics. (219). Berlin, Heidelberg: Springer Berlin Heidelberg, 1976. DOI: 10.1007/978-3-642-66165-5
- Kravchuk A.S., Neittaanmäki P.J. Variational and Quasi-Variational Inequalities in Mechanics. (147). Dordrecht: Springer Netherlands, 2007. DOI: 10.1007/978-3-642-66165-5
- Panagiotopoulos, P.D. Inequality Problems in Mechanics and Applications. Convex and Nonconvex Energy Functions. Birkhäuser: Boston-Base-Stuttgart, 1985. DOI: 10.1007/978-1-4612-5152-1
- Eck, C., Jarusek, J., Krbec, M. Unilateral Contact Problems. New York: CRC Press, 2005. DOI: 10.1201/9781420027365
- Sofonea, M., Matei, A. Mathematical Models in Contact Mechanics. Cambridge: Cambridge University Press, 2012. DOI: 10.1201/9781420027365
- Aleksandrov, V.M., Kalker, J.J., Pozharsky, D.A. The spatial contact problem for two-layered of elastic base with pre-unknown contact area. Izv. RAN, Mekhanika tverdogo tela. 1999. (4). Pp. 51–55. URL: <http://mtt.ipmnet.ru/ru/Issues.php?y=1999&n=4>
- Vorovich, I.I., Aleksandrov, V.M. Mekhanika kontaktnykh vzaimodeistvii [Contact Mechanics Interaction]. Moscow: Fizmatlit, 2001. URL: https://www.rubr.ru/rffi/ru/books/o_460?FILTER_ID=23@2
- Raous, M. Art of Modeling in Contact Mechanics. The Art of Modeling Mechanical Systems. (570). Springer, 2016. Pp. 203–276. DOI: 10.1007/978-3-319-40256-7_4
- Kravchuk, A.S. The variational method in contact problems. The present state of the problem and trends in its development. Journal of Applied Mathematics and Mechanics. 2009. № 3(73). Pp. 351–357. DOI: 10.1016/j.jappmathmech.2009.07.004
- Azbelev, N., Bravyi, E., Gusarenko, S. On a New Approach to Some Problems of Classical Calculus of Variations. Nonlinear Dynamics and Systems Theory. 2002. № 2(2). Pp. 117–124. URL: https://www.researchgate.net/publication/2664169-80_On_a_new_approach_to_some_problems_of_classical_calculus_of_variations
- Ignatyev, A.V., Ignatyev, V.A., Onischenko, E.V. Analysis of Systems with Unilateral Constraints through the Finite Element Method in the Form of a Classical Mixed Method. Procedia Engineering. 2016. (150). Pp. 1754–1759. DOI: 10.1016/j.proeng.2016.07.166
- Morozov, N.F., Tovstik, P.Y. Bending of a two-layer beam with non-rigid contact between the layers. Journal of Applied Mathematics and Mechanics. 2011. № 1(75). Pp. 77–84. DOI: 10.1016/j.jappmathmech.2011.04.012
- Lovtsov, A.D. Algoritmy metoda peremeshchenij dlya raschyota sistem s odnostoronnimi svyazyami [Algorithms of the displacements method for the calculation of systems with unilateral constraints]. Scientific and technical bulletin of St. Petersburg State Polytechnic University. 2004. 2(36). Pp. 220–227. URL: <https://engtech.spbstu.ru/issue/36/>
- Lovtsov, A.D. Algoritmy rascheta sistem s odnostoronnimi svyazyami metodom sil [Algorithms of the force method for the calculation of systems with unilateral constraints]. Scientific and technical bulletin of St. Petersburg State Polytechnic University. 2003. 3(33). Pp. 186–192. URL: <https://engtech.spbstu.ru/issue/33/>
- Rozin, L.A., Lovtsov, A.D. Izgib balki-truboprovoda, vzaimodejstvuyushchej s uprugim osnovaniem pri dejstvii treniya Kulona [Bending of a beam-pipeline, interacting with an elastic base under the action of Coulomb friction]. Izvestie Vusov. Stroitelstvo. 2005. 7(559). Pp. 17–22. URL: <http://izvuzstr.sibstrin.ru/uploads/publication/fulltext/N7-2005.pdf>
- Rozin, L.A., Lovtsov, A.D. Izgib balki-truboprovoda, vzaimodejstvuyushchej s nelinejno-uprugim osnovaniem, pri uchete treniya Kulona [Beam-Pipeline Interacting with Nonlinear Elastic Foundation considering Coulomb Friction Bending Analysis]. St.-Petersburg State Polytechnical University Scientific and Technical Bulletin. 2005. 3(41). Pp. 132–142. URL: <https://engtech.spbstu.ru/issue/41/>
- Rozin, L.A., Lovtsov, A.D., Smirnov, M.S. Prodol'naya deformaciya mnogoprolyotnoj balki s treniem i podatlivost'yu opor [Longitudinal deformation of a multi-span beam with friction and compliance of supports]. Izvestie Vusov. Stroitelstvo. 2004. 8(548). Pp. 17–22. URL: <http://izvuzstr.sibstrin.ru/uploads/publication/fulltext/8-2004.pdf>
- Kikuchi, N., Oden, J.T. Contact Problems in Elasticity. Philadelphia: Society for Industrial and Applied Mathematics, 1988. DOI: 10.1137/1.9781611970845
- Bathe, K.J., Chaudhary, A.A. A solution method for planar and axisymmetric contact problems. International Journal for Numerical Methods in Engineering. 1985. 21. Pp. 65–88. DOI: 10.1002/nme.1620210107
- Klarbring, A. A mathematical programming approach to three-dimensional contact problems with friction. Computer Methods in Applied Mechanics and Engineering. 1986. 58. Pp. 175–200. DOI: 10.1016/0045-7825(86)90095-2
- Landenberger, A., El-Zafrany, A. Boundary element analysis of elastic contact problems using gap finite elements. Computers and Structures. 1999. No. 6(71). Pp. 651–661. DOI: 10.1016/S0045-7949(98)00303-4
- Parisch, H. A consistent tangent stiffness matrix for three-dimensional non-linear contact analysis. International Journal for Numerical Methods in Engineering. 1989. No. 8(28). Pp. 1803–1812. DOI: 10.1002/nme.1620280807

24. Zhiltsov, A.V. Modified duality scheme for numerical simulation of the contact between elastic bodies. *Mathematical notes of NEFU*. 2016. No. 4(23). Pp. 99–114. URL: <http://www.mzsvfu.ru/index.php/mz/article/view/modified-duality-scheme-for-numerical-simulation-of-the-contact-between-elastic-bodies>
25. Semenov, A.S., Semenov, S.G., Melnikov, B.E., Tikhonov, V.S. Modeling of indentation and slip of wedge punch. *Magazine of Civil Engineering*. 2017. 74(6). Pp. 78–101. DOI: 10.18720/MCE.74.8
26. Barboteu, M., Ouakik, Y., Sofonea, M. Numerical modelling of a dynamic contact problem with normal damped response and unilateral constraint. *Journal of Theoretical and Applied Mechanics*. 2018. No. 2(56). Pp. 483–496. DOI: 10.15632/jtam-pl.56.2.483
27. Lukashovich, A.A., Rozin, L.A. On the decision of contact problems of structural mechanics with unilateral constraints and friction by step-by-step analysis. *Magazine of Civil Engineering*. 2013. 36(1). Pp. 75–81. DOI: 10.5862/MCE.36.9
28. Lukashovich, A.A. Computational modelling of stiffness and strength properties of the contact seam. *Magazine of Civil Engineering*. 2018. 81(5). Pp. 149–159. DOI: 10.18720/MCE.81.15
29. Boki, I.B. Chislennyj podhod k resheniyu kontaktnoj zadachi vzaimodejstviya dvuh uprugih tel s uchyotom treniya i istorii prilozheniya vneshnego nagruzheniya [Numerical approach to the solution of the contact problem of the interaction of two elastic bodies, taking into account the history of the application of external loading]. *Vestnik YSU*. 2006. No. 3(3). Pp. 42–46. URL: <https://cyberleninka.ru/article/n/chislennyj-podhod-k-resheniyu-kontaktnoy-zadachi-vzaimodejstviya-dvuh-uprugih-tel-s-uchetom-treniya-i-istorii-prilozheniya-vneshnego>
30. Berezhnoi, D.V., Sagdatullin, M.K. Calculation of interaction of deformable designs taking into account friction in the contact zone by finite element method. *Contemporary Engineering Sciences*. 2015. No. 23(8). Pp. 1091–1098. DOI: 10.12988/ces.2015.58237
31. Fedorova, V.S., Lovtsov, A.D. The calculation of corrugated culvert as arch, which interacts with an elastic medium through coulomb friction. *New ideas of the new century: proceedings of the Thirteenth International Scientific Conference: in 3 vol.* 2013. 3. Pp. 469–473. URL: <https://elibrary.ru/item.asp?id=19138399>
32. Fedorova, V.S., Stepanova, N.O., Lovtsov, A.D. Lemke algorithm for analyzing of slope stability. *New ideas of the new century: materials of the Eleventh International Scientific Conference of the IAS TOGU: in 2 vol.* 2011. 2. Pp. 144–149. URL: <https://elibrary.ru/item.asp?id=18964360>
33. Popov, A.N., Lovtsov, A.D. The calculation of a culvert in a high mound of a road as a contact problem with friction. *IOP Conference Series: Materials Science and Engineering*. 2018. No. 1(456). DOI: 10.1088/1757-899X/456/1/012085
34. Negrut, D., Serban, R., Tasora, A. Posing multibody dynamics with friction and contact as a differential complementarity problem. *Journal of Computational and Nonlinear Dynamics*. 2018. No. 1(13). Pp. 6. DOI: 10.1115/1.4037415
35. Stankevich, I. Mathematical Modeling of Contact Problems of Elasticity Theory with Continuous Unilateral Contact. *Mathematics and Mathematical Modeling*. 2015. 4. Pp. 93–110. DOI: 10.7463/mathm.0515.0812348
36. Streliaev, Y.M. A nonlinear boundary integral equations method for the solving of quasistatic elastic contact problem with Coulomb friction. *Journal of Samara State Technical University, Ser. Physical and Mathematical Sciences*. 2016. No. 2(20). Pp. 306–327. DOI: <https://doi.org/10.14498/vsgtu1471>
37. Mitra, G., Cottle, R.W., Giannessi, F., Lions, J.L. Variational Inequalities and Complementarity Problems – Theory and Application. *The Journal of the Operational Research Society*. 1981. No. 9(32). Pp. 848. DOI: 10.2307/2581414
38. Liao, L.Z., Qi, H.D. A neural network for the linear complementarity problem. *Mathematical and Computer Modelling*. 1999. No. 3(29). Pp. 9–18. DOI: 10.1016/S0895-7177(99)00026-6
39. Liao, L.Z., Qi, H.D., Qi, L. Solving nonlinear complementarity problems with neural networks: A reformulation method approach. *Journal of Computational and Applied Mathematics*. 2001. 131. Pp. 343–359. DOI: 10.1016/S0377-0427(00)00262-4
40. Lemke, C.E. Bimatrix Equilibrium Points and Mathematical Programming. *Management Science*. 1965. No. 7(11). Pp. 681–689. DOI: 10.1287/mnsc.11.7.681
41. Lemke, C.E. Some pivot schemes for the linear complementarity problem. *Complementarity and Fixed Point Problems*. 7. 1978. Pp. 15–35. DOI: 10.1007/bfb0120779
42. Lovtsov, A.D. Primenenie algoritma Lemke k zadache izgiba balki, vzaimodejstvuyushchej s uprugim osnovaniem posredstvom treniya Kulona [Application of the Lemke algorithm to the problem of bending a beam, interacting with an elastic base by means of Coulomb friction]. *Bulletin of Civil Engineers*. 2006. No. 6(1). Pp. 110–114. URL: <https://elibrary.ru/item.asp?id=12859487>

Contacts:

Aleksandr Popov, sanyapov@mail.ru

Alexander Lovtsov, Lovtsov@bk.ru



DOI: 10.18720/MCE.100.2

Free vibration of axially loaded multi-cracked Timoshenko beams

Y.S. Al Rjoub^a, A.G. Hamad^b

^a Civil Engineering Department, Jordan University of Science and Technology, Irbid, Jordan

^b Jordan University of Science and Technology, Irbid, Jordan

* E-mail: ysalrjoub@just.edu.jo

Keywords: cracked Timoshenko beam, shear deformation, rotary inertia, free vibration, buckling load, transfer matrix.

Abstract. In this paper, the free vibration of axially-loaded, multi-cracked Timoshenko beams with differing boundary conditions, namely, hinged-hinged, fixed-fixed, fixed-hinged, and fixed-free is studied. The cracked beam system is represented as several beam segments connected by massless rotational springs with sectional flexibility. Each segment is assumed to obey the Timoshenko beam theory. A simple transfer matrix method is used to derive the characteristic equation of the axially-loaded, multi-cracked beam with differing boundary conditions. The characteristic equation and corresponding mode shapes are a function of natural frequency, crack size and location, and physical parameters of the beam. In this paper, the effects of crack depth, number of cracks, position of cracks, axial load, shear deformation and rotary inertia on the dynamic behavior of multi-cracked beams are studied in detail. It is found that there is good agreement between the results obtained in this study and results available in the literature. Additionally, interesting observations overlooked by other researchers are obtained.

1. Introduction

Many engineering structures suffer from mechanical vibrations, environmental effects, corrosion, extended service and cyclic loading, etc. that create structural defects, including cracks. These cracks change the dynamic properties of the structure, such as natural frequency and mode shape. A crack in a beam element introduces local flexibility due to strain energy concentrations in the vicinity of the crack tip under load. This flexibility changes the dynamic behavior of the structural member.

There has been much experimental and analytical research performed on the effects of cracking and damage on the safety of structures [1–5]. In this paper, the local flexibility method is used, which considers the cracked beam as several beam segments with the same properties connected by massless rotational springs. Local flexibility is used by [6] to estimate the crack stress intensity factor. The authors of [7–9] used Castigliano's theorem and fracture mechanics to compute the flexibility of the cracked region of a uniform beam with a transverse surface crack, which is a function of the ratio of crack depth to the height of the cross-section. The function was obtained experimentally, according to the measurements provided by [10]. This factor can also be obtained from [11]. Many researchers studied the free vibration of cracked Euler-Bernoulli and Timoshenko beams, both analytically and experimentally, [12–19]. The free vibration of cracked Timoshenko beams with various boundary conditions is studied by [20] using ultraspherical polynomials. The authors of [21] analyzed the free vibration of Euler-Bernoulli and Timoshenko beams resting on Pasternak and generalized elastic foundations. The free and forced vibration of cracked beams is investigated by [22–24]. Other researchers have studied the free vibration of cracked, functionally-graded Euler-Bernoulli and Timoshenko beams [25–29]. A dynamic stiffness method is used by the authors of [30] to study the free and forced vibration of multi-cracked, continuous, functionally-graded beams. An analytical solution of the forced vibration of cracked Timoshenko beams with damping is obtained by [31]. The free vibration of functionally-graded cracked Timoshenko beams is studied by [32–33]. A differential quadrature method is used by [34] to study the free and forced vibration of multi-cracked Timoshenko beams carrying a moving mass. A method is proposed by [35] which is based on the measurements of natural frequencies to detect a single crack in functionally-graded Timoshenko beam. In this paper, the transfer matrix method (TMM) is used



to study the free vibration of axially-loaded, cracked beams. This method was first introduced by [36], and used by other researchers [37–41] to study the free vibration of cracked beams. Other researchers solved the problem using the finite element method, [42–44].

According to the authors' knowledge, the effects of four cracks on the dynamic behavior of axially-loaded Timoshenko beams have not been studied in detail in the existing literature. In this paper, the dynamic behavior of a multi-cracked beam under axial loading including the shear deformation and rotary inertia and their coupling effects with differing boundary conditions with an arbitrary number of transverse cracks is investigated. The simple transfer matrix method is used to ascertain the natural frequencies and corresponding mode shapes of the beam. Some results obtained in this paper are compared to those results available in literature.

2. Methods

2.1. Theoretical model

Consider a multi-cracked beam with length l , cross-sectional area of width b and height h , and a number of single-sided, open cracks located at points $x_{c1}, x_{c2}, \dots, x_{ci}$ with sizes $a_{c1}, a_{c2}, \dots, a_{ci}$, respectively, as shown in Fig. 1.

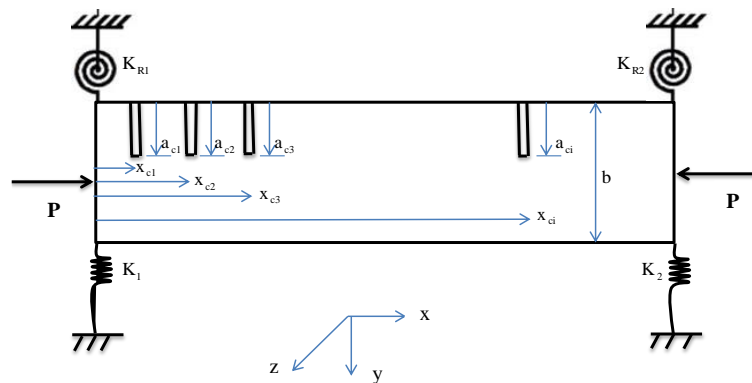


Figure 1. A multi-cracked, axially loaded beam with i edge open cracks, restrained by linear and rotational springs at both ends.

The boundary conditions are represented with linear and rotational springs at both ends ($K_1, K_{R1}, K_2,$ and K_{R2}). Timoshenko (1921) proposed a beam theory which adds the effects of shear and rotation to the governing equation of motion of an Euler- Bernoulli beam. The total slope $\frac{\partial y(x,t)}{\partial x}$ is a combination of the bending slope $\psi(x,t)$ and the shear slope $\gamma_{xy}(x,t)$ [46], which can be written as:

$$\frac{\partial y(x,t)}{\partial x} = \psi(x,t) + \gamma_{xy}(x,t) \quad (1)$$

where $\psi(x,t)$, $\gamma_{xy}(x,t)$, and t are the bending slope, the shear slope, and the time parameter, respectively.

In [47], it was assumed that the component of axial load P on the cross section is acting on the plane of the total slope. Accordingly, the shear force can be written as:

$$V(x,t) + P \frac{\partial y(x,t)}{\partial x} = \left[\frac{\partial y(x,t)}{\partial x} - \psi(x,t) \right] k' \quad (2)$$

where V is the shear force (along the y -axis), A is the area of beam cross section, G is the shear modulus and k' is the shear correction factor (assumed equal to $5/6$ in this paper). The dynamic equilibrium equations for the free-body diagram shown in Fig. 2.b becomes:

$$-V(x,t) + \frac{\partial M(x,t)}{\partial x} - P \frac{\partial y(x,t)}{\partial x} + \rho I \frac{\partial^2 \psi}{\partial t^2} = 0 \quad (3)$$

And,

$$\frac{\partial V(x,t)}{\partial x} = \frac{\partial^2 y(x,t)}{\partial t^2} \quad (4)$$

where M is the bending moment (about the z -axis), ρ is the material density, and I is the moment of inertia. Using Eqns. (3) and (4), one can obtain the governing equation for the transverse vibration of a uniform Timoshenko beam subjected to constant axial force as:

$$EI \left(\frac{k'GA - P}{k'GA} \right) \frac{\partial^4 y(x,t)}{\partial x^4} + m + P \frac{\partial^2 y(x,t)}{\partial x^2} - mr^2 \left(\frac{k'GA - P}{k'GA} \right) \frac{\partial^4 y(x,t)}{\partial x^2 \partial t^2} - \frac{mEI}{k'GA} \frac{\partial^4 y(x,t)}{\partial x^2 \partial t^2} + \frac{m^2 r^2}{k'GA} \frac{\partial^4 y(x,t)}{\partial t^4} = 0 \quad (5a)$$

In a similar manner, Eqn. (5a) can be written in terms of the deflection slope alone as:

$$EI \left(\frac{k'GA - P}{k'GA} \right) \frac{\partial^4 \psi(x,t)}{\partial x^4} + m + P \frac{\partial^2 \psi(x,t)}{\partial x^2} - mr^2 \left(\frac{k'GA - P}{k'GA} \right) \frac{\partial^4 \psi(x,t)}{\partial x^2 \partial t^2} - \frac{mEI}{k'GA} \frac{\partial^4 \psi(x,t)}{\partial x^2 \partial t^2} + \frac{m^2 r^2}{k'GA} \frac{\partial^4 \psi(x,t)}{\partial t^4} = 0 \quad (5b)$$

where m is the mass per unit length, r is the radius of gyration; $K'A$ is the effective shear area of the cross section.

It is clear that Eqn. (5a) reduces to Euler beam theory (EBT) when the shear deformation and rotary inertia are equal to zero. Then Eqn. (5a) become:

$$EI \frac{\partial^4 (y,t)}{\partial x^4} + m \frac{\partial^2 (y,t)}{\partial x^2} + P \frac{\partial^2 (y,t)}{\partial x^2} = 0$$

A simple transfer matrix method is used to get the general form of the characteristic equation for the axially-loaded cracked beam, which is a function of frequency, axial load, the locations and sizes of the cracks, boundary conditions, and the geometrical and physical parameters of the beam. It is assumed that a beam with n segments is joined by massless, rotational springs, as shown in Fig. 2.

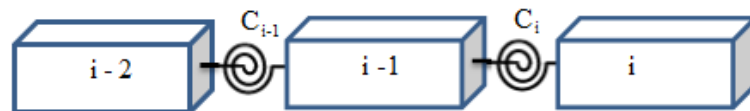


Figure 2. Beam elements joined by massless, rotational spring.

The free vibration solution for a Timoshenko beam (TBT) subjected to axial load can be found using the method of separation of variables as:

$$y(x,t) = Y(x)e^{i\omega t} \quad (6a)$$

$$\psi(x,t) = \psi(x)e^{i\omega t} \quad (6b)$$

where, $Y(x)$, $\psi(x)$, ω , i , and x are the normal function of $y(x,t)$, the normal function of $\psi(x,t)$, the circular frequency, the imaginary number, and the spatial position on the x -axis, respectively.

Substituting Eqn. (6a) into Eqn. (5a) leads to:

$$EI \left(\frac{k'GA - P}{k'GA} \right) \frac{\partial^4 Y(x)}{\partial x^4} + m\omega^2 Y(x) + P \frac{\partial^2 Y(x)}{\partial x^2} - mr^2 \omega^2 \left(\frac{k'GA - P}{k'GA} \right) \frac{\partial^2 Y(x)}{\partial x^2} - \frac{mEI\omega^2}{k'GA} \frac{\partial^2 Y(x)}{\partial x^2} + \frac{m^2 r^2 \omega^4}{k'GA} Y(x) = 0 \quad (7a)$$

And, substituting Eqn. (6b) into Eqn. (5b) yields:

$$EI \left(\frac{k'GA - P}{k'GA} \right) \frac{\partial^4 \psi(x)}{\partial x^4} + m\omega^2 \psi(x) + P \frac{\partial^2 \psi(x)}{\partial x^2} - mr^2 \omega^2 \left(\frac{k'GA - P}{k'GA} \right) \frac{\partial^2 \psi(x)}{\partial x^2} - \frac{mEI\omega^2}{k'GA} \frac{\partial^2 \psi(x)}{\partial x^2} + \frac{m^2 r^2 \omega^4}{k'GA} \psi(x) = 0 \quad (7b)$$

The general-form solutions of Eqn. (7a) and (7b) are:

$$Y(x) = A_1 \cos(\alpha x) + A_2 \sin(\alpha x) + A_3 \cosh(\beta x) + A_4 \sinh(\beta x) \quad (8a)$$

$$\psi(x) = m_1 A_1 \cos(\alpha x) + m_1 A_2 \sin(\alpha x) + m_2 A_3 \cosh(\beta x) + m_2 A_4 \sinh(\beta x) \quad (8b)$$

where,

$$\alpha = \sqrt{\frac{1}{2} \left(\frac{mr^2 \omega^2}{EI} + \frac{m\omega^2}{k'AG\xi} + \frac{P}{EI\xi} \right)^2 + \frac{1}{2} \sqrt{\left(\frac{mr^2 \omega^2}{EI} + \frac{m\omega^2}{k'AG\xi} + \frac{P}{EI\xi} \right)^2 - 4 \left(\frac{mr^2 \omega^2}{EI k'GA\xi} - \frac{m\omega^2}{EI\xi} \right)}}$$

$$\beta = \sqrt{-\frac{1}{2} \left(\frac{mr^2 \omega^2}{EI} + \frac{m\omega^2}{k'AG\xi} + \frac{P}{EI\xi} \right)^2 + \frac{1}{2} \sqrt{\left(\frac{mr^2 \omega^2}{EI} + \frac{m\omega^2}{k'AG\xi} + \frac{P}{EI\xi} \right)^2 - 4 \left(\frac{mr^2 \omega^2}{EI k'GA\xi} - \frac{m\omega^2}{EI\xi} \right)}}$$

where $\xi = \frac{k'GA - P}{k'GA}$, $m_1 = \frac{\rho A \omega^2}{k'GA\alpha} - \alpha$, $m_2 = \frac{\rho A \omega^2}{k'GA\beta} + \beta$ and A_1 to A_4 are unknown constants.

The slope $\theta(x)$, bending moment $M(x)$, and shear force $V(x)$ can be obtained as:

$$\theta(x) = \frac{\partial Y(x)}{\partial x} = m_1 [-A_1 \sin(\alpha x) + A_2 \cos(\alpha x)] + m_2 [-A_3 \sinh(\beta x) - A_4 \cosh(\beta x)] \quad (9a)$$

$$M(x) = n_1 [-A_1 \cos(\alpha x) - A_2 \sin(\alpha x)] + n_2 [A_3 \cosh(\beta x) + A_4 \sinh(\beta x)] \quad (9b)$$

$$V(x) = b_1 [A_1 \sin(\alpha x) - A_2 \cos(\alpha x)] + b_2 [A_3 \sinh(\beta x) + A_4 \cosh(\beta x)] \quad (9c)$$

where $n_1 = E \operatorname{Im}_1 \alpha$, $n_2 = -E \operatorname{Im}_2 \beta$, $b_1 = E \operatorname{Im}_1 \alpha^2 - m_1 \rho I \omega^2$, $b_2 = -E \operatorname{Im}_2 \alpha^2 - m_2 \rho I \omega^2$.

The $[S(x)]$ matrix can be obtained from Eqn. (8a) and (9a-c) as:

$$[S(x)] = \begin{bmatrix} \cos(\alpha x) & \sin(\alpha x) & \cosh(\beta x) & \sinh(\beta x) \\ -m_1 \sin(\alpha x) & m_1 \cos(\alpha x) & -m_2 \sinh(\beta x) & -m_2 \cosh(\beta x) \\ -n_1 \cos(\alpha x) & -n_1 \sin(\alpha x) & n_2 \cosh(\beta x) & n_2 \sinh(\beta x) \\ b_1 \sin(\alpha x) & -b_1 \cos(\alpha x) & b_2 \sinh(\beta x) & b_2 \cosh(\beta x) \end{bmatrix} \quad (10)$$

The compatibility requirements at the crack position, x_c , which are the continuity of the deflection, bending moment, shear force, and the discontinuity of slopes for segments i and $i+1$, can be written in matrix form as:

$$\begin{Bmatrix} Y_{i+1}(x_c) \\ \theta_{i+1}(x_c) \\ M_{i+1}(x_c) \\ V_{i+1}(x_c) \end{Bmatrix} = \begin{bmatrix} 1 & 0 & 0 & 0 \\ 0 & 1 & C_i & 0 \\ 0 & 0 & 1 & 0 \\ 0 & 0 & 0 & 1 \end{bmatrix} \begin{Bmatrix} Y_i(x_c) \\ \theta_i(x_c) \\ M_i(x_c) \\ V_i(x_c) \end{Bmatrix} \quad (11)$$

where C_i is the flexibility coefficient at the i^{th} crack, and depend on the load case of the cracked element.

2.2. Local flexibility due to a crack

An open crack on an elastic structure can be considered a source of local flexibility due to the strain energy concentration at the surrounding area of the crack tip. The idea of replacing a crack with a massless spring is presented to establish the relation between the strain energy concentration and applied loads. The flexibility coefficients are expressed in terms of stress intensity factors, utilizing Castigliano's theorem. Generalized loading conditions for a beam element of circular or rectangular cross section with a transverse surface crack are shown in Fig. 3.

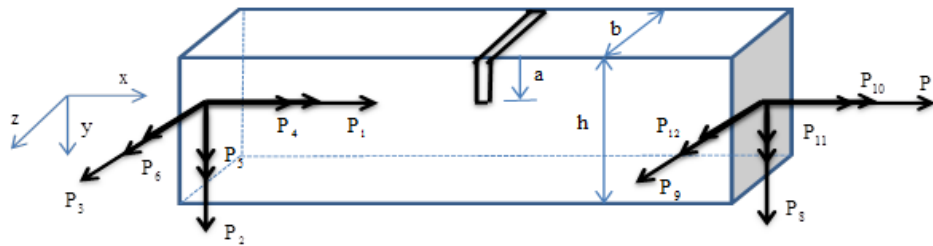


Figure 3. Model of the cracked element.

The crack has a tip line parallel to the z -axis and the bar is loaded by shear forces P_2, P_3, P_8 , and P_9 ; bending moments P_4, P_5, P_{11} , and P_{12} ; axial forces P_1 and P_7 ; and torsional moments P_4 and P_{10} . According to Castigliano's theorem, the additional displacement caused by the crack is given as:

$$u_i = \frac{\partial U}{\partial P_i} = \frac{\partial}{\partial P_i} \left[\int_{A_c} J dA \right] \quad (12)$$

where U , A_c , and J are the strain energy due to the crack, the crack section, and strain energy density function, respectively.

The strain energy density function can be expressed according to [14] for plane stress as: 1

$$J = \left(\frac{1-\nu^2}{E} \right) \left[\left(\sum_{i=1}^6 K_{Ii} \right)^2 + \left(\sum_{i=1}^6 K_{IIi} \right)^2 + (1+\nu) \left(\sum_{i=1}^6 K_{IIIi} \right)^2 \right] \quad (13)$$

where, ν is Poisson's ratio and K_{Ii} , K_{IIi} , K_{IIIi} are the crack stress intensity factors for opening mode, shearing mode, and tearing mode, respectively; $I = 1, 2, \dots, 6$.

Stress intensity factors can be calculated following [14] as:

$$\begin{aligned}
K_{I1} &= \sigma_1 \sqrt{\pi a} F_1(a/h), \sigma_1 = \frac{P_1}{bh} \\
K_{I5} &= \sigma_5 \sqrt{\pi a} F_1(a/h), \sigma_5 = \frac{12P_5 z}{b^3 h} \\
K_{I6} &= \sigma_6 \sqrt{\pi a} F_2(a/h), \sigma_6 = \frac{6P_6}{bh^2} \\
K_{I2} &= K_{I3} = K_{I4} = 0 \\
K_{II2} &= \sigma_2 \sqrt{\pi a} F_{II}(a/h), \sigma_2 = \frac{kP_2}{bh} \\
K_{II4} &= \sigma_4 \sqrt{\pi a} F_{II}(a/h), \sigma_4 = \frac{P_4}{bh} \\
K_{II1} &= K_{II3} = K_{II5} = K_{II6} = 0 \\
K_{III3} &= \sigma_3 \sqrt{\pi a} F_{III}(a/h), \sigma_3 = \frac{kP_3}{bh} \\
K_{III4} &= \sigma_{4III} \sqrt{\pi a} F_{III}(a/h), \sigma_{4III} = \frac{P_4}{bh} \\
K_{III1} &= K_{III2} = K_{III5} = K_{III6} = 0
\end{aligned} \tag{14}$$

where

$$\begin{aligned}
F_1(a/h) &= \sqrt{\frac{2h}{\pi a} \tan\left(\frac{\pi a}{2h}\right)} \frac{0.752 + 2.02\left(\frac{a}{h}\right) + 0.37\left(1 - \sin\left(\frac{\pi a}{2h}\right)\right)^3}{\cos\left(\frac{\pi a}{2h}\right)} \\
F_2(a/h) &= \sqrt{\frac{2h}{\pi a} \tan\left(\frac{\pi a}{2h}\right)} \frac{0.923 + 0.199\left(1 - \sin\left(\frac{\pi a}{2h}\right)\right)^4}{\cos\left(\frac{\pi a}{2h}\right)} \\
F_{II}(a/h) &= \frac{1.122 - 0.561\left(\frac{a}{h}\right) + 0.085\left(\frac{a}{h}\right)^2 + 0.18\left(\frac{a}{h}\right)^3}{\sqrt{1 - \left(\frac{a}{h}\right)}} \\
F_{III}(a/h) &= \sqrt{\frac{2h}{\pi a} \tan\left(\frac{\pi a}{2h}\right)}
\end{aligned} \tag{15}$$

From Eqns. (12), (14) and (15), the flexibility coefficients can be calculated as:

$$C_{11} = (1 - \nu^2) \frac{2\pi}{Eb^2} \left[\int_0^\varphi \phi F_1^2(\phi) d\phi \right] \int_{-b/2}^{b/2} dz$$

$$\begin{aligned}
C_{15} = C_{51} &= (1-\nu^2) \frac{24\pi}{Eb^4} \left[\int_0^\varphi \phi F_1^2(\phi) d\phi \right] \int_{-b/2}^{b/2} z dz \\
C_{16} = C_{61} &= (1-\nu^2) \frac{12\pi}{Eb^2 h} \left[\int_0^\varphi \phi F_1(\phi) F_2(\phi) d\phi \right] \int_{-b/2}^{b/2} dz \\
C_{22} &= (1-\nu^2) \frac{2k^2\pi}{Eb^2} \left[\int_0^\varphi \phi F_{II}^2(\phi) d\phi \right] \int_{-b/2}^{b/2} dz \\
C_{24} = C_{42} &= (1-\nu^2) \frac{2k\pi}{Eb^2} \left[\int_0^\varphi \phi F_{II}^2(\phi) d\phi \right] \int_{-b/2}^{b/2} dz \\
C_{33} &= (1-\nu^2) \frac{2k^2\mu\pi}{Eb^2} \left[\int_0^\varphi \phi F_{III}^2(\phi) d\phi \right] \int_{-b/2}^{b/2} dz \\
C_{34} = C_{43} &= (1-\nu^2) \frac{2k\mu\pi}{Eb^2} \left[\int_0^\varphi \phi F_{III}^2(\phi) d\phi \right] \int_{-b/2}^{b/2} dz \\
C_{44} &= (1-\nu^2) \frac{2\pi}{Eb^2} \left[\int_0^\varphi \phi (F_{II}^2(\phi) + \mu F_{III}^2(\phi)) d\phi \right] \int_{-b/2}^{b/2} dz \\
C_{55} &= (1-\nu^2) \frac{288\pi}{Eb^6} \left[\int_0^\varphi \phi F_1^2(\phi) d\phi \right] \int_{-b/2}^{b/2} z^2 dz \\
C_{56} = C_{65} &= (1-\nu^2) \frac{144\pi}{Eb^4 h} \left[\int_0^\varphi \phi F_1^2(\phi) F_2(\phi) d\phi \right] \int_{-b/2}^{b/2} z dz \\
C_{66} &= (1-\nu^2) \frac{72\pi}{Eb^2 h^2} \left[\int_0^\varphi \phi F_2^2(\phi) d\phi \right] \int_{-b/2}^{b/2} dz
\end{aligned} \tag{16}$$

where $\mu = 1 + \nu$, $\phi = \frac{a}{h}$ and k is a shape coefficient for a rectangular cross section.

In this study, the flexural vibration of the beam is the only significant load in the equations above. Therefore, the contribution of the axial load component to the strain energy of the system is very small. Hence, the only component in the flexibility matrix is C_{66} .

2.3. Transfer matrix method

Equation (11) can be written as:

$$\{Q_{i+1}(x_i)\} = [C_i] \{Q_i(x_i)\} \tag{17}$$

At the location of open edge crack, the two beam segments i and $i+1$ are connected by a massless, rotational springs, as shown in Fig. 2. Equation (6a) and Eqn. (8a) and Eqns. (9a) to (9c) can be written in matrix form for both segments i , and $i+1$, respectively, as:

$$\begin{Bmatrix} Y_i(x) \\ \theta_i(x) \\ M_i(x) \\ V_i(x) \end{Bmatrix} = [S(x)] \begin{Bmatrix} A_{1,i} \\ A_{2,i} \\ A_{3,i} \\ A_{4,i} \end{Bmatrix} \quad (18a)$$

$$\begin{Bmatrix} Y_{i+1}(x) \\ \theta_{i+1}(x) \\ M_{i+1}(x) \\ V_{i+1}(x) \end{Bmatrix} = [S(x)] \begin{Bmatrix} A_{1,i+1} \\ A_{2,i+1} \\ A_{3,i+1} \\ A_{4,i+1} \end{Bmatrix} \quad (18b)$$

Equation (18a) can be rewritten for a segment, $x_{i-1} < x < x_i$, as:

$$\{Q_i(x)\} = [S(x)]\{A_i\} \quad (19)$$

where,

$$\{Q_i(x)\} = \begin{Bmatrix} Y_{i+1}(x_c) \\ \theta_{i+1}(x_c) \\ M_{i+1}(x_c) \\ V_{i+1}(x_c) \end{Bmatrix}, \text{ and } \{A_i\} = \begin{Bmatrix} A_{1,i} \\ A_{2,i} \\ A_{3,i} \\ A_{4,i} \end{Bmatrix}$$

The boundary conditions of the beam using equilibrium equations can be expressed as:

$$M(0) = K_{R1}\theta(0) \quad (20a)$$

$$V(0) = -K_1Y(0) \quad (20b)$$

$$M(l) = -K_{R2}\theta(l) \quad (20c)$$

$$V(l) = K_2Y(l) \quad (20d)$$

In order to calculate the natural frequencies and corresponding mode shapes, the characteristic equation can be derived as in [48].

The continuity conditions of the deflection, slope, moment, and shear at $x = 0$ and $x = l$ leads to:

$$\begin{Bmatrix} Y_{i+1}(l) \\ \theta_{i+1}(l) \\ -K_{R2}\theta_{i+1}(l) \\ K_2Y_{i+1}(l) \end{Bmatrix} = [T] \begin{Bmatrix} Y_1(0) \\ \theta_1(0) \\ K_{R1}\theta_1(0) \\ -K_1Y_1(0) \end{Bmatrix} \quad (21)$$

$$\text{where } [T] = \begin{bmatrix} T_{11} & T_{12} & T_{13} & T_{14} \\ T_{21} & T_{22} & T_{23} & T_{24} \\ T_{31} & T_{32} & T_{33} & T_{34} \\ T_{41} & T_{42} & T_{43} & T_{44} \end{bmatrix}$$

Rewriting equation (21) as:

$$\begin{Bmatrix} Y_{i+1}(l) \\ \theta_{i+1}(l) \end{Bmatrix} = \begin{bmatrix} T_{11} - K_1T_{14} & T_{12} + K_{R1}T_{13} \\ T_{21} - K_1T_{24} & T_{22} + K_{R1}T_{23} \end{bmatrix} \begin{Bmatrix} Y_1(0) \\ \theta_1(0) \end{Bmatrix} \quad (22a)$$

$$\begin{Bmatrix} -K_{R2}\theta_{i+1}(l) \\ K_2 Y_{i+1}(l) \end{Bmatrix} = \begin{bmatrix} T_{31} - K_1 T_{34} & T_{32} + K_{R1} T_{33} \\ T_{41} - K_1 T_{44} & T_{42} + K_{R1} T_{43} \end{bmatrix} \begin{Bmatrix} Y_1(0) \\ \theta_1(0) \end{Bmatrix} \quad (22b)$$

The characteristic equation can be obtained by substitution of Equation (22a) into Equation (22b).

$$F_1 F_4 - F_2 F_3 = 0 \quad (23)$$

where,

$$F_1 = -K_{R2} T_{21} + K_1 K_{R2} T_{24} - T_{31} + K_1 T_{34}$$

$$F_2 = -K_{R2} T_{22} - K_{R1} K_{R2} T_{23} - T_{32} - K_{R1} T_{33}$$

$$F_3 = K_2 T_{11} - K_1 K_2 T_{14} - T_{41} + K_1 T_{44}$$

$$F_4 = K_2 T_{12} + K_2 K_{R1} T_{13} - T_{42} - K_{R1} T_{43}$$

Characteristic Eqn. (23) can be derived for different boundary conditions as:

a. For fixed-free boundaries ($K_1 = K_{R1} = \infty$),

$$T_{34} T_{43} - T_{33} T_{44} = 0$$

b. For pinned-pinned boundaries ($K_1 = K_2 = \infty$),

$$T_{34} T_{12} - T_{32} T_{14} = 0$$

c. For fixed-pinned boundaries, ($K_1 = K_2 = K_{R1} = \infty$),

$$T_{34} T_{13} - T_{33} T_{14} = 0$$

d. For fixed-fixed boundaries, ($K_1 = K_2 = K_{R1} = K_{R2} = \infty$),

$$T_{24} T_{13} - T_{23} T_{14} = 0$$

e. For free-free boundaries,

$$T_{31} T_{42} - T_{32} T_{41} = 0$$

2.4. The corresponding mode shapes

In order to obtain the mode shape of the axially-loaded, cracked Euler beam, the unknown constants $\{A_i\}$ for each sub-segment of the cracked beam can be determined. At first, the unknown coefficients for the first segment, $\{A_1\}$, are determined. Then, the unknown coefficients for the other segments may be obtained, using the following procedure.

1. At $x = 0$, Eqn. (19) can be written as:

$$\begin{Bmatrix} Y_1(0) \\ \theta_1(0) \\ K_{R1}\theta_1(0) \\ -K_1 Y_1(0) \end{Bmatrix} = \begin{bmatrix} 1 & 0 & 1 & 0 \\ 0 & \alpha & 0 & \beta \\ -EI\alpha^2 & 0 & EI\beta^2 & 0 \\ 0 & -(EI\alpha^3 - P_\alpha) & 0 & (EI\beta^3 + P\beta) \end{bmatrix} \begin{Bmatrix} A_{1,1} \\ A_{2,1} \\ A_{3,1} \\ A_{4,1} \end{Bmatrix} \quad (24)$$

Eqn. (24) can be rewritten as:

$$\begin{Bmatrix} Y_1(0) \\ \theta_1(0) \end{Bmatrix} = \begin{bmatrix} 1 & 0 & 1 & 0 \\ 0 & \alpha & 0 & \beta \end{bmatrix} \begin{Bmatrix} A_{1,1} \\ A_{2,1} \\ A_{3,1} \\ A_{4,1} \end{Bmatrix} \quad (25a)$$

$$\begin{Bmatrix} -K_1\theta_1(0) \\ K_{R1}Y_1(0) \end{Bmatrix} = \begin{bmatrix} -EI\alpha^2 & 0 & EI\beta^2 & 0 \\ 0 & -(EI\alpha^3 - P\alpha) & 0 & (EI\beta^3 + P\beta) \end{bmatrix} \begin{Bmatrix} A_{1,1} \\ A_{2,1} \\ A_{3,1} \\ A_{4,1} \end{Bmatrix} \quad (25b)$$

Substituting Eqn. (25a) into Eqn. (25b) yields:

$$\begin{bmatrix} Q_{11} & Q_{12} & Q_{13} & Q_{14} \\ Q_{21} & Q_{22} & Q_{23} & Q_{24} \end{bmatrix} \begin{Bmatrix} A_{1,1} \\ A_{2,1} \\ A_{3,1} \\ A_{4,1} \end{Bmatrix} = 0 \quad (26)$$

where,

$$\begin{aligned} Q_{11} &= n_1, \quad Q_{12} = K_{R1}m_1, \quad Q_{13} = -n_2, \quad Q_{14} = -K_{R1}m_2, \\ Q_{21} &= -K_1, \quad Q_{22} = b_1, \quad Q_{23} = -K_1, \quad Q_{24} = -b_2 \end{aligned} \quad (27)$$

2. At $x = l$, substituting Eqns. (10), (20c), (20d), and (19) into Eqn. (21) yields:

$$\begin{Bmatrix} Y_{i+1}(l) \\ \theta_{i+1}(l) \end{Bmatrix} = \begin{bmatrix} T_{11} - EI\alpha^2 T_{13} & (T_{12}\alpha - T_{14}(EI\alpha^3 - P\alpha)) & T_{11} + EIT_{13}\beta^2 & (T_{12}\beta + T_{14}(EI\beta^3 + P\beta)) \\ T_{21} - EIT_{23}\alpha^2 & (T_{22}\alpha - T_{24}(EI\alpha^3 - P\alpha)) & T_{21} + EIT_{23}\beta^2 & (T_{22}\beta + T_{24}(EI\beta^3 + P\beta)) \end{bmatrix} \begin{Bmatrix} A_{1,1} \\ A_{2,1} \\ A_{3,1} \\ A_{4,1} \end{Bmatrix} \quad (28a)$$

$$\begin{Bmatrix} -K_{R2}\theta_{i+1}(l) \\ K_2 Y_{i+1}(l) \end{Bmatrix} = \begin{bmatrix} T_{31} - EI\alpha^2 T_{33} & (T_{32}\alpha - T_{34}(EI\alpha^3 - P\alpha)) & T_{31} + EIT_{33}\beta^2 & (T_{32}\beta + T_{34}(EI\beta^3 + P\beta)) \\ T_{41} - EIT_{43}\alpha^2 & (T_{42}\alpha - T_{44}(EI\alpha^3 - P\alpha)) & T_{41} + EIT_{43}\beta^2 & (T_{42}\beta + T_{44}(EI\beta^3 + P\beta)) \end{bmatrix} \begin{Bmatrix} A_{1,1} \\ A_{2,1} \\ A_{3,1} \\ A_{4,1} \end{Bmatrix} \quad (28b)$$

Substituting Eqn. (38a) into Eqn. (38b) leads to:

$$\begin{bmatrix} Q_{31} & Q_{32} & Q_{33} & Q_{34} \\ Q_{41} & Q_{42} & Q_{43} & Q_{44} \end{bmatrix} \begin{Bmatrix} A_{1,1} \\ A_{2,1} \\ A_{3,1} \\ A_{4,1} \end{Bmatrix} = 0 \quad (29)$$

where,

$$\begin{aligned} Q_{31} &= -K_{R2}(T_{21} - n_1 T_{23}) - T_{31} + n_1 T_{33} \\ Q_{32} &= -K_{R2}(m_1 T_{22} - b_1 T_{24}) - (m_1 T_{32} - b_1 T_{34}) \\ Q_{33} &= -K_{R2}(T_{21} + n_2 T_{23}) - T_{31} - n_2 T_{33} \\ Q_{34} &= -K_{R2}(-m_2 T_{22} + b_2 T_{24}) - (-m_2 T_{32} + b_2 T_{34}) \\ Q_{41} &= K_2(T_{11} - n_1 T_{13}) - T_{41} + n_1 T_{43} \\ Q_{42} &= K_2(m_1 T_{12} - b_1 T_{14}) - (m_1 T_{42} - b_1 T_{44}) \\ Q_{43} &= K_2(T_{11} + n_2 T_{13}) - T_{41} - n_2 T_{43} \\ Q_{44} &= K_2(-m_2 T_{12} + b_2 T_{14}) - (-m_2 T_{42} + b_2 T_{44}) \end{aligned} \quad (30)$$

Combining Eqn. (26) and Eqn. (29) yields:

$$\begin{bmatrix} Q_{11} & Q_{12} & Q_{13} & Q_{14} \\ Q_{21} & Q_{22} & Q_{23} & Q_{24} \\ Q_{31} & Q_{32} & Q_{33} & Q_{34} \\ Q_{41} & Q_{42} & Q_{43} & Q_{44} \end{bmatrix} \begin{Bmatrix} A_{1,1} \\ A_{2,1} \\ A_{3,1} \\ A_{4,1} \end{Bmatrix} = 0 \quad (31)$$

The unknown coefficients of Eqn. (31) correspond to the mode shapes of the first crack position, i.e. at $x = x_{c1}$. For other crack locations, the unknown coefficients can be obtained using the coefficients of the previous crack as:

$$\{A_i\} = [S(x_{i-1})]^{-1} [C_{i-1}] [S(x_{i-1})] \{A_{i-1}\} \quad (32)$$

3. Results and Discussion

3.1. Validation of results

The present results obtained are compared with those found by [45]. Three different boundary conditions are used, namely, hinged-hinged, fixed-hinged, and fixed-fixed. Also, two different values of P/P_{cr} are used, which are 0.2 and -0.2. P_{cr} is the critical buckling load of the intact beam and it is equal to

$$\frac{P_E}{1 + \frac{P_E}{kGA}}$$

, where P_E is the Euler buckling load. Values of $l = 1$ m, $b = 0.1$ m, $h = 0.2$ m, $E = 200$ GPa, $\rho = 7850 \text{ kg/m}^3$, and $\nu = 0.3$ are used as the geometrical and material properties of the intact beam. Fig. 4 a-c show the first non-dimensional natural frequency ratio ω_{1c}/ω_{1i} obtained in this study versus the non-dimensional crack location x/l for a beam with $a/h = 0.1$, $a/h = 0.3$, and $a/h = 0.5$, for hinged-hinged, fixed-hinged, and fixed-fixed beams, respectively, compared with those obtained by [45]. As you can see, the obtained results agree well with those reported by [45].

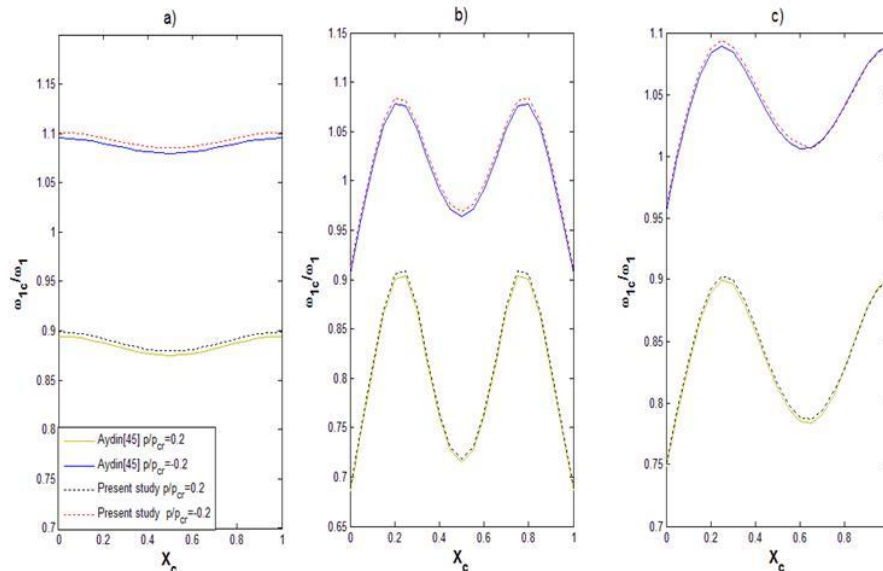
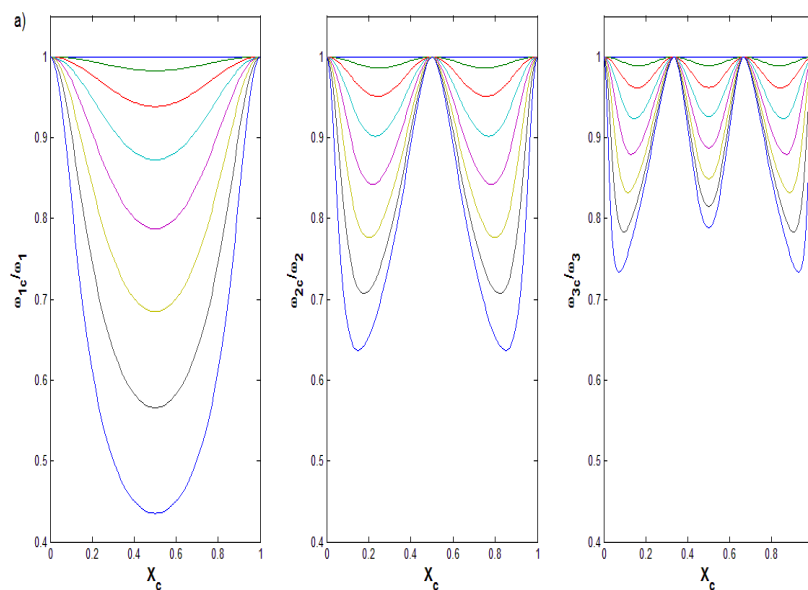


Figure 4. The first non-dimensional natural frequencies of a) hinged-hinged beam with single crack with $a/h = 0.1$, b) fixed-fixed beam with single crack with $a/h = 0.3$, and c) fixed-hinged beam with single crack with $a/h = 0.5$. The curves are obtained for P/P_{cr} values of -0.2, and 0.2 (from top to bottom).

3.2. Effects of One Crack and Axial Load on Natural Frequencies

In all subsequent sections, the geometrical and material properties of the intact beam are the same as those used in validation section, unless otherwise noted. The first three non-dimensional natural frequencies of a beam with a single crack versus crack location, for hinged-hinged, fixed-fixed, fixed-hinged, and fixed-free

boundary conditions, respectively, are shown in Fig. 5, 6, 7, and 8. In all figures, figure a) represents $P/P_{cr} = 0$, figure b) represents $P/P_{cr} = -0.3$, and figure c) represents $P/P_{cr} = 0.3$. Also, in all figures, eight values of aspect ratio a/h are used, 0, 0.1, 0.2, 0.3, 0.4, 0.5, 0.6, and 0.7. It is clear that the natural frequencies do not change with differing values of aspect ratio (a/h) at the location of zero-crossing of the mode shape and at critical points for a given frequency but do vary with differing boundary conditions. As an example, the zero-crossing points for hinged-hinged boundary conditions are located at 0.33/ and 0.66/ for the third, non-dimensional natural frequency. The critical points are located at 0.11/ and 0.89/ for fixed-fixed boundary conditions and at 0.12/ for fixed-hinged boundary conditions for the second, non-dimensional natural frequency. An interesting observation overlooked by researchers is that the locations of critical points for the first non-dimensional frequencies are shifted toward the center of the beam when the beam is axially loaded in compression and toward the fixed supports of the beam when the beam is axially loaded in tension for fixed-fixed and fixed-hinged boundaries. Those locations are at 0.23/, 0.77/ and at 0.21/ and 0.79/ for compression- and tension-loaded beams, respectively, for fixed-fixed boundaries, and 0.27/ and 0.25/ for tension- and compression-loaded beams, respectively, for fixed-hinged boundaries. As most researchers have found, the beam's natural frequencies are independent of crack location. Also, the natural frequency decreases with increasing aspect ratio. The first non-dimensional frequencies are most affected by the severity of cracks and the magnitude of the axial force. For axially loaded beams, since the compressive force softens the beam and tensile force stiffens the beam, the non-dimensional natural frequencies for all modes of the beam under compressive force are smaller than those of the same beam under tensile load for all boundary conditions. The first non-dimensional natural frequency shows a maximum 14 % and 20 % increase when the cracks are located near the supports and 16 % and 29 % decrease when the cracks are located at mid-span of the beam for $P/P_{cr} = 0.3$ and $P/P_{cr} = -0.3$, respectively, for an aspect ratio of 0.5, for an axially-loaded, hinged-hinged beam. For axially-loaded fixed-fixed beams, the first non-dimensional natural frequency shows a maximum 12 % increase when the cracks are located near the supports and 15 % decrease when the cracks are located at mid-span of the beam for $P/P_{cr} = -0.3$ and $P/P_{cr} = 0.3$ respectively, for aspect ratio of 0.1, and a maximum 15 % increase and 19 % decrease for $P/P_{cr} = -0.3$ and $P/P_{cr} = 0.3$ respectively, for an aspect ratio of 0.5. The values of percent increase or decrease are increased as the value of aspect ratio increases. For axially-loaded, fixed-hinged beam, the first non-dimensional natural frequency shows a maximum 13 % increase and 16 % decrease for $P/P_{cr} = -0.3$ and $P/P_{cr} = 0.3$ respectively, for an aspect ratio of 0.1, and a maximum 16 % increase and 20 % decrease for $P/P_{cr} = -0.3$ and $P/P_{cr} = 0.3$ respectively, for an aspect ratio of 0.6. Again, for axially-loaded fixed-free beam, the first non-dimensional natural frequency shows a maximum 15 % decrease and 13% increase for $P/P_{cr} = -0.3$ and $P/P_{cr} = 0.3$ respectively, for an aspect ratio of 0.1. A maximum 24 % decrease and 16% increase are obtained for $P/P_{cr} = -0.3$ and $P/P_{cr} = 0.3$ respectively, for an aspect ratio of 0.5. Another interesting point overlooked by researchers that for fixed-free beam, the first non-dimensional natural frequencies is not affected by crack location, aspect ratio of the crack, or the magnitude of axial load beyond 0.86/ and 0.8/ of the beam for zero axial load, tensile load and compressive load, respectively.



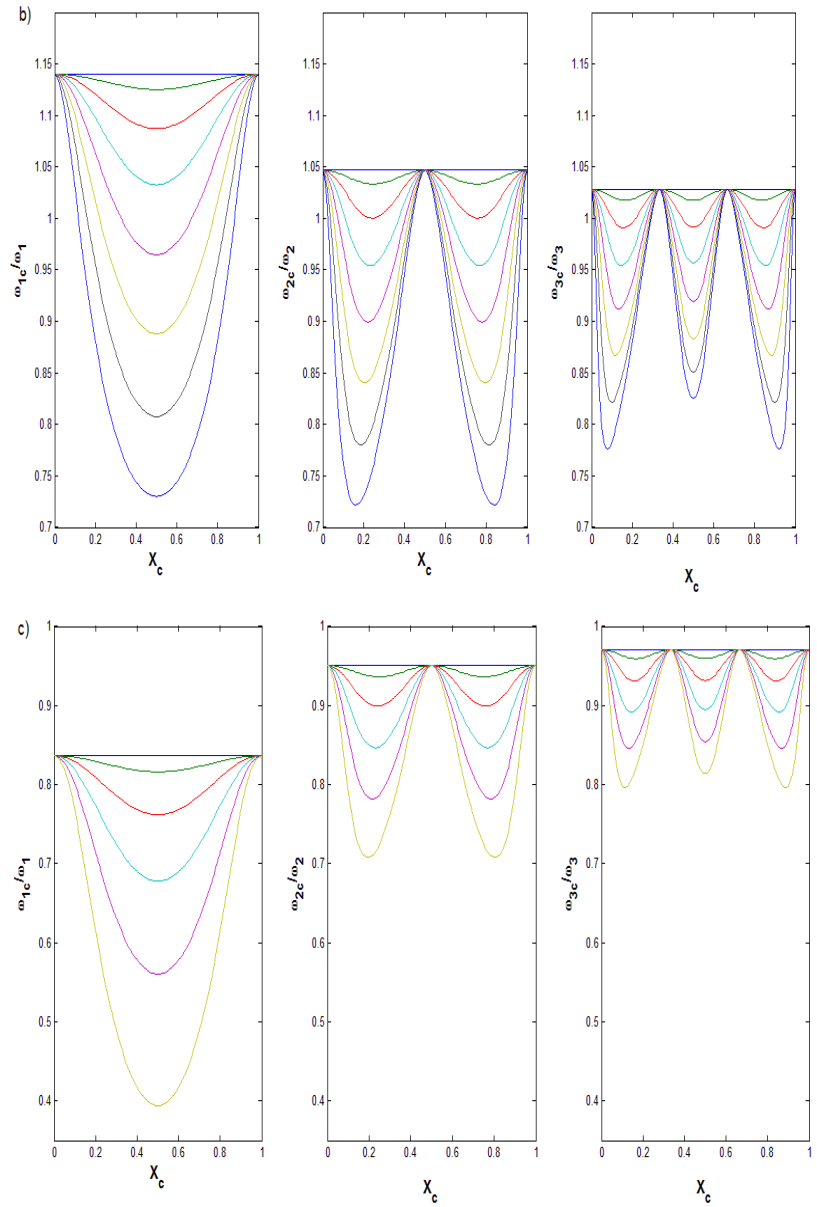
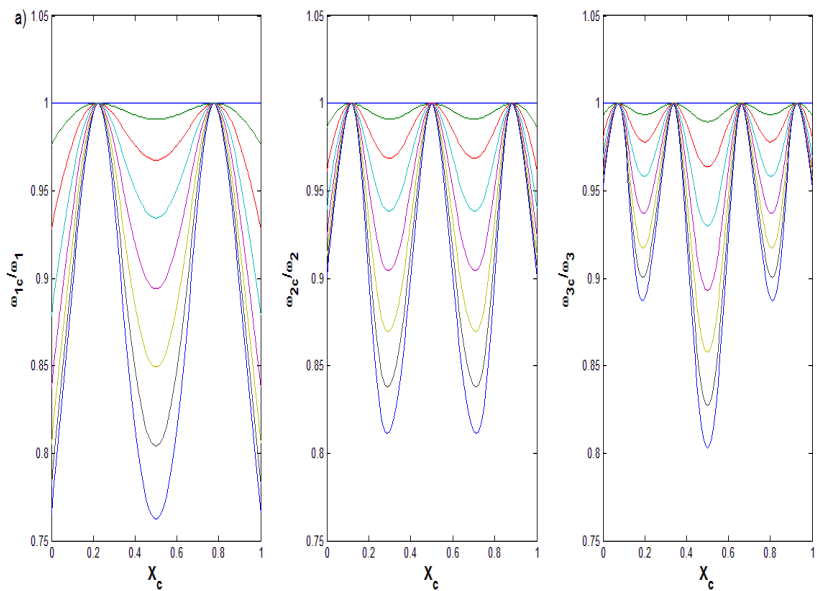


Figure 5. The first three non-dimensional natural frequencies of a hinged-hinged beam with a single crack for a) $P/P_{cr}=0$, b) $P/P_{cr}=-0.3$, and c) $P/P_{cr}=0.3$. The curves are obtained for a/h values of 0, 0.1, 0.2, 0.3, 0.4, 0.5, 0.6, and 0.7 (from top to bottom), and c) $P/P_{cr}=0.3$ with values of $a/h= 0, 0.1, 0.2, 0.3, 0.4,$ and 0.5 .



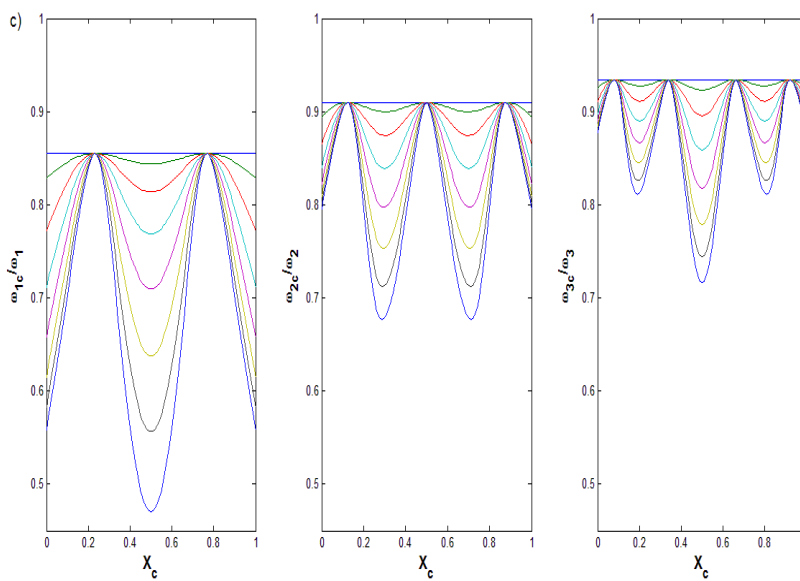
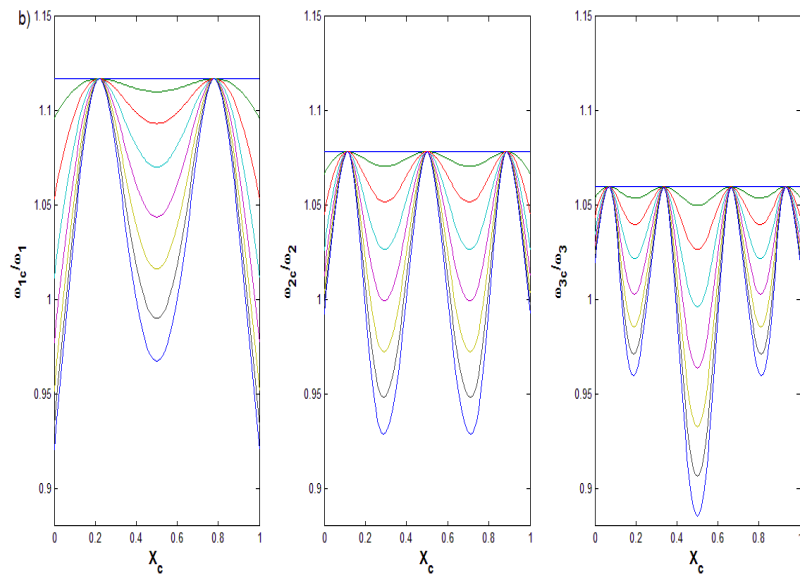
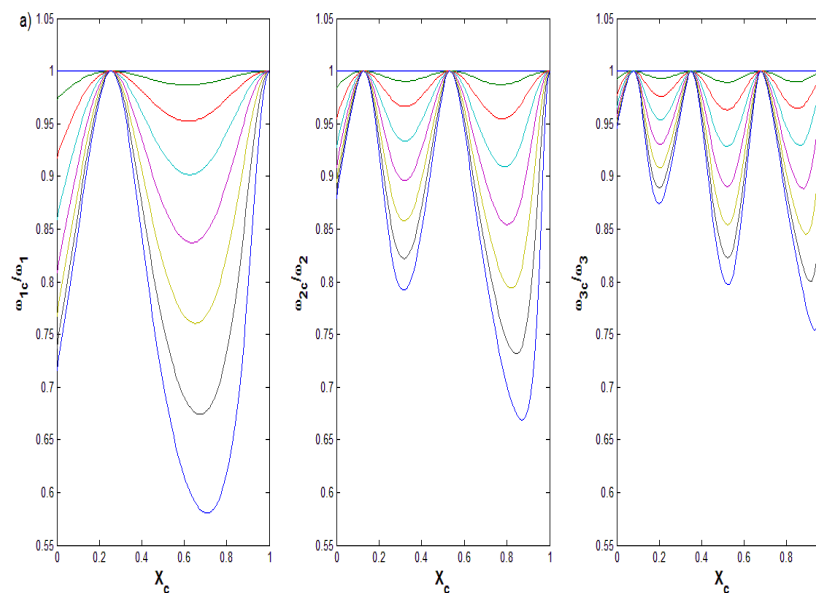


Figure 6. Same as Fig. 5 but with fixed-fixed boundary and values of $a/h = 0, 0.1, 0.2, 0.3, 0.4, 0.5, 0.6$ and 0.7 for c).



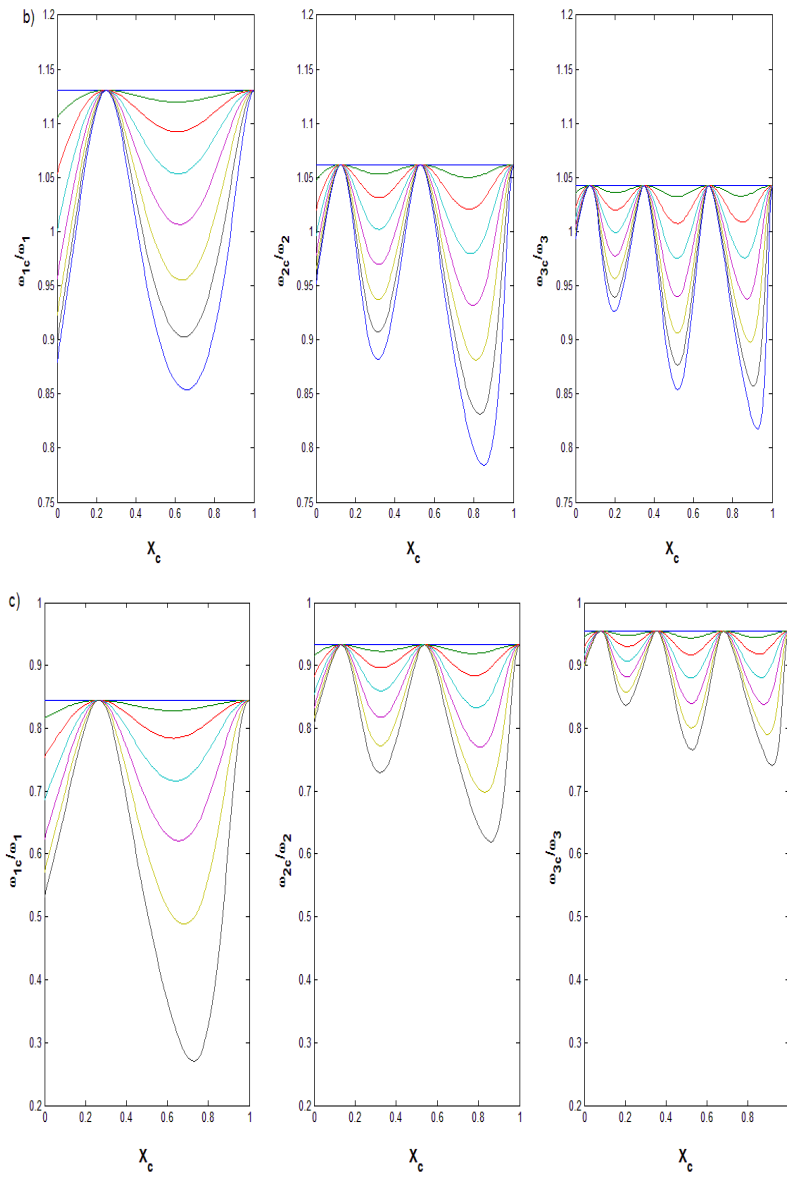
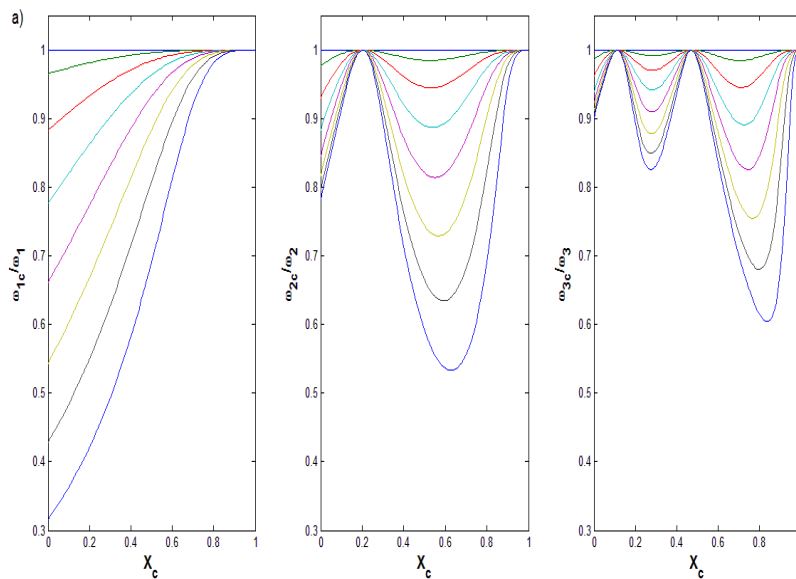


Figure 7. Same as Fig. 5 but with fixed-hinged boundary and values of $a/h = 0, 0.1, 0.2, 0.3, 0.4, 0.5, \text{ and } 0.6$ for c).



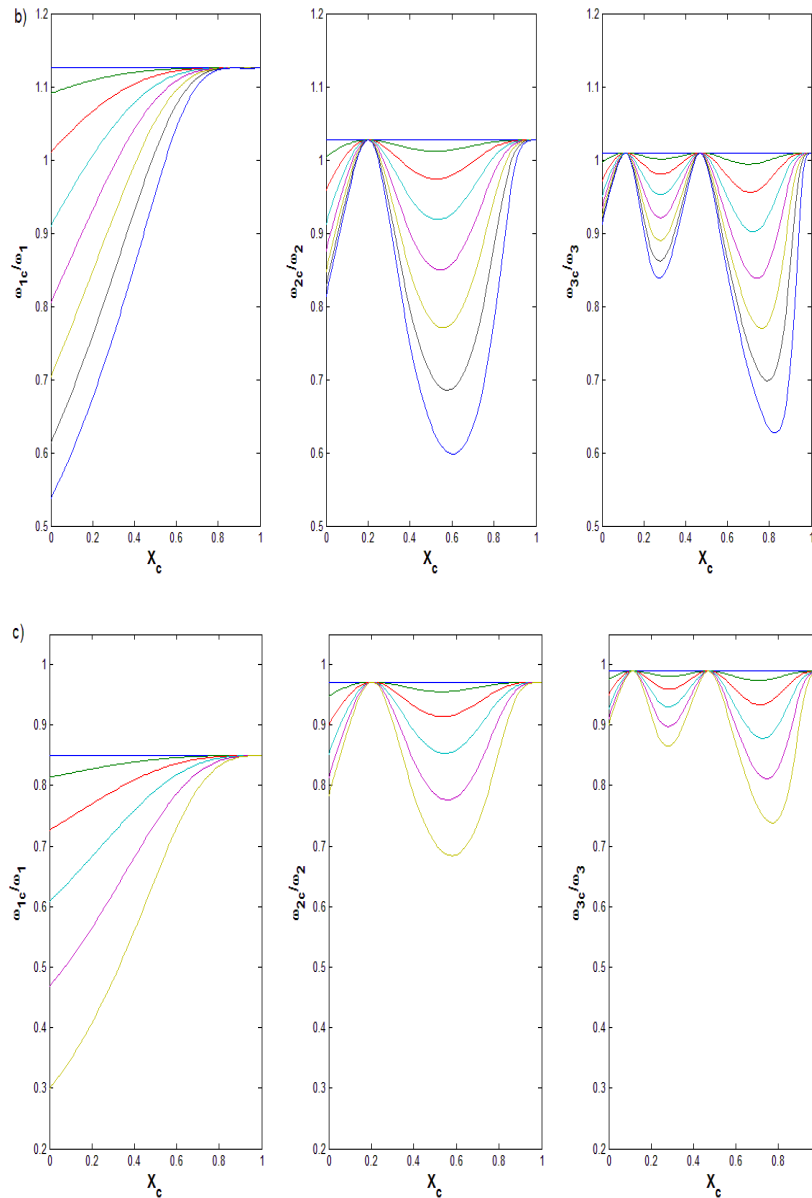


Figure 8. Same as Fig. 5 but with fixed-free boundary and values of $a/h = 0, 0.1, 0.2, 0.3, 0.4,$ and 0.5 for c).

3.3. Effects of multiple cracks and axial load on natural frequencies

Fig. 9 and 10 show the first three non-dimensional natural frequencies of a beam with four cracks versus crack location, for hinged-hinged and fixed-free boundaries, respectively. For brevity, the fixed-fixed and fixed-hinged results are not shown here. Five values of aspect ratio a/h are used in all figures (0, 0.1, 0.2, 0.3, and 0.4). Three cracks are fixed at locations of maximum variation of non-dimensional frequencies: 0.15 l , 0.5 l , and 0.85 l , and at 0.01 l , 0.6 l , and 0.8 l for hinged-hinged and fixed-free boundaries, respectively, while the fourth crack moves along the beam. As seen, the presence of four cracks in the beam lowers the non-dimensional natural frequencies, with or without axial load relative to the case of a single crack. A maximum 17 % and 15 % decrease of the first non-dimensional frequencies is observed for an aspect ratio of 0.4 when the fourth crack is located closer to the supports and mid-span of the beam, for hinged-hinged boundary conditions-compare Fig. 5a) with Fig. 9a). For fixed-free beam, a maximum 14 % and 34 % decrease of the first non-dimensional frequency is observed for an aspect ratio of 0.4 when the fourth crack is closer to the fixed and free supports, respectively-compare Fig. 8 a) with Fig. 10 a). It can be concluded here that the strongest and weakest beam in terms of fundamental natural frequencies is fixed-fixed and fixed-free beam, respectively.

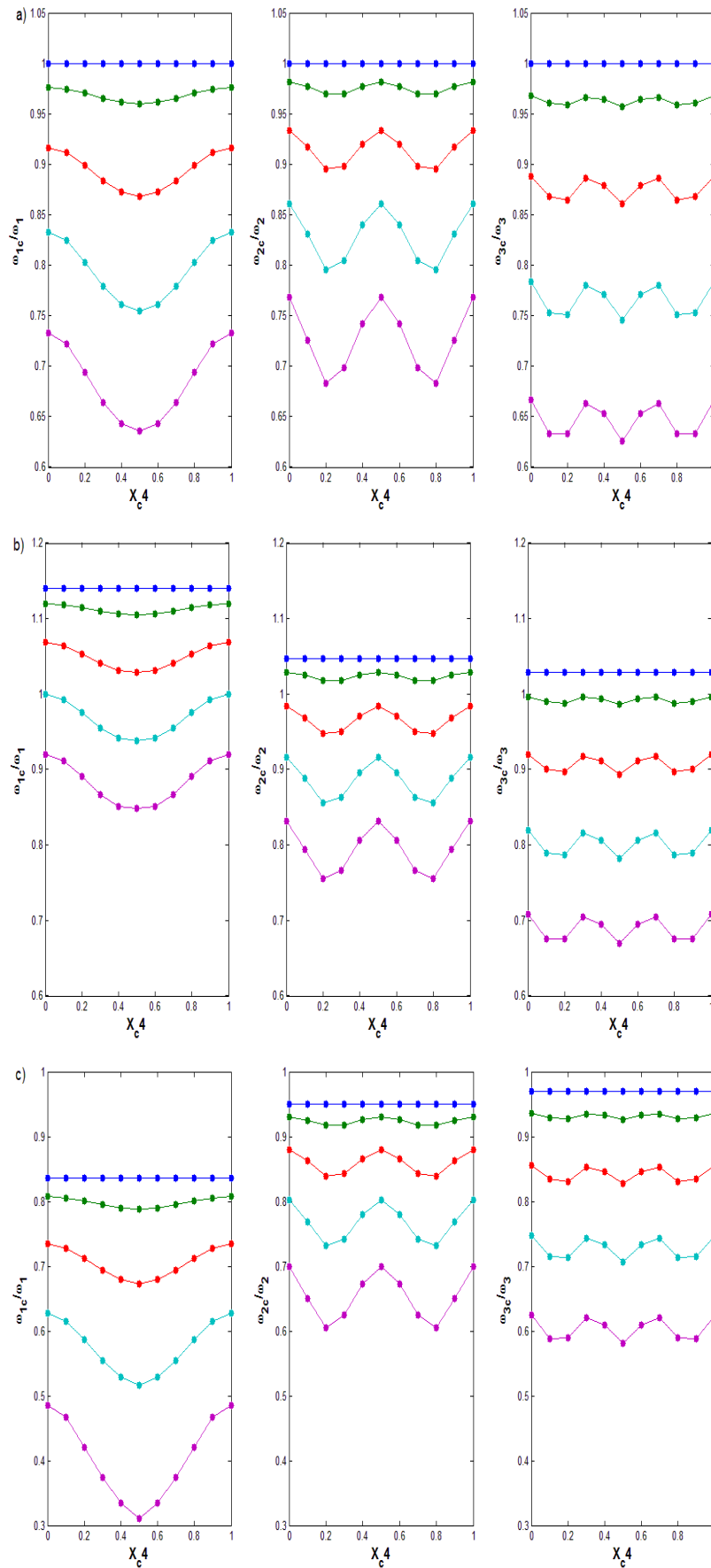


Figure 9. The first three non-dimensional natural frequencies of a hinged-hinged beam with four cracks for a) $P/P_{cr}=0$, b) $P/P_{cr}=-0.3$, and c) $P/P_{cr}=0.3$. The curves are obtained for a/h values of 0, 0.1, 0.2, 0.3, and 0.4 (from top to bottom).

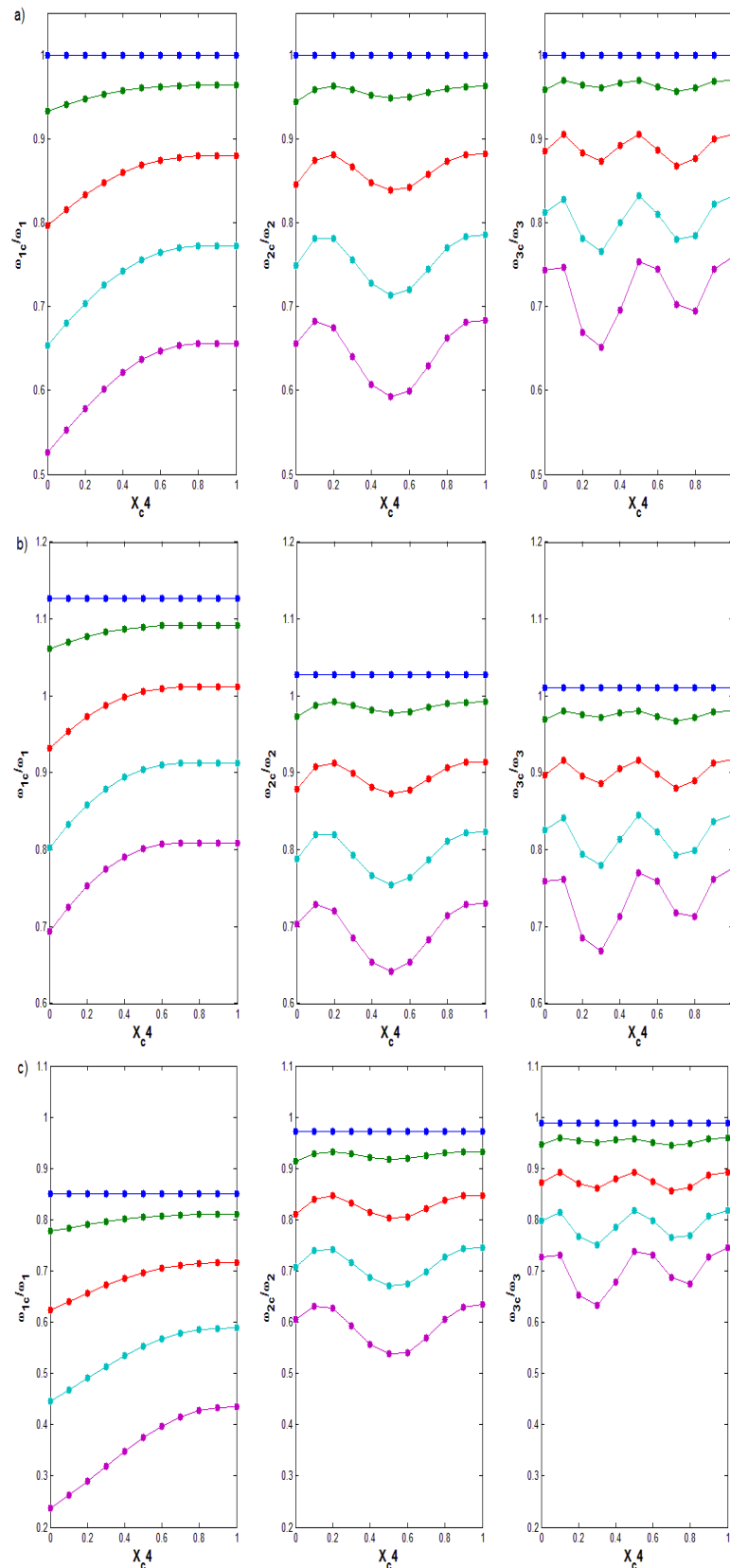


Figure 10. Same as Fig. 9 but with fixed-free boundary.

3.4. Effects of number of cracks on natural frequencies and corresponding mode shapes.

Fig. 11 and 12 show the effect of number of cracks on the first three non-dimensional natural frequencies of a beam for fixed-fixed, and fixed-hinged boundaries, respectively. Again, for brevity, the results of hinged-hinged and fixed-free are not shown here. In all figures, $a/h = 0.3$ is used, figure a) represents $P/P_{cr} = 0$, figure b) represents $P/P_{cr} = -0.3$, and figure c) represents $P/P_{cr} = 0.3$, the solid line represents a beam with one moving crack, the dashed line represents a beam with two cracks: one crack at location $0.2l$ and one moving

crack along the beam, and the dotted line represents a beam with three cracks, cracks located at 0.2/ and 0.4/ and one moving crack along the beam. Increasing the number of cracks leads to a decrease in the non-dimensional natural frequency for all loading cases. Fig. 13 and 14 show the effects of the number of cracks on the first three mode shapes of a beam with hinged-hinged and fixed-free boundaries, respectively. The results of fixed-fixed and fixed-hinged are not shown. Again, in all figures, $a/h = 0.3$ is used, figure a) represents $P/P_{cr} = 0$, figure b) represents $P/P_{cr} = -0.3$, and figure c) represents $P/P_{cr} = 0.3$. It is clear that the number of cracks slightly affects the mode shapes.

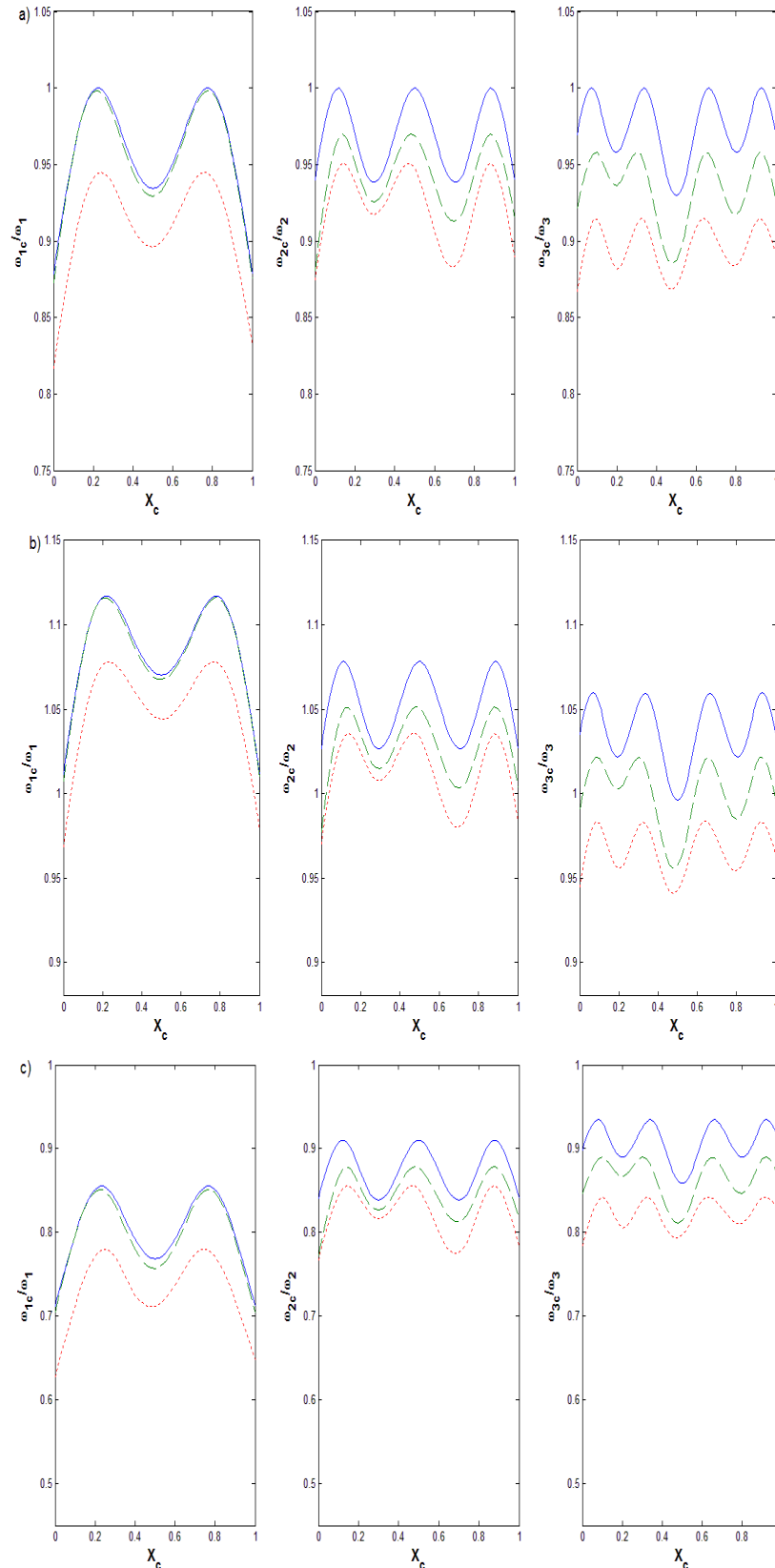


Figure 11. Effects of number of cracks on the first three non-dimensional natural frequencies of fixed-fixed beam for a) $P/P_{cr}=0$, b) $P/P_{cr}=-0.3$, and c) $P/P_{cr}=0.3$.

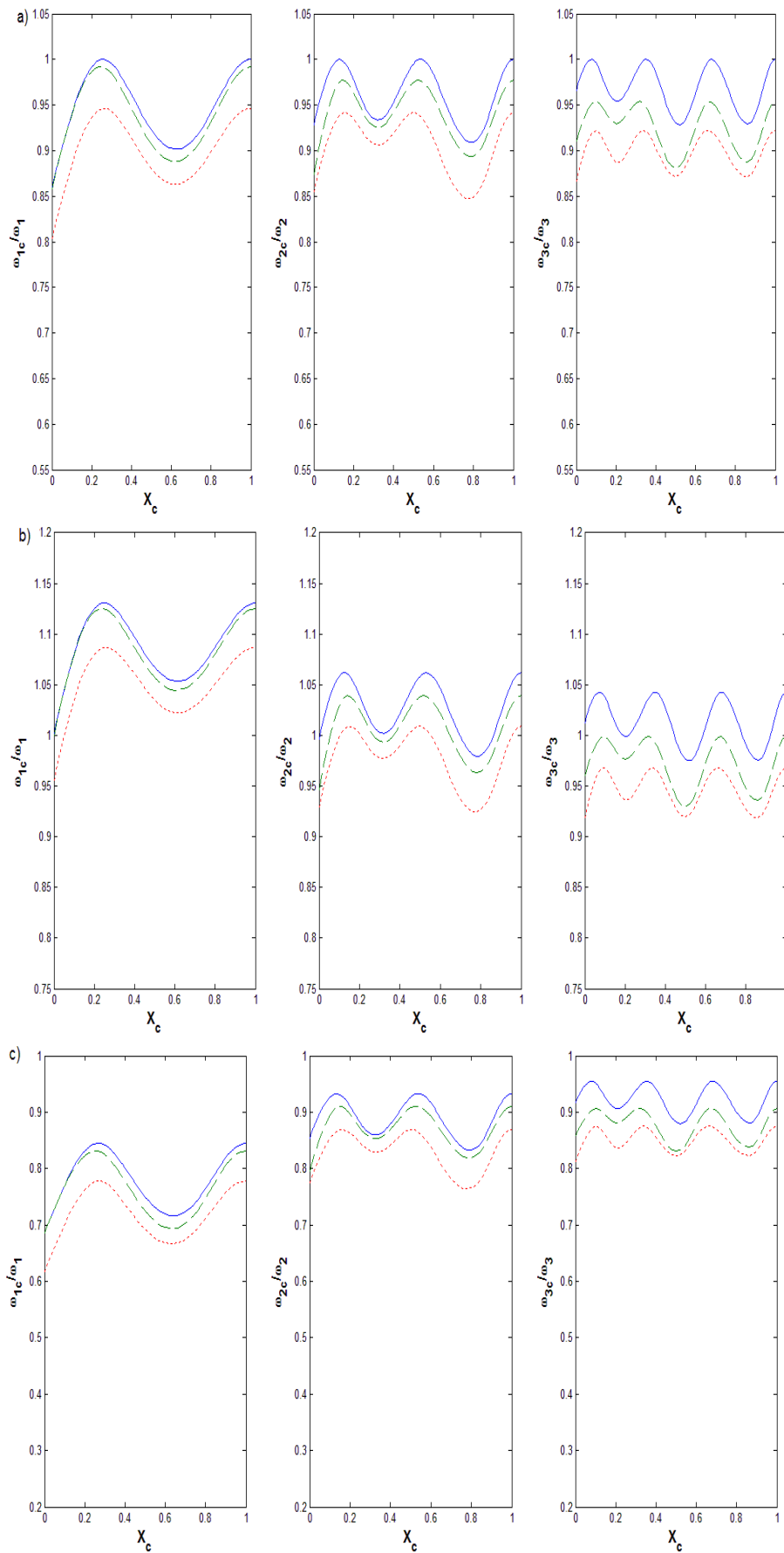


Figure 12. Same as Fig. 11 but with fixed-hinged boundary.

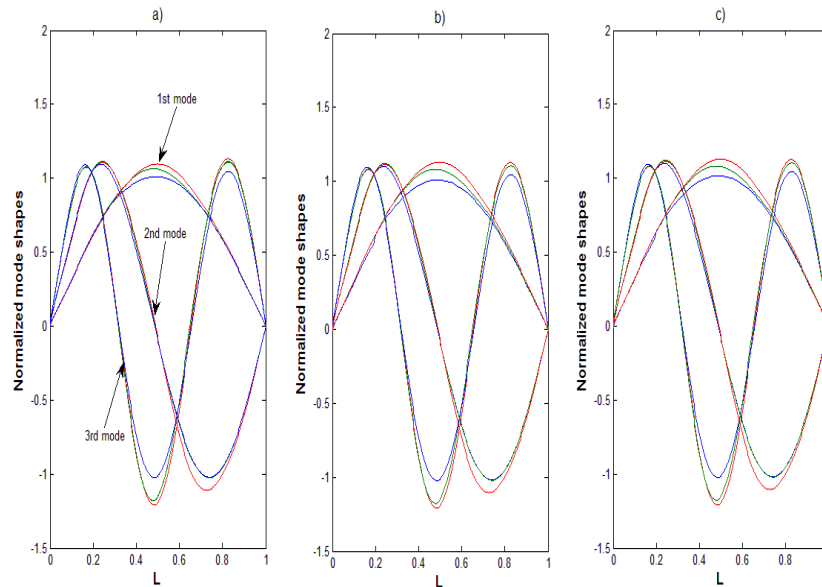


Figure 13. Effects of number of cracks on the first three mode shapes of hinged-hinged beam for a) $P/P_{cr}=0$, b) $P/P_{cr}=-0.3$, and c) $P/P_{cr}=0.3$. (Blue line represents one crack, green line represents two cracks, and red line represents three cracks)

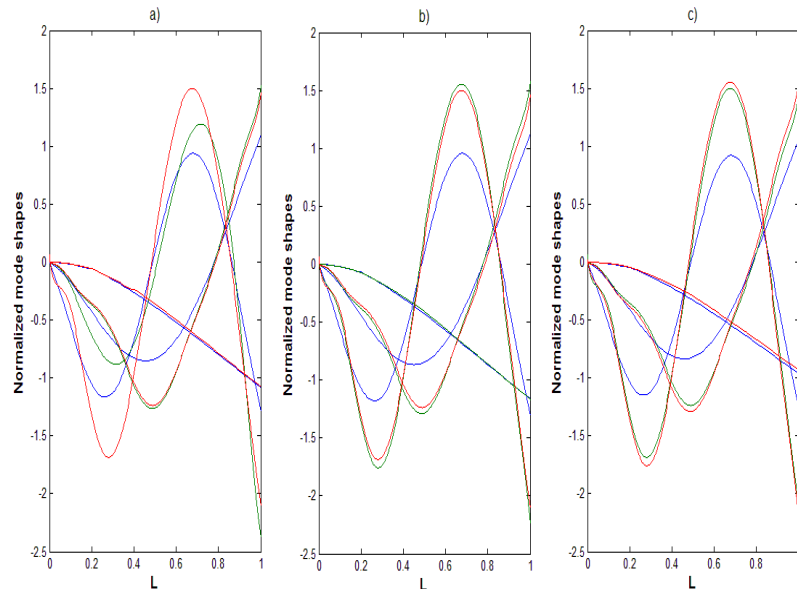


Figure 14. Same as Fig. 13 but with fixed-free boundary.

3.5. Effects of shear deformation and rotational inertia on natural frequencies

Fig. 15 and 16 show the effects of shear deformation and rotational inertia on the first three non-dimensional natural frequencies for fixed-fixed and fixed-hinged boundary conditions, respectively. The results of hinged-hinged and fixed-free are not shown. The y-axis is $\Omega_i = \omega_{ic} \sqrt{\rho / E}$ of the cracked beam and the x-axis is the position of the crack. In all figures, figure a) represents $P/P_{cr} = 0$, figure b) represents $P/P_{cr} = -0.3$, and figure c) represents $P/P_{cr} = 0.3$. Three values of slenderness ratio are used 5, 10, and 20. The value of a/h used is 0.3. It can be seen that the non-dimensional natural frequencies decrease as the value of slenderness increases. Also, it can be seen that the fundamental non-dimensional natural frequencies obtained by EBT and TBT gradually coincide at L/h greater than 10. A remarkable difference is observed on the fundamental non-dimensional natural frequencies obtained by EBT and TBT at L/h less than 10. At higher modes, the effects of L/h become more noticeable for all boundary conditions. In all figures, the results of $L/h = 20$ are not shown because the EBT and TBT results coincide with each other.

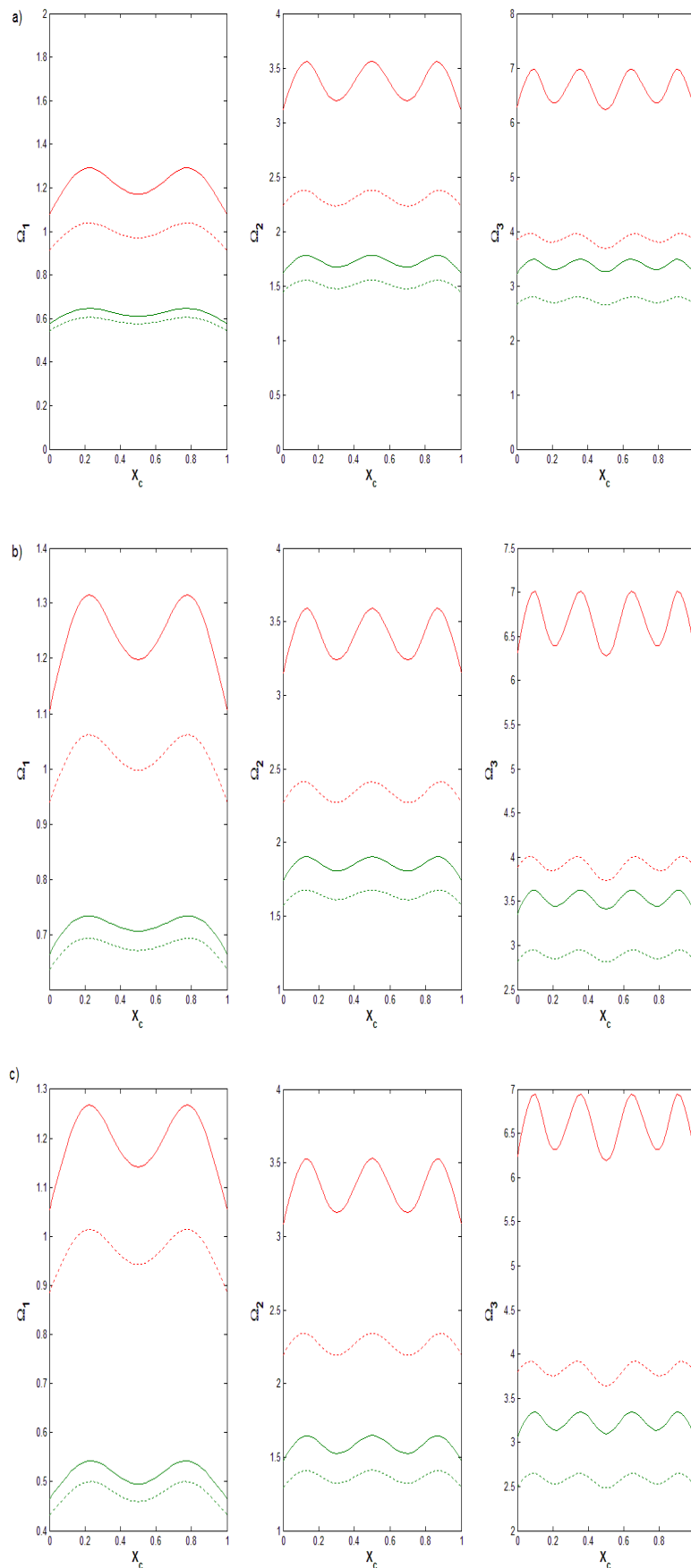


Figure 15. The first three non-dimensional frequencies of fixed-fixed beam with a single crack obtained by Euler–Bernoulli model with $L/h = 5$, Timoshenko model with $L/h = 5$, Euler–Bernoulli model with $L/h = 10$, and Timoshenko model with $L/h = 10$ (represented by solid red, dashed red, solid green, and dashed green lines, respectively); a) $P/P_{cr}=0$, b) $P/P_{cr}=-0.3$, and c) $P/P_{cr}=0.3$.

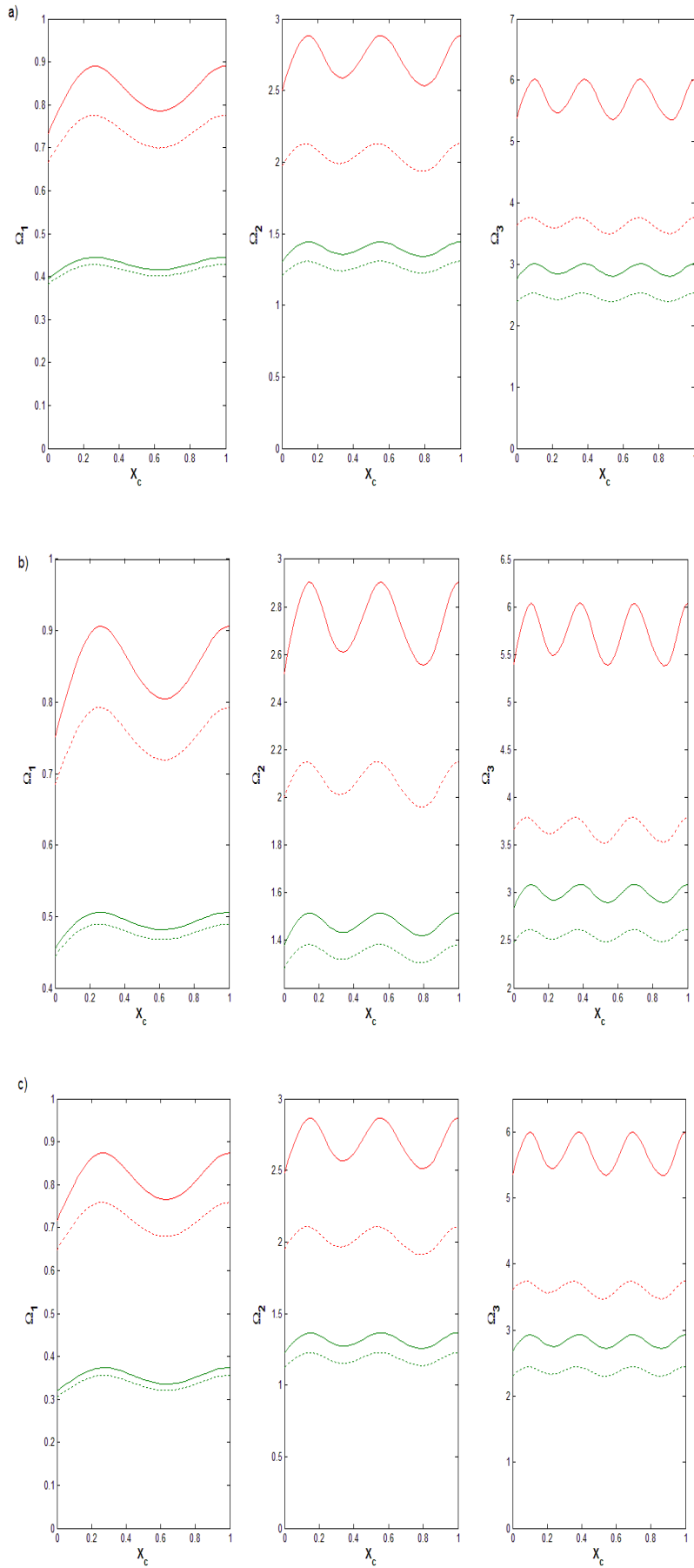


Figure 16. Same as Fig. 15 but with fixed-hinged boundary.

4. Conclusions

A simple transfer matrix method is used to study the vibrational behavior of axially-loaded, multi-cracked Timoshenko beams with differing boundary conditions. The effects of slenderness ratio, axial load, aspect ratio, a/h , boundary conditions, and number of cracks on the non-dimensional natural frequencies and the corresponding mode shapes are investigated. The following conclusions can be drawn:

1. The tensile force stiffens the beam while the compressive force softens the beam.
2. For the first mode, the severity of the cracks and the magnitude of the axial load affect the non-dimensional frequencies.
3. A decrease in the natural frequency is observed as the number of cracks increases, due to increased flexibility of the beam.
4. For specific crack location, the natural frequency decreases as the aspect ratio, a/h , increases.
5. At the location of the zero-crossing of the mode shape, and at critical points along the beam, the natural frequencies do not change with differing aspect ratios.
6. For the first non-dimensional frequencies, the compressive force shifts the locations of critical points toward the center of the beam. The tensile force shifts them toward the supports for fixed-fixed and fixed-hinged boundaries.
7. The first non-dimensional natural frequency is not affected by the crack location, aspect ratio of the crack, or the value of axial load beyond a certain location of the fixed-free beam.
8. A remarkable difference of the non-dimensional natural frequencies obtained by the Euler-Beam theory and Timoshenko beam theory is observed at values of L/h less than 20.

References

1. Liebowitz, H., Claus, W.D. Failure of notched columns, *J. Eng. Fract. Mech.* 1986. 1. Pp. 379–383. DOI: 10.1016/0013-7944(68)90010-6
2. Dimarogonas, A.D. Vibration of cracked structures: a state of the art review. *Engineering Fracture Mechanics*, 1996. 55 (5). Pp. 831–857. DOI: 10.1016/0013-7944(94)00175-8
3. Zheng, T., Ji, T. Equivalent representations of beams with periodically variable cross-sections. *Engineering Structures*. 2011. 33 (3). Pp. 706–719. DOI: 10.1016/j.engstruct.2010.11.007
4. Christides, S., Barr, A.D.S. Torsional vibration of cracked beams of non-circular cross-section. *International Journal of Mechanical Sciences*. 1986. 28 (7). Pp. 473–490. DOI: 10.1016/0020-7403(86)90067-6
5. Chondros, T.G., Dimarogonas, A. D., Yao, J. A continuous cracked beam vibration theory. *Journal of Sound and Vibration*. 1998. 215(1). Pp. 17–34. DOI: 10.1006/jsvi.1998.1640
6. Dimarogonas, A.D. *Vibration Engineering*. West Publishing Company, St. Paul, 1976. 568 p.
7. Liebowitz, H. Vanderveldt, H., Harris, D.W. Carrying capacity of notched columns. *International Journal of Solids and Structures*. 1967. 3(4). Pp. 489–500. DOI: 10.1016/0020-7683(67)90003-0
8. Liebowitz, H., Claus Jr., W.D. Failure of notched columns. *Engineering Fracture Mechanics*. 1968. 1(2). Pp. 379–383. DOI: 10.1016/0013-7944(68)90010-6
9. Okamura, H., Liu, H.W., Chu, C.S., Liebowitz, H. A cracked column under compression. *Engineering Fracture Mechanics*. 1969. 1(3). Pp. 547–564. DOI: 10.1016/0013-7944(69)90011-3
10. Brown, W.F., Srawley, J.E. *Plane Strain Crack Toughness Testing of High Strength Metallic Materials*. ASTM International. 1966. Pp. 1–129. DOI: 10.1520/STP44663S
11. Tada, H., Paris, P.C., Irwin, G.R. *The stress analysis of cracks handbook*, 3rd edn. ASME Press, New York .2000. 698 p. DOI: 10.1115/1.801535
12. Fernandez-saez, J., Navarro, C. Fundamental frequency of cracked beams in bending vibrations: an analytical approach. *Journal of Sound and Vibration*. 2002. 256(1). Pp. 17–31. DOI: 10.1006/jsvi.2001.4197
13. Yoon, H., Son, I., Ahn, S. Free vibration analysis of Euler-Bernoulli beam with double cracks. *Journal of Mechanical Science and Technology*. 2007. 21(3). Pp. 476–485. DOI: 10.1007/BF02916309
14. Loya, J.A., Rubio, L., Fernandez-saez, J. Natural frequencies for bending vibrations of Timoshenko cracked beams. *Journal of Sound and Vibration*. 2006. 290(3–5). Pp. 640–653. DOI: 10.1016/j.jsv.2005.04.005
15. Zhong, S.C., Oyadiji, S.O. Analytical predictions of natural frequencies of cracked simply supported beams with a stationary moving mass. *Journal of Sound and Vibration*. 2008. 311(1–2). Pp. 328–352. DOI: 10.1016/j.jsv.2007.09.009
16. Naguleswaran, S. Vibration and stability of an Euler–Bernoulli beam with up to three-step changes in cross-section and in axial force. *International Journal Mechanical Sciences*. 2003. 45(9). Pp. 1563–1579. DOI: 10.1016/j.ijmecsci.2003.09.001
17. Gomes, H.M., de Almeida, F.J.F. An analytical dynamic model for single-cracked beams including bending, axial stiffness, rotational inertia, shear deformation and coupling effects. *Applied Mathematical Modelling*. 2014. 38(3). Pp. 938–948. DOI: 10.1016/j.apm.2013.07.019
18. Aydin, K. Vibratory characteristics of Euler-Bernoulli beams with an arbitrary number of cracks subjected to axial load. *Journal of Vibration and Control*. 2008. 14(4). Pp. 485–510. DOI: 10.1177/1077546307080028
19. Neves, A.C., Simões, F.M.F., da Costa, A.P. Vibrations of cracked beams: Discrete mass and stiffness models. *Computers and Structures*. 2016. 168. Pp. 68–77. DOI: 10.1016/j.compstruc.2016.02.007

20. Kwanghun, K., Sok, K., Kyongjin, S., Pak, C., Kwangbok, H. A modeling method for vibration analysis of cracked beam with arbitrary boundary condition. *Journal of Ocean Engineering and Science*. 2018. 3(4). Pp. 367–381. DOI: 10.1016/j.joes.2018.11.003
21. Batihan, A.Ç., Kadioğlu, F.S. Vibration Analysis of a Cracked Beam on an Elastic Foundation. *International Journal of Structural Stability and Dynamics*. 2016. 16(05). 1550006 p. DOI: 10.1142/S0219455415500066
22. Khorrarn, A., Rezaeian, M., Bakhtiari-Nejad, F. Multiple cracks detection in a beam subjected to a moving load using wavelet analysis combined with factorial design. *European Journal of Mechanics A/solids*. 2013. 40. Pp. 97–113. DOI: 10.1016/j.euromechsol.2012.12.012
23. Heydari, M., Ebrahimi, A., Behzad, M. Forced vibration analysis of a Timoshenko cracked beam using a continuous model for the crack. *Engineering Science and Technology, an International Journal*. 2014. 17(4). Pp. 194–204. DOI: 10.1016/j.jestch.2014.05.003
24. Yang, J., Chen, Y., Xiang, Y., Jia, X.L. Free and forced vibration of cracked inhomogeneous beams under an axial force and a moving load. *Journal of Sound and Vibration*. 2008. 312(1-2). Pp. 166–181. DOI: 10.1016/j.jsv.2007.10.034
25. Khiem, N.T., Lien, T.V., Ninh, V.T.A. Natural Frequencies of Multistep Functionally Graded Beam with Cracks. *Iranian Journal of Science and Technology, Transactions of Mechanical Engineering*. 2019. 43, Pp. 881–916. DOI: 10.1007/s40997-018-0201-x
26. Lien, T.V., Duc, N.T., Khiem, N.T. Free Vibration Analysis of Multiple Cracked Functionally Graded Timoshenko Beams. *Latin American Journal of Solids and Structures*. 2017. 14(9). Pp. 1752–1766. DOI: 10.1590/1679-78253693
27. Kou, K.P., Yang, Y. A meshfree boundary-domain integral equation method for free vibration analysis of the functionally graded beams with open edged cracks. *Composites Part B: Engineering*. 2019. 156. Pp. 303–309. DOI: 10.1016/j.compositesb.2018.08.089
28. Khiem, N.T., Tran, H.T., Nam, D. Modal analysis of cracked continuous Timoshenko beam made of functionally graded material. *Mechanics Based Design of Structures and Machines*. 2019. DOI: 10.1080/15397734.2019.1639518
29. Chen, W., Chang, H. Vibration Analysis of Functionally Graded Timoshenko Beams. *International Journal of Structural Stability and Dynamics*. 2018. 18(01). 1850007 p. DOI: 10.1142/S0219455418500074
30. Lien, T.V., Duc, N.T., Khiem, N.T. Free and forced vibration analysis of multiple cracked FGM multi span continuous beams using dynamic stiffness method. *Latin American Journal of Solids and Structures*. 2019. 16(2). Pp. 1–26. DOI: 10.1590/1679-78255242
31. Chen, B., Zhao, X., Li, Y.H., Guo, Y. Forced vibration analysis of multi-cracked Timoshenko beam with the inclusion of damping by virtue of Green's functions. *Applied Acoustics*. 2019. 155. Pp. 477–491. DOI: 10.1016/j.apacoust.2019.06.016
32. Khiem, N.T., Huyen, N.N., Long, N.T. Vibration of Cracked Timoshenko Beam Made of Functionally Graded Material. In: Harvie J., Baqersad J. (eds) *Shock & Vibration, Aircraft/Aerospace, Energy Harvesting, Acoustics & Optics*. Conference Proceedings of the Society for Experimental Mechanics Series. Springer, Cham. 2017. 9. Pp. 133–143. DOI: 10.1007/978-3-319-54735-0_15
33. Lien, T.V., Duc, N.T., Khiem, N.T. Mode Shape Analysis of Multiple Cracked Functionally Graded Timoshenko Beams. *Latin American Journal of Solids and Structures*. 2017. 14(7). Pp. 1327–1344. DOI: 10.1590/1679-78253496
34. Chouiyakh, H., Azrar, L., Alnefaie, K., Akourri, O. Vibration and multi-crack identification of Timoshenko beams under moving mass using the differential quadrature method. *International Journal of Mechanical Sciences*. 2017. 120. Pp. 1–11. DOI: 10.1016/j.ijmecsci.2016.11.014
35. Khiem, N.T., Huyen, N.N. A method for crack identification in functionally graded Timoshenko beam. *Nondestructive Testing and Evaluation*. 2017. 32. Pp. 319–341. DOI: 10.1080/10589759.2016.1226304
36. Pestel, E.C., Leckie, F.A. *Matrix methods in elasto mechanics*, McGraw-Hill, London, 1963. 435 p.
37. Attar, M. A transfer matrix method for free vibration analysis and crack identification of stepped beams with multiple edge cracks and different boundary conditions. *International Journal of Mechanical Sciences*. 2012. 57(1). Pp. 19–33. DOI: 10.1016/j.ijmecsci.2012.01.010
38. Khiem, N.T., Lien, T.V. The dynamic stiffness matrix method in forced vibration analysis of multiple-cracked beam. *Journal of Sound and Vibration*. 2002. 254(3). Pp. 541–555. DOI: 10.1006/jsvi.2001.4109
39. Khiem, N.T., Lien, T.V. A simplified method for natural frequency analysis of a multiple cracked beam. *Journal of Sound and Vibration*. 2001 245(4). Pp. 737–751. DOI: 10.1006/jsvi.2001.3585
40. Bozyigit, B., Bozyigit, I., Yesilce, Y., Abdel Wahab, M. Crack Identification in Multi-Span Beams on Elastic Foundation by Using Transfer Matrix Method, 2020. *Proceedings of the 13th International Conference on Damage Assessment of Structures*. Lecture Notes in Mechanical Engineering. Springer, Singapore.
41. Tan, G., Liu, Y., Gong, Y., Shen, Y., Liu, Z. Free Vibration of the Cracked Non-uniform Beam with Cross Section Varying as Polynomial Functions. *KSCSE Journal of Civil Engineering*. 2018. 22(1). Pp. 4530–4546. DOI: 10.1007/s12205-018-1833-5
42. Kisa, M. Vibration and stability of multi-cracked beams under compressive axial loading. *International Journal of Physical Sciences*. 2011. 6(11). Pp. 2681–2696. DOI: 10.5897/IJPS11.493
43. Nguyen, K.V. Mode shapes analysis of a cracked beam and its application for crack detection. *Journal of Sound and Vibration*. 2014. 333(3). Pp. 848–872. DOI: 10.1016/j.jsv.2013.10.006
44. Zheng, D. Y., Kessissoglou, N.J. Free vibration analysis of a cracked beam by finite element method. *Journal of Sound and Vibration*. 2004. 273(3). Pp. 457–475. DOI: 10.1016 /S0022-460X(03)00504-2
45. Aydin, K. Vibratory characteristics of axially loaded Timoshenko beams with arbitrary number of cracks. *Journal of Vibration and Acoustics*. 2007. 129(3). Pp. 341–354. DOI: 10.1115/1.2731411
46. Weaver Jr.W., Timoshenko, S.P., Young, D.H. *Timoshenko, S., Jr, W.W. Vibration Problems in Engineering*. 5th edn. Wiley. New York, 1990. 624 p.
47. Cheng, F.Y. *Matrix Analysis of Structural Dynamics: Applications and Earthquake Engineering*. 1st edn. Marcel Dekker Inc., New York, 2000. 997 p.
48. Al Rjoub, Y.S., Hamad, A.G. Free Vibration of Axially Loaded Multi-Cracked Beams Using the Transfer Matrix Method. *International Journal of Acoustics and Vibration*. 2019. 24(1). Pp. 119–138. DOI: 10.20855/ijav.2019.24.11274

Contacts:

Yousef Al Rjoub, ysalrjoub@just.edu.jo

Azhar Hamad, co.azhar@yahoo.com



DOI: 10.18720/MCE.100.3

Durability behaviors of foam concrete made of binder composites

V.S. Lesovik^{a,b}, E.S. Glagolev^c, V.V. Voronov^a, L.Kh. Zagorodnyuk^a, R.S. Fediuk^{*d}, A.V. Baranov^d,
A.Kh. Alaskhanov^e, A.P. Svintsov^f

^a V.G. Shukhov Belgorod State Technological University, Belgorod, Russia

^b Research Institute of Building Physics of the Russian Academy of Architecture and Building Sciences, Moscow, Russia

^c Administration of the Belgorod region, Belgorod, Russia

^d Far Eastern Federal University, Vladivostok, Russia

^e Grozny State Oil Technical University named after Academician M.D. Millionshchikov, Grozny, Russia

^f Peoples' Friendship University of Russia, Moscow, Russia

* E-mail: roman44@yandex.ru

Keywords: cements, cement-based composites, binders, concretes, durability.

Abstract. The article is devoted to the determination of the patterns of the formation of the microstructure of foam concrete using Portland cement, opoka marl and fly ash. Binder composites obtained by joint grinding of these were prepared in the form of new compounds, on the basis of which concrete with improved mechanical properties and performance characteristics are created. The complex of experimental studies included studies of the thermal intensity of hydration, shrinkage, average density and compressive strength. A number of operational characteristics were also comprehensively investigated: frost resistance, thermal conductivity and vapor permeability. Both microstructural and morphological studies of the developed composites were investigated using the analysis of SEM images, X-ray diffraction patterns and DTA patterns. The experimental results of composite binders and foam concrete based on it are presented. The mechanism of the influence of fly ash on the formation of the microstructure of the foam concrete mixture for building envelopes is determined. Binder composites obtained by co-grinding the components have a compressive strength of up to 60 MPa with Portland cement savings of up to 40 %. Based on the binder composites, foam concrete with a density of 500–700 kg/m³ and compressive strength above 4 MPa was obtained. In addition, a technological scheme was developed for the production of non-autoclaved foam concrete for the manufacture of blocks, as well as for monolithic construction.

1. Introduction

The natural energy resources are running out and are becoming more expensive, but at the same time the construction industries spend huge large quantities and very uneconomically [1–2]. About 30 % of fuel resources are spent on creating thermal comfort in the premises. At the same time, almost a third of these resources are lost in the process of transportation, as well as through leaks through the enclosing structures of buildings and structures [3–4]. Only through the introduction of energy-efficient building materials that combine multifunctionality and low cost, it can optimize the construction and improve the thermal characteristics of buildings and structures [5–7]. One such material is cellular concrete [8–10].

Naturally, to reduce energy costs, it is necessary to exclude autoclave processing from the list of technological processes necessary for the production of this class of concrete. However, it is rather difficult to obtain a durable material with an optimal pore structure. Complex modification of the mixture through the use of active mineral components contributes to the quality indicators of the cellular material. This, on the one hand, increases the stability and viability of the foam concrete mix, and on the other hand, increases the complex of physicomechanical quality indicators of the composite [11–15].

Using special composite binders that optimize the synthesis process at all stages from foaming and porosity of the mixture to curing and operation of the composite, it is possible to increase the efficiency of

Lesovik, V.S., Glagolev, E.S., Voronov, V.V., Zagorodnyuk, L.Kh., Fediuk, R.S., Baranov, A.V., Alaskhanov, A.Kh., Svintsov, A.P. Durability behaviors of foam concrete made of binder composites. Magazine of Civil Engineering. 2020. 100(8). Article No. 10003. DOI: 10.18720/MCE.100.3



This work is licensed under a CC BY-NC 4.0

these building materials [16–18]. The selection of silica-containing components from both technogenic and natural raw materials is the most important task on this path. The use of these additives allows not only to reduce the consumption of the most energy-consuming and expensive component of foam concrete – Portland cement, but also allows you to control the structure formation of the cellular composite [19–21].

Among the main advantages of foam concrete (Fig. 1), is that, Chica and Alzate [22] highlighted the low weight of the material and structures made using foam concrete, which reduces the load on the foundations and, thus, reduces the cost of their construction. The low weight of the products results in low transportation costs. The article [23] states that foam concrete is characterized by high vapor permeability with a simultaneous coefficient of thermal conductivity. This indicates a very important fact – the material "breathes", while not violating the humidity conditions, both indoors and inside the structure itself. Other researchers [24] cite facts characterizing the high durability of non-autoclave foam concrete.

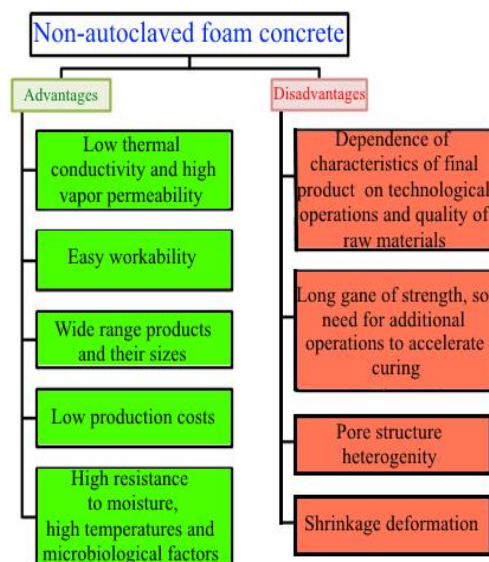


Figure 1. Advantages and disadvantages of non-autoclaved foam concrete.

A wide range of products and their sizes is made possible thanks to the simple workability of the material and the possibility of using both blocks and monolithic foam concrete. There are a number of technology foam concrete blocks, for example, as a result of pouring into molds to match the size of the product, or cutting into blocks of larger arrays. The authors of article [25] highlight the simplicity and affordability of technology, as well as the low cost of production, as advantages of non-autoclaved foam concrete. Given all this, there is a huge number of manufacturers of both raw materials (foaming agents and binders - traditionally use Portland cement), and the blocks themselves made of foam concrete. Despite this, foam concrete has a number of drawbacks, the main one of which is shrinkage resulting from a long-term increase in strength [26–27]. Immediately after the preparation of the foam, processes of spontaneous destruction immediately arise, which cease only when the composite is significantly hardened. Accordingly, to reduce these deformations, it is necessary to ensure stable characteristics of the foam [28–29]. It is known that for cement composites it is necessary to control that the hydration of clinker minerals takes place in full; only in this case is the required strength of the hardened composite

Given all of the above, it can be concluded that the process of forming the macrostructure of aerated concrete is difficult to control and regulate [32–33]. This conclusion is explained by the need to simultaneously control a large number of technological parameters: the quality of the raw material and the accuracy of its dosage, the water-solid ratio of the system and its rheological characteristics, temperature and pH of the medium, which change during the manufacturing and curing of foam concrete [34–36].

Using prescription and technological methods, it is possible to reduce the negative effect of these shortcomings. The use of modifying additives, the selection and development of foaming additives, quality control of materials and the flow of technological processes can improve the efficiency of the manufactured cellular concrete.

Summarizing all of the above, we note the following. Despite the fact that a lot of research has been done on foam concrete, there are many “white spots” that need to be addressed as soon as possible. Thus, the object of the study are non-autoclave foam concrete. And the subject of research in this case will be the durability characteristics of these promising materials.

The goal of the study is to optimize the durability of non-autoclaved foam concrete using a composite binder. In the course of achieving this goal, a number of tasks were solved:

- a) research of optimal compositions of foam concrete on binder composites via both organic and mineral admixtures;
- b) study of the possibility of controlling the processes of structure formation at the synthesis of foam concrete made based on binder composites;
- c) study of the properties of modified foam cement systems and the development of materials science and technological methods for their regulation;
- d) research and development of composites for both structural and heat-insulating un-autoclaved foam materials.

2. Materials and Methods

2.1. Materials

For synthesise of binder composite and foam concrete for monolithic construction, opoka marl (OM) and Portland cement CEM I 42.5N (Belgorod cement, Russian Federation) were used. Foam concrete for the production of blocks was prepared on the binder composite using the same Portland cement as well as fly ash (FA) from Novotroitskaya TPP (Russian Federation). The chemical content of the CEM I 42.5N used are shown in Table 1.

Table 1. Chemical content of CEM I 42.5N.

Chemical composition (%)						
calcium oxide	silica	aluminium oxide	iron oxide	magnesium oxide	sulfur oxide	sodium oxide
65.9	21.7	5.0	4.2	1.25	0.40	0.78

The opoka marl belongs to the group of medium and highly leached marls, which contain CaO – 28.0–33.0 %. This is a dense rock of gray color with a green tint, often fractured with thin deposits of iron hydroxides along the crack planes, a random texture, pelitomorphous globular, relict organogenic structure with varying silica and calcium carbonate contents. The main rock-forming mineral of the opoka-like marl is represented by organogenic calcite, the average content of which is 35 ... 38 %, opal – up to 15 %, the rest is mixed-layer clay formations and zeolites, clay minerals are replaced by opal. A feature of these minerals is that some of them are amorphous or have a defective crystal lattice, which determines their sorption and pozzolanic activity. The natural moisture content of the rock is 21–26 %; porosity – about 47 %; the ductility number is about 12.3 %; a fraction content of less than 0.005 mm is 58–65 %; average total radioactivity $A_{eff} = 56.0$ bc/kg). The natural moisture content of the rock is 21–26 %, porosity is about 47 %, and the ductility number is 13.5.

The Muraplast FK 19 superplasticizer (SP) (MC-Bauchemie, Germany) was used for improve the rheological characteristics of the mixes. The alpha olefin sulfonate sodium ASCO 93 (Korea) was used as a foaming agent.

2.2. Methods

A MicroSizer 201 laser particle analyzer (Scientific instruments, Russian Federation), a Reostat 4.1 rotational viscometer (Germany) and a high resolution TESCAN MIRA 3 LMU scanning microscope (Czech Republic) were carried out for the study of raw materials, binder composites and foam concretes. The X-ray diffraction patterns of the samples were tested by an ARL XTRA device (United States) by the method of powder X-ray diffraction. A STA 449 F1 Jupiter derivatograph (NETZSCH, Germany) was used for obtaining the differential-thermal (DTA) patterns of the samples.

A ToniCAL 7338 differential heat flow calorimeter (Toni Technik, Germany) tests the binder hydration in the early stages. The method of a cylindrical probe was used for the study of the thermal conductivity of the cellular concrete by an ITP – MG4 Probe thermal conductivity meter (Stroypribor, Russian Federation). Frost resistance was researched on specimens of 100×100×100 mm size by a Polair CV-105S freezer (Russian Federation) at a temperature of -18°C; each freezing cycle was 150 minutes, the thawing cycle at a temperature of 20°C – 120 minutes. The UNI EN ISO 12572 method using specimens of 200×100×70 mm in size was used to study vapor permeability.

3. Results and Discussion

3.1. Mix design

The structure and properties of binder composites are determined by the choice of starting materials – cement and the type of mineral additive, as well as their ratio, dispersion, activity and interaction. To determine the rational amount of mineral additives in the composition of binder composites, various doses were added, varying the amount of cement in the range 50...90 %, opoka marl – 2.5...12.5 % and fly ash – 10...50 %. The opoka marl was pre-dried, then crushed by a laboratory jaw crusher and then crushed in a vibration mill to a specific surface area up to 500 m²/kg.

In the course of further studies, the nature of the influence of the composition of the binder composite on their physicomechanical characteristics was revealed (Table 2). At the same time, the strength characteristics of the BC specimens with a binary mineral additive (40 % fly ash + 10 % opoka marl) increase up to 70 % compared to cement without additives.

Table 2. Content and properties of binder composites for foam concrete manufacturing.

ID	Composition, %			Specific surface area m ² /kg	with superplasticizer Muraplast FK 19 (0.1 %)			
	Portland cement	Opoka marl	Fly ash		Normal density of cement paste, %	Setting time, min start/end	Compressive strength, MPa	
							7 d	28 d
1	100	–	–	324	27	150/250	19.9	43.5
2	90	10	–	551	23	15/168	45.3	79.3
3	60	–	40	549	24.5	23/168	41.7	62.2
4	50	10	40	552	23	19/169	40.1	72.3

Opoka marl and fly ash in the BC content direct to an raise in the volume concentration of hydrated new growths as a result the interaction of calcium hydroxide with active additives of the binder composite. The quantitative ratio of hydration products (Fig. 2) can be seen by the intensity of diffraction reflections: calcium hydroxide ($d = 4.93; 3.11; 2.63; 1.93; 1.79; 1.69 \text{ \AA}$), alite ($d = 2.76; 2.19 \text{ \AA}$), belite ($d = 2.78; 2.74; 2.19 \text{ \AA}$), ettringite ($d = 9.7; 5.9; 4.92 \text{ \AA}$) and calcium hydrosilicates ($d = 9.8; 4.9; 3.07; 2.85; 2.80; 2.40; 2.80; 2.00; 1.83 \text{ \AA}$) X-ray diffraction patterns showed that in the samples of the binder composite with OM, FA and binary mineral additive (10 % OM + 30 % FA), the reflection intensity of calcium hydroxide decreases by 1.7; 3.3 and 1.6 times, respectively.

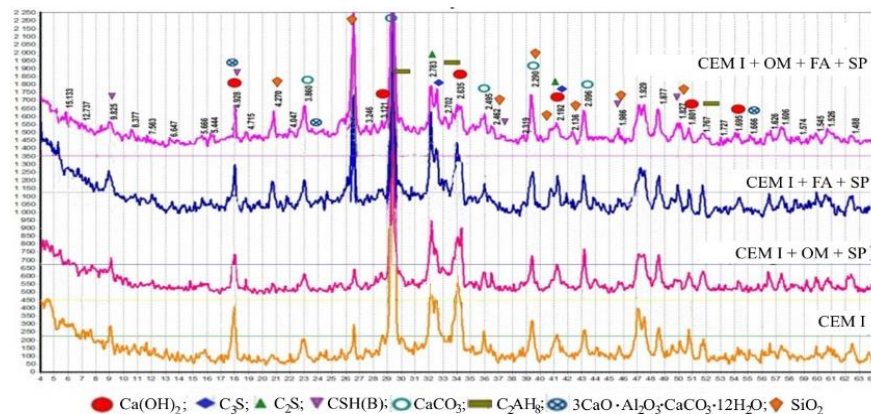


Figure 2. X-ray diffraction pattern of 28-days hardened composite binder with mineral admixtures: 1 – CEM I; 2 – CEM I + OM + SP; 3 – CEM I + FA + SP; 4 – CEM I + OM + FA + SP.

An increased amount of low basic calcium hydrosilicates is also noted. As you know, this has a positive effect on the strength of the cured composite. At the same time, a decrease in the amount of ettringite in all hydrated composites (with opoka marl, fly ash and binary mineral additive) is achieved in comparison with the control composition, this fact is explained by the low basicity of calcium hydroaluminates. Due to the use of superplasticizer in cement and composite compositions with fly ash, it slows down the hydration process in the early stages. In the subsequent stages, for the composite with the opoka marl, as well as the binary FA + OM, the hydration process is accelerated, which leads to an increase in strength compared to non-additive cement and is confirmed by the results of physical and mechanical tests (Table 2). Thus, the structural features of composite binders using the opoka marl and fly ash have been established, which are included in the optimization of the synthesis of new growths due to the multicomponent composition of composite binders. The presence of marl flask in the cementitious composite, which, along with calcite and clay-mixed clay formations, zeolite and opal, as well as fly ash, accelerates the setting process of the foam concrete mixture by the optimal time parameter. The peculiarity of hydration and the influence of mineral components on the properties of the binder composite is confirmed

by the dynamics of heat release, expressed by the dependence $dQ/dt = f(t)$ in the initial curing period (up to 1 day), as well as the total amount of heat released, described by the function $Q = f(t)$ for 3 days using a differential calorimeter (Fig. 3).

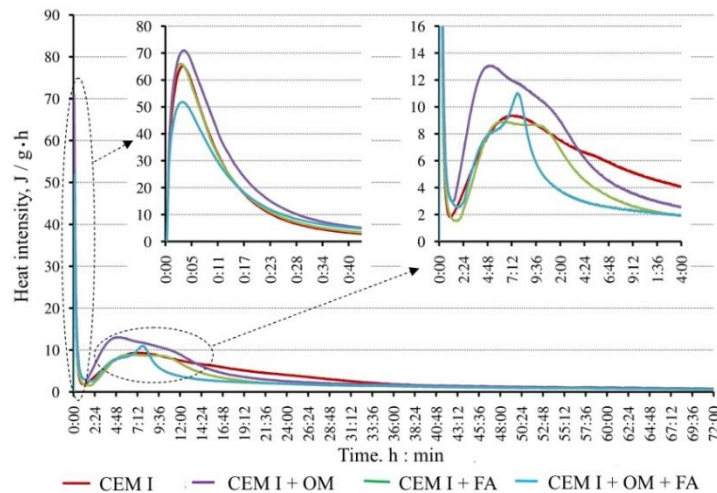


Figure 3. Kinetics of heat release at hydration of binder composites.

This fact can be explained as follows. When opoka marl is added to the cement system, hydration processes intensify during the induction period, which is accompanied by an increase in the completeness of hydration of the clinker minerals. This is due to the manifestation of the pozzolanic reaction and active binding of calcium hydroxide, as well as a higher concentration of accumulated new growths - the calcium hydrosilicates of the second generation. The manufacturing quality of foam concrete is more dependent on three elements: the stability of the foam, obtaining a cellular suspension using cementitious composites, as well as curing the resulting porous mass. High-quality microstructure of foam concrete is achieved by the optimal ratio of time to reach maximum system porosity and setting time. The foam-cement mixture on pure cement, after mixing, foams to a volume of 800 cm³, after 60 minutes it decreases to 700 cm³ and remains at this level for 12 hours of storage (Table 3). The foam-cement-ash mass has half the volume of foaming – 400 cm³, which after 60 minutes of storage drops to 300 cm³, and by 12 h – up to 280 cm³. The expansion volume of the cement-marl composition was 820 cm³, after 60 minutes it dropped to 810 cm³, and after 12 hours it stopped at around 800 cm³. Thus, the cement-marl composition showed the best characteristics.

Table 3. Behaviors of binder composites for cellular concrete manufacturing.

Mix ID	Water/cement ratio	Foamer, % wt.	Volume of foam, cm ³			Multiplicity of system, K _s
			immediately after mixing	after		
				60 min	12 h	
CEM I+SP			800	700	700	3.5
CEM I+FA+SP	0.45	0.2	400	300	280	1.4
CEM I+OM+SP			820	810	800	4

Foam-cement mixtures based on the binder composite (cement-marl) are also characterized by optimal rheological characteristics. This makes it possible to optimize such important parameters as the intensity of formation of a porous microstructure, the onset of setting, and the curing of the system. Table 4 lists the selected formulations for monolithic foam concrete. This selection was carried out taking into account the characteristics of the binder composites, such as water requirements, setting and curing rates, rheological characteristics and activity. The test results of the developed compositions of foam concrete with opoka marl showed that the best is the composition on the developed binder composites for joint grinding of cement and opoka marl in a ratio of 90 %: 10 %. The compressive strength of specimens of foam concrete with a density of 703 kg/m³ was 4.32 MPa, which is 1.8 times greater than that of the reference specimen on pure Portland cement, and significantly higher than that of industrial foam concrete blocks. In general, all synthesized foam concrete with a range of densities of 300–700 kg/m³ obtained on the basis of BC have a compressive strength higher than control specimens prepared on Portland cement, while providing significant economy of Portland cement.

Table 4. Behaviors of foam concrete on binder composites incorporating opoka marl.

Characteristics	Type of binder used,% by weight of cement								
	Reference specimen (CEM I)			Joint milled 90 % CEM I+10 % OM (489 m ² /kg)			Separately milled 90 % CEM I+10 % OM (484 m ² /kg)		
Composition, kg/m ³									
Portland cement	260	435	610	234	385	540	234	385	540
Opoka marl	–	–	–	26	50	70	26	50	70
Water	200	260	320	200	300	370	200	300	370
Foamer, % by CEM I wt.	1.25	1	1.25	1.25	1	1.25	1.25	1	1.25
Characteristics									
Average density, kg/m ³	309	505	701	308	498	703	305	503	695
Compressive strength, MPa	0.39	1.48	2.42	0.58	2.83	4.32	0.55	2.37	3.27
Thermal conductivity, W/m·°C	0.08	0.12	0.18	0.065	0.10	0.16	0.07	0.11	0.18
Frost resistance, cycles	20	20	25	25	30	35	20	25	35
Vapor permeability, mg/mhPa	0.29	0.24	0.21	0.27	0.22	0.18	0.28	0.23	0.18
Shrinkage, mm/m	1.33	1.29	1.22	1.04	0.87	0.96	1.12	1.02	0.95
Note	Compared to specimens on the BC, the reference specimens have larger porosity, looser and more heterogeneous microstructure, and greater water separation			water separation is not observed			water separation is not almost observed		

Using the binder composites obtained by co-grinding Portland cement and 10 % opoka marl to a specific surface area of $489 \text{ m}^2/\text{kg}$, a wide range of foam concrete was developed for monolithic construction with a wide range of densities of $300\text{--}700 \text{ kg/m}^3$. The increase in strength (almost 1.8 times for foam concrete with a density of 700 kg/m^3) is explained by the positive effect of using a binder composites at all stages of the preparation of the composite, from foaming and porosity to hardening and operation. Given the high demand for foam concrete in low-rise individual construction, dry mixes have been developed for monolithic construction. It was found that the compressive strength of foam concrete on binder composites obtained by joint grinding of Portland cement (60 %) and fly ash (40 %) up to a specific surface of $500\text{--}550 \text{ m}^2/\text{kg}$, increases 1.37 times compared to the reference specimens (Table 5) with high Portland cement economy. The values of thermal conductivity, vapor permeability and shrinkage during drying are in accordance with the standards. In this regard the developed foam concrete compositions can be recommended for the manufacture of blocks with strict observance of technological regulations at the cement-ash binder.

The results presented in Tables 4 and 5 are superior to analogues [2, 6–8] in compressive strength, thermal conductivity and frost resistance.

Table 5. Behaviors of foam concrete for the production of wall blocks.

Characteristics	Type of binder used,% by weight of cement								
	Reference specimen (CEM I)			Joint milled 60 % CEM I+40 % FA (497 m ² /kg)			Joint milled 60 % CEM I+30 FA +10 % OM (484 m ² /kg)		
Composition, kg / m ³									
Portland cement	250	430	600	166	385	540	234	385	540
Fly ash	–	–	–	107	175	250	80	130	190
Opoka marl					50	70	26	50	70
Water	200	260	320	220	300	370	220	300	370
Foamer, % by CEM I wt.	1.2	1	1.2	1.2	1	1.2	1.2	1	1.2
Characteristics									
Average density, kg/m ³	295	503	706	303	493	697	293	494	698
Compressive strength, MPa	0.39	1.48	2.42	0.47	2.26	3.18	0.50	2.62	4.26
Thermal conductivity, W/m·°C	0.07	0.12	0.17	0.06	0.10	0.15	0.08	0.12	0.16
Frost resistance, cycles	20	20	25	25	30	35	20	25	35
Vapor permeability, mg/mhPa	0.27	0.23	0.22	0.20	0.24	0.20	0.28	0.22	0.18
Shrinkage, mm/m	1.32	1.30	1.21	1.05	0.86	0.97	1.11	1.03	0.94

Improving the durability characteristics of foam concrete on developed binder composites is explained by the microstructure of the materials obtained (Fig. 4). The SEM-images show that the optimization of the microstructure at the macro level is clearly traceable in comparison with the foam obtained on 100 % Portland cement.

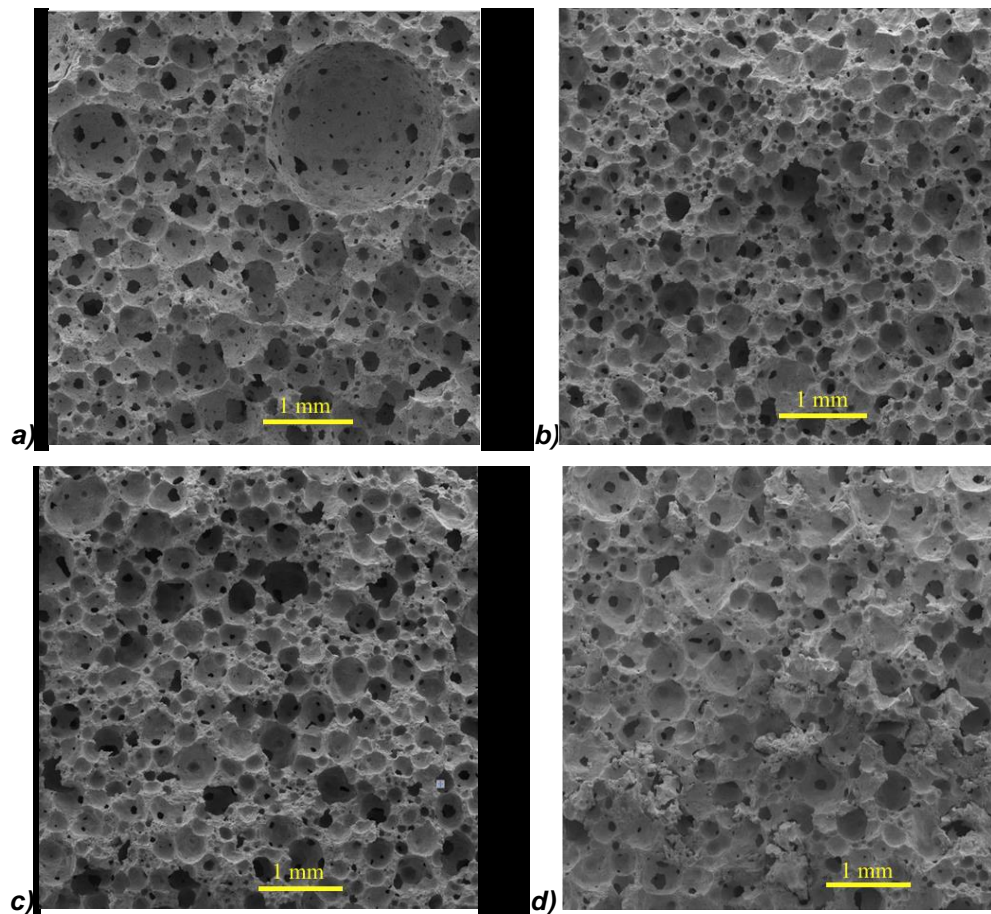


Figure 4. Macrostructure of foam concrete on composites:

a) Portland cement; b) Portland cement 60 % + fly ash 40 %; c) Portland cement 60 % + fly ash 30 % + opoka marl 10 %; d) Portland cement 60 % + fly ash 25 % + opoka marl 15 %.

Here it is necessary to note the important role of optimizing the microstructure of inter-porous partitions, which is formed using the BC, in increasing the physical and mechanical characteristics of foam concrete. The microstructure of the cement paste of the inter-porous foam concrete partitions on the developed BC is more perfect. This is due to the fact that during hydration, the amount of binder water in the curing system is less than in the control compositions due to the presence of opoka marl and fly ash in the BC. In this regard, the liquid phase is more supersaturated with dissolution products, and the conditions for hydration of clinker minerals are improved. It ensures enhance in the number of new growths having a high specific surface area. Enhance in the dispersion of new growths directs to an increase in the number of contacts between new growths and leads to the formation of a denser packing of the microstructure during the formation of thin-layer partitions. This contributes the curing process of the composite. The distraction of part of the water by the components of the opoka marl regulates and improves the plastic and relaxation characteristics, reducing the defectiveness of the inter-porous partitions and reducing their fragility.

Thus, regularities were revealed and substantiated that made it possible to obtain highly efficient foam concrete on the BC using opoka marl for use in monolithic construction with a foam concrete compressive strength of 4.32 MPa at a density of 700 kg/m³; and for organizing the production of blocks at the plant on a cement-ash binder and using a cement-ash binder with the addition of 10 % opoka marl with a compressive strength of 4.26 MPa with high economy Portland cement.

Modern enterprises are mainly small businesses. Therefore, a promising technology for the production of building materials should include the least possible technical re-equipment of factory facilities. The authors developed technological regulations for the production of heat-insulating and both structural and heat-insulating non-autoclaved foam concrete for monolithic construction based on dry construction mixtures prepared on composite binders using opoka marl. The technology for the manufacture of dry construction mixes from a cement-fly ash composite binder with the addition of marl for blocks from non-autoclaved foam

concrete was also improved. Binder composites make it possible to obtain high-quality wall materials directly at the construction site. Moreover, the addition of opoka marl in an amount of 10 % allows you to control the expansion process of the foam concrete mass, and the setting process correlates with the time of maximum porosity of system.

At the final stage of the study, a technological route was developed for the production of non-autoclaved foam concrete, which can be used both for monolithic construction and for the manufacture of blocks (Fig. 5). The technology was based on the possibility and accessibility of material raw materials for small and medium enterprises and the possibility of organizing production at existing production bases of cement and concrete plants.

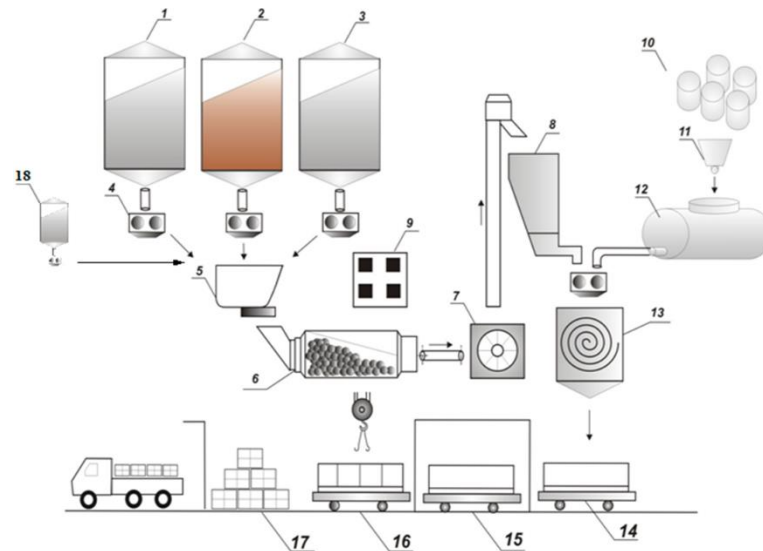


Figure 5. The technological route for non-autoclave foam concrete production:
1 – container for Portland cement; 2 – container for OM; 3 – container for fly ash;
4 – weight batchers; 5 – mill hopper; 6 – vibration mill; 7 – air pump; 8 – container for BC;
9 – control panel; 10 – foamer; 11 – volumetric dispenser; 12 – foam generator;
13 – foam concrete mixer; 14 – molding station; 15 – strength gain station;
16 – stripping station; 17 – packaging and storage; 18 – container for superplasticizer.

Based on the foregoing, the foam concrete compositions on the binder composites were developed and a relationship was established between the microstructure, composition of new growths and the operational characteristics of the composite. The inter-porous foam concrete partitions on the developed BC are nano- and microporous, have a high-density new growth package, consisting mainly of CSH of various basicities. This explains the decrease in the number of microcracks, the increase in the strength of foam concrete in comparison with a composite on a traditional binder with high economy of Portland cement.

4. Conclusions

During the interpretation of the obtained experimental results, the developed binder composites and their influence on the durability characteristics of non-autoclaved foam concrete were studied. As a result, the following valuable findings are established.

1. The theoretical basis of the design and synthesis of foam concrete based on the binder composites are proposed, both for monolithic construction and for the production of blocks. The features of the formation of the microstructure of the binder composites to improve the efficiency of foam concrete, which consist in optimizing the processes of the system "foaming – setting – hardening" due to the polycomponent binder composites, are revealed.

2. The opoka marl in raw mixtures for the production of foam concrete containing, along with calcite and clay minerals, zeolite and opal, accelerates the setting process of the foam concrete mixture, and then, upon curing, amorphous components react with calcium hydroxide, which arises upon hydration of C_3S and C_2S , forming second-generation calcium hydrosilicates. In this case, a dense inter-porous septum forms, which strengthens the final product.

3. The mechanism of the effect of fly ash on the microstructure formation processes of the foam concrete mixture for wall materials is established. The BC obtained by milling components have a compressive strength of up to 60–MPa with Portland cement economy of up to 40 %. Based on the binder composites, the un-autoclaved foam concrete with a compressive strength of up to 4.26 MPa at density of 500–700 kg/m³ was obtained. Fly ash contributes to a valuable change in the microstructure formation, which practically directs to

the absence of $\text{Ca}(\text{OH})_2$ among the new growths, as compared to reference specimens, due to the interaction of active SiO_2 contained in part of the fly ash with $\text{Ca}(\text{OH})_2$, which releases alite during hydration process.

4. The economic efficiency of the production and use of foam concrete based on Portland cement, opoka marl and fly ash, which occurs due to the use of new types of raw materials, has been proved. The expansion of the raw material base for the production of foam concrete at the same time helps to reduce material costs compared to traditionally used raw materials. The technology for the production of binder composites is developed for large-scale production of foam concrete based on binder composites.

5. Prospects for further development of the issue

It makes practical sense to consider transdisciplinary approaches to solving urgent problems of building materials science, to develop foam concrete production technologies for a wide range of building composites, including for the development of the northern regions. The technique described in the work can be used in the development of binders to expand the range of foam concrete production, including to improve a comfortable human environment in the architectural and construction design of composites with various specified operational characteristics.

6. Acknowledgements

This work was financially supported by the following RFBR grants:

1. No. 18-29-24113 "Transdisciplinarity - as a theoretical basis for the rational use of technogenic raw materials for energy-efficient technologies for the production of new generation building composites".

2. No. 18-03-00352 "Technogenic metasomatism in building materials science – as the basis for the design of future composites."

References

- Barabanshchikov, Y., Fedorenko, I., Kostyrya, S., Usanova, K. Cold-Bonded Fly Ash Lightweight Aggregate Concretes with Low Thermal Transmittance: Review. *Advances in Intelligent Systems and Computing*. 2019. 983. Pp. 858–866.
- Mugahed Amran, Y.H., Farzadnia, T., Abang Ali, A.A. Properties and applications of foamed concrete; a review. *Construction and Building Materials*. 2015. No. 101. Pp. 990–1005.
- Usanova, K., Barabanshchikov, Yu., Fedorenko Yu., Kostyrya S. Cold-bonded fly ash aggregate as a coarse aggregate of concrete. *Construction of Unique Buildings and Structures*. 2018. 9(72). Pp. 31–45. DOI: 10.18720/CUBS.72.2
- Volkova, A., Rybakov, V., Seliverstov, A., Petrov, D., Smirnov, A. Strength characteristics of foam concrete samples with various additives. *MATEC Web of Conferences*. 2018. 245. 03015. doi.org/10.1051/mateconf/2018245030155
- Ibragimov, R., Fediuk, R. Improving the early strength of concrete: Effect of mechanochemical activation of the cementitious suspension and using of various superplasticizers. *Construction and Building Materials*. 2019. No. 226. Pp. 839–848.
- Volkova, A., Rybakov, V., Seliverstov, A., Petrov, D., Smirnov, A. Lightweight steel concrete structures slab panels load-bearing capacity. *MATEC Web of Conferences*. 2018. 245. 08007. doi.org/10.1051/mateconf/201824508008
- Rybakov, V.A., Kozinets, K.G., Vatin, N.I., Velichkin, V.Z., Korsun, V.I. Lightweight steel concrete structures technology with foam fiber-cement sheets. *Magazine of Civil Engineering*. 2018. 82(6). Pp. 103–111. DOI: 10.18720/MCE.82.10
- Vatin, N.I., Velichkin, V.Z., Kozinets, G.L., Korsun, V.I., Rybakov, V.A., Zhuvak, O.V. Precast-monolithic reinforced concrete beam-slabs technology with claydit blocks. *Construction of Unique Buildings and Structures*. 2018. 70(7). Pp. 43–59. DOI: 10.18720/CUBS.70.4
- Ramamurthy, K., Nambiar, E.K.K., Ranjani, G.I.S. A classification of studies on properties of foam concrete. *Cement and Concrete Composites*. 2009. 31(6), Pp. 388–396.
- Li, T., Wang, Z., Zhou, T., He, Y., Huang, F. Preparation and properties of magnesium phosphate cement foam concrete with H_2O_2 as foaming agent. *Construction and Building Materials*. 2019. No. 205. Pp. 566–573.
- Hilal, A.A., Thom, N.H., Dawson, A.R. On entrained pore size distribution of foamed concrete. *Construction and Building Materials*. 2015. No. 75. Pp. 227–233.
- Li, T., Huang, F., Zhu, J., Tang, J., Liu, J. Effect of foaming gas and cement type on the thermal conductivity of foamed concrete. *Construction and Building Materials*. 2020. No. 231. Pp. 117–197.
- Nambiar, E.K., Kunhanandan, K. Influence of filler type on the properties of foam concrete. *Cement and Concrete Composites*. 2006. 28(5). Pp. 475–480.
- Klyuev, S.V., Klyuev, A.V., Vatin, N.I. Fiber concrete for the construction industry. *Magazine of Civil Engineering*. 2018. 84(8). Pp. 41–47. doi: 10.18720/MCE.84.4.
- Abirami, T., Loganaganandan, M., Murali, G., Fediuk, R., Vickhram Sreerishna, R., Vignesh, T., Janupriya, G., Karthikeyan K. Experimental research on impact response of novel steel fibrous concretes under falling mass impact. *Construction and Building Materials*. 2019. No. 222. Pp. 447–457.
- Sharonova, O.M., Yumashev, V.V., Solovyov, L.A., Anshits, A.G. The fine high-calcium fly ash as the basis of composite cementing material. *Magazine of Civil Engineering*. 2019. 91(7). Pp. 60–72. DOI: 10.18720/MCE.91.6
- Nambiar, E.K.K., Ramamurthy, K. Fresh State Behaviour of Foam Concrete. *Journal of Materials in Civil Engineering*. 2009. 21(11). Pp. 631–636.
- Zagorodnyuk L.Kh., Lesovik V.S., Sumskey D.A. Thermal insulation solutions of the reduced density. *Construction Materials and Products*. 2018. Vol. 1. No. 1. Pp. 40–50. https://doi.org/10.34031/2618-7183-2018-1-1-40-50
- Ahmaruzzaman, M. A review on the utilization of fly ash. *Progress in Energy and Combustion Science*. 2010. 3(36). Pp. 327–363. DOI: 10.1016/j.pecs.2009.11.003

20. Klyuev, S.V., Khezhev, T.A. Pukharenko, Yu.V., Klyuev, A.V. Fiber concrete on the basis of composite binder and technogenic raw materials. *Materials Science Forum*. 2018. No. 931. Pp. 603–607.
21. Sorelli, L., Constantinides, G., Ulm, F.J., Toutlemonde, F. The nano-mechanical signature of ultra high performance concrete by statistical nanoindentation techniques. *Cement and Concrete Research*. 2008. 12(38). Pp. 1447–1456. DOI: 10.1016/j.cemconres.2008.09.002
22. Chica, L., Alzate, A. Cellular concrete review: New trends for application in construction, *Construction and Building Materials*. 2019. No. 200. Pp. 637–647.
23. Panesar, D.K. Cellular concrete properties and the effect of synthetic and protein foaming agents, *Construction and Building Materials*. 2013. No. 44. Pp. 575–584, DOI: 10.1016/j.conbuildmat.2013.03.024
24. Nandi, S., Chatterjee, A., Samanta, P., Hansda, T. Cellular concrete; its facets of application in civil engineering. *International Journal of Engineering Research*. 2016. <https://doi.org/10.17950/ijer/v5i1/009>
25. Ahmed, R.M., Takach, N.E., Khan, U.M., Taoutaou, S., James, S., Saasen, A., Godøy, R. Rheology of foamed cement, *Cement and Concrete Research*. 2009. No. 39. Pp. 353–361. <https://doi.org/10.1016/j.cemconres.2008.12.004>
26. Jiang, J., Lu, Z., Niu, Y., Li, J., Zhang, Y. Study on the preparation and properties of high-porosity foamed concretes based on ordinary Portland cement. *Materials and Design*. 2015. No. 92. Pp. 949–959. <https://doi.org/10.1016/j.matdes.2015.12.068>
27. Lim, S.K., Tan, C.S., Zhao, X., Ling T.C. Strength and toughness of lightweight foamed concrete with different sand grading, *KSCE Journal of Civil Engineering*. 2015. No. 19. Pp. 2191–2197. <https://doi.org/10.1007/s12205-014-0097-y>
28. Steshenko, A.B., Kudyakov, A.I. Cement based foam concrete with aluminosilicate microspheres for monolithic construction. *Magazine of Civil Engineering*. 2018. 84(8). Pp. 86–96. doi: 10.18720/MCE.84.9.
29. Klyuev, S.V., Khezhev, T.A., Pukharenko, Yu.V., Klyuev, A.V. The fiber-reinforced concrete constructions experimental research. *Materials Science Forum*. 2018. No. 931. Pp. 598–602.
30. Fediuk, R.S., Lesovik, V.S., Liseitsev, Yu.L., Timokhin, R.A., Bituyev, A.V., Zaiakhanov, M.Ye., Mochalov, A.V. Composite binders for concretes with improved shock resistance. *Magazine of Civil Engineering*. 2019. 85(1). Pp. 28–38. DOI: 10.18720/MCE.85.3.
31. Barabanshchikov, Yu.G., Belyaeva, S.V., Arkhipov, I.E., Antonova, M.V., Shkol'nikova, A.A., Lebedeva, K.S. Influence of superplasticizers on the concrete mix properties. *Magazine of Civil Engineering*. 2017. No. 74(6). Pp. 140–146. doi: 10.18720/MCE.74.11
32. Lukutsova, N., Pashayan, A., Khomyakova, E., Suleymanova, L., Kleymenicheva, Y. The use of additives based on industrial wastes for concrete. *International Journal of Applied Engineering Research*. 2016. 11(11). Pp. 7566–7570.
33. Murali, G., Indhumathi, T., Karthikeyan, K., Ramkumar, V.R. Analysis of flexural fatigue failure of concrete made with 100% coarse recycled and natural aggregates. *Computers and Concrete*. 2018. 21(3). Pp. 291–298. <https://doi.org/10.12989/cac.2018.21.3.291>
34. Huseien, G.F., Memon, R.P., Kubba, Z., Sam, A.R.M., Asaad, M.A., Mirza, J., Memon, U. Mechanical, thermal and durable performance of wastes sawdust as coarse aggregate replacement in conventional concrete. *Jurnal Teknologi*. 2019. 81(1). Pp. 151–161.
35. Mosaberpanah, M.A., Eren, O. Relationship between 28-days Compressive Strength and Compression Toughness Factor of Ultra High Performance Concrete Using Design of Experiments. *Procedia Engineering*. 2016. No. 145 Pp. 1565–1571. DOI: 10.1016/j.proeng.2016.04.197
36. Yoo, D.-Y., You, I., Zi, G., Lee, S.-J. Effects of carbon nanomaterial type and amount on self-sensing capacity of cement paste. *Measurement: Journal of the International Measurement Confederation*. 2019. No. 134. Pp. 750–761.
37. Morozov, V.I., Opubl, E.K., Van Phuc, P. Behaviour of axisymmetric thick plates resting against conical surface. *Magazine of Civil Engineering*. 2019. 86(2). Pp. 92–104. DOI: 10.18720/MCE.86.9

Contacts:

Valeriy Lesovik, naukavs@mail.ru

Evgeniy Glagolev, mail@belgorodstroy.ru

Vasily Voronov, fedyu.rs@dvmfu.ru

Lilia Zagorodnyuk, lh47@mail.ru

Roman Fediuk, roman44@yandex.ru

Andrey Baranov, de_montgomery@mail.ru

Arbi Alaskhanov, alaskhanov.arbi@mail.ru

Alexander Svintsov, svintsovap@rambler.ru

© Lesovik, V.S., Glagolev, E.S., Voronov, V.V., Zagorodnyuk, L.Kh., Fediuk, R.S., Baranov, A.V., Alaskhanov, A.Kh., Svintsov, A.P., 2020



DOI: 10.18720/MCE.100.4

The influence of reinforcing joints on the fire resistance of reinforced concrete structures

V.A. Rybakov^{*a}, O.V. Zhuvak^b, A. Hoffmann^c, F.A. Sergeeva^a, P.A. Verigo^a

^a Peter the Great St. Petersburg Polytechnic University, St. Petersburg, Russia

^b JSC Atomproekt, St. Petersburg, Russia

^c HALFEN GmbH, Langenfeld/Rheinld, Germany

* E-mail: fishermanoff@mail.ru

Keywords: Coupling joint, welded joint, rod reinforcement, fire resistance, fire protection, reinforced concrete

Abstract. This article analyzes the behavior of reinforcing joints when exposed to a fire load. The scientific work presents the results of an experiment on the fire resistance of reinforcing samples with coupling and welded joints. Experimental studies of cold and hot tensile samples were carried out. A test of loaded, heated and cooled rods was also performed, simulating the real effect of a fire on a loaded structure. During all three experiments, the values of the deformation and strength characteristics of the mechanical and welded joints of the bar reinforcement were compared. The experiment was verified in the Abaqus software package for the coupling connection in flexible reinforced concrete structures. Coefficients were derived that take into account the decrease in the strength of a reinforcing specimen with a sleeve connection depending on the heating temperature in the stressed state. Based on the data obtained using the studies, it can be concluded that the coupling and welded joints of the reinforcing bars give additional rigidity to the samples, without compromising the strength characteristics of the reinforcing bar. In the course of the experiments, the coupling and welded joints proved to be approximately the same, it should be noted that from the point of view of application efficiency, coupling joints have significant technological advantages compared to the welded joint.

1. Introduction

Currently, there is a need to use a large number of bent reinforced concrete structures that can withstand serious loads arising from the fire impact. The limit of fire resistance of the bent reinforced concrete structures on bearing capacity can come as a result of warming up of working armature to critical temperature that can lead to serious deformations of reinforced concrete and formations of plastic hinges. This occurs as a result of reducing the time resistance of rupture of the stretched reinforcement, which causes intensive crack opening in the concrete and accelerating the heating of the reinforcement.

Rebar is a key component of reinforced concrete and turns concrete into a durable and practical material. Therefore, it is necessary to monitor and observe the quality of work when creating a reinforcement cage. To create a strong "skeleton" of a reinforced concrete structure, it is necessary to use a strong reinforcement connection: coupling or welded. A welded joint is an all in one joint made by welding. A feature of the mechanical connection is the use of a reinforcing sleeve, which is a hollow metal cylinder with an internal parallel or conical thread corresponding to the external thread, which is cut or rolled at the ends of the connecting reinforcing rods. In addition to the use of these types of connections in civil construction, coupling and welded joints are used in the construction of largescale facilities, such as nuclear power plants, hydroelectric power plants, thermal power plants.

Currently, the behavior of reinforcement joints under fire is of scientific interest, because this issue has not been studied and not covered. No such studies are known to us. Prior to the experiments, the existing scientific research in the field of couplings and welds was studied. In the article [1] results of

Rybakov, V.A., Zhuvak, O.V., Hoffmann, A., Sergeeva, F.A., Verigo, P.A. The influence of reinforcing joints on the fire resistance of reinforced concrete structures. Magazine of Civil Engineering. 2020. 100(8). Article No. 10004. DOI: 10.18720/MCE.100.4



This work is licensed under a CC BY-NC 4.0

researches of reinforcing hire regarding weldability, endurance and relaxation of stresses according to requirements of the project of new Russian State Standard GOST 34028-2016 «hire reinforcing for reinforced concrete designs" are resulted». According to the results of the research and in the process of harmonization of the draft new Russian State Standard GOST, it is possible to note that the use of mechanical threaded connection valves allows to reduce construction time, reduce costs, and improve efficiency. The performed calculation of comparison of costs of reinforcing connections allows to be convinced that the mechanical threaded connection is cheaper for welding. In the article [2] Korenko and other authors the advantages of mechanical threaded connection of fittings in comparison with traditional lap joint and bath welding are considered. A comparable calculation of the cost comparison of reinforcement joints is performed. To assess the strength characteristics of the mechanical threaded connection was experimentally tested reinforcing rod class A500C diameter of 25 mm using coupling SS25A12 on the breaking machine. In article [3] group of authors carry out research of forecasting of quality of welded connections at contact butt welding by reflow on static characteristics. Authors presented the results of computational experiments to determine the effect of transverse dimensions of reinforcing bars of a sickle-shaped profile of class A500C on the stress-strain state of the anchor connection on acrylic adhesives [4]. Article [5] considers features of the complex scheme of formation of organizational and technological decisions on increase of efficiency of welding connections and their influence on threading of installation and realization of means of complex mechanization and automation of production processes and, as a consequence, on reliability of construction of objects of capital construction. In article [6] Klochanov I.E. options of connection of reinforcement of a periodic profile at reinforcement of building designs which provide continuity of formation of reinforcing frameworks are considered. The advantages and disadvantages of traditional methods of joining valves are determined and the technologies of threaded couplings, the nature of destruction during static strength tests for valves of class A500C are given. A variety of domestic reinforcing steels both by the methods of factory production and by the type of periodic profile, determines a special approach to the use of coupling connections on the thread. The direct dependence of the strength and deformation parameters of the threaded connection on the length of screwing and mechanical characteristics of the connected elements is shown. The author sets the task of creating a unified type of couplings when using for all widespread classes of valves of periodic profile. Dyachkov V.V. [7] dealt with the application of threaded and pressed mechanical joints of reinforcement in reinforced concrete structures.

Many domestic and foreign authors were engaged in fire resistance of bent reinforced concrete structures. In article [8] develop a mathematical model for calculating the temperature field of structural elements under various combined boundary conditions. As a criterion for the destruction of reinforced concrete structures, a critical temperature of 600°C at a depth of 2 mm from the heated surface at different heating speeds is proposed. Authors have resulted in the article typical graphic dependences of a limit of fire resistance on temperature of various materials and characteristics of fire resistance of building designs [9]. Zaitsev A.M. gave an analytical solution to the problem of non-stationary thermal conductivity to determine the heating of the enclosing structure under fire. He also gave the calculation methodology, specific examples of calculation and analysis of the results [10]. Belyavsky I.M. considered mathematical approaches to determining the ultimate fire resistance of building structures in accordance with the requirements of fire safety [11]. Authors gave a brief overview of Russian and international approaches to assessing the fire resistance of building structures [12]. Authors considered the development of regulatory requirements for fire resistance and basic design provisions [13]. Authors group described the study of nonlinear elemental analysis, which is able to predict the fire resistance of reinforced concrete slabs [14]. Li G.Q., Zhang N.S., Jiang J. in their article described the experimental studies of thermal and mechanical changes of floors under the action of fire [15]. Nazare S. and other authors in their study analyzed the factors that can affect the results of the flame impact test on the surface [16]. Authors group described tests in which more than 14 different samples of flame retardant coatings were affected by heat flows, in order to study the relationship between the thickness of the coating and the time of heat exposure [17]. Authors conducted a study in which they evaluated the effect of high temperatures and fire on concrete structures [18]. In article [19], the results of fire tests on suspended ceilings under standard fire temperature regime are presented in this study. Markus E. and others in [20] showed the application of the thermal pyrolysis model to predict flame spread over continuous and discrete fire load. The authors tested fire-resistant plaster coatings in work [21]. In article [22], the results of calculation of the quality control of holes for reinforced concrete structures are given by the example of fire-retardant coatings. The authors in their work [23] consider a special type of destruction of a heavy type of concrete under fire action, the so-called explosive spallation. The design of prestressed reinforced concrete slabs without the joint work of concrete and reinforcement is presented in article [24]. The author deals with the fire resistance assessment of compressed reinforced concrete elements in article [25].

Thus, the experimental base for studying the behavior of reinforcing joints in a fire is absent. The study of this issue should be continued, since reinforcing joints are involved in the formation of the frame of reinforced concrete structures, which significantly affects its strength.

In this paper a model of reinforced concrete floor considers, which is assembled on the armature joints, which is subjected to unilateral fire. It is assumed the formation of cracks in the stretched reinforced concrete curved structure at the joints of reinforcing bars under the influence of fire load (Fig. 1).

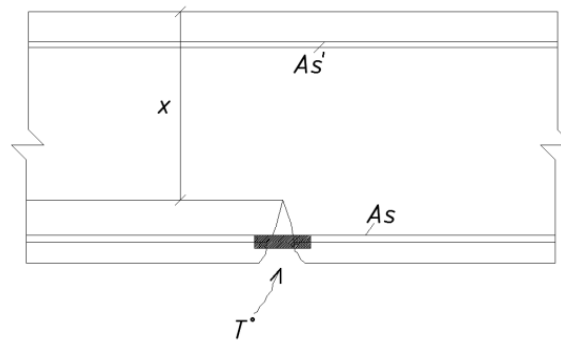


Figure 1. Fire damage of joints of connection of reinforcing bars.

Object of tests-coaxial coupling and welded joints of steel bar fittings and control steel bars of valves with $R_{s,n} = 500$ MPa $\varnothing 32$ mm.

The purpose of this work is to analyze the behavior of reinforcement joints under the influence of fire load. The following tasks follow from the set goal: definition and comparison of values of deformation and strength characteristics of mechanical and welded joints of steel bars fittings. It is necessary to establish experimentally the main parameters characterizing the strength characteristics of samples, such as:

- temporary resistance σ_b to rupture the stress corresponding to the highest load P_{max} , preceding the destruction of the sample.
- actual yield strength σ_t is the mechanical characteristic of a material that characterizes the stress at which strains continue to increase without increasing the load.
- deformability Δ is residual elongation of the sample after removal of the load $0.6 \sigma_t$.
- absolute elongation values δ at different loads and different times-a numerical value indicating how much the length of the sample has changed.

This article is an extended version of the report presented on the International Scientific Conference on Energy, Environmental and Construction Engineering (EECE 2019) [26].

2. Methods

The methodology of experimental studies is based on Russian State Standard GOST 34227-2017 "Mechanical reinforcement joints for reinforced concrete structures. The research model is the coupling joint of bar reinforcement. The dimensions of the samples are shown in Fig. 2.

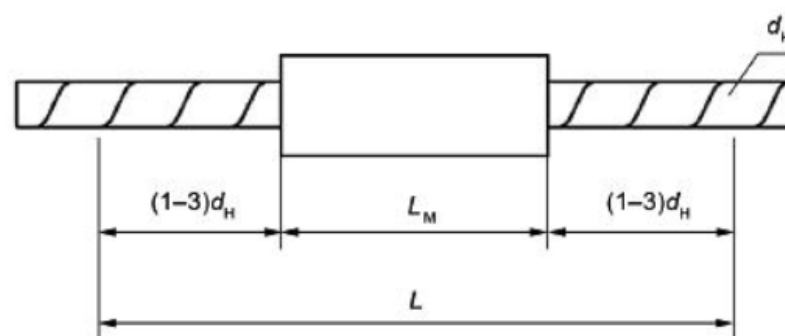


Figure 2. Determination of the length of the mechanical connection elongation measurement base.

L_M is coupling length = 72 mm;

D_H is nominal diameter of reinforcing bar = 32 mm;

L is gauge length for measuring elongation of a mechanical joint
 $=L_M+4D_H=72 \text{ mm}+128 \text{ mm}=200 \text{ mm}$.

Control steel bar is a piece of reinforcement with $R_{s,n} = 500 \text{ MPa } \varnothing 32 \text{ mm}$, cut from the same steel bar from which the samples are made connections.

Types of force loading:

1) a single static axial tension of the specimen up to $0.6 \sigma_t$ to obtain the deformability values (clauses 7.1.5-7.1.11 Russian State Standard GOST 34227-2014).

In order to measure the deformability of mechanical connections of reinforcing rods, the position of the measuring devices should correspond to Fig. 3:

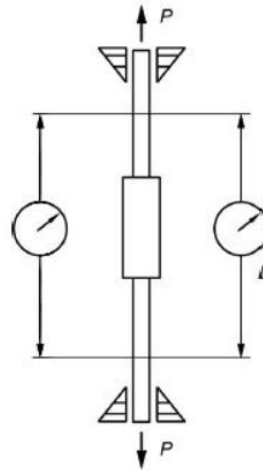


Figure 3. The scheme of installation of measuring devices at tests of samples of mechanical connections of reinforcing bars on tension.

2) axial tension of the specimen to obtain the actual tensile strength (before specimen rupture).

The specimen heating rate should correspond to the standard fire rate. Cooling to room temperature in natural mode. Monitoring the temperature change of samples with an accuracy of 5 % of the nominal value. During the test, the temperature change of the sample should not exceed 5 % of the nominal value.

If possible, it is necessary to minimize the effect of convective heating of the tensile testing machine and measuring instruments. The set temperature and constant tensile strength of the sample are simultaneously maintained during the initial stage of test No. 3.

Tensile tests of reinforcing bars and their joints were performed on the tensile testing machine R-100 of the Armavir plant with a maximum force of 100 000 kg_f (Fig. 4).



Figure 4. General view of the test machine R-100 Armavir plant and the number of the certificate of verification.

Temperature control was performed using a Raytek Raynger St (60) pyrometer with an accuracy of $0.5 \text{ }^\circ\text{C}$ (Fig. 5).



Figure 5. Thermometer Raytek Raynger ST (60).

During the experiment, digital and analog dial gauges were used to measure the deformability of reinforcement samples with an accuracy of 0.01 mm (Fig. 6).



Figure 6. The indicator of hour type ICH-10 and mechanical measuring sensors ICH-10 of hour type.

Three experiments were conducted.

2.1. "Cold" experiment No 1: tensile test to rupture of "cold" samples, at room temperature 20°C

At the beginning measuring instruments were installed on the sample, the measurement base was equal to $L_M + 4D_H = 72 \text{ mm} + 128 \text{ mm} = 200 \text{ mm}$; Next, the Sample was installed in the bursting machine (Fig. 7).



Figure 7. Installation of the sample in the measuring machine.

The Sample was stretched to $0.6 \sigma_t$, the values of absolute elongation δ_1 were determined. Every 5 tons readings were taken from the measuring sensors. Deformability Δ was measured. Next, the sensors were deduced at zero. The Sample was stretched to σ_t , thus determining the value of δ_2 . The readings were taken from the sensors.

In the end, measuring instruments were removed, the sample was loaded to its destruction, the force value corresponding to σ_b was determined. The value of the relative residual elongation was fixed.

2.2. " Hot "experiment No 2: tensile testing prior to rupture of" hot " samples preheated to 500°C

Further, some actions were performed. Measuring instruments were installed on the sample, the measurement base was equal to $L_M+4D_H=72\text{ mm}+128\text{ mm}=200\text{ mm}$. The Sample was installed in the bursting machine. With the help of a gas burner, the reinforcing joints were heated to a temperature of $\approx 500^\circ\text{C}$. The actual temperature of the sample was controlled by the instrument. Further, the sample was stretched to $0.6\sigma_t$, the value of absolute elongation δ_1 was determined. Every 5 tons readings were taken from sensors. The deformability was measured Δ . Next, the sensors were brought to zero. The Sample was stretched to σ_t , thus determining the value of δ_2 . Readings were taken from sensors. Measuring instruments were removed, the sample was loaded to its destruction, the force value corresponding to σ_b was determined. The value of the relative residual elongation was fixed.

2.3. Experiment No 3: Test of loaded, heated and cooled steel bars simulating the real impact of fire on the loaded structure

Further, some actions were performed. The Sample was installed in the breaking machine; the temperature was controlled corresponding to normal room conditions. Measuring instruments were installed on the sample, the measurement base was equal to $L_M+4D_H=72\text{ mm}+128\text{ mm}=200\text{ mm}$. The Sample was stretched to $0.6\sigma_t$, the value of absolute elongation δ_1 was determined. Was the measurement made deformability of Δ . Next, the sensors were brought to zero. The Sample was rest retched to $0.6\sigma_t$, the absolute elongation value δ_1 was re-determined. The reinforcement joints were heated to a temperature equal to 500°C under a load of $0.6\sigma_t$, the value of the absolute elongation δ_2 was determined, the readings from the sensors were recorded. Next, the sample cooled to room temperature, readings were taken from sensors to determine the elongation of δ_3 . The Sample was stretched to σ_t , thus determining the value of δ_4 . Readings were taken from sensors. Measuring instruments were removed, the sample was loaded to its destruction, the force value corresponding to σ_b was determined. The value of the relative residual elongation was fixed.

3. Results and Discussion

3.1. Experiment No 1. Cold samples

The values obtained as a result of the experiments are presented in Table 1 and Fig. 8.

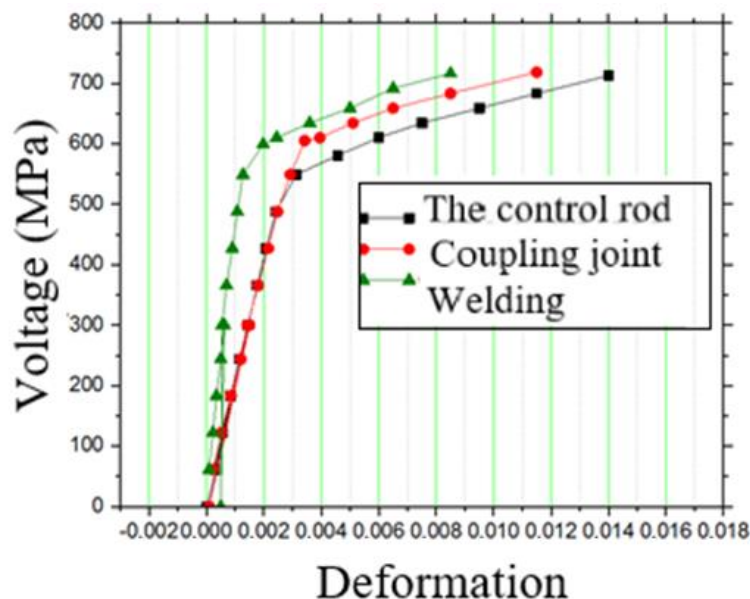


Figure 8. Stress-strain diagram in this experiment.

Final data obtained after the first experiment:

Table 1. The final results of experiment No 1. Testing of cold samples.

Test sample	Elongation sensor readings δ_2 at R_T , mm		Ab. elongation at R_T , mm	R_T Force, kgf	R_B Force, kgf	δ_p , %
One-piece steel bar	0.89	0.94	0.915	47600	58420	8
Socket joint	0.69	0.68	0.685	49600	58880	8
Welded joint	0.50	0.29	0.395	49100	58700	8.8

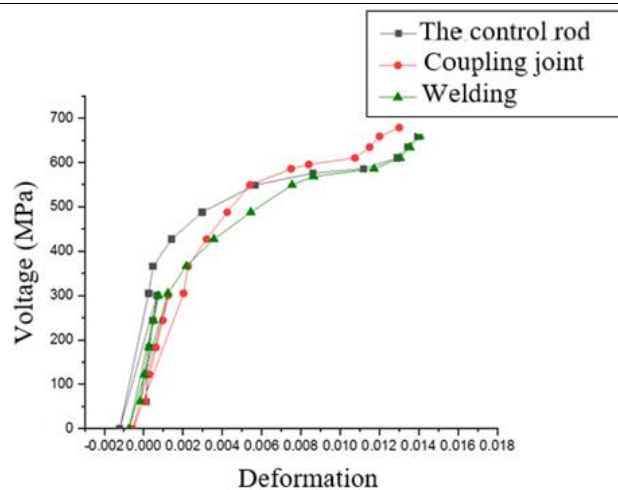
Thus, can see that the greatest value of the breaking force was achieved in the coupling connection, the smallest in the solid steel bar. In this experiment, none of the samples exploded within the compounds. The greatest values of deformations were obtained at the control steel bar.

3.2. Experiment No 2. Hot samples

The values obtained as a result of the experiments are presented in Table 2 and Fig. 9.

Table 2. The final results of experiment No 2. Testing of hot samples.

Test sample	Temperature, °C	R_T Force, kgf	R_B Force, kgf	δ_p , %
Socket joint	200	48800	55600	3.8
Welded joint	200	46600	54000	6.85

**Figure 9. "Stress-strain" diagram for hot experiment.**

In comparison with experiment No 1, the strength of the sample under temperature influence in the control steel bar decreased by 3 %, in the steel bar with the coupling by 5.5 %, in the welded joint by 8 %.

3.3. Experiment No 3. Testing of heated and cooled samples under load

The results of experiment 3 are presented in Table 3, 4 and Fig.10.

Table 3. Results of experiment No 3.

Test sample	Elongation sensor readings δ_2 at R_T , mm		Ab. elongation at R_T , mm	R_T Force, kgf	R_B Force, kgf	δ_p , %
One-piece steel bar	3.44	2.17	$\delta_4 = 2.805$	48400	53400	3.1
Socket joint	1.25	0.73	$\delta_4 = 0.99$	48200	58200	3.5
Welded joint	0.84	0.7	$\delta_4 = 0.77$	46400	56000	4.65

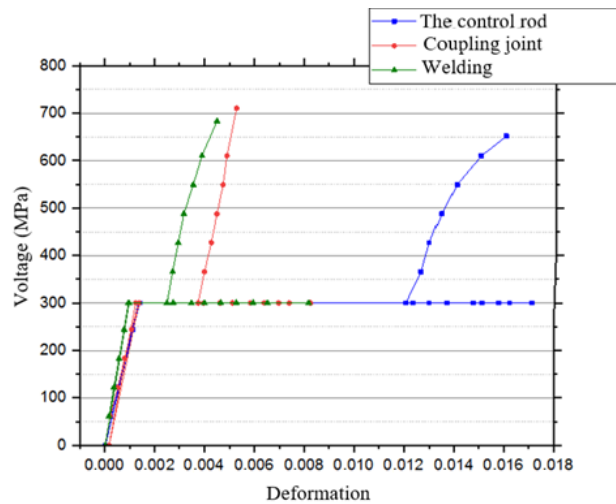


Fig. 10 Diagram of "stress-strain" experiment No 3

In comparison with experiment No 1, the strength of the sample after temperature exposure in the control strength decreased by 8.6 %, in the strength with the coupling by 1.16 %, in the welded joint by 4.6 %.

Table 4. Results of experiment No 3.

	Absolute elongations (mm) occurring in the sample at:		
	1) $t = \text{const}(20^\circ\text{C})$; $P \uparrow$ (0 to 24600 kgf), tensile force.	2) $t \uparrow$ (20°C to 500°C); $P = \text{const}$ (24600 kgf), t° stretching.	3) $t \downarrow$ (500°C to 20°C); $P = \text{const}$ (24600 kgf), t° compression.
Control strength	0.27	$3.42 - 0.27 = 3.15$	$3.42 - 2.415 = 1.005$
Socket joint	0.25	$1.65 - 0.25 = 1.4$	$1.65 - 0.75 = 0.9$
Welded joint	0.19	$1.635 - 0.19 = 1.445$	$1.635 - 0.5 = 1.135$
Residual temperature absolute elongation under constant tensile load after removal of temperature influence			
Control strength: 2.145 mm			
A sample with a t & C connection: 0.5 mm			
The specimen with a welded joint: 0.31 mm			

In experiment No 3, the temperature absolute value of residual elongation at the welded joint was between 0.31 mm, for socket was 0.5 mm, the difference between the absolute values of the temperature elongation of welded and coupling was 0.2 mm. However, the value of the temporary resistance is larger in a sample with socket connection. It is stronger than the sample with a welded joint by 2.2 tons. Also, we can conclude that the mechanical and welded joints of reinforcing bars give additional rigidity to the samples, which can be seen in the example of absolute elongation under the influence of tensile and temperature loads. The information obtained in the work allows us to reasonably expand the field of study of reinforcement joints to identify the best sample having high strength characteristics, and corresponding to the requirements of fire safety and fire resistance. The places of rupture of the samples after the third experiment can be seen in Fig. 11.



Figure 11. Places of rupture of samples after the 3rd experiment.

After the experiments, it was noted that no sample broke within the compound. All the breaks occurred outside of the compounds.

3.4. Discussion

Next, the results obtained compare with the results obtained by another calculation method - the finite element method. In article [26] a generic three-dimensional (3D) finite element (FE) based numerical model is presented for predicting thermo-mechanical behavior of load bearing reinforced concrete (RC) walls exposed to fire. This papers [27–28] presents a three-dimensional nonlinear finite element analysis for evaluating the fire response of reinforced concrete beams using ANSYS. In article [29] the numerical model utilizes a macroscopic finite element based approach to trace thermo-mechanical response of FRP-strengthened RC slabs from linear elastic stage to collapse under fire conditions.

Program complex "Simulia ABAQUS CAE 2017" will be used as a verification software package. In article [30], a finite element based numerical model is developed in ABAQUS for tracing the response of reinforced concrete beams exposed to fire. The authors in article [31] performed modeling and numerical analysis of the interaction of concrete and reinforcement using volumetric finite elements taking into account the nonlinearity of the work of materials.

Based on the experiments and the data obtained, a second experiment was conducted in the program complex "Abaqus". The properties of the material, depending on temperature, were set, such as: density, elastic modulus, coefficient Poisson, thermal conductivity, linear expansion coefficient, specific heat. The coefficients were derived, taking into account the de-crease in the strength of the reinforcing sample with a coupling connection depending on the heating temperature in the stressed state (Table 8). This coefficient is found by the formula 1:

$$\gamma_A = \frac{\sigma_b}{(\sigma_{b,actual})} \quad (1)$$

where, $\sigma_{v, fact} = 7.18 \cdot 10^8$ Pa. The value of the time resistance of the sample is obtained from an earlier experiment at 20 °C for the coupling.

The stress distribution in the finite element model of the sample with a sleeve connection is shown in Fig. 12, the temperature distribution in Fig. 5, the fracture zone in Fig. 14.

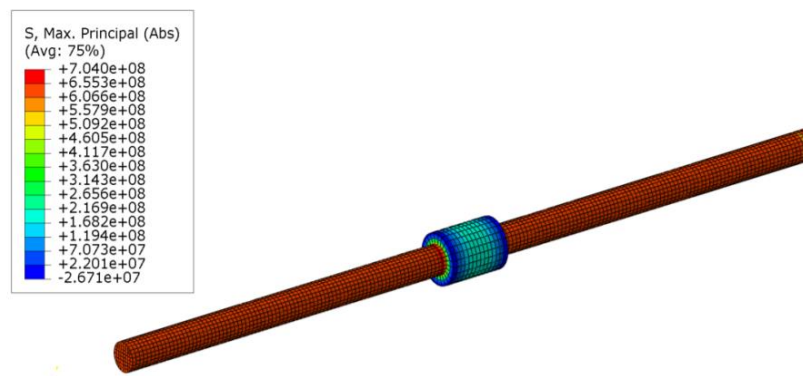


Figure 12. Stress at 200°C in a finite element model of a coupling specimen.

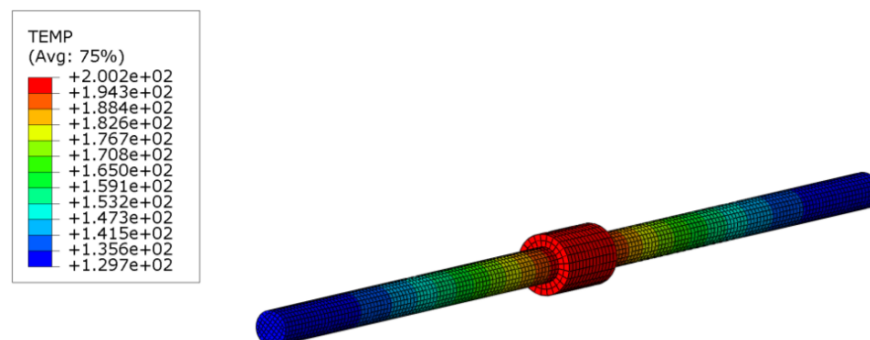


Figure 13. The temperature applied to the sample.



Figure 14. Fracture zone at 200°C.

Table 5. Coefficient γ_A at different temperatures.

Temperature	20°C	100°C	200°C	300°C	400°C	500°C
Temporary resistance in a heated sample	$7.15 \cdot 10^8$	$7.10 \cdot 10^8$	$7.04 \cdot 10^8$	$6.8 \cdot 10^8$	$6.3 \cdot 10^8$	$5.8 \cdot 10^8$
σ_B (MPa)						
γ_A	0.995	0.988	0.979	0.946	0.876	0.807

4. Conclusion

On the basis of the data obtained with the help of the conducted studies, it is possible to draw conclusions:

1. Coupling and welded joints do not degrade the strength characteristics of the reinforcing steel bar and reinforcement structures in General.
2. Coupling and welded joints of reinforcing bars give additional rigidity to the samples. This is noticeable in terms of absolute elongation.
3. According to the results of hot experiment № 2, the strength of the sample in the control steel bar decreased by 3 %, in the steel bar with the coupling by 5.5 %, in the welded joint by 8 %. According to the results of experiment № 3, the strength of the sample after temperature exposure in the control steel bar decreased by 8.6 %, in the steel bar with the coupling by 1.16 %, in the welded joint by 4.6 %. It is necessary to expand the field of study of reinforcement joints to identify the sample having the best strength characteristics.
4. The temperature lowers the strength characteristics of the structure, in addition, there is an increase in the value of deformability due to thermal action (thermodeformativity).
5. Since in General, during the experiments, the coupling and welded joints have shown themselves to be approximately the same, it should be noted that from the point of view of the effectiveness of the coupling joints have significant technological advantages compared to the welded joint.

5. Acknowledgments

We express our gratitude:

1. The research is funded by the Ministry of Science and Higher Education of the Russian Federation as part of World-class Research Center program: Advanced Digital Technologies (contract No. 075-15-2020-934 dated 17.11.2020).
2. Ancon for providing materials and preliminary information that was useful in the conduct of this study.
3. To employees of separate division of LLC FPG "ROSSTRO" – "PKTI", in particular, to Belov Ivan Pavlovich, for the help in carrying out research.

References

1. Tsyba, O.O., Dyachkov, V.V., Savrasov, I.P., Panchenko, A.I. On the new interstate standard GOST 34028-2016 "reinforcing bars for reinforced concrete structures". Bull. BSTU. V. G. Shukhov. 2017. (3). Pp. 23–31.
2. Korenko, S.S., Komarov, D.A., Rudenko, A.A. To an estimation and efficiency of mechanical connection of metal armature. Science and education. 2017. 6. Pp. 1–8.

3. Chvertko, E.P., Shevchenko, N.V., Pirumov, A.E. Forecasting the quality of welded joints in contact butt welding by reflow according to statistical characteristics. Bulletin of the Donbass state machine-building Academy. 2012. 3(28). Pp. 274–279.
4. Babaev, V.N., Shishkin, E.A., Sklyarov, V.A., Garbuz, A.O. Influence of transverse dimensions of reinforcing bars of sickle-shaped profile with R_s , $n = 500$ MPa on the stress-strain state of the anchor connection. Komunalne gospodarstvo mist. Naukovotekhnichny zbirnik. 2012. 107. Pp. 27–32.
5. Torkatyuk, V.I., Denisenko, A.P. Formation of parameters of organizational and technological decisions on increase of efficiency of welding connections. Municipal economy of cities. Scientific and technical. 2015. 77. Pp. 192–205.
6. Klochanov, I.E. Influence of mechanical properties of materials of couplings of armature. Modern problems of Science and Education. 2014. 2. Pp. 1–6.
7. Dyachkov, V.V. Properties and features of application in reinforced concrete structures of threaded and pressed mechanical joints of reinforcement. The dissertation for the degree of candidate of technical sciences. 2009.
8. Enaleev, R.Sh. Sh. et al. Fire resistance of elements of building structures at high-intensity heating. Pozharovzrybozopasnost. 2010. 19(5). Pp. 48–53.
9. Trukhina, A.M., Ismagilova, E.P., Agashkov, E.M., Gavrishchuk, V.I. Review of modern ways to increase fire resistance of building structures. Key safety issues in the development of natural-industrial systems. 2016. Pp. 70–78.
10. Zaitsev, A.M. Calculation of fire resistance of building envelopes in different conditions of heat transfer on the opposite surfaces. Bulletin of the Voronezh Institute of the State Fire Service of the Ministry of Emergencies of Russia. 2017. 23(2). Pp. 46–58.
11. Belyavsky, I.M. Determination of fire resistance of building structures according to safety requirements. Actual problems and prospects of development of economy, management and education. 2016. Pp. 26–30.
12. Eremina, T.Y., Minailov, D.A. Improving the regulatory framework in the field of fire resistance of building materials. Fire and emergency. 2014. (3). Pp. 32–36.
13. Krivtsov, Y.V., Pronin, D.G. Fire Resistance of buildings and structures: regulatory requirements and design justification. Herald SIC construction. 2014. (11). Pp. 55–66.
14. Dr. Ayad A. Abdul-Razzak. Geometric and material nonlinear analysis of reinforced concrete slabs at fire environment. Tikrit Journal of Engineering Science. 2013. 15(6). Pp. 1–16. DOI: <https://doi.org/10.1007/s10409-011-0520-2>
15. Guo-Qiang, L., Nasi Zhang, J.J. Experimental investigation on thermal and mechanical behavior of composite floors exposed to standard fire. Fire Safety Journal. 2017. (89). Pp. 63–76.
16. Nazaré, S., Pitts, W.M., Shields, J., Davis, R. Factors for consideration in an Open-Flame test for assessing fire blocking performance of barrier fabrics. Polymers. 2016. Pp. 342.
17. Grigonis, M., Mačiulaitis, R., Lipinskas, D. Fire Resistance Tests of Various Fire Protective Coatings. Medziagotyra. 2011. Pp. 93–98.
18. Morales, G., Campos, A., Faganello, A. The action of the fire on the components of the concrete. Seminar: Ciências Exatas e Tecnológicas. 2011. (32). Pp. 47–55. DOI: <https://doi.org/10.5433/1679-0375.2011v32n1p47>
19. Gravit, M.V., Golub, E.V., Grigoriev, D.M., Ivanov, I.O. Fireproof suspended ceilings with high fire resistance limits. Magazine of Civil Engineering. 2018. 84(8). Pp. 75–85. DOI: 10.18720/MCE.84.8
20. Markus, E., Snegirev, A., Kuznetsov, E., Tanklevskiy, L. Application of the thermal pyrolysis model to predict flame spread over continuous and discrete fire load. Fire Safety Journal. 2019. 108(January). Pp. 102825. DOI: 10.1016/j.firesaf.2019.102825
21. Gravit, M.V., Golub, E.V., Antonov, S.P. Fire protective dry plaster composition for structures in hydrocarbon fire. Magazine of Civil Engineering. 2018. 79(3). Pp. 86–94.
22. Gravit, M.V., Dmitriev, I., Ishkov, A. Quality control of fire retardant coatings for reinforced concrete structures. IOP Conference Series: Earth and Environmental Science. 2017. 90(1). Pp. 4.
23. Gravit, M.V., Golub, E. Improving the fire resistance of reinforced concrete structures with polypropylene microfiber. MATEC Web Conference. 2018. 245. Pp. 7.
24. Polevoda, I.I., Zainudinova, N.V., Chaychits, N.I. The results of the fire test of reinforced concrete prestressed slabs without adhesion of reinforcement to concrete. University of Civil Protection of the Ministry of Emergencies of the Republic of Belarus. 2016. 23(1). Pp. 37–44.
25. Ilyin, N.A. Determination of fire resistance of compressed reinforced concrete structures of buildings. Bulletin of the SSACU. Urban Planning and Architecture. 2015. 18(1). Pp. 82–89.
26. Rybakov, V., Zhuvak, O., Verigo, R., Sergeeva, F., Verkhushkin, D., Riabov, A., Hoffmann, A. Thermomechanical Characteristics of Coupling and Welded Joints in Reinforced Concrete Structures. Proceedings of EECE 2019. Lecture Notes in Civil Engineering. 2020. Pp. 613–624. doi.org/10.1007/978-3-030-42351-3

Contacts:

Vladimir Rybakov, fishermanoff@mail.ru

Oksana Zhuvak, zhuwak2010@mail.ru

Andre Hoffmann, andre.hoffmann@halfen.ru

Faina Sergeeva, faasergeeva811@gmail.com

Polina Verigo, melomanka50@icloud.com

© Rybakov, V.A., Zhuvak, O.V., Hoffmann, A., Sergeeva, F.A., Verigo, P.A., 2020



DOI: 10.18720/MCE.100.5

Distribution of corrosion products at the steel-concrete interface of XD3 concrete samples

S.A. Abdulsada*, F. Kristaly, T.I. Torok

University of Miskolc, Miskolc, Hungary

* E-mail: qkosha86@uni-miskolc.hu

Keywords: reinforced concrete, green inhibitor, superplasticizers, X Ray Diffraction, corrosion.

Abstract. This research paper deals with the steel/concrete interface of concrete samples with and without green inhibitor (orange peel extract) and with different two types of superplasticizers (Mapei Dynamon SR 31 and Oxydtron) after an 18 months exposure in aqueous chloride environment. XRD, SEM, and light optical micrograph techniques were applied to investigate the chemical compositions and the spatial distribution of the corrosion products. The experimental results revealed and illustrate that the corrosion products were visible in samples without inhibitor and appeared less noticeable in samples with Mapei Dynamon SR 31 but in the samples with Oxydtron were almost non-existent.

1. Introduction

As it is stated in many relevant publications, the corrosion of steel reinforcement is a major problem influencing the long-term performance of reinforced concrete structures. It typically occurs due to onslaught of aggressive agents such as chloride ions from marine environment, deicing salt or chloride contaminated aggregate [1–3]. One of exposure classification for reinforced concrete according to EN 1992-2 [4] was XD3 and the corrosion for this class induced by chlorides other than from seawater and it be Cyclic wet and dry, this exposure may occur in parts of bridges exposed to spray containing chlorides, pavements, car park slabs. In presence of chloride, these ions are known to be able to locally damage passivating films on metals and alloys that exhibit complete passivity against many natural environments in their absence (as shown in Fig. 1). The formation of corrosion products (rust) involves a substantial volume increase, i.e. the volume of corrosion products is greater than that of original steel bar. Therefore, expansive stresses are induced around corroded steel bars causing possible cracking, spalling of concrete cover and loss of bond between the steel and the concrete matrix and thus reducing the serviceability of steel reinforced concrete structures [5–11].

Cracking of the concrete cover is a critical limit state and this is often modelled as a two-stage process that consists of a) an initiation phase, defined as the time taken for corrosion to commence, and b) propagation phase, where the accumulation of corrosion products induces expansive stresses and damage [12–14].

Anyhow, as a preventive measure against steel rebar corrosion, it is highly recommended by many corrosion experts [e.g. 16–19] studying the mechanism of the reinforcing steel corrosion in concretes, that inhibitors added to the fresh concrete mixtures can effectively defer the initiation phase of corrosion as well as decrease its rate during the propagation phase.

As it is well known, the corrosion inhibitors are chemical substances that when added in small amount to concrete mix decrease or slow down corrosion rate by changing the surface condition of the reinforced steel [20]. Most of the corrosion inhibitors are classified as organic and inorganic ones according to their chemical nature as well as anodic, cathodic or mixed inhibitors according to the electrochemical reaction on the steel surface with its environment [21].



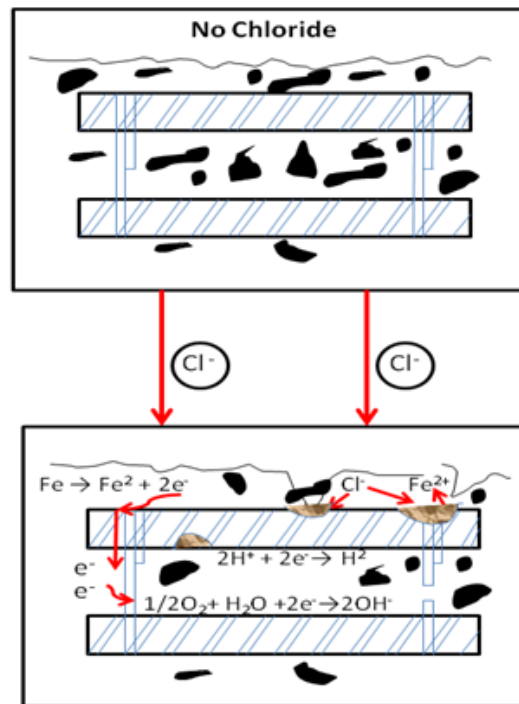


Figure 1. Electrochemical corrosion processes triggered by Cl⁻ ions reaching reinforcements, (modified from [11]).

The main purpose of this paper is to present an experimental study pursued by SEM-EDS, XRD analysis and light optical microscopy to monitor and evaluate corrosion products at the steel-concrete interface of XD3 concrete with green inhibitor and two types of superplasticizers.

2. Methods

2.1. Materials and Experimental work

2.1.1. Materials Used

All materials were used in this work conformed to the European Standards starting with cement (Portland slag cement CEM II/A-S 42.5R conforming to the EN 197-1 [22]) and then aggregates (fine and coarse according standard EN 12620 [23]). Steel rebar samples selected with diameter of 8 mm for this work. Tap water was used for both making and curing the specimens. Used three types from admixtures during preparing concrete samples, one of these admixtures was orange peels extract as a green inhibitor (this inhibitor was selected because it cheap, not harmful and eco-friendly as we mention it in previous published work [1, 2]), the other two admixtures were Mapei Dynamon SR 31 and Oxydtron (nanocement) as a superplasticizers.

2.1.2. Samples Preparation

The European mix design method type XD3 class was used to preparing concrete mixes. The cover depth of concert we select the structure class type S2 with depth 35mm have service life of 10 to 25 years according to the EN 1990 [24]. The composition of the mix prepared for casting the specimens was as follows:

Cement: 400 kg/m³ (CEM II/A-S 42.5 R), Water: 172 kg/m³ ($w/c = 0.43$ planned/targeted value).

Admixtures: 2.4 kg/m³, Additive: 1815 kg/m³ [(sand 0/4: 60 % 1089 kg/m³) and (gravel 4/8: 40 % 726 kg/m³)].

Mass percentages of the two special additives compared to the amount of cement type CEM II/A-S 42.5R for the prepared concrete samples are given in Table 1. The samples had been immersed and kept in 3.5 % NaCl solution for 18 months then the samples were removed from the 3.5 % NaCl solution as shown in Figs. 2, 3.

Table 1. The concrete mixtures (specimens) prepared for this study.

Type of Mixtures		
Symbol of Mix	Type of Admixture	Concentration of Green Inhibitor
A1 (Reference)	MapeiDynamon SR 31	without
B1	MapeiDynamon SR 31	1% byweight of cement
C1	MapeiDynamon SR 31	3% byweight of cement
A2 (Reference)	Oxydtron	without
B2	Oxydtron	1% byweight of cement
C2	Oxydtron	3% byweight of cement

**Figure 2. Reinforced concrete samples were immersed in 3.5 % NaCl solution for 18 months.****Figure 3. Reinforced concrete samples removed after 18 months immersion in 3.5% NaCl solution.**

After drying, the concrete cubes/blocks (15 cm×15 cm) were cut into several parts as shown in Fig.4 after that the steel rebar were taken out from the cubes.

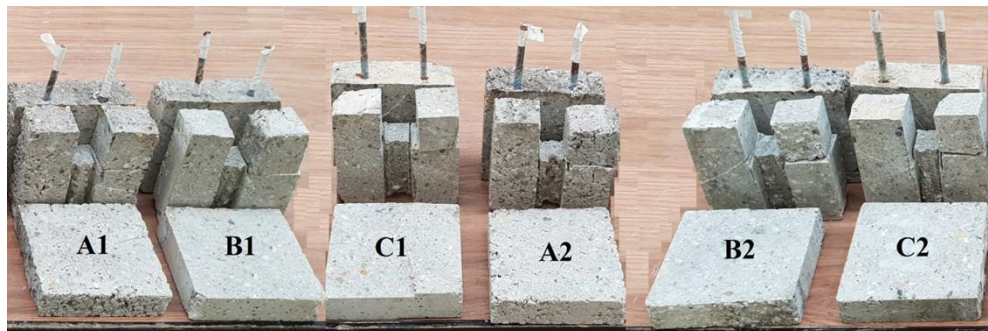


Figure 4. Reinforced concrete samples after cutting and removing one reinforcing steel bar from each sample.

2.2. SEM observation

It is well-known that not all corrosion products participate in concrete cracking as some of them fill the voids around the rebars and some of them migrate from the steel/concrete interface to the pores in concrete. Scanning electron microscopy (SEM) imaging and EDS elemental mapping were employed on the surface of the steel rebars after detaching them from the concrete blocks in order to assess spatial distribution of corrosion products at the steel/concrete interface. Measurements were done on Zeiss EVO/MA10, using accelerating voltage of 15 kV.

2.3. Optical microscopy

Thin sections (thickness 1cm) were also cut from each sample to examine with light optical microscopy. The cut sections were dried in air, impregnated with epoxy resin under vacuum, and finally grounded and polished by silicon carbide papers of up to 1200 grit; 6-mm and 3-mm diamond spray and finally, 0.05-mm Al_2O_3 suspension, etched (in 3% Nital, for approximately 10 s). In this study, light optical microscopy was especially used to detect the extent and spatial distribution of rust, capillary porosity and secondary precipitated phases in voids and cracks at the steel-concrete interface of the samples.

2.4. XRD analysis

To clarify the rust compositions and diffusion of water and chloride ions, small concrete parts were sampled from the concrete in direct contact with the steel bars as shown in Fig. 5. These parts were then ground and analyzed by powder X-ray diffraction (XRD). The powder samples (size $< 5 \mu\text{m}$) were analyzed by the XRD technique using $\text{CuK}\alpha$ -radiation at angles from $2\theta = 2^\circ$ to 70° ($0.007^\circ/2\theta/24$ sec counting time) on a Bruker D8 Advance instrument, in parallel beam geometry obtained with Göbel mirror, equipped with Vantec-1 position sensitive detector (1° opening).

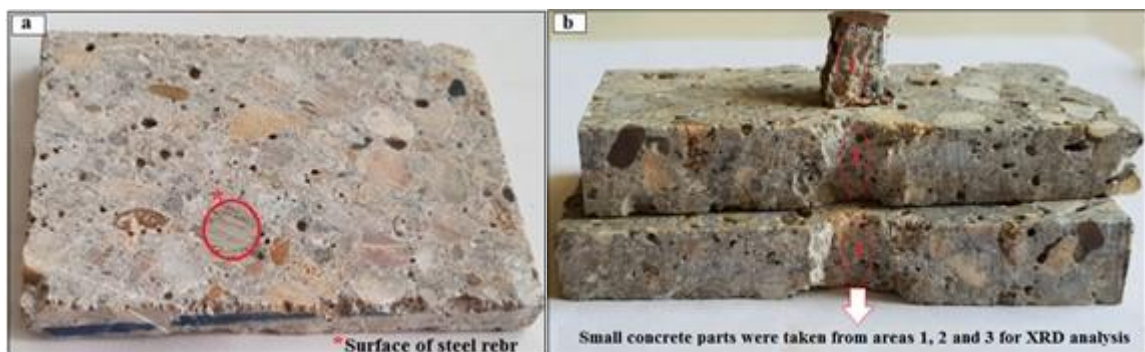


Figure 5. Concrete samples after cut and prepared for XRD analysis, a) before cut, b) after cut and removed the steel rebar.

3. Results and Discussion

3.1. SEM-EDS Microstructural and Composition Analysis of the Steel Rebar Surface

For the microstructural SEM investigations the steel rebar specimens/rods first had to be removed from the concrete blocks which had previously been kept immersed in 3.5% NaCl solution for 18 months. After that the SEM-EDS analysis could be commenced and the results are presented in Fig. 6. The chemical elementary compositions determined at some selected surface points on the steel rebars (as marked clearly in Figure 6) were obtained by the EDS method being coupled to the scanning electron microscope (SEM) and are given in wt% in Table 2.

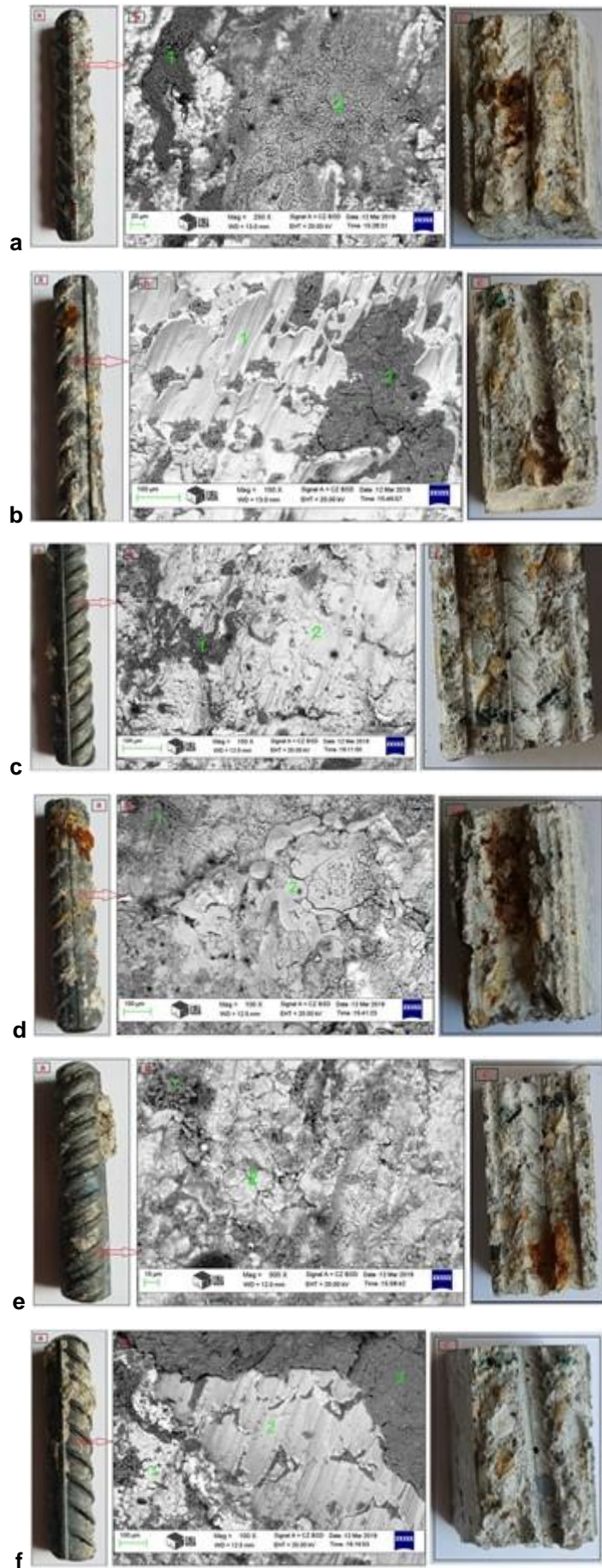


Figure 6. a) Close-up image of a steel rebar for sample: a) A1, b) B1, c) C1, d) A2, e) B2, f) C2, after removal from the concrete, b) SEM Micrograph of the section indicated in (a), c) Representative image of a split concrete specimen after removal of the steel rebar.

Table 2. The approximate chemical composition (expressed as oxides) of some small selected surface areas (as indicated in Fig. 6) of the steel rebars after removal from the concrete blocks by SEM-EDS

Components (as Oxides)	Composition by EDAX (ZAFcorrection) given in wt%, not normalised												
	A1		B1		C1		A2		B2		C2		
	Point 1	Point 2	Point 1	Point 2	Point 1	Point 2	Point 1	Point 2	Point 1	Point 2	Point 1	Point 2	Point 3
Na ₂ O	0.13	0.46	3.61	1.38	2.36	1.40	0.14	0.35	13.61	6.01	3.61	6.45	0.61
MgO	0.00	0.30	1.42	4.13	2.29	2.26	1.16	0.25	3.13	2.31	3.15	0.50	4.28
Al ₂ O ₃	0.19	0.95	1.21	10.9	5.62	1.22	1.26	0.59	2.35	1.32	2.39	0.57	2.77
SiO ₂	1.38	2.01	3.41	17.6	24.7	10.7	0.59	1.07	10.6	7.80	10.6	3.11	16.7
SO ₃	1.04	0.55	1.10	5.75	4.93	2.28	0.23	0.28	0.58	0.38	0.58	7.39	2.18
Cl ₂ O	3.51	0.23	1.83	0.68	3.98	0.31	5.10	2.06	0.24	0.11	0.20	1.90	0.91
K ₂ O	0.11	0.16	0.98	0.84	0.96	1.25	0.10	0.07	0.45	0.17	0.5	1.75	0.54
CaO	0.51	2.54	9.65	52.6	40.4	21.1	1.00	0.84	39.2	15.5	39.2	16.0	58.4
MnO	0.91	0.87	0.83	0.67	0.72	1.08	0.09	0.15	2.79	1.68	2.79	0.66	0.71
FeO	92.2	91.9	75.9	5.32	2.36	55.4	92.3	94.3	47.1	64.7	37.1	61.7	12.9

Fig. 6a represents the reinforcing steel specimen for sample A1, which showed an oxidized surface state (small oxidized areas spread over most of the specimen surface) and its composition was found similar to that of pure FeO as it contained about 92.23 wt% FeO at point 1 and 91.93 wt% at point 2. It is seen from Table 2 at point 2 that at the steel surface of the same sample A1 also some compound-bound chlorine (expressed as Cl₂O of 3.51 wt%) could be detected, which indicates that the chloride ions migrated inwards and could reach the surface of steel rebar. As this concrete sample did not contain any corrosion inhibitor (namely the orange peel extract), the chloride ions could diffuse easily and fast to the steel surface and even initiate and/or enhance its corrosion with the probable later formation of different iron-oxide-hydroxide(rust) compounds, although the marked and EDS tested two points may also be related to the original mill-scale coverage of the steel bars received directly from a reinforcing steel rod producer and studied also by use earlier [2, 3]. Anyhow, the presence of chlorine observed right at the steel/concrete interface is a strong indication of the chloride ion ingress reaching to the rebars surface also at some other samples (see in Table 2) after 18 months immersion in the given aqueous chloride salts solution.

Figure 6b shows the steel rebar specimen in sample B1 that presents a little bit oxidized area on the surface but at the spot that was selected for testing and is marked as point 1 had FeO in 75.97 wt%, which means this point(s) were attacked by pitting corrosion due probably to the rather low concentration of the green inhibitor (1 %) that could not prevent the break down of the thin passive surface oxide layer. Hence, at some "weakest points" this protective layer could be "destroyed" (i.e. chemically modified and dissolved away) from the steel surface due primarily to the attack of chloride ions (given as Cl₂O of 1.83 wt%) which could reach the surface of steel as shown in Table 2 at point 1 of B1.

In Fig. 6c the surface of the reinforcing steel in sample C1 appears almost free of oxidation, but in the micro-structure analysis test made by EDS it showed FeO in ~66.06 wt%, and CaO ~15.45 wt% at point 2 and in the same point it also had some chlorine (expressed in Cl₂O of about 0.31 wt%), so these oxides not only as a rust in this point but also came from concrete composition.

From Fig. 6d can note the effect of chloride on the surface of steel rebar in sample A2 because it has oxidized areas clear and widespread on the surface (FeO ~ 92.33 wt%, at point 1 and 94.34 wt%, at point 2). This sample has no ability to resist the corrosion and the amount of chloride ions that reached to the surface of steel its high (Cl₂O ~ 5.10 wt% at point 1 and 2.06 wt% at point 2) and this quantity consider risk and the probability of corrosion its high also.

Fig. 6e represents the steel rebar in sample B2 had only in micro-structure by EDAX test a little bit oxidized composition but it does not appear clearly on the surface (FeO ~ 64.74 wt% at point 2), also the amount of chlorides in this sample not high as shown in Table 2 at point 2.

In Fig. 6f the reinforcing steel in sample C2 considers the best one because it had a very little bit oxide areas and this oxide is not appeared on the surface of steel only detected by EDAX test compare with other samples, it means that there is a very low probability to corrosion risk in this sample.

The observed micro-structure by SEM technique features (presented in Fig. 6) and the EDS analysis for composition (Table 2) indicate the effects of the changing bulk and boundary materials properties, like the porosity and pore solution, as well as alterations at the metal/solution interfaces inside the concrete samples being immersed up to 18 months in 3.5 % NaCl solution. In this respect our observations are in harmony with those of some other researchers [25, 26] having dealt with somewhat similar systems and explained the observed phenomena by the formation of porous corrosion products modifying the charge transfer resistance at the steel/solution interface.

The increases in the corrosion (by formation oxidized area) can mainly be related to the structural consequences of the hydration processes (so-called hardening) of the concrete bodies, that is the liberation of calcium hydroxide, Ca(OH)_2 , and/or the formation of the well known cementitious compounds C3S or C3A, etc. The tested two admixtures (Oxydtron /nanocement/ and Mapei Dynamon SR 31) added to the fresh concrete during the preparation step of the samples gave rise to reducing the water/cement ratio during the concrete blocks hardening, therefore there was not enough time for the formation of Ca(OH)_2 and/or C3S and/or C3A, .. etc. (which compounds cause greater capillary porosity in concrete and weakens the properties). While discussing the topic of the so-called nanocement admixtures as well, Yakub et al. [27] described some relevant details of the so-called pozzolanic reaction of vitreous silica with calcium hydroxide (Ca(OH)_2 also abbreviated as C–H). During this hydration reaction of the Ordinary Portland Cement (OPC) this binder is producing additional calcium silicate hydrate (C–S–H) that resembles tobermorite or jennite structure, which is the main constituent for providing the strength and density in the hardening binder paste. The pozzolanic activity includes two parameters; the amount of lime (Ca(OH)_2) that pozzolan can react with it and the rate of reaction. The rate of the pozzolanic activity is related to the surface area of pozzolan particles where higher surface area of pozzolan particle (or finer particle) gives more pozzolanic reactivity. And, due to the very high specific surface area and the spherical particle shape of the synthetic nanosilica admixture, it can potentially enhance the performance of binder mainly due to its reaction with C–H to develop more of the strength-carrying compound in binder structure: C–S–H [27]. Hence, just by analogy, it can be stated with high probability, that the Oxydtron (nanocement) admixture should also behave in a somewhat similar fashion to that of the nanosilica admixture.

Nevertheless, the admixture Oxydtron did reduce the ratio of water/cement less than Mapei Dynamon SR 31, which means that the capillary porosity in the structure of the concrete body is higher than with SR 31. So after adding the green inhibitor (especially in 3 % as in C2 sample) to the fresh concrete, this inhibitor can and will work as a retarder, i.e. it retards the action of Ca(OH)_2 and/or C3S and/or C3A and also will diffuse through the pores and give a more closed structure of the samples. And so, eventually it will provide the samples better resistance against chloride diffusion and the concrete will be more resistant to steel rebar corrosion.

Usually, chloride ions cannot penetrate enough deep into the concrete within short time. However, after a long time in chloride ions containing environment chloride ions can arrive to and accumulate in a sufficiently high concentration at the metallic surface of the steel rebar in the concrete samples to initiate corrosion. This behavior is mainly due to distortion of passive layer (caused by the green inhibitor) on the surface of reinforced steel in agreement with the observations of the researchers Magdy A. et al. [28].

3.2. Optical Microscopy

Light optical micrograph for all concrete samples is presented in Fig. 7.



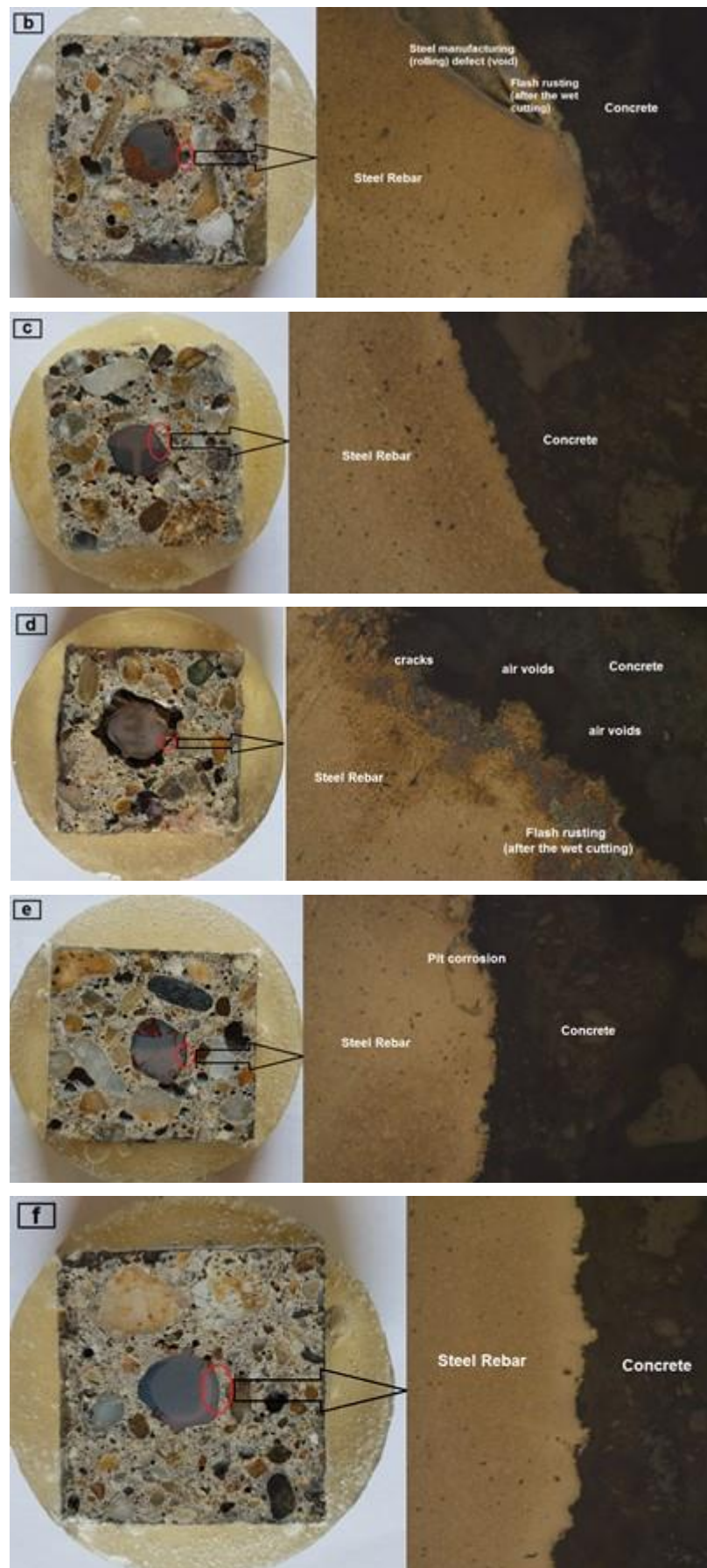


Figure 7. Light optical micrograph of the steel-concrete interface section with magnification 50X of the sample: a) A1, b) B1, c) C1, d) A2, e) B2, f) C2, showing the microstructure and the corrosion attack.

The visual examination revealed that in 75 % of all cases, corrosion initiated between the rebar ribs or directly at the rib edge as shown in Fig. 7a,d (samples A1 A2) and the type of corrosion as a flash rusting (after wet cutting for samples), also the cracks and air void appeared in these samples.

Fig. 7b (sample B1) illustrates there's a steel manufacturing (rolling) defect (void) and small a flash rusting (after wet cutting for samples) areas.

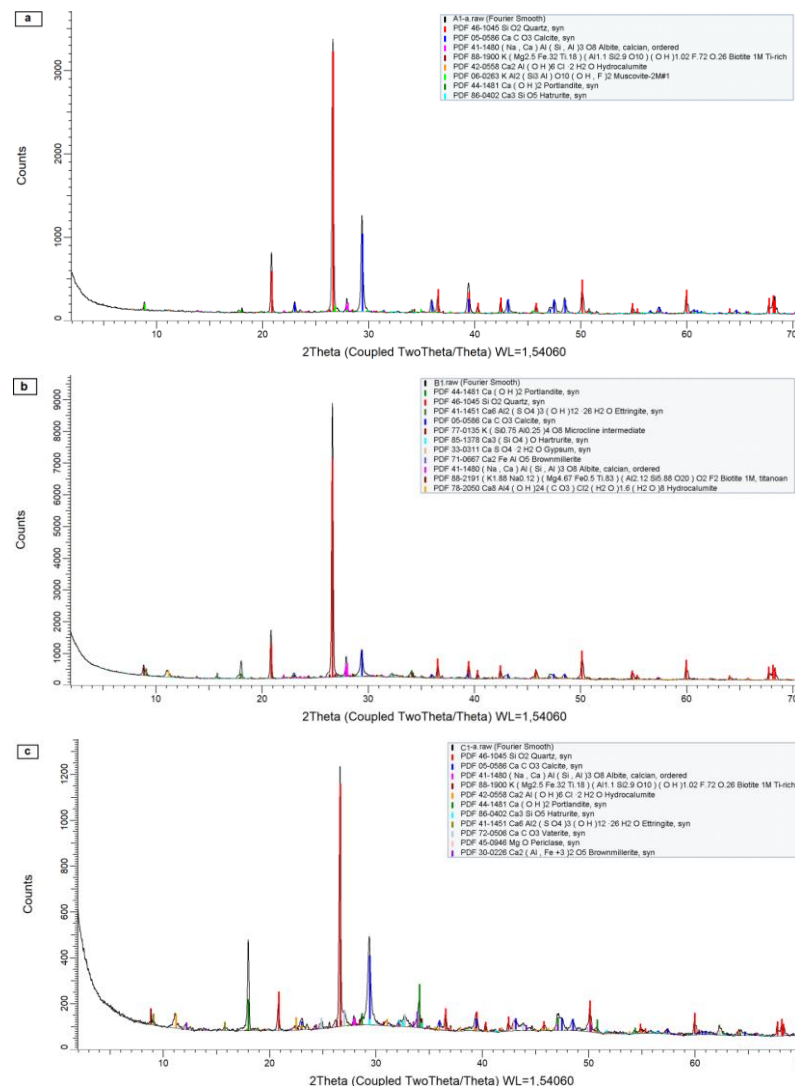
Inspection of the steel-concrete interface upon corrosion initiation typically revealed the presence of one distinct corroding spot, which in some cases was surrounded by significantly smaller corrosion pits, all of them within an area of maximum approximately 1 mm² as shown in Fig. 7e (samples B2). The small corrosion pits were interpreted as sites where corrosion had initiated but was not able to reach stable pit growth (in contrast to the dominating corrosion site), these pits were typically covered with a crust of corrosion products, which occasionally remained even after the chemical cleaning process in inhibited hydrochloric acid.

Inspection of the samples C1 and C2 (Fig. 7c,f) showed there is no pits corrosion or cracks at the steel-concrete interface.

3.3. Composition analysis of corrosion products by XRD test

In Fig. 8 all the XRD records measured for the concrete samples at their steel-concrete interfaces are collected and presented from a) to f).

X-ray diffraction measurements detected the same products (Portlandite very low content and abundant content from calcite plus corrosion products (Brownmillerite, Biotite, Muscovite, Hydrocalumite, Ettringite, Chlorite) middle content), in concrete at its interface with concrete, as for free inhibitor samples. But the amount of calcite is lower and low or very low content amount of corrosion products in concrete samples containing inhibitor (samples with 1 %, 3 % green inhibitor) than in the other specimens. Amorphous material was also detected, and is a product of corrosion and is made up by Fe-oxyhydroxides („rust”) and Ca-Al-silicate hydrates.



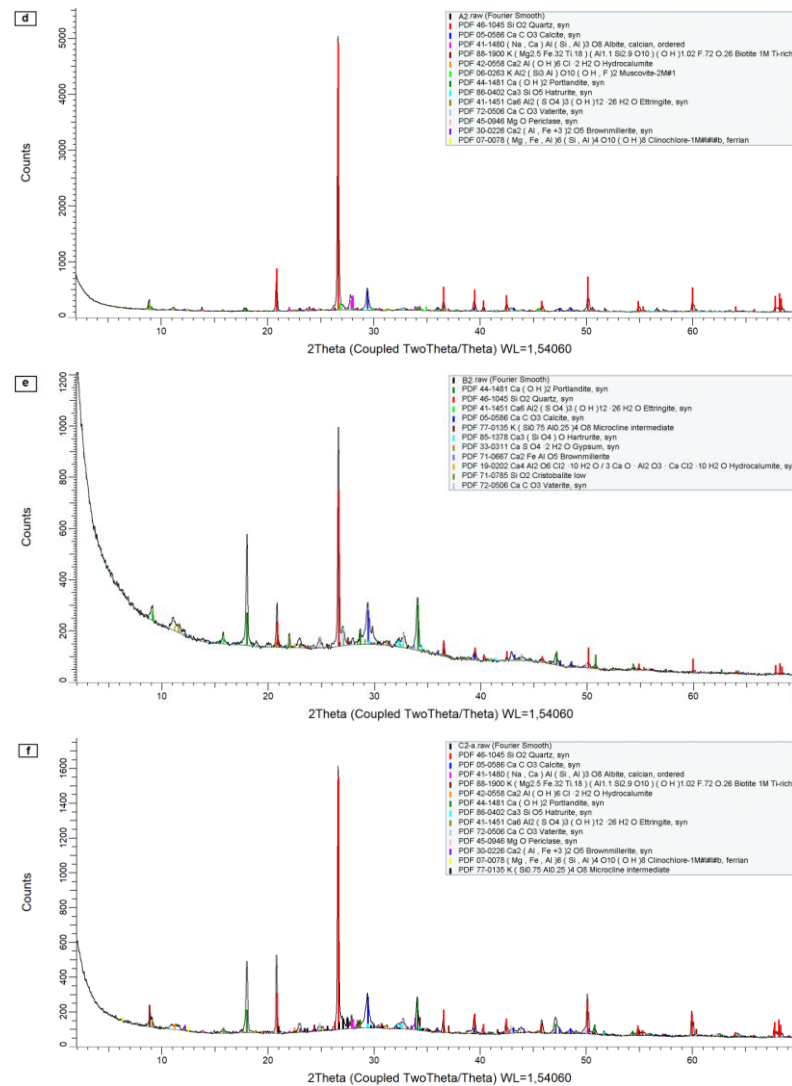


Figure 8. XRD pattern of corrosion products in the interface between steel and concrete for sample: a) A1, b) B1, c) C1, d) A2, e) B2, f) C2, after immersion in 3.5% NaCl for 18 months.

Table 3. The qualitative content of the main crystalline hydration products in samples at concrete-steel interface by XRD analysis.

Compound name with formula	Qualitative content of compounds					
	A1	B1	C1	A2	B2	C2
Portlandite [Ca(OH) ₂]	+	+++	+++	+	+++	++++
Calcite [CaCO ₃]	++++	+++	+++	++++	++	+++
Ettringite [Ca ₆ Al ₂ (SO ₄) ₃ (OH) ₁₂ ·26H ₂ O]	+++	+++	++	+++	+++	++
Hydrocalumite [Ca ₂ Al(OH) ₆ Cl·2H ₂ O]	+++	+	++	+++	++	+
Biotite [K(Mg,Fe) ₃ (AlSi ₃ O ₁₀)(F,OH) ₂]	+++	+	+	++	+	+
Brownmillerite [Ca ₂ (Al, Fe) ₂ O ₅]	+++	++	++	+++	+++	+
Muscovite [KAl ₂ (AlSi ₃ O ₁₀)(FOH) ₂]	+++	No	No	+++	No	No
Chlorite [(Mg, Fe, Al) ₆ (Si, Al) ₄ O ₁₀ (OH) ₈]	++	No	No	++	No	No

Notation: ++++: Abundant content; +++: Middle content; ++: Low content; +: Very low content; No: Absence.

The XRD pattern (Fig. 8) for all concrete samples (with and without inhibitors) demonstrates the presence of strong peak is Quartz (SiO₂, deriving from the sand grains in mortar) at about 2θ of 26.5°. The second clear and important peak is Portlandite (Ca(OH)₂) at 2θ = 18° and 34° was created by the hydration of calcium silicates. Calcium hydroxide quantity precipitated at the steel surface is important in resist effect of corrosion. The protective effect of calcium hydroxide was attributed to the dissolution of calcium hydroxide crystals close to emerging pits, thereby preventing the pH drop required for the further propagation of the corrosion pit [29].

Calcite (CaCO_3) of a small peak at 2θ of 29.5° is attributed to carbonation of hydrates on steel surface. The presence of these two last compounds can be explained by the fact that some traces of concrete materials could remain adhered to the rust during the sampling. Because all the samples were subjected to chloride ingress, the presence of Hydrocalumite ($\text{Ca}_2\text{Al}(\text{OH})_6\text{Cl}\cdot 2\text{H}_2\text{O}$) is justifiable and is confirmed by small peaks at $2\theta = 11^\circ$ and 21° in low and very low content for the samples with inhibitors and in middle content for samples without inhibitors. A little amount of Brownmillerite ($\text{Ca}_2(\text{Al}, \text{Fe})_2\text{O}_5$), Biotite ($\text{K}(\text{Mg}, \text{Fe})_3(\text{AlSi}_3\text{O}_{10})(\text{F}, \text{OH})_2$), Muscovite ($\text{KAl}_2(\text{AlSi}_3\text{O}_{10})(\text{FOH})_2$), Ettringite ($\text{Ca}_6\text{Al}_2(\text{SO}_4)_3(\text{OH})_{12}\cdot 26\text{H}_2\text{O}$), Chlorite ($(\text{Mg}, \text{Fe}, \text{Al})_6(\text{Si}, \text{Al})_4\text{O}_{10}(\text{OH})_8$) as a corrosion products can be observed in different quantities in some of concrete samples as shown in Table 3.

However, iron oxides (Hematite (Fe_2O_3) or Maghemite ($\gamma\text{-Fe}_2\text{O}_3$)) cannot be clearly distinguished by this XRD pattern because their diffraction patterns are amorphous phases, only Iron(II) oxide (FeO) we distinguished by SEM technique.

Sample C2 has portlandite in high quantity this can explain the resistance of these samples to the attack of chlorides and very little corrosion products because the electrochemical mechanism of pitting corrosion confirms the inhibitive nature of OH^- in the pore solution. The pH value of the pore solution in concrete is mainly maintained by the portlandite ($\text{Ca}(\text{OH})_2$) from the cement hydration and the alkaline ions (Na^+ , K^+) in the pore solution. The inhibitive effect of OH^- on pitting corrosion is enhanced by the concentrated distribution of $\text{Ca}(\text{OH})_2$ on the concrete–steel interface. The quality of the concrete–steel interface conditions the electrochemical environment of the pitting corrosion: concentrated CH (calcium hydroxide) can effectively inhibit the initiation, while the air voids and cracks at the interface can favor the formation of macrocells and thus accelerate the initiation [30].

An increased amount of CH close to the steel in reinforced concrete as observed in this work may be beneficial, in that it may lead to improved local pH-buffering capacity and thus to better protection against carbonation-induced generalized corrosion; that is, it would take a longer time for the larger amount of CH near the interface to react to form calcium carbonate thus delaying the drop in pH associated with complete carbonation. However, it is possible that this potential benefit might not be realized in practice if the CH simply becomes encased in calcium carbonate whilst the surrounding C–S–H becomes completely carbonated, as has been observed in partially carbonated hardened cement pastes by transmission electron microscopy. Certainly, a partially carbonated zone that consists of completely carbonated C–S–H and regions of CH encased in calcium carbonate would seem to be a very plausible explanation for the observation of corroded steel in regions of concrete that appears ‘uncarbonated’ to the phenolphthalein test [31].

Samples A1, A2 has abundant content from calcite and because this component there's no ability to resist the effect of corrosion risk. Concrete carbonation due to atmospheric CO_2 is one of the main environmental aggression leading to steel corrosion. The high pH (13) of the concrete provides a natural protection against corrosion to the embedded reinforcement by forming a compact insoluble oxide film at the steel surface (passive state). But carbonation leads concrete pH to decrease to about 9 and active steel corrosion to start. Corrosion of steel in carbonated concrete is assumed to be uniform. In this case, anodic and cathodic areas form corrosion microcells which are not separated spatially, leading to a uniform steel loss.

In reinforced concrete structures, CO_2 penetration in the concrete cover is a complex process. Gradients in concrete humidity content affect a lot the carbonation rate, mechanical damage of concrete subjected to excessive tension can lead to a CO_2 penetration increase, the quality of the concrete cover (strength, porosity, permeability, etc.) can be very different in regard to the location in the structure.

Carbonation occurs in concrete because the calcium hydrates present are attacked by carbon dioxide of the air and converted to calcium carbonate (Eq. (1)), leading to a decrease in pH to about 9 and active steel corrosion can start [29]. The concrete will carbonate if CO_2 from air enters the concrete according to: $\text{Ca}(\text{OH})_2 + \text{CO}_2 = \text{CaCO}_3 + \text{H}_2\text{O}$ (1) [32]

The interface is regarded as a major factor in corrosion initiation. Since the pores and voids at the concrete-steel interface are not always saturated by pore solutions, the availability of oxygen (gas phase) and the pore solution (liquid phase) impact on corrosion initiation. Both are necessary to start up the cathodic reaction for corrosion. Accordingly, highly saturated and very dry concretes tend to have high resistance to chloride initiation of corrosion and the structural degradation of the concrete matrix [30].

4. Conclusion

While testing the steel rebar specimens after removal from the steel reinforced concrete blocks previously kept in aqueous salt solutions for 18 months and after analyzing their steel-concrete interfaces we can arrive to the following major concluding points:

1. Corrosion products (FeO , Cl_2O) was detected by SEM- EDAX on the surface of steel rebar after removal from concrete samples increase with decrease concentration of green inhibitor (orange peel extract) and the steel of sample C2 had the lowest rate from corrosion products in the points examined compared to the rest of the steel samples, this can also be seen from the external appearance of the steel surface as it is almost free from corrosion products because it has a strong passive layer.

2. Cracks, porosity, corrosion pits, and air voids clearly appeared at the steel-concrete interfaces of A1, A2 samples which were revealed by the light optical microscopy analysis. Such undesirable features were less observable in samples with Oxydtron+ (1 %, 3 % green inhibitor) and Mapei Dynamon SR 31 (only with 3 % green inhibitor).

3. High quantities of Portlandite and almost non-existent amounts of Hydrocalumite, Biotite, Brownmillerite, Muscovite, Chlorite were detected in the steel-concrete interfaces of B1, C1, B2, C2 samples (in particular with C2 sample) by the XRD analytical technique.

4. The concrete sample C2 (with 3 % green inhibitor and Oxydtron admixture) had lower concentration of infiltrated/ingresses Cl^- ions after immersion in 3.5 % NaCl solution for 18 months in comparison to the other samples. Also this sample showed the best resistance to corrosion.

5. Acknowledgements

We would like to thank Mr. László Köteles, Institute of Mining and Geotechnical Engineering in Faculty of Earth Science and Engineering for cutting the concrete samples and Mr. Kovács Árpád, Institute of Physical Metallurgy, Metalforming and Nanotechnology, Faculty of Material Science and Engineering, both from University of Miskolc for the SEM+EDS measurements.

References

- Shaymaa, A.A., Éva, F., Tamás, I.T. Corrosion testing on steel reinforced XD3 concrete samples prepared with a green inhibitor and two different superplasticizers. *Materials and Corrosion*. 2019. 70. Pp. 1–11. <https://doi.org/10.1002/maco.201810695>
- Abbas, S.A., Török, T.I., Fazakas, É. Preliminary Corrosion Testing of Steel Rebar Samples in 3.5 % NaCl Solution with and without a Green Inhibitor. *építőanyag-Journal of Silicate Based and Composite Materials*. 2018. 70. Pp. 48–53. <https://doi.org/10.14-382/epitoanyag-jsbcm.2018.10>
- Abbas, S.A., Török, T.I., Fazakas, É. Corrosion studies of steel rebar samples in neutral sodium chloride solution also in presence of a bio-based (green) inhibitor. *International Journal of Corrosion and Scale Inhibition*. 2018. 7. Pp. 38–47. <http://dx.doi.org/10.17675/2305-6894-2018-7-1-4>
- EN 1992-2 (2005) (English): Eurocode 2: Design of concrete structures - Part 2: Concrete bridges - Design and detailing rules [Authority: The European Union Per Regulation 305/2011, Directive 98/34/EC, Directive 2004/18/EC.
- Shaymaa, A.A., Tamás, I.T. Measurements and Studying Corrosion Potential of Reinforced Concrete Samples Prepared with and without a Green Inhibitor and Immersed in 3.5 % NaCl Solution. *MultiScience – XXXII. microCAD International Multidisciplinary Scientific Conference*. University of Miskolc. 5–6 September, 2018. <http://dx.doi.org/10.26649/musci.2018.014>
- El-Reedy, M.A. *Steel-Reinforced Concrete Structures: Assessment and Repair of Corrosion*, Second Edition. CRC Press, Taylor & Francis, London, 2018.
- Quraishi, M.A., Nayak, D.K., Kumar, R., Kumar, V. Corrosion of Reinforced Steel in Concrete and Its Control: An overview. *Journal of Steel Structures & Construction*. 2017. 3. Pp. 1–6. <https://doi.org/10.4172/2472-0437.1000124>
- Shaymaa, A.A., Ali, I.A., Ali, A.H. Studying the Effect of Eco-addition Inhibitors on Corrosion Resistance of Reinforced Concrete. *Bioprocess Engineering*. 2017. 1. Pp. 81–86. <http://doi.org/10.11648/j.be.20170103.14>
- Abosra, L., Ashour, A.F., Youseffi, M., Corrosion of Steel Reinforcement in Concrete of Different Compressive Strengths. *Journal of Construction and Building Materials*. 2011. 25. Pp. 3915–3925. <https://doi.org/10.1016/j.conbuildmat.2011.04.023>
- Bertolini, L., Elsener, B., Pedersen, P., Redaelli, E., Polder, R.B. *Corrosion of Steel in Concrete: Prevention, Diagnosis, Repair*, 2nd Edition. Wiley, New York, 2014.
- González, J.A., Otero, E., Feliu, S., Bautista, A., Ramírez, E., Rodríguez, P., López, W. Some considerations on the effect of chloride ions on the corrosion of steel reinforcements embedded in concrete structures. *Magazine of Concrete Research*. 1998. 50. Pp. 189–199. <https://doi.org/10.1680/mac.1998.50.3.189>
- Kim, M.J., Ann, K.Y. Corrosion Risk of Reinforced Concrete Structure Arising from Internal and External Chloride. *Advances in Materials Science and Engineering*. 2018. Pp. 1–7. <https://doi.org/10.1155/2018/7539349>
- Faiz, A.S. Effect of Cracking on Corrosion of Steel in Concrete, *International Journal of Concrete Structures and Materials*. 2018. <https://doi.org/10.1186/s40069-018-0234-y>
- Ming, J., Song, G., Linhua, J., Yu, J., Dan, W., Ruitong, S., Yirui, W., Junqiao, H. Continuous Monitoring of Steel Corrosion Condition in Concrete Under Drying/Wetting Exposure to Chloride Solution by Embedded MnO_2 Sensor. *International Journal of Electrochemical Science*. 2018. 13. Pp. 719–738. <https://doi.org/10.20964/2018.01.92>
- Wong, H.S., Karimi, A.R., Buenfeld, N.R., Zhao, Y.X., Jin, W.L. Microstructure of corroded steel-concrete interface 2012. On the web: <http://www.imperial.ac.uk/structural-engineering/research/structural-materials/microstructure/>
- Zhao, Y.X., Karimi, A.R., Wong, H.S., Hu, B.Y., Buenfeld, N.R., Jin, W.L. Comparison of Uniform and Non-uniform Corrosion Induced Damage in Reinforced Concrete Based on a Gaussian Description of the Corrosion Layer. *Corrosion Science*. 2011. 53. Pp. 2803–2814. <https://doi.org/10.1016/j.corsci.2011.05.017>
- Sagoe-Crentsil, K.K., Glasser, F.P. Steel in Concrete: Part I. A Review of the Electrochemical and Thermodynamic Aspects. *Magazine of Concrete Research*. 1989. 41. Pp. 205–212. <https://doi.org/10.1680/mac.1989.41.149.205>

18. Glasser, F.P., Sogoe-Crentsil, K.K. Steel in Concrete: Part II. Electron Microscopy Analysis, Magazine of Concrete Research. 1989. 41. Pp. 213–220. <https://doi.org/10.1680/mac.1989.41.149.213>
19. Sogoe-Crentsil, K.K., Glasser, F.P. Green Rust, Iron Solubility and the Role of Chloride in the Corrosion of Steel at High pH. Cement and Concrete Research. 1993. 23. Pp. 785–791. [https://doi.org/10.1016/0008-8846\(93\)90032-5](https://doi.org/10.1016/0008-8846(93)90032-5)
20. Burubai, W., Dagogo, G., Comparative Study of Inhibitors on the Corrosion of Mild Steel Reinforcement in Concrete. Agricultural Engineering International: the CIGR Ejournal. 2007. 9. Pp. 1–10.
21. Mahdi, A.S. Urea Fertilizer as Corrosion Inhibitor for Reinforced Steel in Simulated Chloride Contaminated Concrete Pore Solution. International Journal of Advanced Research in Engineering and Technology. 2014. 5. Pp. 30–39.
22. EN 197-1, Cement-Part 1: Composition, specifications and conformity criteria for common cements, European Standard was Approved by CEN National Members on 21 May 2000.
23. EN 12620, Aggregates for Concrete, European Standard was Approved by CEN National Members on September 2002.
24. EN 1990, Eurocode – Basis of structural design, European Standard was approved by CEN on 29 November 2001.
25. Mahallati, E., Saremi, M. An assessment on the mill scale effects on the electrochemical characteristics of steel bars in concrete under DC-polarization. Cement and Concrete Research. 2006. 36(7). Pp. 1324–1329. <https://doi.org/10.1016/j.cemconres.20-06.03.015>
26. Nielsen, A.H., Hvitved, T., Vollertsen, J. Effect of Sewer Headspace Air-Flow on Hydrogen Sulfide Removal by Corroding Concrete Surfaces. Water Environment Research. 2012. 84(3). Pp. 265–273. <https://doi.org/10.2175/106143012X13347678384206>
27. Yakub, I., Sutan, N.M., Kiong, C.S. Characterization of calcium silicate hydrate and calcium hydroxide in nanosilica binder composites. Nano Studies. 2013. 7. Pp. 57–62. https://www.researchgate.net/publication/263738702_Characterization_of_calcium_silicate_hydrate_and_calcium_hydroxide_in_nanosilica_binder_composites
28. Magdy, A.A., Waleed, H. S., Effect of sewage wastes on the physico-mechanical properties of cement and reinforced steel. Ain Shams Engineering Journal. 2013. 4(3). Pp. 391–387. <https://doi.org/10.1016/j.asej.2012.04.011>
29. Sandberg, P. The effect of defects at the steel – concrete interface, exposure regime and cement type on pitting corrosion in concrete. (Report TVBM; Vol. 3081). Division of Building Materials, LTH, Lund University. 1998. [https://portal.research.lu.se/portal/en/publications/the-effect-of-defects-at-the-steel-concrete-interface-exposure-regime-and-cement-type-on-pitting-corrosion-in-concrete\(fa981216-1745-49c7-b73b-f6d7e03659ca\).html](https://portal.research.lu.se/portal/en/publications/the-effect-of-defects-at-the-steel-concrete-interface-exposure-regime-and-cement-type-on-pitting-corrosion-in-concrete(fa981216-1745-49c7-b73b-f6d7e03659ca).html)
30. Kefe, I. Durability Design of Concrete structures, 1st edition. John Wiley & Sons, Singapore Pte. Ltd., 2016.
31. Horne, A.T., Richardson, I.G., Brydson, R.M.D. Quantitative analysis of the microstructure of interfaces in steel reinforced concrete. Cement and Concrete Research. 2007. 37. Pp. 1613–1623. <https://doi.org/10.1016/j.cemconres.2007.08.026>
32. Nasser, A., Clément, A., Laurens, S., Castel, A. Influence of steel–concrete interface condition on galvanic corrosion currents in carbonated concrete. Corrosion Science. 2010. 52. Pp. 2878–2890. <https://doi.org/10.1016/j.corsci.2010.04.037>

Contacts:

Shaymaa Abbas Abdulsada, qkosha86@uni-miskolc.hu

Ferenc Kristaly, askkf@uni-miskolc.hu

Tamas I. Torok, fekt@uni-miskolc.hu

© Abdulsada, S.A., Kristaly, F., Torok, T.I., 2020



DOI: 10.18720/MCE.100.6

The formation mechanism of the porous structure of glass ceramics from siliceous rock

V.T. Erofeev^a, A.I. Rodin^{*a}, V.S. Bochkin^b, A.A. Ermakov^a

^a Ogarev Mordovia State University, Saransk, Respublika Mordoviya, Russia,

^b LLC "Kombinat teploizolyacionnyh izdelij", Saransk, Respublika Mordoviya, Russia,
E-mail: al_rodin@mail.ru

Keywords: glass ceramics, silicates, pore structure, differential thermal analysis, compressive strength, microstructure, mechanical activation

Abstract. Porous glass ceramic materials are widely used in industrial and civil engineering due to a number of redeeming features, such as high strength, low thermal conductivity, incombustibility, environmental friendliness, etc. A large number of researches are devoted to developing the compositions of foam glass ceramic materials based on siliceous rocks (diatomite, tripoli, opoka). Present article is devoted to studying the formation mechanism of the porous structure of glass ceramic materials as a result of heating a mechanically activated mixture (a mixture of siliceous rock and soda ash or thermonatrite). The experimental results were obtained using methods of gas permeability, scanning electron microscopy (SEM), infrared spectroscopy (IR), X-ray diffraction analysis (XRD), differential thermal analysis (DTA) and differential thermal gravimetric (DTG) analysis, physical-mechanical and thermophysical tests. It was determined that the minerals of the crystalline structure in the composition partially transfer to the amorphous phase with an increase in the charge activation time, and the amount of heulandite and sodium hydrosilicates increases. This contributes to an intensive increase in the amount of flux in the composition within the temperature range 700–800 °C. The water vapor generated during the condensation of free OH groups on the surface of silicate is formed in this temperature range. This is the formation source of the material's porous structure. The developed porous glass ceramic materials have increased compressive strength (up to 5 MPa) at a relatively low average density (268.5 kg/m³). This is several times greater than the strength of foam glass from waste glass and from fly or coal ash. The minimum thermal conductivity of glass ceramics (0.0633 W/m·°C) was determined at a sample density of 220.7 kg/m³. The maximum operational temperature of the material was 850 °C, which allows using it as a thermal insulation of industrial equipment, such as melting furnaces, boiler equipment, etc.

1. Introduction

There are a large number of studies in the world scientific literature, which are devoted to developing compositions and studying properties of porous glass ceramics. According to studies, such materials have high strength, low thermal conductivity, are incombustible and ecologically safe [1–2]. They have proven themselves in industrial and civil engineering [3]. A large number of studies in recent years are devoted to the development of foam glass ceramic materials made of waste glass and various ashes [4–6]. Some researches are related to studying the foaming of a charge by introducing MnO₂ into the composition [7, 8]. The structural formation peculiarities and the mechanical properties of glass ceramics from slags of various metallurgical industries, as well as from copper slags [11], lead-zinc mine tail ends, red mud [12] and many others were studied [9, 10]. A large number of researches are devoted to developing the compositions of foam glass ceramic materials from siliceous rocks (diatomite, tripoli, opoka) [13–22]. The technology for producing such materials is mainly mixing siliceous and zeolite-containing rocks with aqueous solutions of NaOH, followed by granulation and burning.

Erofeev, V.T., Rodin, A.I., Bochkin, V.S., Ermakov, A.A. The formation mechanism of the porous structure of glass ceramics from siliceous rock. Magazine of Civil Engineering. 2020. 100(8). Article No. 10006. DOI: 10.18720/MCE.100.6



This work is licensed under a CC BY-NC 4.0

According to the studies [16, 17], sodium hydrosilicates are formed when siliceous rocks are mixed with aqueous solutions of NaOH. When heated, these compounds are dehydrated, and the water vapor released during dehydration forms the porous structure of the material. The foaming intensity of zeolite-containing rocks activated with aqueous NaOH solutions depends on the rock fineness and on presence of zeolites in the composition of minerals that contain Ca in the structure [16]. According to [16, 17], zeolite minerals dehydrate with blockage in the micropores of surface hydroxyl groups (Si–O–H) when heating the charge to 700 °C. Increasing the heating temperature leads to the condensation of such hydroxyl groups with release of water vapor, which forms the porous structure of material. According to the research results [17, 22], the porosity of glass ceramic materials also occurs due to the release of CO₂ at temperatures above 700 °C. However, scientific literature contains ambiguous opinions regarding the nature of CO₂ formed when heating siliceous rocks above 700 °C, activated by alkaline solutions. One theory [17] is that carbon dioxide is released due to decarbonization of the formed Na₂CO₃. Other sources have shown [22] that pore formation occurs due to the release of carbon dioxide from CaCO₃. There is also a theory that CO₂ is released from the structure of silicates. It was determined that amorphization and carbonization of minerals occur during long-term grinding of silicates and aluminosilicates of alkaline earth metals [23, 24]. Carbon dioxide is in the structure of the material in a form similar to dissolved CO₂ in silicate glasses, obtained at high temperature and pressure.

Analyzing the above mentioned, it can be concluded that porous glass ceramic from siliceous rock is obtained mainly by mixing the rock with an aqueous solution of NaOH followed by burning [14–17, 22]. However, the equipment deteriorates rapidly with this production technology, as a result of exposure to alkalis. Moreover, burning the charge is accompanied with the release of harmful substances (NaOH) into the atmosphere [18]. Therefore, the production of these materials is limited to small batches only. It is possible to solve this issue by replacing the alkaline solution with alkali metal salts in dry form, such as soda ash (Na₂CO₃) or thermonatrite (Na₂CO₃·H₂O). It is advisable to mix the components by co-grinding (mechanical activation). The results of studies on developing the compositions of porous glass ceramic materials from mechanically activated siliceous rocks and soda ash were presented by authors [25]. The pore formation mechanism of such materials has not yet been studied.

The goal of research is to study the formation mechanism of the porous structure of glass ceramic materials as a result of heating a mechanically activated mixture (a mixture of siliceous rock and soda ash or thermonatrite).

Objectives:

- to determine the impact of mechanical activation time on the change in the specific surface, phase composition, shape and size of the charge particles;
- to determine the formation mechanism of the porous structure of glass ceramics by the methods of infrared (IR) spectroscopy, thermal analysis (TA) and X-ray diffraction analysis (XRD);
- to determine the impact of the charge's mechanical activation time on the physical, mechanical and thermophysical properties of porous glass ceramic samples.

2. Methods

2.1. Materials

The charge components in order to obtain samples of foam glass materials are as follows:

- siliceous rock (humidity ≤ 1 %) with the following chemical composition: SiO₂ – 67.862 %, CaO – 7.742 %, Al₂O₃ – 7.609 %, Fe₂O₃ – 1.987 %, K₂O – 1.561 %, MgO – 1.073 %, TiO₂ – 0.340 %, Na₂O – 0.167 %, P₂O₅ – 0.151 %, SO₃ – 0.059 %, SrO – 0.055 %, BaO – 0.022 %, ZrO₂ – 0.013 %, V₂O₅ – 0.012 %, MnO – 0.009 %, Cr₂O₃ – 0.008 %, CuO – 0.004 %, ZnO – 0.004 %, NiO – 0.004%, Co₃O₄ – 0.003%, other impurities – 11.315 %. The mineralogical composition of the rock is as follows: cristobalite (SiO₂) – 21.1 %, heylandite ((Ca,Sr,K₂,Na₂)[Al₂Si₆O₁₆]·5H₂O) – 19.2 %, muscovite (KAl₂[AlSi₃O₁₀](OH)₂) – 14.4 %, calcite (CaCO₃) – 12.8 %, quartz (SiO₂) – 10.8 %, tridymite (SiO₂) – 1.7 %, amorphous phase – 20.0%.
- flux agents: technical soda ash (mineral – natrite, chemical formula – Na₂CO₃); thermonatrite (chemical formula – Na₂CO₃·H₂O). Mass fraction of the main substance in both components is not less than 99 %.

2.2. Compositions and technology for the production of samples

The mixture for producing the samples of foam glass ceramic materials was obtained by co-grinding siliceous rock and flux agent (Na₂CO₃ or Na₂CO₃·H₂O). The amount of flux agent was adopted as 18.5 %

of the charge mass in terms of the main substance, which is Na_2CO_3 . The grinding was carried out in a planetary ball mill Retsch PM 400 at a rotational speed of milling pots equal to 250 rpm.

Samples of foam glass ceramic materials were obtained by burning the charge in metal forms in a muffle furnace. The forms were pretreated with kaolin paste. The following charge burning mode was adopted: heating to a temperature of 670 °C at the 4.5 °C/min rate, holding at a temperature of 670 °C for 1 hour, heating to a temperature of 850 °C at a speed of 4.5 °C/min, holding at a temperature of 850 °C for 30 minutes. After cooling the mold with obtained material together with the furnace down to 40 °C, the mold was disassembled, and samples were removed for further testing.

The compositions tested in the study are presented in Table 1.

Table 1. Compositions tested in the study.

Composition number	Charge composition, %			Mechanical activation time, min
	Siliceous rock	Na_2CO_3	$\text{Na}_2\text{CO}_3 \cdot \text{H}_2\text{O}$	
C1				10
C2				30
C3	81.5	18.5	-	60
C4				90
C5				120
C6				10
C7				30
C8	79	-	21	60
C9				90
C10				120

2.3. Analytical techniques

The experimental data was obtained by using following methodologies:

- Specific surface of the charge was determined by the gas permeability method using the PSH-2 device. The arithmetic mean value of the test results for three samples of each composition was adopted as the final result.

- Scanning electron microscopy (SEM) of powdered charge samples was carried out using a Quanta 200 i 3D device (USA) in a low vacuum mode (10^{-3} Pa) with an accelerating voltage of 20 kV and a working distance of 15 mm.

- XRD of the unburnt and burnt charge samples was carried out using an ARL X'tra diffractometer (Switzerland). Samples of the burnt charge were crushed in a mortar with an agate pestle with acetone before passing through a sieve with an aperture of 90 μm . The diffraction patterns were recorded in $\text{CuK}\alpha_{1+2}$ radiation in the angle range $2\theta = 4-80^\circ$ with a rate of 1.2 $^\circ/\text{min}$, in increments of 0.02 $^\circ$, integration time 1 sec. The qualitative phase composition of samples was determined according to the Hanawalt method using the ICDD PDF-2 database. The quantitative phase content was determined according to the Rietveld method using Siroquant 3 Sietronics Pty Ltd software.

- TA of charge samples was carried out using a TGA/DSC1 device (Switzerland). 15 ± 0.1 mg of charge was poured into an alundum pot with a volume of 150 μl . After that, the sample was compacted by tapping the pot on the table. The pot was mounted on a holder and placed in an oven. The sample was heated from 30 to 800 °C at a rate of 10 °C/min.

- IR spectra were obtained in KBr pellets on the InfraLUM FT-02 Fourier spectrometer. In order to prepare the pellets, 3 mg of the sample and 200 mg of single-crystal KBr were used, the mixture was thoroughly ground in an agate mortar, and then the pellets were pressed. Spectral absorption curves of the sample were recorded in the range from 400 to 4000 cm^{-1} .

- Density, compressive strength, water absorption and thermal conductivity of foam glass ceramic materials were determined using dry cubic samples with a face size of 90 ± 5 mm. Water absorption was determined using the ratio of water mass absorbed by dry sample to the sample volume when completely immersed in water for 24 hours. The thermal conductivity of samples was determined by probe method using the MIT-1 device (probe diameter 6 mm). The final result was adopted as the arithmetic mean value of the test results for five samples of each composition.

- Maximum operating temperature of the glass ceramic materials was determined by the residual change in the size of the samples ($90 \times 40 \times 40$ mm) after holding for 2 hours at a given temperature. The

test was aborted if the sample size changed by more than 1 %. The arithmetic mean value of the test results for three samples of each composition was taken as the final result.

3. Results and Discussion

3.1. Charge properties

It is known that the morphological and dimensional characteristics of charge significantly impact the quality of finished goods regarding production of porous glass ceramic materials. The macrostructure of the material becomes homogeneous with decreasing charge particle size, density decreases, strength increases, etc. [26–28]. Within the framework of research, the correlation between change in the specific surface area of charge powder samples (siliceous rock + flux agent) and the time of mechanical activation were determined. Results are presented in Figure 1.

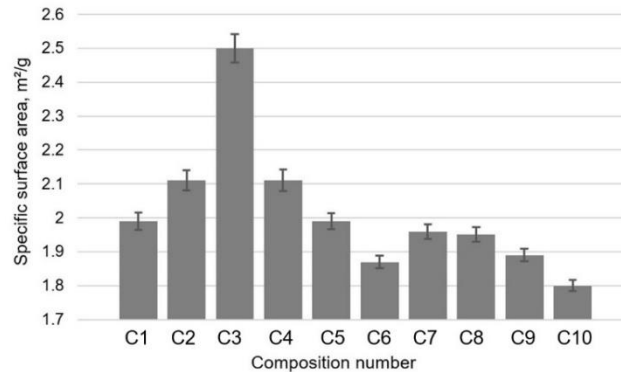


Figure 1. Specific surface of the charge samples.

According to the obtained data (Figure 1), specific surface of charge samples, which contains soda ash as flux agent, increases almost linearly from 1.99 to 2.50 m²/g. The mechanical activation time increases from 10 to 60 minutes at the same time. By increasing the activation time to 120 min, specific surface of the charge decreases in an inverse linear relationship to 1.99 m²/g.

There are no sharp changes regarding the specific surface values during mechanical activation of the mixture (compositions C6–C10, thermonatrite as a flux agent). The highest indicator value for compositions C7 and C8 (30 and 60 min, respectively) is 1.95 m²/g on average. That is more than 20 % lower than the same indicator for the composition with Na₂CO₃ (C3 composition). A further increase in the mechanical activation time up to 120 min leads to a decrease in the specific surface area of charge to 1.8 m²/g. Most likely this is due to the aggregation of charge particles, and the water molecules contained in the thermonatrite composition contribute to this. Microstructural changes in the charge samples after mechanical activation are presented in Figure 2.

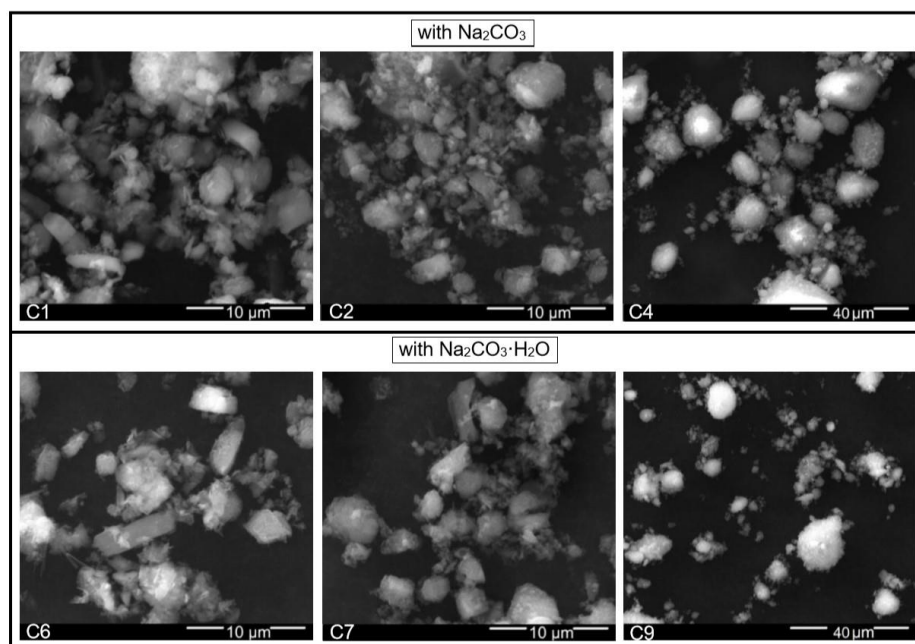


Figure 2. SEM-micrographs of charge samples.

SEM microstructure images of the charge powder samples (Figure 2) clearly demonstrate the effect of mechanical activation duration on the shape and size changes of particles of the starting materials, as well as of newly formed aggregates. After 10 min of mechanical activation (C1, C6), all charge particles have size of no more than 10 μm , regardless of flux agent type in the composition. The shape of most particles is shard with almost no aggregation.

After 30 minutes of mechanical activation of the charge containing soda ash (C2) as flux agent, the particle size decreased compared to sample C1 (10 minutes of mechanical activation). The composition is dominated by shard-shaped particles of size less than 3 μm , as well as by individual spherical aggregates of size less than 5 μm . The particle shape of sample C7 (flux agent is termonatrite) is represented by fragmentary and loose polydisperse aggregates no larger than 5 μm in size. The particle size slightly decreased comparing with C6 sample (10 min of mechanical activation).

With increasing the mechanical activation duration of the charge samples up to 90 min, a significant difference was noted regarding the sizes of the formed aggregates. For sample C4 (flux agent is soda ash), the most of spherical aggregates are 10–15 μm in size. For sample C9 (flux agent is termonatrite), all particles in the form of spherical polydisperse aggregates are not more than 15 μm .

As a result of the study, it was determined that mechanical activation significantly affects the shape of the charge particles in the mixture. Spherical aggregates are formed, the size of which increases with the activation time. The dispersion of aggregates depends on the flux agent type in the composition. The SEM results for the charge are correlated with data on its specific surface area obtained by gas permeability method.

According to the scientific literature, structural defects accumulate in solid particles during intensive grinding, phase transformations occur, as well as amorphization of crystalline minerals [23, 24, 26–28]. The impact of the mechanical activation time on structural changes in the charge for foam glass ceramic has been studied using IR spectroscopy and XRD methods.

The IR spectra of the charge samples after mechanical activation for 10 and 90 minutes are presented in Figure 3.

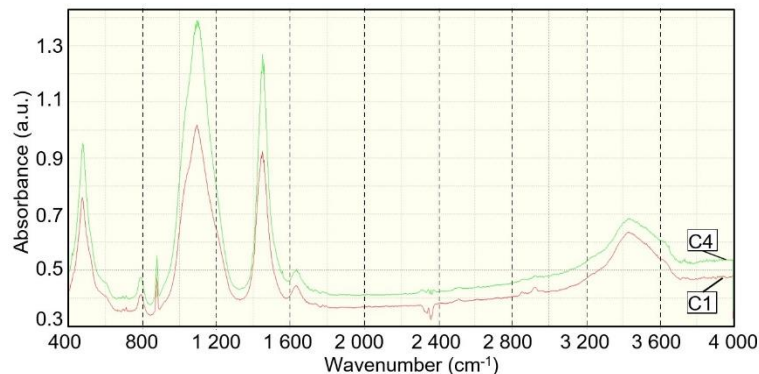


Figure 3. IR spectra of charge samples.

The presence of silicates with different structural types in the tested samples can be detected by using the following absorption bands in the IR spectra (see Figure 3). Intense absorption bands with maxima $\approx 1100 \text{ cm}^{-1}$ and $\approx 470 \text{ cm}^{-1}$ belong to the stretching and deformation vibrations of the Si–O–Si bonds, respectively. The absorption spectrum with a peak $\approx 1050 \text{ cm}^{-1}$, corresponding to stretching vibrations of the Si–O–Si(Al) bonds is clearly visible in the IR spectrum of sample C1. The $\approx 1200 \text{ cm}^{-1}$ band, which indicates the presence of a whole set of structures with Si–O–Si angles $\approx 180^\circ$, is visible as well. According to [29], the absorption band of $\approx 1200 \text{ cm}^{-1}$ appears during quartz fracture, and a decrease in its intensity in the sample's IR spectrum after 90 min mechanical activation (sample C4) is probably a result of $\beta\text{-SiO}_2$ mineral amorphization.

The presence of aluminosilicates in the tested samples can be indicated by changes in the absorption bands intensity $\approx 795 \text{ cm}^{-1}$ (stretching vibrations of the Si–O–Si(Al) bonds), as well as for the bands $\approx 520 \text{ cm}^{-1}$ and $\approx 620 \text{ cm}^{-1}$ (deformation vibrations of the bonds Si–O–Al). Significant changes in the intensity of the absorption bands or frequency of oscillations were not detected.

No significant changes were detected in the vibrational frequency and intensity of the absorption bands $\approx 1460 \text{ cm}^{-1}$, as well as $\approx 880 \text{ cm}^{-1}$ and $\approx 710 \text{ cm}^{-1}$ related to stretching and deformation vibrations in carbonates, respectively.

According to the data in Figure 3, the main changes in the IR spectra of the charge samples after mechanical activation relate to the absorption bands of hydroxyl groups and water molecules.

The absorption band $\approx 1680 \text{ cm}^{-1}$ corresponds to deformation vibrations of water molecules. A wide peak in the range of $3200\text{--}3700 \text{ cm}^{-1}$ demonstrates the superposition of stretching vibration bands of hydroxyl groups and adsorbed H_2O molecules. The intensity of the absorption bands of water molecules in the C4 sample spectrum is slightly lower. This is possibly due to the hydration processes occurred in the charge sample after mechanical activation for 90 min. Such conclusion can be confirmed by an increase in the intensity of absorption band in the range of $980\text{--}880 \text{ cm}^{-1}$ (deformation vibrations of Si-O-H), as well as $\approx 3740 \text{ cm}^{-1}$ (stretching vibrations of surface OH groups in Si-O-H). An increase in the intensity of band $\approx 3650 \text{ cm}^{-1}$ indicates an increase in the number of associated OH groups in Si-O-H .

When analyzing the IR spectra, the absorption bands of carbon dioxide in the range of $2300\text{--}2400 \text{ cm}^{-1}$ were not taken into account, these bands are inevitable consequence of the experimental error (air CO_2).

The XRD of the charge samples after mechanical activation is shown in Figure 4.

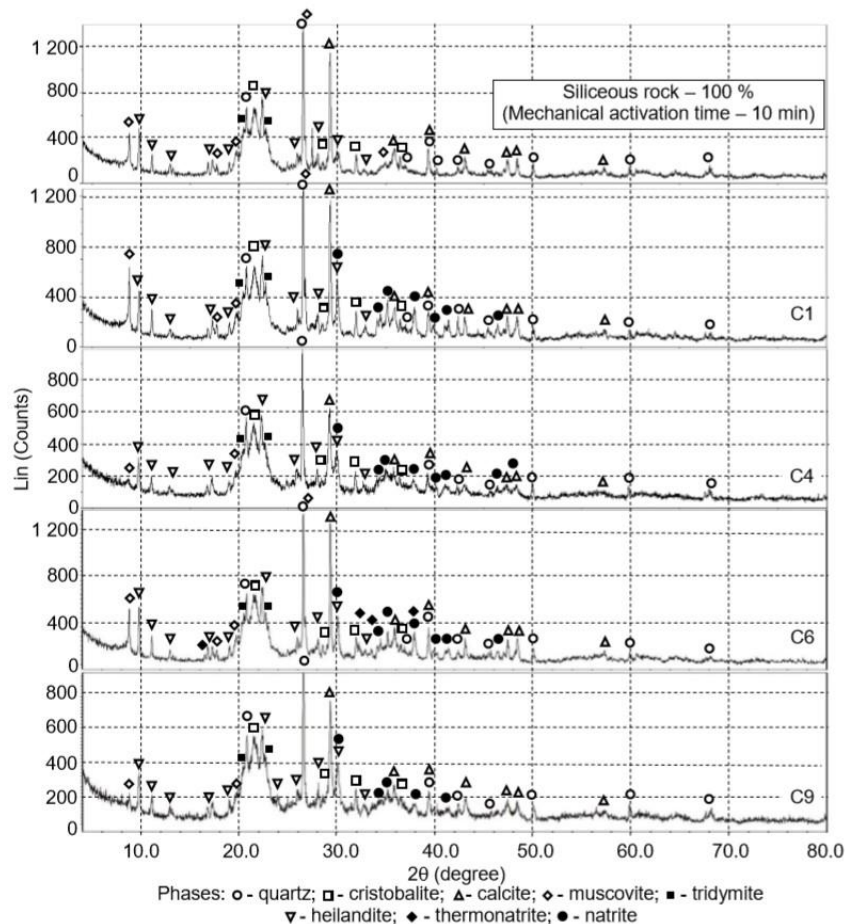


Figure 4. XRD of the charge samples.

According to the data presented in Figure 4, the main changes in the charge's phase composition after mechanical activation are as follows. With an increase in mechanical activation time of the charge, the intensity decreases and the peaks corresponding to calcite, muscovite, quartz, and cristobalite widens. Similar effects appear during the amorphization of crystalline minerals. With an increase in the mechanical activation time, the amount of Na_2CO_3 and $\text{Na}_2\text{CO}_3 \cdot \text{H}_2\text{O}$ decreases significantly. The content of the latter in the charge composition after 90 min of activation was not detected (C9). In parallel, an increase in the intensity of lines corresponding to heilandite is observed. In the X-ray diffraction patterns of samples C4 and C9 (90 min mechanical activation), a wide halo additionally appears in the range $33\text{--}39^\circ$ (2θ). This effect can be attributed to sodium hydrosilicates formed in the charge [16, 17, 23]. An increase of compounds containing OH groups in the charge composition is also evidenced by the data of IR spectroscopy (Figure 3).

3.2. Formation mechanism of the porous structure

The phase transformations occurring in the charge samples after mechanical activation by heating were studied using DTA and DTG methods. Results of the study are presented in Figure 5. The total weight loss of the samples after burning at a temperature of 800°C is shown in Table 2.

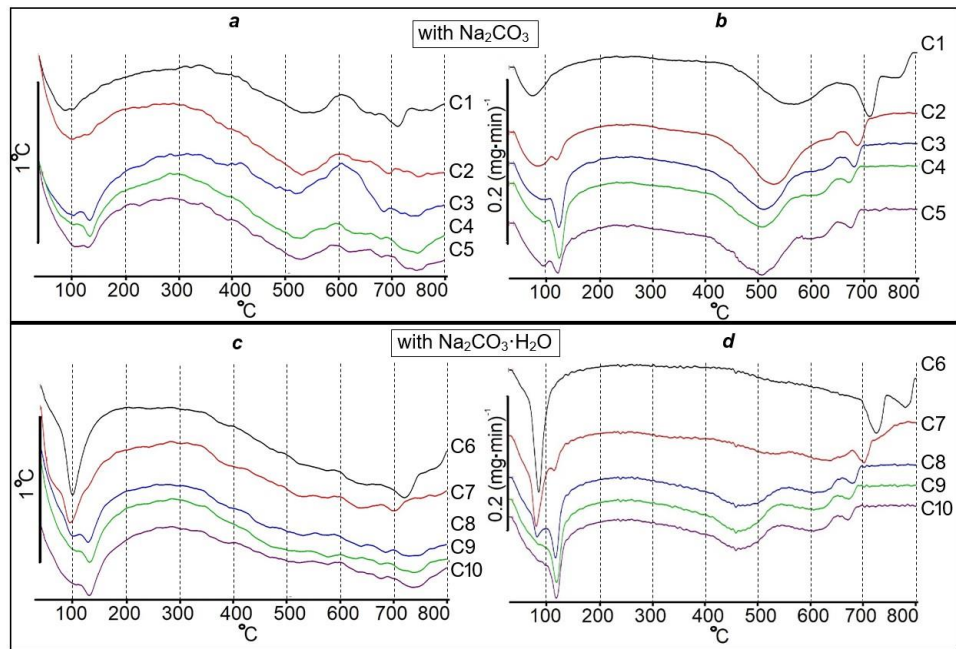


Figure 5. DTA (a, c) and DTG (b, d) curves of charge samples.

Table 2. Weight loss by the charge samples after burning at a temperature of 800 °C.

Composition number	C1	C2	C3	C4	C5	C6	C7	C8	C9	C10
Sample weight loss, %	16.57	17.49	18.04	17.94	17.49	18.88	19.09	19.17	19.00	18.29

According to data presented in Figure 5 and in Table 2, there are following phase transformations occurring in the charge during heating. The first wide peak in the temperature range from 25 to 120 °C (endoeffect) corresponds to the evaporation of unbound water, irrespective of the flux agent type in the composition. An additional peak of strong intensity appears at a maximum of ≈ 95 °C on the DTA (endoeffect) and DTG curves (weight loss) (charge with $\text{Na}_2\text{CO}_3 \cdot \text{H}_2\text{O}$), corresponding to dehydration of thermonatrite. It should be noted that a peak with a maximum of ≈ 95 °C gradually disappears with an increase in the mechanical activation time from 10 to 90 minutes. Moreover, new endothermic effect (Figure 5, a, c) appears at a temperature of ≈ 120 °C, accompanied by weight loss. This effect may be associated with the loss of water from the resulting sodium hydrosilicates. An increase in the amount of these compounds with increasing the charge activation time most likely led to the formation of aggregation of charge particles (Figure 2). The almost total absence of thermonatrite after 90 minutes of mechanical activation is confirmed by XRD data (Figure 4).

The strong endothermic effect and significant weight loss of the samples in the temperature range from 400 to 550 °C is a consequence of the formation of sodium silicates. A similar result was obtained in studies [17, 25]. The effect is accompanied with the release of carbon dioxide and water vapor from individual phases of the charge (CaCO_3 , Na_2CO_3 , etc.). Peak of the effect shifts towards lower temperatures by more than 50 °C with an increase in the time of mechanical activation of the charge from 10 to 90 minutes, respectively. This is due to an increase in the amorphous phase in the composition (Figure 4).

The endoeffect and weight loss in the temperature range from 550 to 650 °C is associated with the release of water vapor during the condensation of OH groups. Similar effect was observed when burning zeolite-containing rocks activated by alkaline solutions [16]. According to the data of various researchers [16, 17, 23], blockage in the micropores of surface hydroxyl groups (Si–O–H) occurs in this temperature range. Based on data presented in Figure 5, peak intensity and mass loss are greater for composition with thermonatrite. This is logical, since thermonatrite consists of H_2O molecules by almost 14.5 %, the molecules are necessary for the formation of OH groups.

According to Figure 5, the endothermic effect with a peak of ≈ 720 °C (decarbonization of unreacted CaCO_3) for compositions C1 and C6 (10 minutes of mechanical activation) shifts by more than 50 °C to lower temperatures after mechanical activation for ≥ 60 minutes.

Mechanical activation duration of the charge also affects the increase in the amount of flux agent in the composition. Confirmation for this is the increase in the endothermic effect in the temperature range 700–800 °C with an increase in activation time to 120 minutes. According to the study [22], an eutectic flux

appears in the $\text{Na}_2\text{O}-\text{CaO}-\text{SiO}_2$ system in this temperature range. The effect is characterized by the weight loss absence in the sample, as evidenced by a straight line on the DTG curves (samples C3–C5, C8–C10). The mixture foams in this temperature range, but only after mechanical activation for 1 hour or more.

The surface macrostructure of porous glass ceramic samples, which are based on charge after mechanical activation of different durations, is presented in Figure 6.

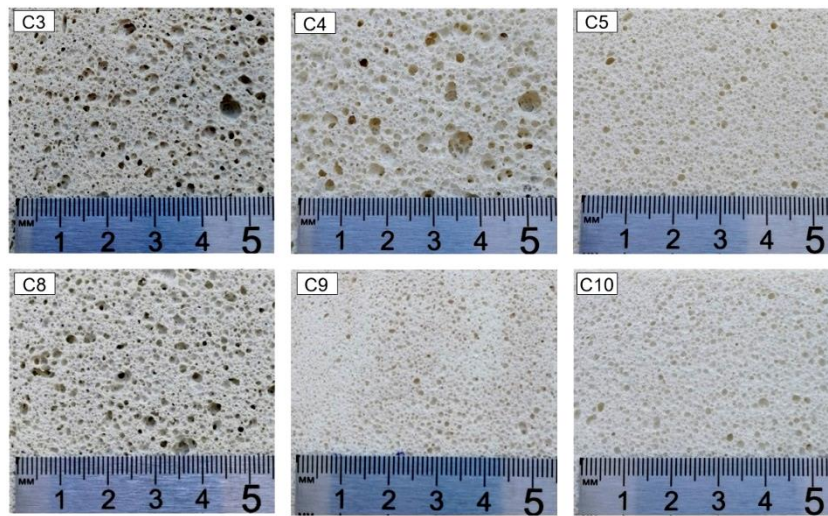


Figure 6. Surface macrostructure of foam glass ceramic samples.

According to the data in Figure 6, it is possible to obtain the optimal porous structure in the samples of foam glass ceramic materials (pore diameter no more than 2 mm) from the presented siliceous rock. However, the rock has to be mechanically activated with $\text{Na}_2\text{CO}_3 \cdot \text{H}_2\text{O}$ (21 % of the charge mass) for at least 90 minutes (samples C9, C10), together with at least 120 minutes of Na_2CO_3 (18.5% of the charge mass) (sample C5).

According to the data presented in Table 3, total weight loss of the sample after burning at a temperature of 800 °C decreases by more than 1 % for a charge with thermonatrite. This occurs in case the mechanical activation duration of the charge is increased for more than 1 hour. Theoretically, this phenomenon is unlikely, since the charge activation was carried out in a closed system. Perhaps, this effect is caused by the part of volatile substances (CO_2 and/or H_2O), which are still in the charge composition and form the porous structure in the glass ceramic samples. As noted above, the process of pore formation in the production of glass ceramic materials can be associated with the release of water vapor during the condensation of free OH groups on the silicate surface [16, 17, 22]. This is a result of decarbonization of CaCO_3 [22], Na_2CO_3 [16] or carbon dioxide from the structure of silicates [23, 24]. In order to confirm any of the mentioned assumptions, the charge samples were tested by XRD and IR spectroscopy after burning at a temperature of 670 °C. The maximum burning temperature (670 °C) was selected based on the thermal analysis data of the charge samples presented above. The burnt samples were milled in an inert gas (argon) in order to exclude the possibility of CO_2 re-entering the silicate structure. The results of the XRD are presented in Figure 7.

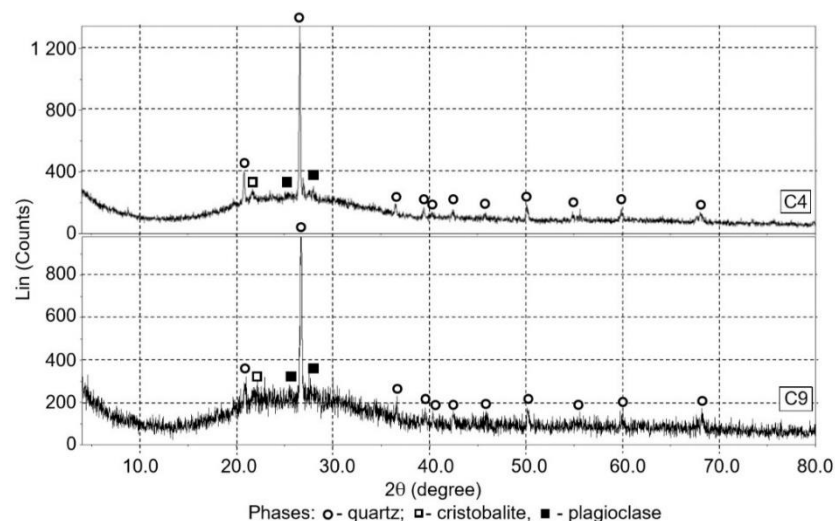


Figure 7. XRD of the charge samples after burning at a temperature of 670 °C.

As a result of the X-ray diffraction analysis of the charge samples after burning at a temperature of 670 °C (Figure 7), the following was determined. Regardless of the flux agent type in the initial charge composition (Na_2CO_3 or $\text{Na}_2\text{CO}_3 \cdot \text{H}_2\text{O}$), the crystalline phase of the burnt samples is mainly represented by quartz. There are individual peaks on radiographs, corresponding to cristobalite and plagioclases. Figure 7 clearly shows an intense amorphous halo in the angle range from 15 to 37° (2θ). The absence of peaks on the X-ray diffraction pattern is determined. These peaks characterize the presence of Na_2CO_3 , CaCO_3 in the composition of samples, as well as other minerals of a crystalline structure that could be involved in the pore formation process.

The final conclusions regarding the possible pore formation cause in the production of porous glass ceramic materials (free OH groups on the surface of silicate [16, 17, 22] or carbon dioxide in the structure of silicates [23, 24]) were made according to the results of IR spectroscopy (Figure 8).

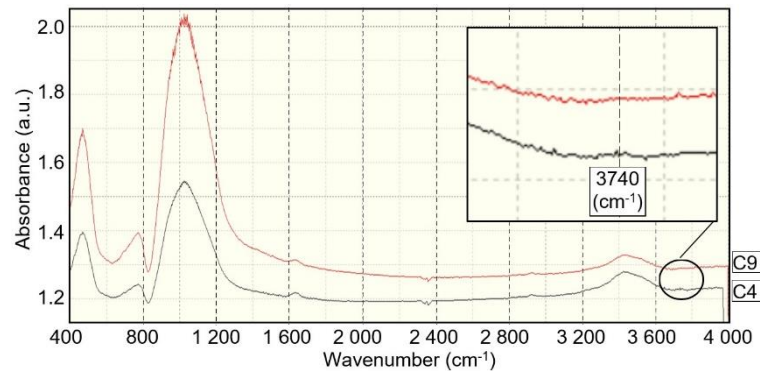


Figure 8. IR spectra of burnt charge samples at a temperature of 670 °C.

According to the IR spectra analysis (Figure 8) of the charge samples after burning at 670 °C, the pore formation of glass ceramic materials (based on the siliceous rock used) occurs due to release of water vapor. The vapor is generated by the condensation of free OH groups on the silicate surface. This is confirmed by the absorption band of a very low intensity $\approx 3740 \text{ cm}^{-1}$. A similar character of pore formation in glass ceramic materials is described in various studies [16, 17, 22].

The assumption regarding the possible pore formation process in glass ceramic materials due to carbon dioxide emission from the structure of silicates [23, 24] has not been confirmed. According to the IR spectra of the charge samples after firing at 670 °C, there are no absorption bands in the range of 1550–1400 cm^{-1} . They are common for stretching vibrations of carbonate groups (samples C4, C9).

When analyzing the IR spectra, absorption bands of carbon dioxide (2300–2400 cm^{-1}) were not taken into account, as well as water molecules ($\approx 1680 \text{ cm}^{-1}$, 3200–3700 cm^{-1}), which are an inevitable consequence of the experimental error (CO_2 from air, H_2O in KBr).

3.3. Properties of samples of foamed glass ceramic materials

The results of studying physical, mechanical and thermophysical properties of porous glass ceramic samples are represented in Table 3.

Table 3. Properties of samples of foam glass ceramic materials.

Composition number	Properties*				
	Average density, kg/m^3	Compressive strength, MPa	Water adsorption, %	Thermal conductivity, $\text{W/m}\cdot^\circ\text{C}$	Resizing of samples after holding at temperature 850°C, %
C4	251.5 (6.5)	4.5 (0.11)	35.35 (1.92)	0.0667 (0.0013)	-0.35 (0.02)
C5	243.3 (5.7)	4.2 (0.10)	18.48 (1.17)	0.0659 (0.0014)	-0.31 (0.02)
C9	268.5 (5.9)	5.0 (0.11)	23.03 (1.25)	0.0705 (0.0011)	-0.38 (0.02)
C10	220.7 (6.1)	2.9 (0.08)	24.84 (1.08)	0.0633 (0.0017)	-0.34 (0.02)

* - the mean square deviation is given in brackets

According to the obtained data (Table 3), an increase in the duration of charge mechanical activation leads to the decrease in average density of foam glass ceramic samples. The effect is more noticeable when the charge with thermonatrite is activated. Thus, the average density of C10 composition samples (120 min of activation) is almost 20 % less than the same indicator for composition C9 (90 min of activation).

Compressive strength of the obtained foam glass ceramic samples is linearly dependent on their average density. The highest compressive strength was recorded for composition C9 (5 MPa) with an

average density of samples equal to 268.5 kg/m^3 . To compare [4], the strength of foam glass samples obtained from waste glass and fly ash is 5 times less ($\approx 1 \text{ MPa}$) at a practically equal average density (267.2 kg/m^3). According to the research [6], similar compressive strengths (5 MPa) of foam glass ceramic samples based on waste glass and coal ash were achieved at a material density of $\approx 460 \text{ kg/m}^3$ (70 % higher than the density of the samples we obtained). C10 composition has the lowest value of compressive strength (2.9 MPa) (see Table 4). It should be noted that samples of this composition have the lowest density (220.7 kg/m^3) and, as a result, thermal conductivity ($0.0633 \text{ W/m}\cdot^\circ\text{C}$).

The analysis of the data presented in Table 4 indicates that the water adsorption of the developed materials also depends on the mechanical activation duration of the charge. With an increase in activation duration, water absorption decreases. This is probably due to an increase in the amount of flux agent in the composition (Figure 5), which helps to reduce the number of open pores in the material structure.

Another positive quality of the developed foam glass ceramic materials is their high maximum operating temperature ($850 \text{ }^\circ\text{C}$). This allows implementing the developed material as a thermal insulation of industrial equipment, such as smelting furnaces, boiler equipment, etc. Considering this indicator, the foam glass is significantly inferior. Its maximum operating temperature rarely exceeds $600 \text{ }^\circ\text{C}$ [1].

4. Conclusions

1. It was determined that mechanical activation of siliceous rock together with Na_2CO_3 or $\text{Na}_2\text{CO}_3\cdot\text{H}_2\text{O}$ significantly affects the change in the specific surface. It also affects the shape and size of the charge particles and its phase composition:

a. Using the gas permeability and SEM methods, the specific surface area of the charge was determined to increase linearly with an increase in activation time up to 60 min. If the charge mechanical activation is longer, the specific surface area decreases and spherical aggregates are formed in the composition. The size of aggregates increases depending on the activation time.

b. Using the X-ray diffraction and IR spectroscopy methods, it was determined that the increase in charge activation time causes the crystalline structure minerals in composition to partially go into the amorphous phase. The amount of heilandite and sodium hydrosilicates increases in this case.

2. The formation mechanism of the porous structure of glass ceramics when heating the charge (siliceous rock + Na_2CO_3 or $\text{Na}_2\text{CO}_3\cdot\text{H}_2\text{O}$) after mechanical activation is determined:

c. According to the thermal analysis results, silicate formation in the charge begins at a temperature of about $400 \text{ }^\circ\text{C}$, the sample weight loss stops almost completely at $670 \text{ }^\circ\text{C}$. The intensive increase in the amount of flux agent in the composition was recorded in the temperature range $700\text{--}800 \text{ }^\circ\text{C}$.

d. The formation of glass ceramic's porous structure is determined to be caused by the release of water vapor at a temperature of more than $700 \text{ }^\circ\text{C}$. Water vapor is formed by the condensation of free OH groups on the silicate surface. A similar pore formation pattern for glass ceramic materials is observed during burning of siliceous (zeolite-containing) rocks activated by alkaline solutions.

e. Obtaining the optimal porous structure in the foam glass ceramic samples (pore diameter no more than 2 mm) from the presented siliceous rock is possible. The rock has to be mechanically activated with $\text{Na}_2\text{CO}_3\cdot\text{H}_2\text{O}$ (21 % of the charge mass) for at least 90 minutes, and also at least for 120 minutes with Na_2CO_3 (18.5% of the charge mass).

3. The developed porous glass ceramic materials have increased compressive strength (up to 5 MPa) at a relatively low average density (268.5 kg/m^3). This is several times greater than the strength of foam glass from waste glass and fly or coal ash. The minimum thermal conductivity at a sample density of 220.7 kg/m^3 was $0.0633 \text{ W/m}\cdot^\circ\text{C}$. The maximum operating temperature of the material is $850 \text{ }^\circ\text{C}$, which allows implementing it as a thermal insulation of industrial equipment, such as melting furnaces, boiler equipment, etc.

5. Acknowledgement

The study was conducted using research grant from the Russian Science Foundation (project No. 18-73-00213).

References

1. Fernandes, H.R., Tulyaganov, D.U., Ferreira, J.M.F. Preparation and characterization of foams from sheet glass and fly ash using carbonates as foaming agents. *Ceramics International*. 2009. 35(1). Pp. 229–235. DOI: 10.1016/j.ceramint.2007.10.019.
2. Vatin, N.I., Nemova, D.V., Kazimirova, A.S., Gureev, K.N. Increase of energy efficiency of the building of kindergarten. *Advanced Materials Research*. 2014. No. 953-954. Pp. 1537–1544. DOI: 10.4028/www.scientific.net/AMR.953-954.1537.
3. Gorshkov A.S., Vatin N.I., Rymkevich P.P., Kydrevich O.O. Payback period of investments in energy saving. *Magazine of Civil Engineering*. 2018. 2(78). Pp. 65–75. DOI: 10.18720/MCE.78.5.

4. Bai, J., Yang, X., Xu, S., Jing, W., Yang, J. Preparation of foam glass from waste glass and fly ash. *Materials Letters*. 2014. No. 136. Pp. 52–54. DOI: 10.1016/j.matlet.2014.07.028.
5. Smolii, V.A., Kosarev, A.S., Yatsenko, E.A. Ash-Slag Based Cellular Glass for Energy-Efficient 3-Ply Construction Panels. *Glass and Ceramics (English translation of Steklo i Keramika)*. 2019. 76(3–4). Pp. 105–108. DOI: 10.1007/s10717-019-00143-0.
6. Zhu, M., Ji, R., Li, Z., Wang, H., Liu, L., Zhang, Z. Preparation of glass ceramic foams for thermal insulation applications from coal fly ash and waste glass. *Construction and Building Materials*. 2016. No. 112. Pp. 398–405. DOI: 10.1016/j.conbuildmat.2016.02.183.
7. König, J., Petersen, R.R., Yue, Y. Fabrication of highly insulating foam glass made from CRT panel glass. *Ceramics International*. 2015. 41(8). Pp. 9793–9800. DOI: 10.1016/j.ceramint.2015.04.051.
8. Petersen, R.R., König, J., Yue, Y. The mechanism of foaming and thermal conductivity of glasses foamed with MnO₂. *Journal of Non-Crystalline Solids*. 2015. No. 425. Pp. 74–82. DOI: 10.1016/j.jnoncrysol.2015.05.030.
9. Cao, J., Lu, J., Jiang, L., Wang, Z. Sinterability, microstructure and compressive strength of porous glass-ceramics from metallurgical silicon slag and waste glass. *Ceramics International*. 2016. 42(8). Pp. 10079–10084. DOI: 10.1016/j.ceramint.2016.03.113.
10. Yatsenko, E.A., Gol'tsman, B.M., Kosarev, A.S., Karandashova, N.S., Smolii, V.A., Yatsenko, L.A. Synthesis of Foamed Glass Based on Slag and a Glycerol Pore-Forming Mixture. *Glass Physics and Chemistry*. 2018. 44(2). Pp. 152–155. DOI: 10.1134/S1087659618020177.
11. Yang, Z., Lin, Q., Lu, S., He, Y., Liao, G., Ke, Y. Effect of CaO/SiO₂ ratio on the preparation and crystallization of glass-ceramics from copper slag. *Ceramics International*. 2014. 40(5). Pp. 7297–7305. DOI: 10.1016/j.ceramint.2013.12.071.
12. Liu, T., Li, X., Guan, L., Liu, P., Wu, T., Li, Z., Lu, A. Low-cost and environment-friendly ceramic foams made from lead-zinc mine tailings and red mud: Foaming mechanism, physical, mechanical and chemical properties. *Ceramics International*. 2016. 42(1). Pp. 1733–1739. DOI: 10.1016/j.ceramint.2015.09.131.
13. Erofeev, V., Korotaev, S., Bulgakov, A., Tretiakov, I., Rodin, A. Getting Fired Material with Vitreous Binder Using Frame Technology. *Procedia Engineering*. 2016. No. 164. Pp. 166–171. DOI: 10.1016/j.proeng.2016.11.606.
14. Ivanov, K.S. Granulated foam-glass ceramics for ground protection against freezing. *Magazine of Civil Engineering*. 2018. 3(79). Pp. 95–102. DOI: 10.18720/MCE.79.10.
15. Ivanov, K.S. Optimization of the structure and properties of foam-glass ceramics. *Magazine of Civil Engineering*. 2019. 89(5). Pp. 52–60. DOI: 10.18720/MCE.89.5.
16. Kazantseva, L.K., Rashchenko, S.V. Chemical processes during energy-saving preparation of lightweight ceramics. *Journal of the American Ceramic Society*. 2014. 97(6). Pp. 1743–1749. DOI: 10.1111/jace.12980.
17. Kazantseva, L.K., Rashchenko, S.V. Optimization of porous heat-insulating ceramics manufacturing from zeolitic rocks. *Ceramics International*. 2016. 42(16). Pp. 19250–19256. DOI: 10.1016/j.ceramint.2016.09.091.
18. Mueller, A., Sokolova, S.N., Vereshagin, V.I. Characteristics of lightweight aggregates from primary and recycled raw materials. *Construction and Building Materials*. 2008. 22(4). Pp. 703–712. DOI: 10.1016/j.conbuildmat.2007.06.009.
19. Sokolova, S.N., Vereshagin, V.I. Lightweight granular material from zeolite rocks with different additives. *Construction and Building Materials*. 2010. 24(4). Pp. 625–629. DOI: 10.1016/j.conbuildmat.2009.10.010.
20. Volland, S., Kazmina, O., Vereshchagin, V., Dushkina, M. Recycling of sand sludge as a resource for lightweight aggregates. *Construction and Building Materials*. 2014. No. 52. Pp. 361–365. DOI: 10.1016/j.conbuildmat.2013.10.088.
21. Zhimalov, A.A., Bondareva, L.N., Igitkhanyan, Y.G., Ivashchenko, Y.G. Use of Amorphous Siliceous Rocks – Opokas to Obtain Foam Glass with Low Foaming Temperature. *Glass and Ceramics (English translation of Steklo i Keramika)*. 2017. 74(1–2). Pp. 13–15. DOI: 10.1007/s10717-017-9916-1.
22. Kazantseva, L.K., Lygina, T.Z., Rashchenko, S.V., Tsyplakov, D.S. Preparation of Sound-Insulating Lightweight Ceramics from Aluminosilicate Rocks with High CaCO₃ Content. *Journal of the American Ceramic Society*. 2015. 98(7). Pp. 2047–2051. DOI: 10.1111/jace.13581.
23. Kalinkin, A.M., Kalinkina, E.V., Zalkind, O.A., Makarova, T.I. Mechanochemical interaction of alkali metal metasilicates with carbon dioxide: 1. Absorption of CO₂ and phase formation. *Colloid Journal*. 2008. 70(1). Pp. 33–41. DOI: 10.1007/s10595-008-1006-1.
24. Kalinkin, A.M., Kalinkina, E.V., Zalkind, O.A., Makarova, T.I. Chemical interaction of calcium oxide and calcium hydroxide with CO₂ during mechanical activation. *Inorganic Materials*. 2005. 41(10). Pp. 1073–1079. DOI: 10.1007/s10789-005-0263-1.
25. Erofeev, V.T., Rodin, A.I., Kravchuk, A.S., Kaznacheev, S.V., Zaharova, E.A. Biostable silicic rock-based glass ceramic foams. *Magazine of Civil Engineering*. 2018. 84(8). Pp. 48–56. DOI: 10.18720/MCE.84.5.
26. Yuan, W., Li, J., Zhang, Q., Saito, F. Innovated application of mechanical activation to separate lead from scrap cathode ray tube funnel glass. *Environmental Science and Technology*. 2012. 46(7). Pp. 4109–4114. DOI: 10.1021/es204387a.
27. Yuan, W., Li, J., Zhang, Q., Saito, F., Yang, B. Lead recovery from cathode ray tube funnel glass with mechanical activation. *Journal of the Air and Waste Management Association*. 2013. 63(1). Pp. 2–10. DOI: 10.1080/10962247.2012.711796.
28. Erofeev, V.T., Rodin, A.I., Yakunin, V.V., Tuvin, M.N. Structure, composition and properties of geopolymers from mineral wool waste. *Magazine of Civil Engineering*. 2019. 90(6). Pp. 3–14. DOI: 10.18720/MCE.90.1.
29. CHukin G. D. Himiya poverhnosti i stroenie dispersnogo kremnezema [Surface chemistry and structure of dispersed silica]. Moscow: Printing house Paladin, 2008. 172 p. (rus)

Contacts:

Vladimir Erofeev, al_rodin@mail.ru

Alexander Rodin, al_rodin@mail.ru

Viktor Bochkin, sovelitnew@mail.ru

Anatolij Ermakov, anatoly.ermakov97@mail.ru



DOI: 10.18720/MCE.100.7

Effect of sorption moisture content of heavy concrete on radon emanation

R.A. Nazirov, I.S. Inzhutov, O.G. Dubrovskaya, E.D. Gunenko, P.Y. Vede*

Siberian Federal University, Krasnoyarsk, Russia

* E-mail: vede@live.ru

Keywords: radon, building materials, concretes, emanation coefficient, water content

Abstract. This article provides the results of a study to determine the emanation coefficient of artificial construction material, namely heavy concrete produced by semi-dry pressing, depending on equilibrium sorption moisture content achieved in the desorption stage. We measured radon volumetric activity in a sealed chamber at different air relative humidity, determined the specific activity of naturally occurring radionuclides (NORs), and calculated the specific effective activity of NORs. Then we obtained mathematical models of the dependence of the emanation ratio on the degree of pores filling with water, and it was determined that the emanation coefficient increases by almost 50 % in the range of relative humidity typical for residential and public buildings, which necessitates the numerical control of this parameter in order to accurately assess the dose load on the population.

1. Introduction

Currently, it has been determined that the main contribution to the population exposure is made directly by natural radionuclides [1], and radon and its decay products make the largest contribution to the total population exposure dose. Due to internal exposure, radon can cause oncological diseases, including lung cancer.

The main radioactive nuclides contained in rocks are radium, thorium, and potassium. Radioactivity of ready-made construction materials is caused by naturally occurring radionuclides (NORs) in original raw materials and is characterized by the value of the specific effective activity (A_{eff}). Radioactivity of construction materials depends on the type and place of extraction of mineral raw materials, and the content of NORs in industrial waste which is used to improve the properties and characteristics of the material or to reduce the cost of its manufacture. In this case, the values of gamma activity and emanation are determined by the composition of building mixes [2, 3, 4, 5, 6].

Such radioactive emanations as radon (Rn) and thoron (Tn) are exhaled from building envelopes and accumulate in the indoor air. Due to the short half-life, thoron makes an insignificant contribution to the total dose load, as only a small fraction of thoron exhales from construction materials into the air of the room and soil under the building. Concentration of radon is largely dependent on the ventilation mode, and low air exchange in the room leads to quite high levels of radiation. Thus, the man-made altered radiation background is formed in building spaces.

It is vital to understand the processes of generation and migration of radon and the factors that influence these processes, to ensure radiation safety and to take appropriate measures to reduce dose commitment on the population.

Radon emanation is a complex process involving the release of radon atom from the solid phase, diffusion in liquid and gas media, adsorption on the walls of cracks and capillaries of materials [7].

Nazirov, R.A., Inzhutov, I.S., Dubrovskaya, O.G., Gunenko, E.D., Vede, P.Y. Effect of sorption moisture content of heavy concrete on radon emanation. Magazine of Civil Engineering. 2020. 100(8). Article No. 10007. DOI: 10.18720/MCE.100.7



The emanation coefficient E of the material is composed of emanating due to the effect of the recoil of radon atoms E_r and emanating due to diffusion E_D :

$$E = E_r + E_D$$

Emanating due to the recoil effect is practically independent of the human environment. Due to the energy released during the decay of radium, a radon atom acquires momentum and shifts by a distance equal to the range of the atomic recoil in the medium. At the expense of the recoil effect, the emanation atoms, formed in the surface layer with a thickness less than the range of atomic recoil, exhale to the media surrounding the sample [8].

After exhaling from the substance grains, radon atoms enter the pore space of the material. Radon can diffuse in pore voids, and some fraction of atoms decays directly in the body of the material, while the other part emanates from the building structure into the room air and decays.

Emanating depends on mineral composition, uniformity of radium-226 (^{226}Ra) distribution in the material, characteristics of pores (sizes, quantity, and type), specific surface area and grain size distribution of the test sample.

The diffusion component of emanation depends on the internal structure of the material and external environmental conditions, such as temperature, humidity, atmospheric pressure, and air mobility near [9].

One of the main external factors that can significantly affect the amount of radon exhaled under normal conditions is humidity. This fact is confirmed by the studies of emanation of rocks and soils.

In article [10], the authors summarize the basic theories about the influence of humidity on emanating of rocks from the insignificant influence of humidity [11, 8] to a stable relationship between these characteristics. An experiment within the research showed that an increase in moisture content for most of the studied samples resulted in a rise in the value of the emanation coefficient. Upon reaching a degree of pores filling with water close to complete water saturation, some samples tended to decrease their emanation, while others remained passive to the external impact of moisture. The authors in [12] studied emanating of radioactive samples into air and water. It turned out that for most of the samples, emanation into water is 1.1 ... 2.5 times more than into the air. Based on the studies conducted under the laboratory conditions, the authors in [10] concluded that there are rocks with a different emanation response to changes in humidity, which causes a discrepancy of the existing data.

The authors in [13] studied the effect of humidity of uranium tailings in the form of sand on the change in the emanation rate. The effect of increasing the emanation coefficient with rising humidity was attributed to the accumulation of radon atoms in pores of the material when the pore space is filled with water, which prevents the introduction of recoil atoms into the crystal lattice of neighbouring grains.

Rising of radon emanation at the increase in the moisture content of the material was also calculated using the modified Monte Carlo program TRIM [14]. In this case, the distribution of moisture in a porous medium is discussed at the level of the capillary theory. It is noted that the emanation of the material quickly reaches the value of emanation in a saturated state when humidity ranges from 10 % to 30 %. Upon reaching 30 %, the pore surface forms a thin film which impedes the incorporation of the recoil radon atom into another part of the pore wall.

The data obtained by the authors in [15] are worth considering. The amount of the maternal isotope of radium-226 in concrete samples increased in two different ways. The first method was to add radium bromide. In the second method, the amount of radium in concrete was increased due to the enrichment of uranium ore. The authors observed a strong dependence of the radiation dose on the enrichment method. For a sample enriched by uranium ore, radon emanation was about ten times less, and the authors observed a pronounced dependence of the radon release on the water content.

The authors of [16] obtained the emanation coefficients for granites, used in construction, for a dry, natural, and wet state, calculated the speed of emanating as well as alpha-equivalent dose. Results of the test showed that even with a slight increase in moisture content, the emanation coefficient increased significantly. Thus, the authors attribute the resulted data to the possibility of trapping radon atoms in the pore space by water.

Production of construction materials utilizes mixtures of natural raw materials which undergo significant changes in the process of technological conversions. The emanation of such materials can vary significantly [17]. Burnt materials such as ceramic bricks, tiles, expanded clay or unhydrated cement demonstrate the least radon release, unlike sand, gravel, hydrated cement, cement concrete, and mortars which show the greatest one.

For instance, as a result of hydration and hardening of hydraulically active cement and lignite coal fly ash, emanating of artificial stones from these materials increases by almost 10 times [2, 3]. Article [3] demonstrates the possibility of analysing the specific effective activity and emanating ability of samples of cement concretes and mortars based on the data on the radioactivity of their components taking into account chemically bound water, change in emanation as a result of cement hydration and time of hardening of the binding. The analysis has revealed that over time, the emanation of cement and cement-ash samples decreases [3, 18].

In general, it is obvious that the effect of humidity on the materials emanation is mostly considered by works connected, mainly, to the rocks and soils representing objects that are different in composition and structure from multi-component building materials obtained as a result of technological conversion (including the usage of hydraulically active artificial binders, such as cement) to ensure the required performance properties. Thus, the question of studying the emanation of building materials under operating conditions of various types of premises is relevant and requires further study in order to ensure radiation safety of the population.

In this research, we set the goal to establish the influence of relative humidity on the emanation of radon from heavy concrete made by semi-dry pressing. During the study, patterns of the formation of the number of emanations were revealed and a mathematical model was proposed.

2. Methods

The paper presents results aimed at identifying changes in the emanation coefficient of heavy concrete samples depending on the relative humidity of the ambient air and the sorption moisture of the samples. Samples were tested in the radiation monitoring laboratory of Siberian Federal University.

To determine the parameters of the radon emanation process from finished construction products, samples of heavy concrete with a total weight of 9.9 kg, a volume of 0.00423 m³, and an estimated average density $\rho = 2340 \text{ kg/m}^3$ in the dry state were selected. Concrete composition per 1m³: CEM I 42.5 GOST 31108-2016 – 520 kg; sand and gravel (aggregate), grain size up to 10 mm – 1810 kg; water – 230 kg. The porosity of the material was 10 %, while the moisture content by volume with complete water saturation of the heavy concrete sample was 9.49 %.

2.1. Determining the specific activity of radionuclides and the specific effective activity

We determined the NORs specific activity in the test material using PROGRESS gamma-spectrometer following the procedure [19]. The PROGRESS software package is designed to analyse spectrograms of a standard radionuclide composition: ⁴⁰K, ¹³⁷Cs, ²³²Th, ²²⁶Ra in equilibrium with daughter products.

A pre-weighed crushed sample with grain sizes of 0.5-1 mm was placed in a standard measuring cell and sealed. To establish a radioactive equilibrium between radon and its daughter products, the sample was aged for 14 days in the same state. The content of basic radionuclides in the test sample was measured on a gamma spectrometer three times with a 180-minute exposure.

The specific effective activity of natural radionuclides was determined by [20]

$$A_{eff} = A_{Ra} + 1.3A_{Th} + 0.09A_K \quad (1)$$

2.2. Determining the radon concentration in the air of a sealed container

AlphaGUARD Radon monitor PQ2000 was used for measuring. The method is based on direct measurement of the volumetric activity of radon in the air of a sealed container under the modes of passive sampling of the air and pumping it through an ionization chamber.

The emanation of radon from concrete into the air of a sealed container was analysed on the samples of various sorption moisture. The test samples were placed into a sealed container of 0.05 m³, where a switched-on radon monitor was installed (Fig. 1).

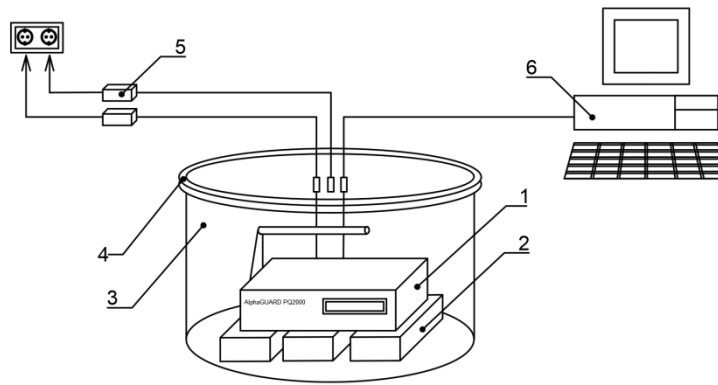


Figure 1. General Installation Diagram:
1 – AlphaGUARD radon monitor with a power supply;
2 – test samples; 3 – sealed steel emanation container; 4 – steel locking ring; 5 – fan power unit;
6 – personal computer.

The volumetric activity measurements were recorded automatically for at least 15 days with a 1-hour interval. The radiometer simultaneously recorded radon concentration, temperature, relative humidity, and barometric pressure in the chamber air. The information on radon concentration in the container was recorded using a PC and AlphaEXPERT software.

The change in the concentration of radon in the air of the sealed container can be described as [9]:

$$\frac{dC}{dt} = \frac{G}{V} - \lambda \cdot C \quad (2)$$

where G is an emanation rate of radon from a sample, Bq/sec; V is a container volume, m^3 ; C is a concentration of radon, Bq/m^3 ; λ is a radon disintegration constant, 0.00755 h^{-1} ; t is exposure time, hrs.

The solution of the equation (2) is:

$$C(t) = \frac{G}{\lambda \cdot V} \cdot (1 - e^{-\lambda \cdot t}) + C_0 \cdot e^{-\lambda \cdot t} \quad (3)$$

where C_0 is an initial concentration of radon, Bq/sec.

Formula 3 can be given as:

$$C(t) = C_{\max} \cdot (1 - e^{-\lambda \cdot t}) + C_0 \cdot e^{-\lambda \cdot t} \quad (4)$$

where C_{\max} is a maximum concentration of radon in the air of the container, Bq/m^3 .

The emanation coefficient during the experiment was determined as:

$$E(t) = \frac{C(t) \cdot V}{(1 - e^{-\lambda \cdot t}) \cdot M \cdot A_{Ra}} \quad (5)$$

where $C(t)$ is a current concentration of radon, Bq/m^3 ; V is free volume inside of the container, m^3 ; t is exposure time, hrs; M is a sample mass, kg; A_{Ra} is a radium specific activity, Bq/kg .

The emanation was calculated by the formula in [21]:

$$E = \frac{C_{Rn} \cdot V}{A_{Ra} \cdot M} \quad (6)$$

where C_{Rn} is an equilibrium concentration of radon, Bq/m^3 , in the sealed container.

At the end of the experiment, the sorption moisture of the samples was determined as:

$$W_s = \frac{m_s - m_d}{m_d} \quad (7)$$

In this formula, m_d and m_s are masses of the samples in dry and in equilibrium states with maximum air humidity achieved during the experiment. We determined open porosity + by sequential moistening, immersing the sample in water, first at 1/3, then at 2/3 of its height. At the last third stage, the water level exceeded the top surface of the samples by 50 mm. The duration of the last stage was determined by the time at which the results of two consecutive weightings differed by no more than 0.1 %.

The value of total water saturation was calculated as:

$$W_f = \frac{m_f - m_d}{m_d} \quad (8)$$

The degree of filling of open pores with water was determined by:

$$\eta = \frac{W_s}{W_f} = \frac{m_s - m_d}{m_f - m_d} \quad (9)$$

In these formulae, m_f is a mass of the samples in a water-saturated state, kg.

3. Results and Discussion

Following the results of gamma-ray spectrometry (Table 1), we obtained the average specific activities of radionuclides of radium, thorium and potassium, and calculated the specific effective activity using formula (1).

Table 1. The results of gamma-ray spectrometry.

^{226}Ra , Bq/kg	^{232}Th , Bq/kg	^{40}K , Bq/kg	A_{eff} , Bq/kg
19.1±0.92	20.8±0.03	338±15.5	76.6±1.67

The rated value of the specific effective activity did not exceed the maximum permissible value for the materials used in construction and restoration of residential and public buildings set at the level of 370 Bq/kg [20].

Fig. 2 shows a representative curve of growth of the radon concentration in the air of the sealed container. As it can be seen in the flowchart below, after 150–200 hours from the beginning of the experiment, the air relative humidity (RH) in the container becomes constant, which indicates a frozen equilibrium between the sorption moisture content of the samples and the air relative humidity.

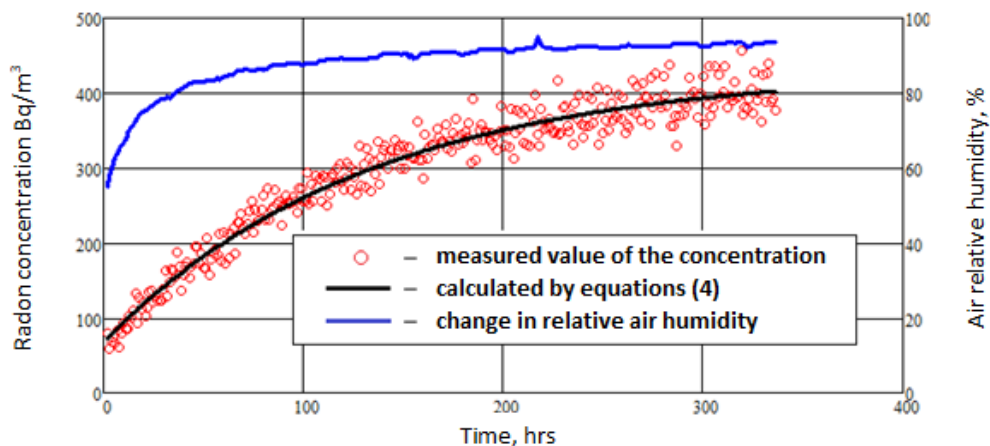


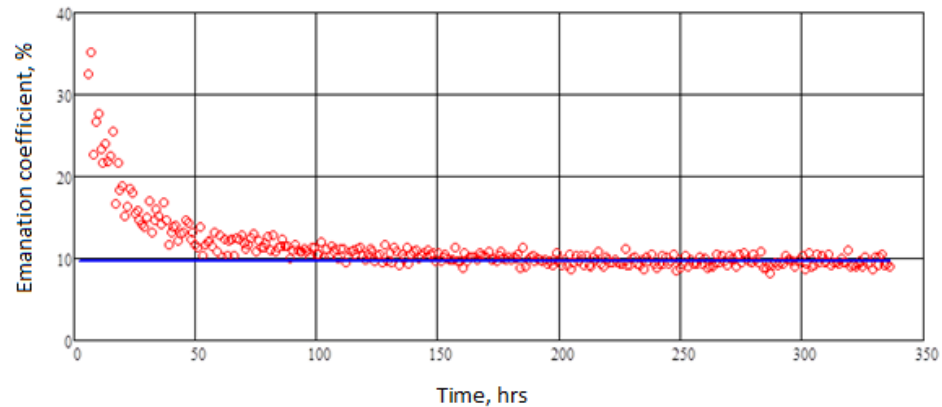
Figure 2. Accumulation of radon and change in air relative humidity in the sealed container.

The statistical analysis of the parameters which was obtained by the least square method is given in Table 2.

Table 2. Analysis of parameters C_{max} and C_0 .

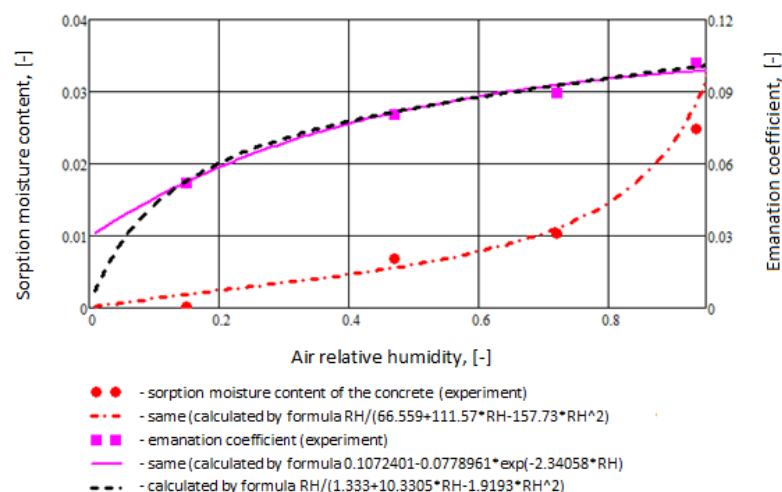
Analysis parameter		Standard error, %	Ranges of limits values at 95% probability	
Symbol	Value, Bq/m ³		Lower, Bq/m ³	Upper, Bq/m ³
C_{max}	432	1.82	428	435
C_0	67.9	2.84	62.3	73.5

Fig. 3 shows the result of calculating the emanation coefficient by equation (5) during 330-hour exposure. It is clearly seen that after 200–250 hours the ratio calculated by equation (5) becomes constant, i.e. we observe equilibrium between the activity of radon in the air of the sealed container and the activity of radon in the samples being studied.

**Figure 3. The analysis of emanating ability using equation (5).**

The value of the emanation coefficient was respectively obtained for a series of experiments with different moisture contents of the test sample.

Fig. 4 presents the approximating curves and their analytical expressions, obtained and discussed below, as the best. The data clearly indicate that with an increase in the relative humidity of the air, the emanation coefficient increases by almost 2 times, however, in contrast to the value of sorption moisture content, which increases with the increasing RH , the rate of emanation increase declines.

**Figure 4. Change in the emanation coefficient of heavy concrete and its sorption moisture content in the stage of desorption depending on air relative humidity.**

An analysis of the curves allows concluding that there is a close correlation between the processes of sorption-desorption of water vapor by the studied samples of semi-dry pressed heavy concrete and the emanation coefficient.

There are many semi-empirical models for calculating the equilibrium sorption moisture content of inorganic, organic, and biological materials depending on the air relative humidity and ambient temperature,

for example, 15 models were analyzed in [22], the authors of [23] performed analysis for 24 models describing the sorption process for ceramic and silicate brick, autoclaved aerated concrete, cement-lime mortar, ordinary cement mortar and mortar modified with polypropylene fibres, to define the sorption model that most accurately describes the isotherms. The results of a similar work for wood for 27 mathematical models are given in [24].

For practical purposes, any dependencies that best and most reliably describe experimentally observed values for a particular material are used for engineering analysis, and at the same time, based on the obtained graphic dependence, one of the six types of sorption isotherms accepted by the International Union of Pure and Applied Chemistry (IUPAC) is taken as the basis [25], paying attention to the behaviour of the curves in the entire range of humidity and, especially, under the humidity being close to maximum.

The change in emanation coefficient (E) and sorption moisture (W_s) depending on the relative humidity of the ambient air (RH) can be described with an appropriate degree of accuracy by formulae (11), (12) and (13).

The Hailwood – Horrobin (HH) model or the Dent model is most consistent with the experimental data on determining the processes of sorption–desorption of water vapour by wood-based materials [24].

$$W_s = \frac{RH}{A + B \cdot RH - C \cdot RH^2} \quad (11)$$

The team at the Technical University of Denmark has compiled a catalogue of sorption isotherms for more than a hundred materials used in construction [26], however, only one mathematical model was used to describe sorption and desorption.

$$W_s = A \cdot \exp\left(\left(-\frac{1}{B}\right) \cdot \ln\left(1 - \frac{\ln(RH)}{C}\right)\right) \quad (12)$$

Here in this formula: A is a maximum hygroscopic content; RH is relative humidity; B and C are empirical coefficients.

A promising model for cement concretes and mortars is the model in [23, 27, 28]:

$$W_s = \frac{A \cdot RH}{(1 + B \cdot RH) \cdot (1 - C \cdot RH)} \quad (13)$$

Table 3 presents the results of the analysis using expressions (11–13).

Table 3. The values of the coefficients in the equations (11), (12), (13) and the correlation of the rated and experimental values (R^2).

Parameters	A	B	C	R^2	Formula
Sorption moisture, W_s	66.559	111.57	-157.73	0.9823	(11)
Same	0.047	0.961	0.107	0.9780	(12)
Same	1.5	2.592	0.915	0.9823	(13)
Emanation coefficient, E	1.333	10.331	-1.919	0.9881	(11)
Same	0.1033	0.077	36.83	0.9777	(12)
Same	0.75	7.93	0.182	0.9881	(13)

As can be seen from the table, equations (11), (12) and (13) describe the process of sorption of concrete and changes in emanating within the range of RH from 0.18 to 0.935 with a high degree of pair correlation (R^2) which may indicate an interconnection of these processes. However, all of them are compromised by the calculated value of $E = 0$ at $RH = 0$. A model free of this remark can be the one which takes into account the emanation coefficient values of dry materials.

The following expressions are proposed to describe the functional dependence of emanation coefficient on the relative humidity of the ambient air and the moisture content of the studied samples:

$$E = E_d + (E_{ms} - E_d) \cdot (1 - \exp(-k \cdot v)) \quad (14)$$

Or

$$E = E_{ms} - (E_{ms} - E_d) \cdot \exp(-k \cdot \nu) \quad (15)$$

where E_d and E_{ms} are the emanation coefficient of the samples correspondingly in a dry state and in a maximum saturated-by-sorption state at $RH \rightarrow 100\%$ ($RH = 93.5\%$ in the experiment); k is empirical constant; ν is a parameter numerically equal to the characteristic of the ambient humidity or the moisture equilibrium state of the material, for example, relative humidity RH , moisture content (by weight or volume) or degree of filling of pores with adsorbed water η .

When we substituted the values of relative humidity into formulae (14) and (15), coefficient of determination $R^2 = 0.9796$ turned out to be somewhat lower than for (11), (12) and (13). At the relative humidity $RH = 0$, however, $E \neq 0$.

An imperial formula for calculating an emanation coefficient for soils was proposed by [29]:

$$E = E_0 \cdot \left[1 + k_1 \cdot (1 - \exp(-k_2 \cdot s)) \right] \quad (16)$$

where: E_0 is emanation coefficient in the dry state; s is soil moisture, k_1 and k_2 are empirical coefficients.

For clay, silt and sand, the values of k_1 and k_2 vary within a fairly narrow range – respectively from 1.53 to 1.85 and from 18.8 to 21.8. In a more recent work [21], formula (16) was used to calculate radon flux density from soil at $k_1 = 1.85$ and $k_2 = 18.8$.

Within a complex process of emanating, caused, on the one hand, by an inhibiting ability of the adsorbed water layer on the emanating surface, and on the other hand, facilitating the movement of radon atoms due to levelling the uneven inner surface of pores and capillaries, it seems relevant to determine the dependence of emanation on the degree of filling the pores with water $E(\eta)$. The results of experimental data and calculations are given in Fig. 5.

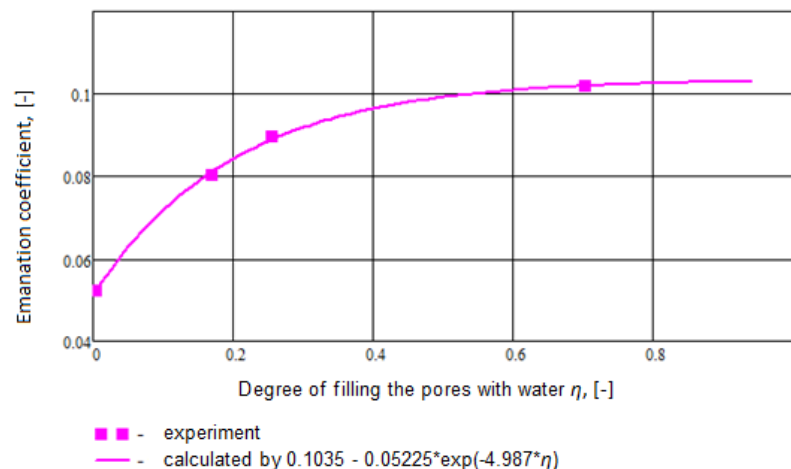


Figure 5. Effect of the degree of pores filling with water on the value of the emanation coefficient.

As we can see, a functional dependence of the change in the emanation of semi-dry pressed concrete and the degree of filling of open pores with water $E(\eta)$ can be represented by expressions similar to (14) and (15), but much more accurately, with $R^2 = 0.9992$.

A statistical analysis of the values of the coefficients calculated by the least square method is given in Table 4.

Table 4. The values of the coefficients in equations (14) and (15).

Indicators	Value
Dry emanation E_d	0.051±0.001
$E_{ms} - E_d$	0.052±0.002
Empirical coefficient k	4.99±0.34
Emanating at maximum sorption moistening E_{ms}	0.1035±0.0013

As can be seen from Table 4, the change in the emanation of semi-dry pressed heavy concrete is characterized by a coefficient value $k = 4.99$. The approximation of the experimental data by formulas (14) and (15) allows predicting the values of E_{ms} almost in the entire range of change in the relative humidity of the air where building structures enveloping rooms are used.

4. Conclusion

In contrast to the majority of previously published studies, where the analysis of the emanation process was performed on samples of rocks or soils, this work provides the results of the analysis of emanation of artificial building material.

1. We found a close correlation of the emanation coefficient of semi-dry pressed heavy concrete, the humidity of the ambient air, and the equilibrium sorption moisture of the material itself in the stage of desorption.

2. Empirical calculation formulas have been proposed for determining emanation coefficient depending on the air relative humidity and the moisture content of heavy concrete. The densest correlation is observed when determining the design parameter depending on the degree of filling of open pores, the value of which is estimated by the method of sequential immersion of the samples.

3. With an increase in the degree of filling of open pores with water from 0 to 70 %, the emanation coefficient increases by almost 2 times in the exponential dependence. In the range of relative humidity typical for residential and public buildings (20 ... 60 %), we observed almost 50 % increase of the emanation coefficient, which necessitates the numerical control of this parameter in order to accurately assess the dose load on the population.

Measurement of emanation coefficient of materials included in enveloping structures and interior finishings should be standardized taking into account moisture and age of samples.

References

- Gonzalez, A., Andere, J. Natural and artificial sources of radiation: nuclear energy in the future. IAEA Bulletin. 1989. Pp. 21–31. URL: https://www.iaea.org/sites/default/files/31205642131_ru.pdf
- Krisuk, E.M. Radiatsionnyi fon pomeshchenii. Energoatomizdat, 1989.
- Nazirov, R.A. Razvitiye nauchnykh osnov i metodov polucheniya stroitelnykh materialov s zadannymi radiatsionno-ekologicheskimi svoystvami [Development of scientific grounds and methods for producing building materials material with targeted radiation-ecological propert 2003.
- Van der Lugt, G., Scholten, L.C. Radon emanation from concrete and the influence of using flyash in ce-ment. Science of the Total Environment, The. 1985. DOI:10.1016/0048-9697(85)90214-1
- Temuujin, J., Surenjav, E., Ruescher, C.H., Vahlbruch, J. Processing and uses of fly ash addressing radio-activity (critical review) 2019.
- Kovler, K., Perevalov, A., Steiner, V., Metzger, L.A. Radon exhalation of cementitious materials made with coal fly ash: Part 1 – Scientific background and testing of the cement and fly ash emanation. Journal of Environmental Radioactivity. 2005. DOI: 10.1016/j.jenvrad.2005.02.004
- Ramenskaya, G.A., Shura, L.P. Ramenskaya G.A., Shura L.P. Metody i rezultaty opredeleniya koeffitsiyenta emanirovaniya radona v laboratornykh usloviyakh [Methods and results of determining the rate of radon emanation in laboratory conditions]. XV Mezhdunarodnaya nauchno-prakticheskaya konferentsiya «Sovremennyye tekhnika i tekhnologii» / Sbornik trudov v 3 tomakh. 2009. 3. Pp. 97–99. URL: <http://www.lib.tpu.ru/fulltext/c/2009/C01/V3/025.pdf>
- Miklyaev, P.S., Petrova, T.B. Vliyaniye vlazhnosti na emanirovaniye peschano-glinistykh porod [The effect of humidity on the emanation of sandy and clay rock]. ANRI. 2009. 1. Pp. 53–57. URL: https://www.elibrary.ru/download/elibrary_12226393_71937844.pdf
- Koeffitsiyenty emanirovaniya Rn-222 iz stroitel'nogo syriya i materialov. Metodika vypolneniya izmereniy s primeneniym Radiometra ob'yemnoy aktivnosti radona-222 "AlphaGUARD" Mod.PQ2000 [Emanation rates of Rn-222 from construction raw materials and building raw materials.Measurement procedure using the Radon-222 Volumetric Activity Radiometer AlphaGUARD Mod.PQ2000]. PT Positron Technology GmbH. 1996.
- Kurguz, S.A., Tarasov, I.V. Vliyaniye vodopogloshcheniya gornoy porody na emaniruyushchuyu sposobnost [Effect of water absorption by rock on emanating ability]. Radioekologiya XXI veka [Radioecology of the 21 century]. 2012. Pp. 150–156. URL: <http://elib.sfu-kras.ru/bitstream/handle/2311/8957/KurguzSA..TarasovIV.pdf?sequence=2>
- Gulabyants, L.A., Zabolotsky, B.Y. Plotnost potoka radona kak kriteriy otsenki radonopasnosti [Radon flux density as a criterion for assessing radon hazard]. ANRI. 2004. 3. Pp. 16–20. URL: https://www.elibrary.ru/download/elibrary_9427515_23460671.pdf
- Shashkin, V.L., Prutkina, M.I. Emanirovaniye radioaktivnykh rud i mineralov [The emanation of radioactive ores and minerals]. Atomizdat. Moscow, 1979.
- Huang, C. hua, Li, S., Ye, Y. jun, Ding, D. xin, Wu, W. hao. Variation rules of the radon emanation coeffi-cient in dump-leached uranium tailing sand. Journal of Radioanalytical and Nuclear Chemistry. 2019. DOI: 10.1007/s10967-018-06408-2
- Sun, H., Furbish, D.J. Moisture content effect on radon emanation in porous media. Journal of Contami-nant Hydrology. 1995. DOI: 10.1016/0169-7722(95)00002-D
- Cosma, C., Dancea, F., Jurcut, T., Ristoiu, D. Determination of 222Rn emanation fraction and diffusion coefficient in concrete using accumulation chambers and the influence of humidity and radium distribution. Applied Radiation and Isotopes. 2001. DOI: 10.1016/S0969-8043(00)00286-4

16. Hassan, N.M., Ishikawa, T., Hosoda, M., Iwaoka, K., Sorimachi, A., Sahoo, S.K., Janik, M., Kranrod, C., Yonehara, H., Fukushi, M., Tokonami, S. The effect of water content on the radon emanation coefficient for some building materials used in Japan. Radiation Measurements. 2011. DOI: 10.1016/j.radmeas.2010.11.006
17. Lukuttsova, N.P., Kozlov, O.Y., Krupnyy, G.I., Rastsvetalov, Y.N., Yanovich, A. On the Emanation Coefficient of Construction Materials. IHEP Preprint. Protvino, 2000.
18. Roelofs, L.M., Schöllen, L.C. The effect of aging, humidity, and fly-ash additive on the radon exhalation from concrete. Health Physics. 1994. DOI: 10.1097/00004032-199409000-00007
19. Metodika izmereniya aktivnosti radionuklidov s ispol'zovaniyem stintillyatsionnogo gammadetektora s programmym obespecheniyem "Progress" [The method for measuring the activity of radionuclides using a scintillational gamma-spectrometer with Progress software]. Mendeleev, All-Russian Scientific Research Institute for Physical-Engineering and Radiotechnical Metrology. 2005.
20. Sanitary Rules and Regulations 2.6.1.-2523-09. "Radiation Safety Standards NRB-99/2009". Moscow. Centre for Sanitary and Epidemiological Regulation, Hygienic Certification and Expert Evaluation, the Ministry of Health Care of Russia. 2009.
21. Ishimori, Y., Lange, K., Martin, P., Mayya, Y.S., Phaneuf, M. Measurement and Calculation of Radon Re-leases from NORM Residues 2013.
22. Andrade P, R.D., Lemus-mondaca, R., Pérez C., C.E. Models of sorption isotherms for food: uses and limitations. VITAE. 2011.
23. Stolarska, A., Garbalińska, H. Assessment of suitability of some chosen functions for describing of sorption isotherms in building materials. Heat and Mass Transfer/Waerme- und Stoffuebertragung. 2017. DOI: 10.1007/s00231-016-1926-y
24. Nazirov, R.A., Verkhovets, S. V., Inzhutov, I.S., Bazhenov, R. V., Tarasov, I. V. Moisture sorption models for wood. Magazine of Civil Engineering. 2016. DOI: 10.5862/MCE.68.3
25. Sing, K.S.W., Everett, D.H., Haul, R.A.W., Moscou, L., Pierotti, L.A., Rouquerol, J., Siemieniewska, T. International union of pure and applied chemistry physical chemistry division reporting physisorption data for gas/soils systems with special reference to the determination of surface area and porosity. Pure Appl. Chemistry. 1985. DOI: 10.1351/pac198557040603
26. Hansen, K.K. Sorption isotherms: a catalogue. Technical University of Denmark (DTU), 1986.
27. Chen, Y., Chen, Z. Transfer function method to calculate moisture absorption and desorption in buildings. Building and Environment. 1998. DOI: 10.1016/S0360-1323(97)00057-7
28. Agata, S., Jarosław, S. Mathematical description of sorption isotherms of autoclaved aerated concrete. Energy Procedia. 2015. DOI: 10.1016/j.egypro.2015.11.167
29. Zhuo, W., Iida, T., Furukawa, M. Modeling radon flux density from the earth's surface. Journal of Nuclear Science and Technology. 2006. DOI: 10.1080/18811248.2006.9711127

Contacts:

Rashit Nazirov, nazirovra@gmail.com

Ivan Inzhutov, ivaninzhutov@gmail.com

Olga Dubrovskaya, olgadubrovskaya2016@gmail.com

Evgeniya Gunenko, jane-gunenko@mail.ru

Petr Vede, vede@live.ru

© Nazirov, R.A., Inzhutov, I.S., Dubrovskaya, O.G., Gunenko, E.D., Vede, P.Y., 2020



DOI: 10.18720/MCE.100.8

Impact of loading rate on asphalt concrete deformation and failure

A. Iskakbayev^a, B.B. Teltayev^b, C.O. Rossi^c, G. Yensebayeva^a, B. Abu^b, K. Kutimov^a

^a Al-Farabi Kazakh National University, Almaty, Republic of Kazakhstan

^b Kazakhstan Highway Research Institute, Almaty, Republic of Kazakhstan

^c University of Calabria, Arcabacata di Rende (CS), Italy

E-mail: iskakbayeva@inbox.ru

Keywords: asphalt concrete, direct tension, loading rate, strain, stress, failure time, specific work of deformation

Abstract. The results for experimental determination of characteristics have been given and analyzed in this article for deformation and failure of an asphalt concrete at eleven loading rates from 0.000563 MPa/s to 0.652 MPa/s differing in 1158 times. A hot fine-grained dense asphalt concrete of type B prepared with a viscous bitumen of grade BND 100/130 which is traditionally used in road construction has been selected for the research. The tests have been performed at the temperature of 22–24 °C in a specially invented and assembled device according to the scheme of direct tension. The asphalt concrete samples had a shape of rectangular beam with dimensions 5×5×15 cm. It is found that from the moment of loading to the moment of failure the asphalt concrete is deformed nonlinearly. The rate of nonlinearity is increased with the load increase. Loading rate effects greatly the characteristics of deformation and failure of the asphalt concrete: failure time, specific work of deformation and failure deformation are decreased in 242, 160 and 3 times respectively at the loading rate increase in 1158 (nearly 1200) times from 0.000563 MPa/s to 0.652 MPa/s and the strength is increased in 5 times. Dependences for characteristics of the asphalt concrete failure (failure time, failure deformation, specific work of deformation and strength) on a loading rate are described with a high accuracy by power functions.

1. Introduction

It is known that deformation and strength characteristics of many road materials and soils depend considerably on value and load duration [1–6]. The vehicles of different axle load (up to 13 tons and more) move along modern highways and their speed is varied within a wide range depending on specific road conditions [7–9]: the speed is equal to 0 at stops, at crossings, in front of auto barrier, etc., it can reach 200–220 kph and more at midblocks.

The above provisions show the importance for the study of loading rate impact on deformation and strength properties of road materials including asphalt concretes and soils.

Literature review [1–6, 10–17] shows that such situation emerged in road material science: practically all types of tests for the asphalt concretes are performed at the target strain rates. For example, the compression tests for the cylindrical asphalt concrete samples are performed at the strain rate of 3 mm/min [15]. The strength of the asphalt concretes at uniaxial tension is determined at the strain rate of 2 mm/min. The fatigue characteristics of the asphalt concretes are performed at harmonic bending deflection variation (deformation amplitude remains constant till failure) [17]. Meanwhile, the above standard strain rates (2 and 3 mm/min) are incomparably higher than in real conditions.

In this work the samples of a conventional hot fine-grained dense asphalt concrete have been tested under the scheme of direct tension to failure at the temperature of 22–24 °C in conditions of loading with a constant rate. The loading rate was varied from 0.000563 MPa/s to 0.652 MPa/s, i.e. in 1158 (nearly 1200) times. Correlation relationships have been established for failure time, failure strain, strength and specific work of failure of the asphalt concrete on the loading rate. “Stress-strain” dependence (deformation diagram) has been constructed and analyzed for the asphalt concrete at different loading rates.

Iskakbayev, A., Teltayev, B.B., Rossi, C.O., Yensebayeva, G., Abu, B., Kutimov, K.S. Impact of loading rate on asphalt concrete deformation and failure. Magazine of Civil Engineering. 2020. 100(8). Article No. 10008.

DOI: 10.18720/MCE.100.8



This work is licensed under a CC BY-NC 4.0

2. Materials and Methods

In this paper a bitumen of grade 100-130 has been used meeting the requirements of the Kazakhstan standard ST RK 1373-2013 [18]. The bitumen grade on Superpave is PG 64-40 [19]. The bitumen has been produced by the Pavlodar processing plant from a crude oil of Western Siberia (Russia) by the direct oxidation method.

A hot dense asphalt concrete of type B meeting the requirements of the Kazakhstan standard ST RK 1225-2013 [15] was prepared using aggregate fractions of 5–10 mm (20 %), 10–15 mm (13 %), 15–20 mm (10 %) from Novo-Alekseevsk rock pit (Almaty region), sand of fraction 0–5 mm (50 %) from the plant “Asphaltconcrete-1” (Almaty city) and activated mineral powder (7%) from Kordai rock pit (Zhambyl region). Granularmetric curve of the asphalt concrete is shown in Figure 1.

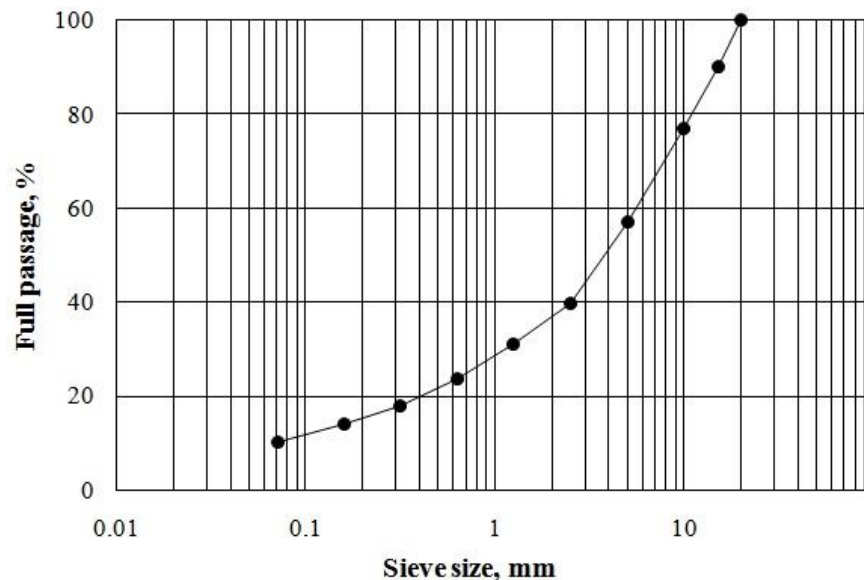


Figure 1. Granularmetric curve of the asphalt concrete.

The bitumen content of grade 100-130 in the asphalt concrete is 4.8 % by weight of the dry mineral material.

Samples of the hot asphalt concrete (Figure 2) were prepared in form of a rectangular prism with length of 150 mm, width of 50 mm and height of 50 mm in two step procedures. The first step, the asphalt concrete samples were prepared in form of a square slab (Figure 3) by means of the Cooper compactor (UK, model CRT-RC2S) (Figure 4) according to the standard EN 12697-33 [20]. The second step, the samples were cut from the asphalt concrete slabs in form of a prism. Deviations in sizes of the samples did not exceed 2 mm.

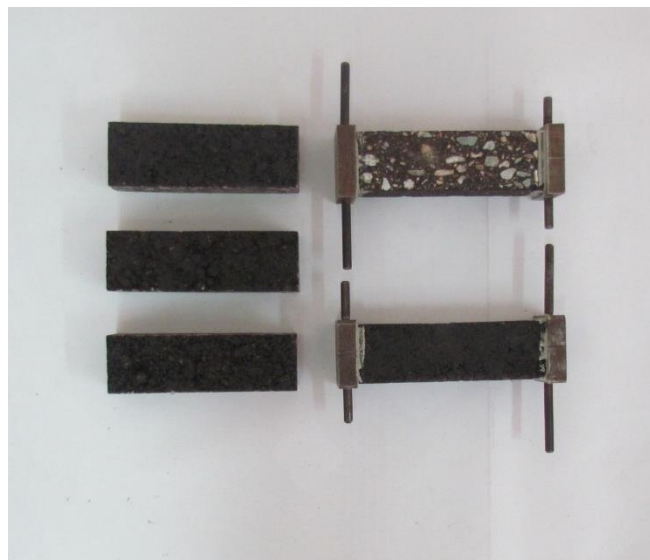


Figure 2. The asphalt concrete samples in the shape of rectangular prism (150×50×50 mm).



Figure 3. The asphalt concrete sample in the shape of square slab (300×300×100mm).



Figure 4. The Cooper compactor.

A detailed information about standard characteristics of the bitumen and the asphalt concrete and about the asphalt concrete samples one can find in the authors' works [21–23] published earlier.

The tests have been performed at the temperature of 22–24°C in a specially invented and assembled device [24, 25] (Figure 5) in Kazakhstan Highway Research Institute according to the scheme of direct tension. Loading rates were equal to (MPa/s): 1 – 0.000563; 2 – 0.001698; 3 – 0.005507; 4 – 0.007244; 5 – 0.015137; 6 – 0.023918; 7 – 0.048869; 8 – 0.058036; 9 – 0.205869; 10 – 0.467757; 11 – 0.651864. As it is seen a loading rate is varied within a wide range – 1158 (nearly 1200) times.



Figure 5. The device for determination of mechanical characteristics for materials.

3. Results and Discussions

According to the test results performed under the method described in Section 2 the graphs have been constructed for variation of stress, strain, specific work of deformation in time and the graphs of dependence “stress-strain” at the considered loading rates. By way of illustration the mentioned graphs for five loading rates are shown in Figures (6–9). As it is seen, the strain is varied to a significant degree nonlinearly (Figure 7) at linear variation of stress in time (Figure 6). Nonlinearity of the asphalt concrete strain is increased with the stress increase. It is seen in Figure 8 that it is difficult to distinguish some initial section within the limits of which it could be possible to adopt linear strain and to introduce an elasticity modulus.

As a consequence of nonlinear deformation, the specific work of deformation is also varied in time to a significant degree nonlinearly (Figure 9). Meanwhile, the biggest values of the specific strain energy occur at the moment of failure. We can also note that approximately during the first half of loading at all loading rates the specific strain energy has relatively small values; it has the biggest values in the last quarter of the loading process.

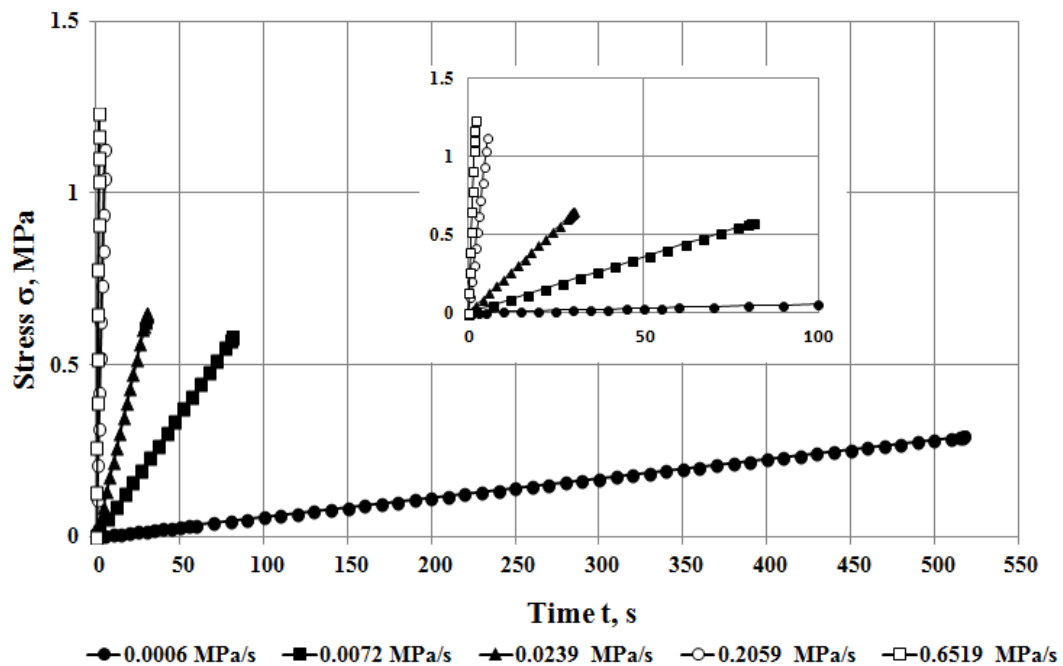


Figure 6. Graphs of stress variation in time at various loading rates.

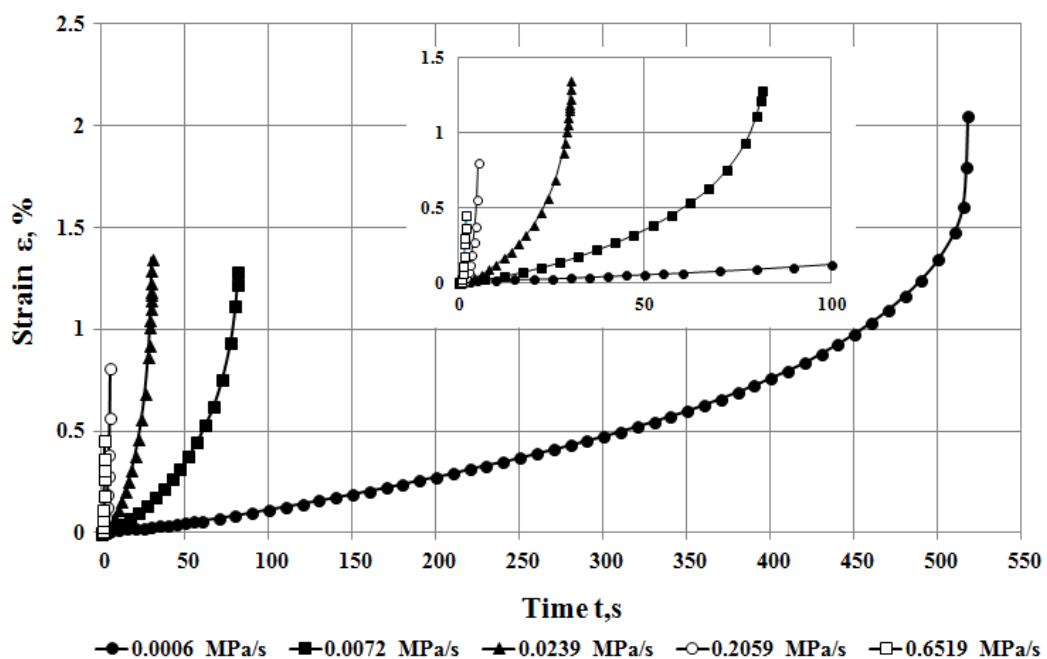


Figure 7. Graphs of strain variation in time at various loading rates.

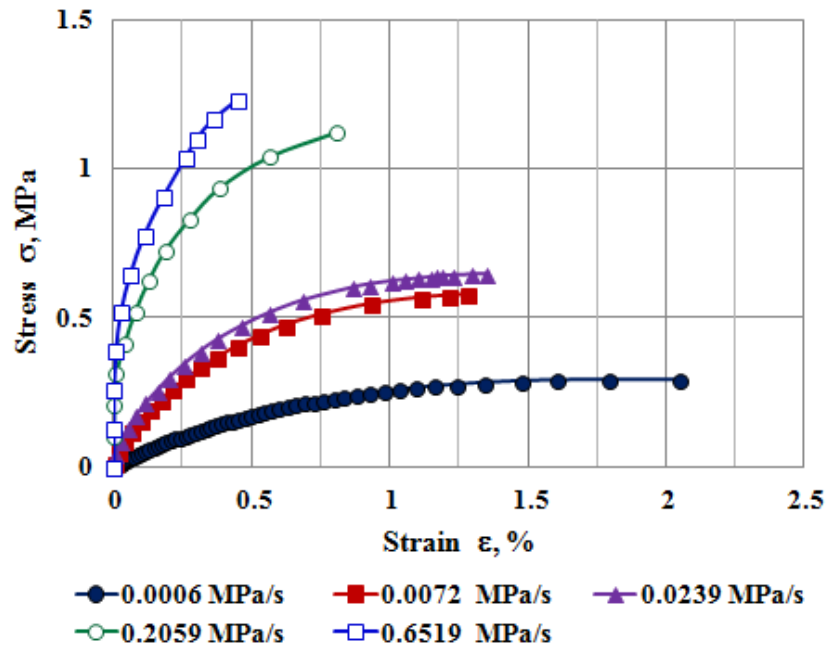


Figure 8. Graphs of “stress-strain” relationship at various loading rates.

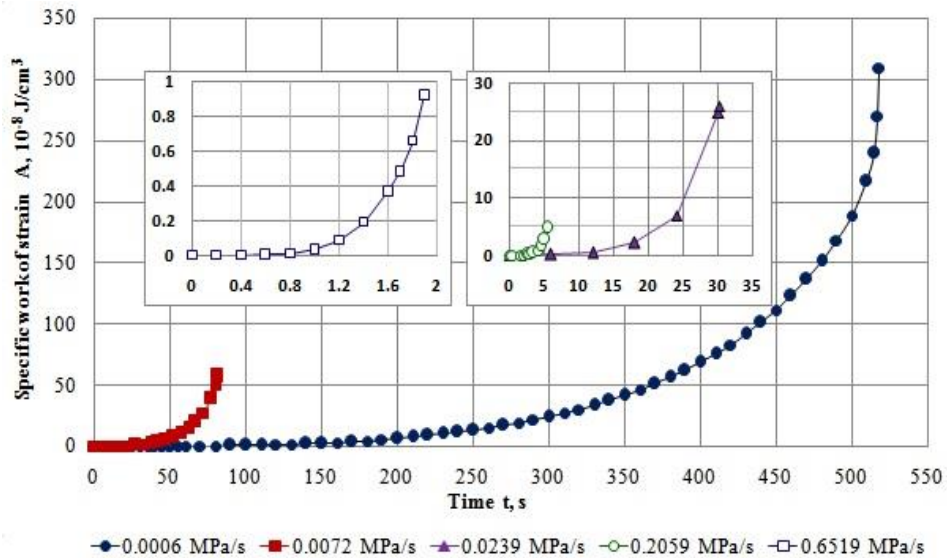


Figure 9. Graphs for variation of specific work of deformation at various loading rates.

Important characteristics of failure are time of failure, strain, stress (strength) and specific work of deformation of the material at the moment of its failure. Dependence of these characteristics for the asphalt concrete on loading rate is represented in Figures 10-13. As it is seen a loading rate impacts greatly on the characteristics of the asphalt concrete. For example, at the loading rate increase in 1158 (nearly 1200) times from 0.000563 MPa/s to 0.652 MPa/s failure time, specific work of deformation and failure strain are decreased in 242,160 and 3 times respectively, and the strength is increased in 5 times.

It is known that depending on specific and traffic conditions the vehicles move with different speeds along the highways (on various road sections). The results of experimental investigations performed in this work show that the characteristics of deformation and failure of an asphalt concrete depend greatly on the loading rate. The above regulations cause the idea that the highways should be divided into sections with the fixed estimated speeds for vehicles and the mechanical characteristics of asphalt concrete layers of a pavement should be defined considering these estimated speeds at designing of pavement structures.

Our previous works [21–23, 26] have determined experimentally that dependences of long-term strength (failure time) and steady-state strain of an asphalt concrete at creep on stress is approximated by a power function with a high accuracy. As it is seen from Figures 10–13 the characteristics of failure for the asphalt concrete are also described by power functions at loading with a constant rate. Meanwhile, as it is expected, failure time of an asphalt concrete is decreased with loading rate increase (with the working stress increase in time). Failure strain and specific work of the asphalt concrete failure are also decreased

with the loading rate increase. And the asphalt concrete strength, on the contrary, is increased with the loading rate increase. Failure time and specific work of deformation have been found to be the most sensitive to the loading rate among the considered characteristics of the asphalt concrete failure: these characteristics are varied for 0.77 and 0.70 orders respectively at a loading rate variation for one order. Failure strain has the least sensitivity to the loading rate: power coefficient is equal to $n = 0.14$. The strength of the asphalt concrete has the intermediate sensitivity: $n = 0.23$.

The essential influence of the strain rate on characteristics of deformation and failure of asphalt concretes is also determined in the works of other researchers [10–12, 27–30]. Fakhri M. et al. [27] have reported that a strain rate influences greatly on fracture energy of an asphalt concrete at intermediate temperatures (5 °C, 15 °C and 25 °C). Zolotaryov V.A. et al. [10] and Islam M.D.R. et al. [12] have determined that dependence of strength for the asphalt concretes at three-point and four-point bending, compression, tension and initial stiffness at three-point bending on strain rate is satisfactorily described by a power function.

Good correlation relationships have been found in the work [28] between tensile strength of the asphalt concretes and the deformation rate at the temperatures of 10 °C, 0 °C and -20 °C, and they represent the straight lines in the logarithmic coordinates; and the tensile strength of the asphalt concrete does not depend on the deformation rate at the temperature of -20 °C. Similar correlation relationships for a number of “neat” and modified asphalt concretes have been determined in the work [29] as well. The test temperatures are 5 °C, 15 °C, 25 °C and 35 °C, the deformation rate is 50 mm/min. Meanwhile, it is found that the strength of a “neat” asphalt concrete at the temperature of 25 °C is equal to 1.7 MPa; such strength according to our experimental data corresponds to a loading rate of 0.7 MPa/s. The paper [30] determines that the asphalt concretes strength at the deformation rates of 1 mm/min and 50 mm/min and at the temperature of 0 °C is equal to 0.9 MPa and 2.6 MPa respectively, i.e. deformation rate variation in 50 times provides the asphalt concrete strength variation approximately in 3 times.

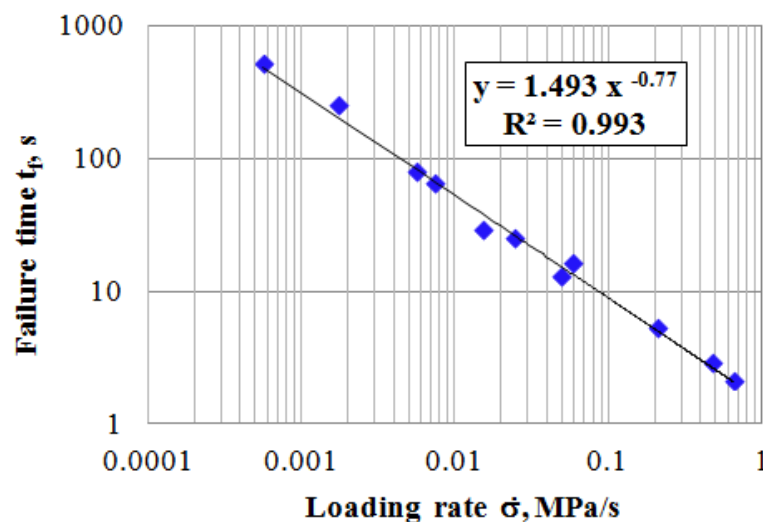


Figure 10. Dependence of failure time of the asphalt concrete on loading rate.

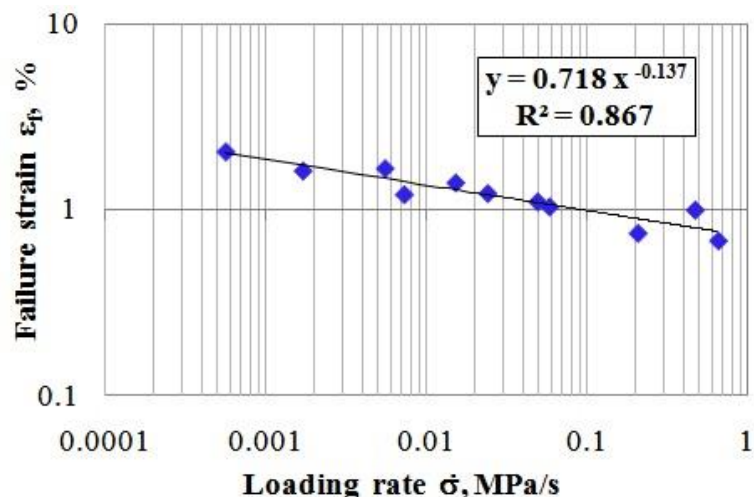


Figure 11. Dependence of strain failure of the asphalt concrete on loading rate.

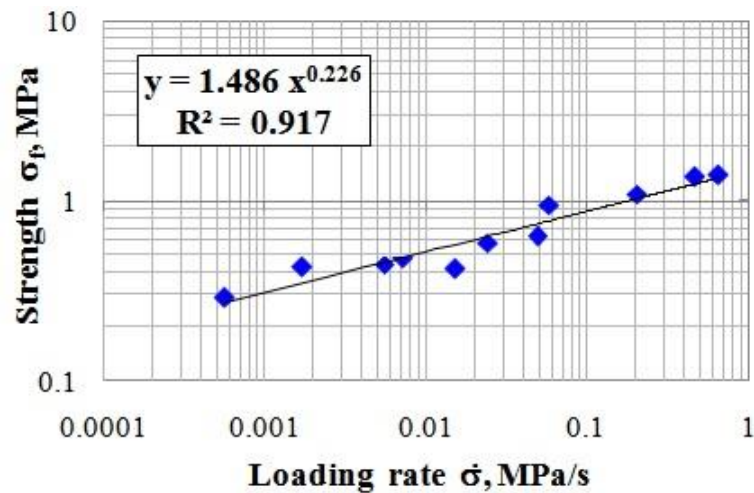


Figure 12. Dependence of the asphalt concrete strength on loading rate.

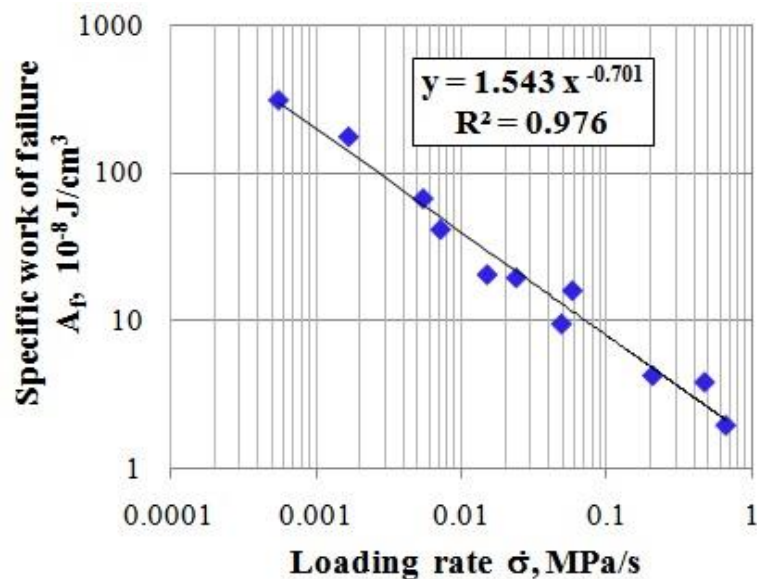


Figure 13. Dependence of specific work for the asphalt concrete failure on loading rate.

4. Conclusions

The results for experimental determining of characteristics of deformation and failure of the asphalt concrete at direct tension at the temperature of 22–24°C at the considered loading rates differing in 1158 times allowed drawing the following conclusions:

1. From the beginning of loading to the moment of failure the asphalt concrete is deformed nonlinearly. The rate of nonlinearity is increased with the load increase. It is difficult to distinguish some initial section on the graph “stress-strain”, within the limits of which it could be possible to postulate linear strain and introduce elasticity modulus.

2. The loading rate impacts greatly on the characteristics of deformation and failure of the asphalt concrete: failure time, specific work of deformation and failure strain are decreased in 242, 160 and 3 times respectively at the loading rate increase in 1158 (nearly 1200) times from 0.000563 MPa/s to 0.652 MPa/s, and the strength is increased in 5 times.

3. Dependences of characteristics for the asphalt concrete failure (failure time, failure strain, specific work of failure and strength) on a loading rate are described by power functions with a high accuracy.

4. On the designing stage highways should be divided into sections with the fixed estimated speeds of vehicles and mechanical characteristics of asphalt concrete layers should be defined considering these estimated speeds at designing of pavement structures.

References

1. Huang, Y.H. Pavement analysis and design. 2nd edition. Pearson Education, Inc., Upper Saddle River, New Jersey, 2004, 775 p.
2. Verruljt, A. Soils mechanics. Delft, Delft University of Technology, 2001, 340 p.
3. Smith, G.N., Smith, I.G.N. Element of Soil mechanics. 7th edition. Oxford, Blackwel Science, 1990, 509 p.
4. MS-2. Asphalt mix design methods. 7th edition. Lexington, Asphalt Institute, 2014, 199 p.
5. The asphalt handbook. 7th edition. Lexington, Asphalt Institute, 2008, 832 p.
6. Kim, R. (ed.) Modeling of asphalt concrete. McGraw-Hill Education, New York, 2008, 460 p.
7. Drew D.R. Traffic flow theory and control. McGraw-Hill, New York, 1968.
8. Gerlough, D.L., Huber, M.J. Traffic flow theory. TRB Special Report 165, Washington, D.C., 1975, 233 p.
9. Knoop, V.L. Introduction to traffic flow theory. 2nd edition. Delft University of Technology, Delft, 2018, 202 p.
10. Zolotaryov, V., Efreinov S., Khamad R.A. Influence of type and level of stress strain behavior on plasticity coefficient of an asphalt concrete. Bulletin of Donbas National Academy of Civil Engineering and Architecture. 2012. 1(93). Pp. 41-47.
11. Cai, W., McDowel, G.R., Airey, G.D. Discrete element modeling of uniaxial constant strain rate tests on asphalt mixtures. Granular Matter. 2013. 15. Pp. 163-174. doi: 10.1007/s10035-013-0396-x
12. Islam, M.D.R., Ahmad, M., Tarefder, R.A. Effect of loading rate on the properties of asphalt concrete using three-point bending test. Advanced Materials Research. 2015. Vol. 1096. Pp. 553-556. doi:10.4028/www.scientific.net/AMR.1096.553
13. Yoder, E.J., Witczak, M.W. Principles of pavement design. John Wiley & Sons, Inc. New Jersey. 1975, 736 p.
14. Papagiannakis, A., Masad, E. Pavement design and materials. John Wiley & Sons, Inc. New Jersey, 2008.
15. ST RK 1225-2019. Hot mix asphalt for roads and airfields. Technical specifications. Kazakhstan Highway Research Institute, Astana, 2019, 62 p.
16. EN 12697-46. (Draft). Bituminous mixtures. Test methods for hot mix asphalt. Part 46: Low temperature cracking and properties by uniaxial tension tests. European committee for standardization, Brussels, 2004, 25 p.
17. BS EN 12697-24. Bituminous mixtures. Test method for hot mix asphalt, Part 24: Resistance to fatigue. European committee for standardization, Brussels, 2018, 64 p.
18. ST RK 1373-2013, Bitumen and bituminous binders. Oil road viscous bitumens, Technical specifications. Kazakhstan Highway Research Institute, Astana, 2013, 46 p.
19. Superpave series No. 1. Performance graded asphalt binder specification and testing, Asphalt Institute, Lexington, 2003.
20. EN 12697-33. Bituminous Mixtures. Test Methods for Hot Mix Asphalt. Part 33: Specimen prepared by roller compactor. European Committee for Standardization, Brussels, 2003, 19 p.
21. Iskakbayev, A., Teltayev, B., Rossi, C. Oliviero. Steady-state creep of asphalt concrete. Applied Sciences, 2017, 7. Pp. 2-13. doi: 10.3390/app7020142
22. Teltayev, B.B., Iskakbayev, A., Rossi, C. Oliviero. Regularities of creep and long-term strength of hot asphalt concrete under tensile. Proceedings of the 4th Chinese-European Workshop on Functional Pavement Design, Cew 2016, Delft, The Netherlands, 2016. Pp.169-178. doi: 10.1201/9781315643274-20
23. Iskakbayev, A., Teltayev, B., Rossi, C. Oliviero. Deformation and strength of asphalt concrete under static and step loadings. Transport Infrastructure and Systems. Proceedings of the AIIT International Congress on Transport Infrastructure and Systems (TIS 2017), Rome, Italy, 10-12 April 2017. Pp. 3-8. doi: 10.1201/9781315281896-2
24. Teltayev, B.B., Iskakbayev, A.I., Andriadi, F.K. Patent of the Republic of Kazakhstan for invention 33244, Device for determining the mechanical characteristics of materials under tension, Astana, 2018.
25. Iskakbayev A., Teltayev B., Abu B., Estayev K. Long-term strength of asphalt concrete and its applications. Construction and Building Materials. 2020. 244. Pp. 1-11. <https://doi.org/10.1016/j.conbuildmat.2020.118325>
26. Iskakbayev, A., Teltayev, B., Andriadi, F., Estayev, K., Suppes, E., Iskakbayeva, A. Experimental research of creep, recovery and fracture processes of asphalt concrete under tension. Proceedings of the 24th International Congress of Theoretical and Applied Mechanics (XXIV ICTAM), Montreal, Canada, 2016. Pp. 1-2.
27. Fakhri, M., Kharrazi, E.H., Aliha, M.R.M., Berto, F. The effect of loading rate of fracture energy of asphalt mixture at intermediate temperatures and under different loading modes. Frattura ed Integrita Strutturale. 2018. 43. Pp. 113-132. doi: 10.3221/IGF-ESIS.43.09
28. Steiner, D., Hofko, B., Dimitrov, M., Blab R. Impact of loading rate and temperature on tensile strength of asphalt mixtures at low temperatures. 8th RILEM International Conference on Mechanisms of Cracking and Debonding in Pavements, RILEM Bookseries 13, Springer, 2016. Pp. 69-74.
29. Vasconcelos K.L., Bernucci L.B., Chaves J.M. Effect of temperature on the indirect tensile strength test of asphalt mixtures. 5th Eurasphalt and Eurobitume Congress, Istanbul, Turkey, 13-15th June 2012. Pp.1-9.
30. Si W., Li N., Ma B., Tian Y-x., Zhou X-y. Temperature Response to tensile characteristics of the hot asphalt mixtures. Journal of Civil Engineering. 2016. 20(4). Pp.1336-1346.

Contacts:

Alibai Iskakbayev, iskakbayeva@inbox.ru
Bagdat Teltayev, bagdatbt@yahoo.com
Cesare Rossi, cesare.oliviero@unical.it
Gulzat Yensebayeva, gulzat-y83@list.ru
Bekdaulet Abu, a.bekdaulet@gmail.com
Kiyas Kutimov, kiyas6@mail.ru



DOI: 10.18720/MCE.100.9

Hydration and structure formation of chloride-activated cement paste

T.S. Shepelenko^a, N.I. Vatin^b, O.A. Zubkova^a

^a Tomsk State University of Architecture and Building, Tomsk, Russia

^b Peter the Great St. Petersburg Polytechnic University, St. Petersburg, Russia

* E-mail: shepta72@mail.ru

Keywords: cements hydration, hydrated cement paste, structure formation, hydrochloric acid, binder additive, hydrates, silicates, silicate minerals, strength, acid corrosion, accelerating admixtures, accelerating effect, Kuzel's salt, Friedel's Salt.

Abstract. The result of the research is the formulation of chloride-activated high-strength cement paste with accelerated hardening, increased strength, and without heat treatment. The cement paste was activated by introducing a chloride-containing additive into the cement-water system. The additive was synthesized by keeping the cement in a 3 % hydrochloric acid solution, i.e. under conditions of acid corrosion of the binder. The additive is the solid part of the cement-HCl suspension, aged for 24 hours at a ratio of solid and liquid phases of 1:10. The optimized amount of additive is 5 % by weight of dry cement. The effect of the additive on the hardening kinetics, structure, and strength of the activated cement paste was studied. It was established that acid corrosion products of cement have structure-forming activity. A significant increase of the compressive strength of the activated cement paste relative to the control sample was found over the entire hardening interval (1–3–7–28 days). At the daily age of normal hardening, the strength of activated cement paste increased by 165 %. At 28 days of age, the strength increased by 42 %. The X-ray phase and infrared spectral analysis results suggest the following. The acceleration of setting and the increase in the strength of the cement composite is realized due to the intensification of hydration processes and the binding of portlandite, the early formation of structure-forming phases as ettringite and Kuzel salt $\text{Ca}_4\text{Al}_2(\text{OH})_{12}\text{Cl}(\text{SO}_4)_{0.5}\cdot 6\text{H}_2\text{O}$ (analog of Friedel's salt), as well as weakly crystallized calcium hydrosilicates with a tobermorite-like structure.

1. Introduction

Additives affecting the setting and hardening of concrete mixes are widely used [1–5]. Previously, the authors of this article synthesized cement additives in the form of suspensions. Suspensions were obtained as a result of hydration of the same cement in solutions that cause corrosion of cement under conditions of excess liquid phase [6–9]. In such suspensions, hydration of cement occurred simultaneously with its chemical corrosion. It was established that the products of clinker materials' hydration in suspensions, the liquid phase of which are corrosive to cement, have structure-forming properties.

The use of the solid part of suspensions as additives to cement provides an increase in the strength of cement paste. For the synthesis of additives, solutions of aluminum chloride or iron chloride were used. Upon hydrolysis of these salts, a decrease in the pH of the medium occurs. Therefore, hydration in such suspensions proceeded under conditions of acid corrosion of cement [9]. After the introduction of additives in the composition of the cement paste, the compressive strength increased. The increase was 23 % when using additives synthesized with iron chloride and by 30 % when using additives synthesized with aluminum chloride.

Further development of this approach may consist in increasing the aggressiveness of the liquid medium in cement suspensions, namely, during the hydration of cement in a solution of hydrochloric acid HCl. When mixing cement with an HCl solution, neutralization reactions proceed at a very high speed. The suspension is almost instantly saturated with calcium chloride. The presence of calcium chloride in the liquid phase of the suspension significantly affects the phase composition of hydrates formed during the synthesis of additives.

Shepelenko, T.S., Vatin, N.I., Zubkova, O.A. Hydration and structure formation of Chloride-Activated Cement Paste. Magazine of Civil Engineering. 2020. 100(8). Article No. 10009. DOI: 10.18720/MCE.100.9



This work is licensed under a CC BY-NC 4.0

Calcium chloride is the first documented additive for concrete and belongs to the class of hardening accelerators. An analytical review of the works devoted to the influence of CaCl_2 on the structure and properties of clinker minerals and cement, in general, was published by V.S. Ramachandran et al. [10]. The evolution of the use of calcium chloride since the issuance of a patent for the use of this additive in 1885 until today is widely known in interested scientific and industrial circles. The problem of the use of additives containing chloride ions was discussed, among other things, in [9]. It was noted that the indisputable advantages of such additives are high solubility in water, affordability, low cost, and reliable performance. Chloride additives can be used without restrictions in the production of cellular and lightweight concrete, concrete blocks, road construction elements, and the implementation of small architectural projects.

Chloride ions chemically bind to cement minerals when interacting with the hydroxyl groups of the AFm phases through ion exchange reactions [11–14]. As a result of this interaction, calcium hydrochloroaluminates $\text{CaOAl}_2\text{O}_3\text{CaCl}_2 \cdot 10\text{H}_2\text{O}$ and/or calcium hydrochloroferrites $\text{CaOFe}_2\text{O}_3\text{CaCl}_2 \cdot 10\text{H}_2\text{O}$ are formed [15–17]. The synthesis of hydrochloroaluminates in the presence of calcium chloride during hydration proceeds according to the scheme:



Calcium hydrochloroaluminates and calcium hydrochloroferrites were named Friedel's salts by the name of the scientist who first synthesized calcium hydrochloroaluminate in 1897. The possibility of the formation of analogues of Friedel salts containing not only chloride ions, but also carbonate ions ($\text{AFm}-(\text{CO}_3^{2-}, \text{Cl}^-)$) or sulfate ions ($\text{AFm}-(\text{SO}_4^{2-}, \text{Cl}^-)$) was proved in [18–20]. The crystal structure of the Kuzel's salt $\text{Ca}_4\text{Al}_2(\text{OH})_{12}\text{Cl}(\text{SO}_4)_{0.5} \cdot 6\text{H}_2\text{O}$ was determined by synchrotron powder diffraction [18]. Calcium hydrochlorosulfoaluminate belongs to the Layered Double Hydroxides family [15, 21, 22]. Layered Double Hydroxides is designated by the general formula $[\text{M}^{\text{II}}_{1-x}\text{M}^{\text{III}}_x(\text{OH})_2]^{x+}[\text{A}^{m-}]_{x/m} \cdot n\text{H}_2\text{O}$.

They represent a group of minerals, the structure of which consists of fixed positively charged brucite-like layers formed by ions of multivalent metals and hydroxide ions, the charge of which is balanced by mobile anions located in the interlayer spaces. The layers are formed as a result of the partial replacement of trivalent octahedrally coordinated metal cations with divalent cations. Intercalated molecular water provides the connection of the layers through hydrogen bonds.

In the fixed main layers of Kuzel's salt there are $[\text{Ca}_2\text{Al}(\text{OH})_6]^+$ cations of a fixed composition, between which in the interlayer spaces there are layers of $[\text{Cl}_{0.5}(\text{SO}_4)_{0.5} \cdot 2.5\text{H}_2\text{O}]^-$ anions that can move. In the unmovable basic layers of salts, cations of unchanged composition are fixed, between which moving layers of anions are in the interlayer spaces. Chloride and sulfate ions are arranged in two independent crystallographic regions and can be relatively easily replaced by other anions (for example, $(\text{CO}_3)^{2-}$ and others) without destroying the layered structure of Kuzel's salts.

Studies [13, 14, 23, 24] showed that chlorine ions in hydrated cement chemically bind to hydrated neoplasms of cement, changing their phase composition. Also, it is necessary to take into account the possibility of physical adsorption binding of chlorine ions. Sorption occurs due to the mutual attraction of the Cl^- anions and the hydrated surfaces of the binder minerals due to the van der Waals forces. The reason for this interaction is the dissociation of molecules of hydrated neoplasms of cement, as a result of which hydrates become carriers of surface charges. In [13], the results of a study of the mechanisms of charge formation in cement hydrates and their effect on the adsorption of chloride ions were published. For example, diagrams of the processes of Friedel's salt dissociation and adsorption of chloride ions by cations $[\text{Ca}_2\text{Al}(\text{OH})_6]^+$ are given:



It can be seen from these examples that during adsorption interaction with chlorine anions, the cation charge is compensated (neutralized). Adsorption is described by the Freundlich isotherm, and the results of the adsorption experiment are verified by measuring the ξ -potential [13].

In dissociation of the Kuzel salt, cations of the composition $[\text{Ca}_2\text{Al}(\text{OH})_6]^+$ are also formed. Therefore, the dissociated Kuzel's salt can adsorb chloride ions during the synthesis of the additive in a suspension of cement and HCl, balancing the positive charge.

Molecular dynamics computer simulations are performed to study the structure and dynamical behavior of chloride and associated cations at the interfaces between aqueous solutions and portlandite $\text{Ca}(\text{OH})_2$, Friedel salt $[\text{Ca}_2\text{Al}(\text{OH})_6]\text{Cl} \cdot 2\text{H}_2\text{O}$, tobermorite $\text{Ca}_5\text{Si}_6\text{O}_{16}(\text{OH})_2$, and ettringite $\text{Ca}_6[\text{Al}(\text{OH})_6]_2[\text{SO}_4]_3 \cdot 26\text{H}_2\text{O}$ [25]. The simulations take into account the flexibility of surface OH-groups and allow for energy and momentum transfer between the solid and solution to effectively simulate the sorption. Studies have shown that the ability to bind Cl^- anions on the surfaces of hydrated neoplasms of cement decreases in subsequence:

Friedel's salt > portlandite > ettringite > tobermorite.

In [13], data are also given on the ability of portlandite to participate in adsorption interactions with a chloride ion. The authors of [24] believe that under certain conditions there is a likelihood of interactions of this kind between ettringite and Cl^- . However, most scientists agree that the participation of these phases in the process of physical binding of chlorine ions is unlikely, very insignificant.

It is generally accepted [13, 26, 27] that among all hydration products present in ordinary Portland cement, only two are almost completely responsible for the ability to interact with chloride ions: CSH gel and AFm phases (for example, monosulfate hydrate). In this case, the CSH gel has a dominant value in the process of physical bonding of chlorine ions, due to the high value of the specific surface and the mass content of this phase in the composition of hydrated cement.

Despite a detailed analysis of the structure-forming effects of the cement hydration process, the available publications do not contain detailed information on cement hydration in solutions containing hydrochloric acid, as well as on the use of products of such hydration as an additive to cement.

The study is aimed at obtaining the formulation of chloride-activated cement paste with the increased strength and accelerated hardening, without heat treatment.

2. Methods

The additive and cement paste are made from Portland cement of class CEM II / A-Sh 32.5H manufactured by Topkinsky Cement LLC (Topki, Kemerovo Region, Russia). Cement met the requirements of the Russian State Standard GOST 31108-2003 "General structural. Portland clinker cements. Specifications". Table 1 shows the synthesis conditions of the additive and the control specimen.

Table 1. The synthesis conditions of the additive, control sample and activated cement paste.

The specimen	The composition of the additive	The ratio of the components of the additive	The composition of the cement paste
The additive, the modified cement paste	Cement and 3 % HCl solution	1:10	Cement, the additive 5 % by weight, water with a W / C ratio of 0.34
Reference specimen	Cement and water	1:10	Cement, water with a W / C ratio of 0.34

The synthesis of additives and chloride-activated cement paste was carried out as follows.

1. To prepare a 3 % HCl solution, hydrochloric acid was used according to the Russian State Standard GOST 3118 Reagents. Hydrochloric acid. Specifications ($\rho = 1.13 \text{ g/cm}^3$) and distilled water according to the Russian State Standard GOST 6709 Distilled water. Specifications.

2. Cement was kept in a 3 % HCl solution at a solid to liquid ratio of 1:10 for 24 hours after thoroughly mixing this suspension.

3. After 24 hours, the solid part of the suspension was separated from the liquid by filtration. To stop the hydration processes, the solid residue was treated with acetone and dried in a desiccator over calcium chloride CaCl_2 to constant weight.

4. The dry solid residue was crushed before passing through a 0.08 mm square opening sieve according to Russian State Standard GOST 6613-86 "Square meshed woven wire cloths. Specifications". The crushed residue was used as an additive in cement.

5. The additive was used in amounts of 2 %, 5 % and 10 % by weight of dry cement.

6. The prepared additive was mixed with cement and shut with water at a W/C ratio of 0.34. specimens in the form of cubes with a 2 cm edge were made of non-admixture cement paste and modified cement paste. specimen s solidified under normal conditions. After reaching the 28-day maturity of the specimens, their compressive strength was measured. The compressive strength of cement paste at the age of 1, 3, 7, and 28 days was determined based on six measurements for each age. The arithmetic average value of strength was calculated based on the 3 closest values. This provided an error of no more than 4.1 %.

7. The specimens destroyed during the test were crushed before passing through a 0.08 mm square opening sieve according to the Russian State Standard GOST 6613-86 "Square meshed woven wire cloths. Specifications" and were dried in a desiccator over calcium chloride CaCl_2 to constant weight.

The structure of the additive, control specimen, non-additive cement paste, and modified cement paste was studied by X-ray diffraction (XRD) and infrared spectroscopy. The X-ray diffraction meter Shimadzu

XRD-700 with a copper anode in range of 5–90 deg and the Fourier spectrometer "Varian Excalibur HE 3600" at the frequency range 400–4000 cm^{-1} was used.

3. Results and Discussion

3.1. The age-strength relation of cement paste at different percentages of additives

Table 2 shows the compressive strength of chloride-activated cement pastes depending on the amount of additive. It is seen that a stable result of an increase in strength during the entire hardening period is provided by an additive introduced in an amount of 5 % by weight. Therefore, an additive in the amount of 5 wt.% Was used to activate the cement paste. After hardening within 24 hours, the strength of such a cement paste increased by 165 % compared with non-additive samples; at the age of 28 days, the increase in strength was 42 %.

Table 2. The effect of the amount of additive on the strength of cement pastes.

Cement age, days	Additive by dry cement mass, %			
	0%	2%	5%	10%
	The compressive strength of cement paste, mPa			
1	4.3	1.6	11.4	1
3	31	20	42.9	7
7	37	32	52.3	16
28	43.5	52	61.8	32

3.2. The X-ray phase analysis and infrared spectra of the additive and the control specimen

Holding the cement in the HCl solution changes the result of the hydration process. X-ray diffraction revealed qualitative and quantitative differences in the phase composition of the synthesized additive as compared to the control specimen (pure cement and water). From Fig. 1 it can be seen that in the structure of the additive the following changes take place in comparison with the control specimen:

- a significant decrease in the intensity of reflections of silicate phases – alite and belite;
- lack of reflections of portlandite and ettringite;
- formation of the Kuzel salt $\text{Ca}_4\text{Al}_2(\text{OH})_{12}\text{Cl}(\text{SO}_4)_{0.5} \cdot 6\text{H}_2\text{O}$.

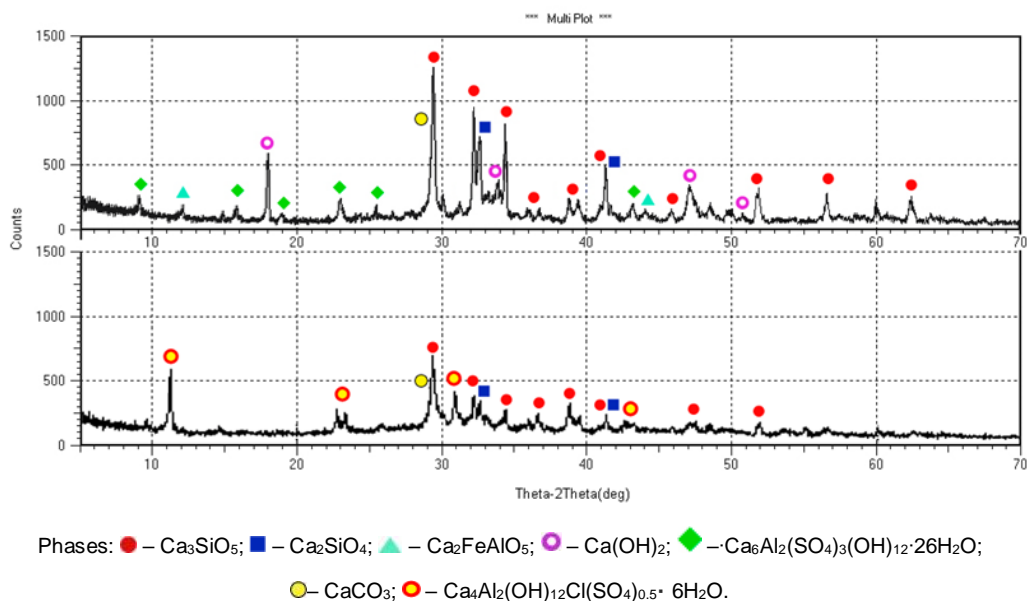
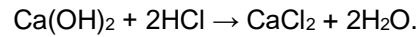


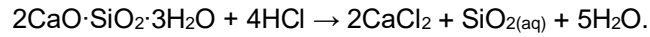
Figure 1. The XRD graphs of the additive (lower curve) and the control specimen (upper curve).

The noted features of phase formation occurring in the cement – HCl slurry suspension are explainable. Thus, a sharp decrease in the reflections of silicate phases in the X-ray phase analysis curves of the additive indicates an acceleration of the binder hydration in the presence of hydrochloric acid.

The absence of portlandite in the composition of the additive is due to the occurrence of neutralization reactions between clinker cement minerals of an alkaline nature and hydrochloric acid. In this case, the least chemically resistant to acid is precisely Portlandite, since Portlandite begins to decompose even at pH = 12.5 [28]:



Calcium hydrosilicates interact with acid by the reaction:



X-ray phase analysis data are consistent with the results obtained by infrared spectroscopy (Fig. 2). An increase in the height of absorption bands with maxima of 3410 (+71 %) and 1640 cm^{-1} (+200 %) indicates an intensification of the formation of compounds containing chemically bound water. A signal amplification with a maximum of 969 cm^{-1} (+136 %) indicates an increase in the rate of accumulation of weakly crystallized tobermorite-like hydrosilicates in the additive.

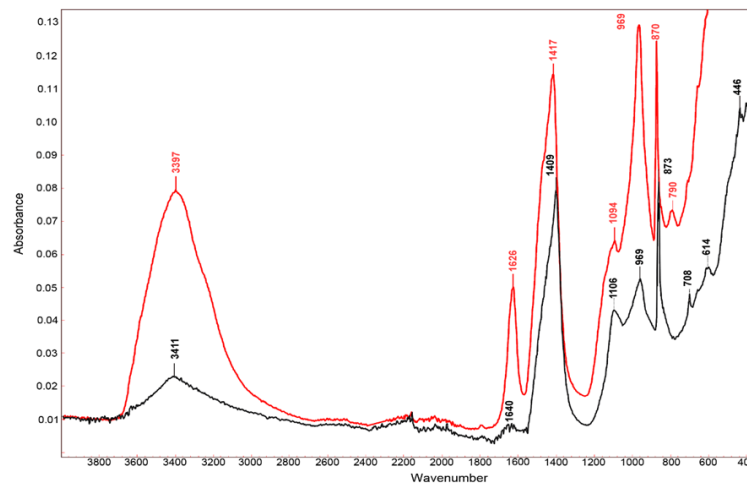


Figure 2. Infrared spectra of the additive (red) and the control specimen (black).

3.3. The X-ray phase analysis and infrared spectra of the modified cement paste and non-additive cement paste

The X-ray phase analysis of the additive shows that the presence of calcium chloride in the liquid phase of the suspension affects the process of cement hydration. The presence of calcium chloride causes the synthesis of Kuzel salt. Also, ettringite does not form during the 24-hour preparation procedure. The authors [23, 29–32] also showed the possibility of phase transformations:



in cement pastes with the participation of chlorine ions in hydration processes. However, the X-ray diffraction pattern of the chloride-containing additive contains reflections of both Kuzel salt and ettringite. In this case, the height of the reflections of calcium hydrosulfoaluminate recorded in the diffraction patterns for the 28-day non-additive cement paste and the modified cement paste is the same. This means that the introduction of the additive does not create competitive conditions for the formation and growth of AFt and AFm phases. Kuzel salt microcrystals germinating in a hydrating cement paste (mainly in the pores) do not create any chemical or physical, including steric, obstacles for the development of ettringite and other structure-forming phases. On the contrary, the formation of a crystalline framework with the introduction of additives is significantly accelerated. This is evidenced by the high daily strength of the modified cement paste (Table 2). The hardening of the modified cement paste is also facilitated by the binding of portlandite. The binding of portlandite in a chloride-containing cement paste is seen in the decrease in Ca(OH)_2 reflections by 7–9 % compared to a non-additive cement paste (Fig. 3). In the infrared spectrum of the modified cement paste, the height of the absorption band with a maximum of 951 cm^{-1} was increased by 22 % (Fig. 4). This indirectly confirms the increase in the number of tobermorite-like hydrosilicates, which are the main carriers of the strength of cement paste.

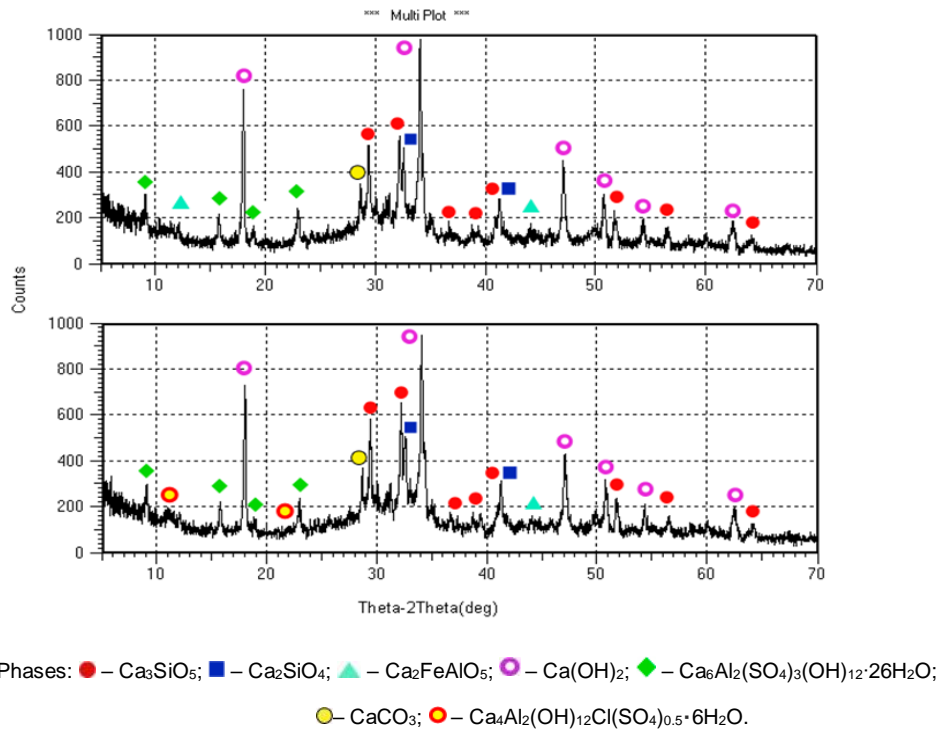


Figure 3. The XRD graphs of the modified cement paste (lower curve) and non-additive cement paste (upper curve).

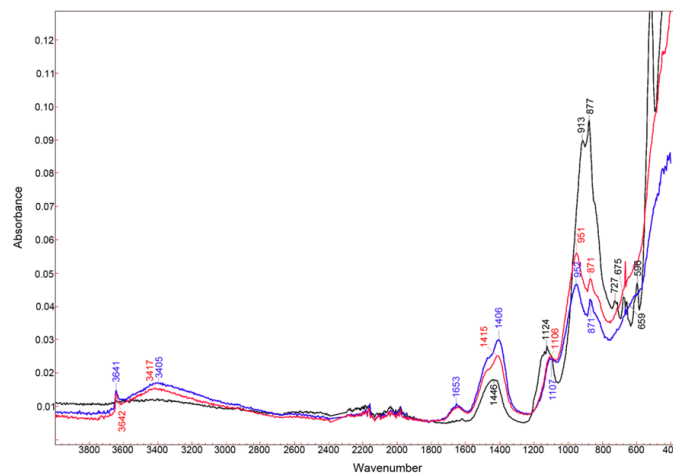


Figure 4. Infrared spectra of the initial cement (black), non-additive cement paste (blue), modified cement paste (red). The cement pastes' age is 28 days.

An increase in the intensity of reflexes of silicate phases (29 , 32 , 41.5° on a 2θ scale) in the structure of chloride-activated cement paste by 8–12 % compared with non-additive cement paste indicates a more complete hydration of the chloride-activated cement paste when reaching 28 days age. This can be explained by the fact that the reflections of the phases of highly basic hydrosilicates (CSH II) are superimposed on the reflections of silicate phases. Therefore, the reflex height of these phases is summed. [33].

4. Conclusions

The studies and the interpretation of the results proposed in the article allow to draw the following conclusions:

1. The additive synthesized by keeping cement in a 3 % HCl solution at a solid to liquid ratio of 1:10 for 24 hours, i.e. under conditions of acid corrosion of cement, it has structure-forming properties. The use of the additive significantly accelerates the setting and increases the strength of the cement paste. In the daily age of normal hardening, the strength of the cement paste increases by 165 %, in the 28-day age increases by 42 %.

2. The results of studying the structure of modified cement paste by XRD and IR methods suggest that the acceleration of setting and increase in strength characteristics are caused by the intensification of hydration processes and the binding of portlandite, the early formation of structure-forming phases of ettringite and Kuzel salt $\text{Ca}_4\text{Al}_2(\text{OH})_{12}\text{Cl}(\text{SO}_4)_{0.5}\cdot 6\text{H}_2\text{O}$, as well as the early formation of weakly crystallized calcium hydrosilicates of a tobermorite-like structure.

3. The proposed chloride-activated cement paste formulation after final refinement can be recommended for concrete building mixtures with accelerated hardening, increased strength, and without heat treatment.

5. Acknowledgements

1. The research is partially funded by the Ministry of Science and Higher Education of the Russian Federation as part of World-class Research Center program: Advanced Digital Technologies (contract No. 075-15-2020-934 dated 17.11.2020).

2. The authors are deeply grateful to Professor Sarkisov, Yuri Sergeyevich, Tomsk State University of Architecture and Building, Tomsk, Russian Federation, for the proposed concept of this area of research and his positive critical attitude to the development of this topic.

References

- Fediuk, R., Mochalov, A., Timokhin, R. Review of methods for activation of binder and concrete mixes. *AIMS Materials Science*. 2018. 5(5). Pp. 916–931. DOI: 10.3934/mat.2018.5.916
- Klyuev, S.V., Klyuev, A.V., Vatin, N.I. Fiber concrete for the construction industry. *Magazine of Civil Engineering*. 2018. 84(8). Pp. 41–47. DOI: 10.18720/MCE.84.4
- Bogdanov, R.R., Ibragimov, R.A. Process of hydration and structure formation of the modified self-compacting concrete. *Magazine of Civil Engineering*. 2017. 5(73). Pp. 14–24. DOI: 10.18720/MCE.73.2
- Ke, G., Zhang, J., Xie, S. Rheological behavior of calcium sulfoaluminate cement paste with supplementary cementitious materials. *Construction and Building Materials*. 2020. 243. URL: <https://doi.org/10.1016/j.conbuildmat.2020.118234>
- Klyuev, S.V., Klyuev, A.V., Abakarov, A.D., et al. The effect of particulate reinforcement on strength and deformation characteristics of fine-grained concrete. *Magazine of Civil Engineering*. 2017. 75 (7). Pp. 66–75. DOI: 10.18720/MCE.75.6
- Akimova, N.V., Shepelenko, T.S., Sarkisov, U.S., Sarkisov, D.U. Vliyanie produktov saxarnoj korrozii na kinetiku strukturoobrazovaniya sistemy «cement–voda». [The effect of sugar corrosion products on the structure formation of the cement-water system]. *Vestnik TGASU*. 2015. No. 6(53). Pp. 128–134. (rus)
- Shepelenko, T.S., Zubkova, O.A., Subbotina, N.V. i dr. Kompozitsionnyye tsementy, sodержashchiye sakharozu [Composite cements, containing sucrose]. *Vestnik TGASU*. 2017. 5. Pp. 151–158. (rus)
- Shepelenko, T.S., Sarkisov, U.S., Gorlenko, N.P., et al. Structure-forming processes of cement composites, modified by sucrose additions. *Magazine of Civil Engineering*. 2016. No. 6. Pp. 3–11. DOI: 10.5862/MCE.66.1
- Shepelenko, T.S., Gorlenko, N.P., Zubkova, O.A. Structurization processes of cement composites, modified with electrolytic additives. *Magazine of Civil Engineering*. 2018. 5(81). Pp. 125–134. DOI: 10.18720/MCE.81.13
- Ramachandran, V.S., Feldman, R.F., Kolepard, M., et al. *Dobavki v beton [Additives in concrete]*. Stroyizdat, 1988. 575 p. (rus)
- Jiayu, M.A., Zhibao, L.I., Yuehua, J.I., Xiaoping, Y. Synthesis, Characterization and Formation Mechanism of Friedel's Salt (FS): $3\text{CaO}\cdot\text{Al}_2\text{O}_3\cdot\text{CaCl}_2\cdot 10\text{H}_2\text{O}$ by the Reaction of Calcium Chloride with Sodium Aluminate. *J. of Wuhan University of Technology-Mater. Sci. Ed*. 2015. 30(1). Pp. 76–83. DOI: 10.1007/s11595-015-1104
- Kim, T., Kang, C., Hong, S., and Seo, Ki-Y. Investigating the Effects of Polyaluminum Chloride on the Properties of Ordinary Portland Cement. *Materials*. 2019. 12(20):3290. Pp. 1–15. DOI: 10.3390/ma12203290
- Elakneswaran, Y., Nawa, T., Kurumisawa, K. Electrokinetic potential of hydrated cement in relation to adsorption of chlorides. *Cem. Concr. Res.* 2009. 39(4). Pp. 340–344. DOI: [org/10.1016/j.cemconres.2009.01.006](https://doi.org/10.1016/j.cemconres.2009.01.006)
- Carrara, P., Lorenzis, L. De, Bentz, D.P. Chloride diffusivity in hardened cement paste from microscale analyses and accounting for binding effects. *Model Simul Mat Sci Eng*. 2016. 24(6): 065009. DOI: 10.1088/0965-0393/24/6/065009
- Renaudin, G., Mesbah, A., Dilnesa, B. Z., et al. Crystal Chemistry of Iron Containing Cementitious AFm Layered Hydrates. *Current Inorganic Chemistry*. 2015. 5(2). 1–10. DOI: 10.2174/1877944105666150420235831
- Galan, I., Perron, L., Glasser, F. P. Impact of chloride-rich environments on cement paste mineralogy. *Cement and Concrete Research*. 2015. 68. 174–183. DOI: [org/10.1016/j.cemconres.2014.10.017](https://doi.org/10.1016/j.cemconres.2014.10.017)
- Rapin, J.-P., Renaudin, G., Elkaim, E., Francois, M. Structural transition of Friedel's salt $3\text{CaO}\cdot\text{Al}_2\text{O}_3\cdot\text{CaCl}_2\cdot 10\text{H}_2\text{O}$ studied by synchrotron powder diffraction. *Cem. Concr. Res.* 2002. 32(4). Pp. 513–519. DOI: 10.1016/j.cemconres.2011.01.015
- Mesbah, A., François, M., Cau-dit-Coumes, C., et al. Crystal structure of Kuzel's salt $3\text{CaO}\cdot\text{Al}_2\text{O}_3\cdot 1/2\text{CaSO}_4\cdot 1/2\text{CaCl}_2\cdot 11\text{H}_2\text{O}$ determined by synchrotron powder diffraction. *Cement. Cem. Concr. Res.* 2011. 41(5). Pp. 504–509. DOI: [org/10.1016/j.cemconres.2011.01.015](https://doi.org/10.1016/j.cemconres.2011.01.015)
- Mesbah, A., Cau-dit-Coumes, C., Frizon, F., et al. A new investigation of the Cl^- – CO_3^{2-} substitution in AFm phases. *J. Am. Ceram. Soc.* 2011. 94. (6). Pp. 1901–1910. DOI: [org/10.1111/j.1551-2916.2010.04305.x](https://doi.org/10.1111/j.1551-2916.2010.04305.x)
- Balonis, M., Lothenbach, B., Le Saout, G. and Glasser, F.P. Impact of chloride on the mineralogy of hydrated Portland cement systems. *Cem. and Concr. Res.* 2010. Vol. 40. Pp. 1009–1022. DOI: 10.1016/j.cemconres.2010.03.002
- Mills, S.J., Christy, G., Génin, J.-M.R., et al. Nomenclature of the hydroxalite supergroup: natural layered double hydroxide. *Mineral. Mag.* 2012. 76 (5). Pp. 1289–1336. DOI: 10.1180/minmag.2012.076.5.10
- Ke, X., Bernal, S.A., Provis, J.L. Uptake of chloride and carbonate by Mg–Al and Ca–Al layered double hydroxides in simulated pore solutions of alkali-activated slag cement. *Cem Concr Res.* 2017. 100. Pp. 1–13. DOI: 10.1016/j.cemconres.2017.05.015
- Florea, M.V.A., Brouwers, H.J.H. Chloride binding related to hydration products Part I: Ordinary Portland Cement. *Cem. Concr. Res.* 2012. Vol. 42 (2). Pp. 282–290. DOI: 10.1016/j.cemconres.2011.09.016

24. Hirao, H., Yamada, K., Takahashi, H., Zibara, H. Chloride binding of cement estimated by binding isotherms of hydrates. *J. Adv. Concr. Technol.* 2005. 3(1). Pp. 77–84. DOI.org/10.3151/jact.3.77
25. Kalinichev, A.G., Kirkpatrick, R.J. Molecular dynamics modelling of chloride binding to the surfaces of calcium hydroxide, hydrated calcium aluminates, and calcium silicate phases. *Chemistry of Materials* 2002. 14(8). Pp. 3539–3549. DOI.org/10.1021/cm0107070
26. Hirao, H., Yamada, K. Takahashi, H. and Zibara H. Chloride binding of cement estimated by binding of isotherms of hydrates. *J. of Advanced technology.* 2005. 3(1). 77–84. DOI. org/10.3151/jact.3.77
27. Yuan, Q., Shi, C., De Schutter, G., et al. Chloride binding of cement-based materials subjected to external chlo-ride environment – A review. *Construction and Building Materials.* 2009. 23(1). Pp. 1–13. <https://doi.org/10.1016/j.conbuildmat.2008.02.004>
28. Loseva, I.V. Issledovanie protsessov massoperenosa pri kislotnoi korrozii tcementnykh betonov [Investigation of mass transfer processes during acid corrosion of cement concrete]. 2017. Pp. 1–159. URL: <https://ds.ivgpu.com/storage/docs/theses/33/1510570023loseva-iu-v.pdf> (date of application: 30.05.2020).
29. Ekolu, S. Thomas, M.D.A., Hooton, D. 2006. Pessim effect of externally applied chlorides on expansion due to delayed ettringite formation: Proposed mechanism. *Cement and Concrete Research.* 36. 688–696. 10.1016/j.cemconres.2005.11.020. DOI: 10.1016 / j.cemconres.2005.11.0
30. Geng, J., Easterbrook, D., Li, L. Y, Mo, L. W. The stability of bound chlorides in cement paste with sulfate attack. *Cement and Concrete Research.* 2015. 68. pp. 211–222. <https://doi.org/10.1016/j.cemconres.2014.11.010>
31. Baoguo, Ma, Ting, Zhang, Hongbo, Tan, et al. Effect of TIPA on Chloride Immobilization in Cement-Fly Ash Paste. *Advances in Materials Science and Engineering.* Volume 2018, Article ID 4179421, Pp. 1–11. <https://doi.org/10.1155/2018/4179421>
32. Ipavec, A., Vuk, T., Gabrovšek, R., Kaučič, V. Chloride binding into hydrated blended cements: The influence of limestone and alkalinity *Cement and Concrete Research.* 2013. 48. Pp. 74–85. <https://doi.org/10.1016/j.cemconres.2013.02.010>
33. Sumskoi, D.A. Modifitsirovannye viazhushchie teploizoliatcionnogo naznacheniiia [Modified binders for thermal insulation purposes]. 2019. Pp. 1–196. URL: http://gos_att.bstu.ru/shared/attachments/204284 (date of application: 30.05.2020).

Contacts:

Tatiana Shepelenko, shepta72@mail.ru

Nicolai Vatin, vatin@mail.ru

Olga Zubkova, zubkova0506@mail.ru

© Shepelenko, T.S., Vatin, N.I., Zubkova, O.A., 2020



DOI: 10.18720/MCE.100.10

Influence of raw greywater on compressive strength of concrete

M.M. Hasan^{*a}, M.A. Pial^b, M.S. Arafat^c, M.J. Miah^a, M.S. Miah^d

^a University of Asia Pacific, Green Road, Dhaka, Bangladesh

^b Bangladesh Water Development Board, Dhaka, Bangladesh

^c Max Infrastructure Limited, Mohakhali, Dhaka, Bangladesh

^d International University of Business Agriculture and Technology, Uttara, Dhaka, Bangladesh

* E-mail: drhasan@uap-bd.edu

Keywords: Alternative water source, greywater, freshwater, water quality, concrete, compressive strength

Abstract. Raw greywater, as an alternative water source, was used in concrete production with an aim to save the freshwater sources. Therefore, the variations of compressive strength, the most important and impact causing property of the concrete as regards to its quality and service, were assessed. Greywater was collected from a household where blackwater and greywater were separately disposed of. Total 162-cylinder specimens were cast by using the collected greywater and freshwater (municipally supplied tap water). The specimens were tested for compressive strength after 7, 14 and 28 days of curing. The investigation was carried out considering several experimental conditions: difference in the quality of water in the casting phase, curing phase and casting-curing phase and, also in types of coarse aggregates. A total of 28 water quality parameters (physical, chemical and biological) were tested for both greywater and freshwater. Some tests (turbidity, salinity, solids, organic matter, ammonium, nitrate, phosphate, calcium, magnesium, potassium, sodium, and zinc) exhibited higher (about 2 to as high as 1800 times) and a few others (dissolved oxygen, chloride and iron) showed lower values (about 5 to 8 times) for greywater in comparison to freshwater were decreased. The compressive strength of concrete decreased by about 20 % when greywater was used in the casting-curing phase. Whereas, this reduction was found to be only up to 4 % when greywater was used in the casting phase. Raw greywater could be used in concrete for some specified structures considering its lower strengths as found in this study. But in such cases, the impact of the greywater on other important characteristics of concrete and the consequent changes in the phase-structural parameters of the material also need to be clarified through further research.

1. Introduction

Freshwater scarcity boosts to consider wastewater as a resource in recent days. On one side, the uses of untreated or treated wastewater lessen the pressure on freshwater sources and on the other side, help manage the substantial amount of generated wastewater effectively to ensure sustainable environmental protection [1]. Literature reports that raw and/or treated wastewater is considered as a non-conventional water resource and contributed 70 million cubic meters per year if managed properly [2]. Therefore, replacement of freshwater by using some specified wastewater (raw or in treated condition) in different water-consuming sectors is becoming reality and among all types of wastewater, greywater becomes the first choice for this purpose.

Greywater means that part of domestic wastewater originating from non-toilet activities in a household such as baths, showers, hand basins, washing machines, dishwashers, and kitchen sinks [3–5]. Due to having less polluted quality (contains only 30 % of the organic fraction, lower pathogen content and 9–20 % of the nutrients) rather than other types of wastewater but of vast generation (70–80 % of total domestic wastewater), greywater is already widely used in different non-potable sectors instead of freshwater such as toilet flushing, car washing, landscaping, plant watering, agricultural irrigation of non-food crops, ornamental fountains, fire protection, air conditioning and alike. [3, 6–12].



Concrete (a composite, versatile construction material made from a mixture of cement, aggregates, and water; can be easily produced and fabricated which hardens and attains considerable strength within a short time) in manufacturing sector plays a major role in world's infrastructure development where water is a vital issue in both mixing phase (a procedure of homogeneous mixing of water and other materials that ensures high quality of concrete) and curing phase (a procedure for ensuring the hydration of the cement in newly placed concrete keeping controlled moisture loss and sometimes temperature that increase concrete strength and abrasion resistance, lessen the concrete scaling, surface dusting and cracking) as well [13–16]. Water is an unavoidable ingredient in the concrete manufacturing sector and consumes a substantial amount of freshwater (industry alone consumes more than one trillion gallons water per year worldwide without including wash water and curing water [17], another statistic reports that approximately 150 liters of water are required per cubic meter of concrete production, without considering other applications of water in the concrete industry [18]). Therefore, the use of non-fresh water in the aforementioned sector could be an option of saving precious and scarce freshwater resources. Although the use of several non-fresh water sources in concrete production is reported in existing literature such studies were limited in numbers that include: partially processed wastewater from a sewage treatment plant, industrial wastewater, domestic wastewater, wastewater coming from a ready-mixed concrete plant, etc. [18–23].

Besides, not only in terms of quantity but water is also worth in concrete in terms of quality as it actively participates in the chemical reactions of the hydration process of cementation materials and curing [24, 25]. The present impurities of water that used in mixing and/or curing phases of concrete production may interfere with the setting time of the cement, may affect shrinkage, the durability of concrete, and may also lead to corrosion of the reinforcement [26]. Therefore, the quality of the water needs to be carefully elucidated while using concrete. Although, in terms of quality, usually potable water (the water which is drinkable i.e. free from physical, chemical and biological impurities) is considered as an ideal one for casting and curing of concrete as most of the codes and specifications recommended such criterion for its known chemical composition and well-regulated [2, 27–29], but these specifications may not be the best basis for evaluation of the suitability of water as mixing and curing water. Some waters which do not meet potable criteria but reasonably clean and free from oil, acid, and other deleterious chemical substances, have been found to produce concrete of satisfactory quality [30]. Furthermore, as the most widely used material worldwide with a substantial amount of water consumption, the concrete manufacturing sector should take the environmental and societal responsibility to ensure sustainable development as well [18].

Therefore, keeping in mind the protection of natural water resources, the use of greywater, in terms of both quantity and quality, in concrete production could be examined as its degree of impurity is much lower but with significant quantity. Moreover, this research would be more practicable in Bangladesh context, as the country is on the edge of entering the directory of water-stressed countries and at the same time it is developing vastly in terms of infrastructures from last few decades to achieve its development mark "RUPOKOLPO (*VISION*) 2041".

The main objective of this study was to assess the possible use of raw greywater in concrete production in terms of compressive strength since this is considered as the most important and impact causing property of the concrete so long its quality and service are concerned [31, 32]. Consequently, the specified tasks included as follows:

Firstly, the collected raw greywater and freshwater were characterized physico-chemically and compared with the standard limits set as different concrete manufacturing codes and specifications worldwide. Then, these waters were used in different phases (e.g., casting-curing phase, casting phase, and curing phase) of concrete production. Finally, the variations in compressive strengths were evaluated to justify the possibility of the use of raw greywater.

2. Methods

2.1. Water Sampling

About 120 liters of greywater was collected from an outlet, before entering sewage line, of a residential building located in Matuail, Jattrabari, Dhaka, (23.697206N, 90.471151E) where blackwater and greywater were separately discharged. Fig. 1 shows the location of the greywater sampling source. Freshwater was collected from a tap in the University of Asia Pacific, supplied by the Dhaka Water Supply Authority (DWASA).

Collected sample waters were used for specimen casting and curing. Therefore, both tap water and greywater were characterized in terms of their physical, chemical and biological properties. Consequently, a total of 30 different water quality parameters were selected and tested for greywater and freshwater. The tested parameters include pH, Dissolved Oxygen (DO), Temperature, Color, Turbidity, Hardness, Salinity, Total Suspended Solids (TSS), Total Dissolved Solids (TDS), Total solids, Alkalinity as CaCO₃, Conductivity, Biochemical Oxygen Demand (BOD), Chemical Oxygen Demand (COD), Phosphate, Nitrite, Nitrate, Ammonia, Chloride, Sulphate, Cadmium, Calcium, Copper, Iron, Lead, Magnesium, Nickel, Potassium, Sodium, and Zinc.

2.2. Water Quality Parameters Testing

Water quality parameters pH, DO and Eh values were measured with an HQ 40d multi parameter-189 and PHC30H, LDO101 and MTC101 probes respectively supplied by HACH company.

Analyses of $\text{NH}_4\text{-N}$, $\text{NO}_2\text{-N}$, $\text{NO}_3\text{-N}$, TP, TSS, SO_4^{2-} , COD and color compounds were carried out using HACH 2800, HACH 1900 spectrophotometers and a HACH DRB 200 reactor block based on standard procedures, as highlighted by the supplier. BOD_5 measurement was carried out with manometric instruments (HACH BOD TRAK II) and incubators operated at 20°C . Cadmium, Calcium, Copper, Iron, Lead, Magnesium, Nickel, Potassium, Sodium, and Zinc were measured by using Atomic Absorption Spectrophotometry (AAS). All the tests except heavy metals were performed at Environmental Engineering Laboratory, University of Asia Pacific (UAP) and heavy metals were tested in the laboratory of NGO Forum for Public Health, Bangladesh branch.

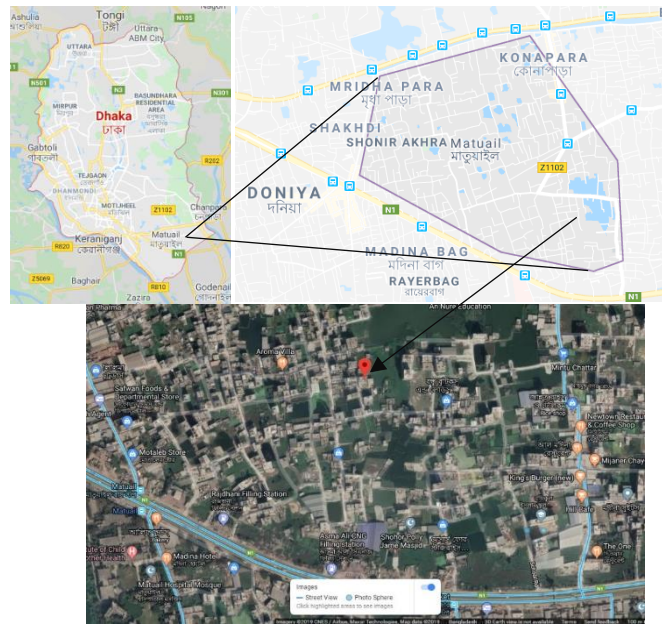


Figure 1. Greywater sampling location.

2.3. Concrete Materials Collection

Coarse aggregates (CA) (Standard brick chips and stone chips made from standard quality bricks and stone materials, respectively) and fine aggregate (FA) (Sylhet sand) were collected from the local market (namely, Gabtoli Beribadh) in Dhaka. Cement (Ordinary Portland Composite, Seven Rings Cement Brand, one of the popular brands of cement in Bangladesh having specifications and composition of BDS EN 197-1:2003, CEM II/B-M(S-V-L), Grade – 42.5 N/mm^2 ; Clinker – 65%–79%; Slag, fly ash and limestone – 21%–35%; Gypsum – 0%–5%) was collected from a local market.

2.4. Materials Properties and Mix Design of Concrete

Coarse aggregates, having a rough texture and angular shape, were crushed manually as a size of 20 mm (3/4 downsize). Unit weight test, specific gravity test, sieve analyses were done for both CA and FA using ASTM C127 and ASTM C136 standard methods. Both brick chips and stone chips were washed properly to avoid dust and other impurities before performing any tests. Besides, saturated surface dry conditions of the aggregates were ensured for the casting of the specimen. A volumetric concrete mix design was carried out with a ratio of 1:1.5:3 (Cement: FA: CA) having a water-cement ratio of 0.5. Table 1 showed the physical properties of the materials used in the concrete mix design.

Table 1. Physical properties of concrete materials.

Aggregates		Bulk sp. gr.	Fineness modulus
Coarse	Stone	2.64	--
	Brick	2.09	--
Fine	Local sand	2.48	2.52

2.5. Specimen Casting, Curing, and Testing

Total 162 cylindrical specimens (8" * 4") of six different experimental cases (differences in casting water and curing water (freshwater and greywater) and coarse aggregates (brick chips and stone chips)) were prepared (Table 2) with the above-mentioned mix design. Specimens of two cases (FBF (1st letter for casting (mixing) water, 2nd letter for coarse aggregate, 3rd letter for curing water, i.e., FBF: casting with fresh (tap) and curing with fresh (tap) water and use of brick chips as coarse aggregate) and FSF) were cast and cured with freshwater and with similar preparation to serve as a control to the others cases. Before casting, the coarse aggregates were kept 24 hours in tap water for FBF and FSF specimens and those were kept in greywater for FBG, GBG, FSG and GSG specimens for 24 hours. After that the aggregates were separated from water and kept to dry for some times in the room temperature ensuring SSD condition. After casting of each case, the specimens were left to dry for 24-hours and then remold and cured for specified days in specified waters. Compressive strength was tested using ASTM C 39 method after curing of 7 days, 14 days and 28 days. All the tests were performed at Engineering Materials Laboratory, University of Asia Pacific (UAP).

Table 2. Specimen details.

ID Name*	Casting water	Curing water	Coarse Aggregate	Nos. of specimens
FBF	Tap	Tap	Brick	27
FSF	Tap	Tap	Stone	27
GBG	Grey	Grey	Brick	27
GBF	Grey	Tap	Brick	27
GSG	Grey	Grey	Stone	27
GSF	Grey	Tap	Stone	27

*1st letter for casting (mixing) water, 2nd letter for coarse aggregate, 3rd letter for curing water e.g. GBF: casting with greywater but curing with fresh (tap) water and use of brick chips as coarse aggregate.

3. Results and Discussion

3.1. Characteristics of greywater and freshwater

Table 3 summarized the quality of greywater and freshwater (municipality supplied tap water) used in this study. The greywater quality data showed significantly higher concentrations compared to freshwater (2 to 1800 times higher) in the parameters include turbidity, salinity, solids, organic matter, ammonium, nitrate, phosphate, Ca, Mg, K, Na and Zn whereas the concentrations of DO and Fe were low. Comparing with other greywater standards from the literature it could be characterized as weak to medium strength in terms of pollution [33].

Table 3 also presented the permissible limits of each quality parameter of water that can be used in concrete production. It is found that the concentrations of all the constituents of greywater were within the respective permissible limits.

Table 3. Water quality details.

Water quality parameter	Unit	Tap water	Greywater	Limit	References
pH	--	6.58	5.59	3	[34, 35]
				> 5	[36, 37]
				6	[38]
				6-8	[39]
				7-9	[40]
Dissolved Oxygen (DO)	mg/L	5.06	0.61	--	--
Color	Pt-Co	5	18	--	--
Turbidity	JTU	17.62	260.59	2000	[30]
Salinity	mg/L	0.1	0.2	--	--
Total Solids (TS)	mg/L	179.6	384	50000	[41]
				5000-10000	[42]
Total Suspended Solids (TSS)	mg/L	8	193	4000	[35]
				2000	[38, 43, 44]

Water quality parameter	Unit	Tap water	Greywater	Limit	References
Total Dissolved Solids (TDS)	mg/L	171.6	191	50000	[45]
				2000	[38, 40, 43]
				< 6000	[30]
Biochemical Oxygen Demand (BOD)	mg/L	< 0.2	360	--	--
Chemical Oxygen Demand (COD)	mg/L	1.2	1420	--	--
Nitrate	mg/L	0.001	0.004	500	[46]
Nitrite	mg/L	0.3	0	--	--
Total Hardness	mg/L	137	118	--	--
Alkalinity as CaCO ₃	mg/L	132	117	500	[40]
				1000	[39, 44]
				360	[47]
Chloride	mg/L	< 60	< 60	500	[36, 37, 43]
				2000	[38]
				4500	[46]
Conductivity	S/m	356	39.5	--	--
Copper	mg/L	< 0.01	0.26	500	[44]
				600	[29]
				400	[38]
				600	[47]
Sulphate	mg/L	< 1	< 1	1000	[36, 46, 48]
				2000	[36, 37, 45]
				3000	[41]
Total Phosphate	mg/L	0	10.1	100	[36, 46]
Cadmium	mg/L	< 0.002	< 0.002	--	--
Calcium	mg/L	14.7	82	2000	[40]
Iron	mg/L	2.44	0.45	--	--
				100	[46]
Lead	mg/L	< 0.05	0.002	500	[44]
				600	[29]
				2000	[40]
Magnesium	mg/L	9	20	2000	[40]
Potassium	mg/L	3.1	8	2000	[40]
Sodium	mg/L	13.2	90	2000	[40]
				100	[46]
Zinc	mg/L	< 0.005	0.09	500	[44]
				600	[29]

3.2. Compressive strength of concrete: Effect of casting-curing water (FBF Vs GBG; FSF Vs GSG)

Fig. 2 showed the effect of the quality of water on the compressive strengths of concrete. Utilizing brick chips as coarse aggregate the compressive strengths of concrete were found 16.6 ± 0.9 MPa, 19.5 ± 0.5 MPa and 23.8 ± 1.5 MPa after 7 days, 14 days and 28 days curing respectively using greywater as casting-curing water (GBG) (Fig. 2a). In contrast, in FBF (using tap water as casting -curing water with brick chips), the corresponding values were found 20.0 ± 0.5 MPa, 24.5 ± 0.7 MPa and 29.6 ± 0.6 MPa. Therefore, while replacing tap water (conventionally considered as freshwater for concrete production in Bangladesh) with greywater the strength reduced by 17.0 %, 20.4 % and 19.6 % in 7 days, 14 days and 28 days curing period respectively (Fig. 5a). Similarly, using greywater with stone chips as coarse aggregate (GSG) the strengths in 7 days, 14 days and 28 days curing period were found 15.2 ± 0.7 MPa, 19.8 ± 0.6 MPa and 22.5 ± 0.7 MPa, respectively. Corresponding results in the case of tap water (FSF) were 19.2 ± 0.3 MPa, 24.9 ± 0.4 MPa and 28.7 ± 0.3 MPa, respectively (Fig. 2b). These exhibited consistent strength reduction trend in compressive strengths of concrete having values of 20.8 %, 20.5 % and 21.6 %, respectively (Fig. 5b). These results

(strength reduction of around 20 %) are not so much undesirable as in literature it is stated that the acceptable level of unknown water compressive strength of concrete is about 20 % of potable water [29]. The trend in increment in the compressive strengths was clearly found with the increment of the curing ages for all cases having similar qualities of water.

Fig. 2 also showed the changes in density with the quality of water. Density was reduced by 2.3 % (from $2148.8 \pm 30.7 \text{ Kg/m}^3$ to $2099.7 \pm 20.1 \text{ Kg/m}^3$), 0.5 % (from $2118.3 \pm 15.4 \text{ Kg/m}^3$ to $2107.2 \pm 37.8 \text{ Kg/m}^3$) and 1.2 % (from $2132.6 \pm 31.9 \text{ Kg/m}^3$ to $2106.6 \pm 26.2 \text{ Kg/m}^3$) for curing periods of 7, 14 and 28 days, respectively for greywater with brick chips as coarse aggregate (Fig. 2a). Corresponding strength's reduction were 2.0 % (from $2374.0 \pm 28.0 \text{ Kg/m}^3$ to $2326.6 \pm 7.3 \text{ Kg/m}^3$), 2.2 % (from $2366.7 \pm 37.8 \text{ Kg/m}^3$ to $2315.2 \pm 40.6 \text{ Kg/m}^3$) and 3.0 % (from $2369.4 \pm 35.7 \text{ Kg/m}^3$ to $2299.2 \pm 12.3 \text{ Kg/m}^3$), respectively for greywater and stone chips (Fig. 2b). It was evident that a percent reduction was found higher in the case of stone chips.

3.3. Compressive strength of concrete: Effect of casting water (FBF vs GBF; FSF vs GSF)

The effects of the quality of casting water on the compressive strength of concrete were shown in Fig. 3. The compressive strengths of concrete were found $17.2 \pm 0.5 \text{ MPa}$, $19.7 \pm 0.4 \text{ MPa}$ and $26.5 \pm 1.1 \text{ MPa}$ after curing periods of 7, 14 and 28 days, respectively with greywater as casting water and brick chips as coarse aggregate (GBF) (Fig. 3a). These indicate the strength reductions of 14.0 %, 19.6 % and 10.5 % respectively (Fig. 5b) comparing with the FBF case.

On the other hand, the use of greywater with stone chips (GSF) the strengths in 7 days, 14 days and 28 days curing period were obtained $19.1 \pm 1.6 \text{ MPa}$, $23.1 \pm 1.1 \text{ MPa}$ and $27.6 \pm 2.9 \text{ MPa}$, respectively. These indicated the reductions of 0.5 %, 7.2 % and 3.8 % respectively (Fig. 5b) in compressive strengths.

Fig. 3 also showed the changes in density with the quality of casting water. Density was reduced by 1.4 % (from $2148.8 \pm 30.7 \text{ Kg/m}^3$ to $2119 \pm 19.0 \text{ Kg/m}^3$), 0.3 % (from $2118.3 \pm 15.4 \text{ Kg/m}^3$ to $2112.9 \pm 7.5 \text{ Kg/m}^3$) and 1.5 % (from $2132.6 \pm 31.9 \text{ Kg/m}^3$ to $2101.1 \pm 12.4 \text{ Kg/m}^3$) with use of greywater and brick chips (Fig. 5a) and 2.1 % (from $2374.0 \pm 28.0 \text{ Kg/m}^3$ to $2325.1 \pm 6.6 \text{ Kg/m}^3$), 1.5 % (from $2366.7 \pm 37.8 \text{ Kg/m}^3$ to $2331.2 \pm 22.7 \text{ Kg/m}^3$) and 0.6 % (from $2369.4 \pm 35.9 \text{ Kg/m}^3$ to $2354.0 \pm 23.7 \text{ Kg/m}^3$) with use of greywater and stone chips (Fig. 5b) in 7 days, 14 days and 28 days curing period respectively.

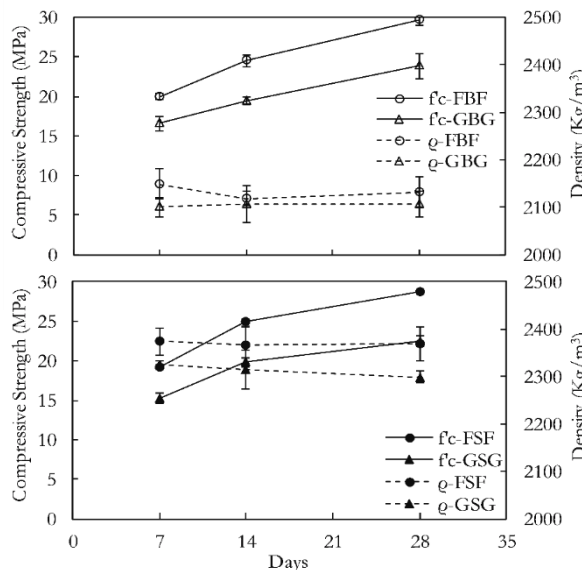


Figure 2. Compressive strengths of concrete made with tap water and greywater a) brick chips as coarse aggregate b) stone chips as coarse aggregate.

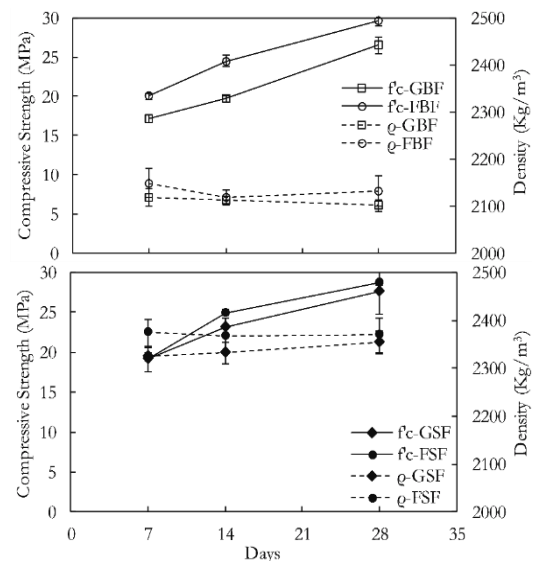


Figure 3. Compressive strengths of concrete with casting water difference a) brick chips as coarse aggregate b) stone chips as coarse aggregate.

3.4. Compressive strength of concrete: Effect of curing water (GBF vs GBG; GSF vs GSG)

The variation of compressive strengths with the variation in the quality of curing water was shown in Fig. 4, although greywater was used during the casting phase of concrete. The compressive strengths of concrete reduced by 3.5 %, 1.0 % and 10.2 % in 7 days, 14 days and 28 days curing respectively with the use of greywater in curing phase and brick chips as coarse aggregate (GBF) (Fig. 4a).

On the other hand, with the use of greywater and stone chips (GSF) the reduction of strengths in 7 days, 14 days and 28 days of curing period were 20.4 %, 14.3 % and 18.5 % respectively (Fig. 5b).

Fig. 4 also showed the changes in density with the changes in the quality of curing water. Utilizing greywater and brick chips, no significant reduction of density was observed but 2.3 % reduced with the use of stone chips as coarse aggregate only in 28 days curing period.

3.5. Compressive strength of concrete: Effects of coarse aggregates

Fig. 5 showed the comparison of compressive strengths of concrete with stone chips and brick chips as coarse aggregate. It was found that the increasing trends of compressive strengths with time were the same between the cases (FSF and FBF, GSG and GBG, GSF, and GBF. The strengths did not vary remarkably when stone chips were used instead of brick chips, except for the cases GBF and GSF. Compressive strength was found higher with stone chips (GSF) rather than with brick chips (GBF) and that was typical.

3.6. Failure pattern of specimen

The fracture pattern of cylindrical specimens was recorded during the experiment. The fracture pattern confirmed the combined failure of the specimens in each of the six cases (Fig. 6).

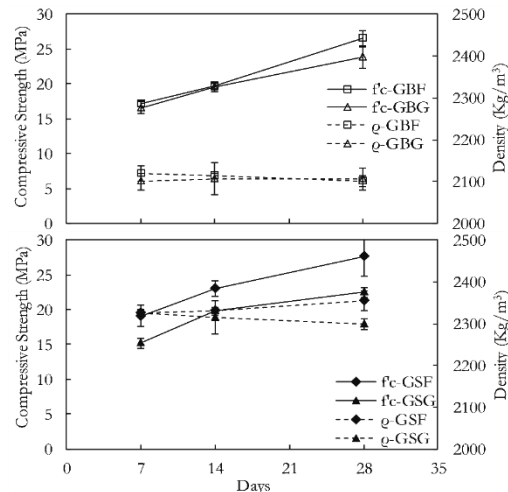


Figure 4. Compressive strengths of concrete with curing water difference a) brick chips as coarse aggregate b) stone chips as coarse aggregate.

3.7. Compressive strength of concrete: Effect of water quality parameters

High concentrations of solid contents (total solids), organic contents (BOD, COD) and heavy metals (Ca, Mg, Na) and very low concentration of dissolved oxygen in greywater might influence to reduce the compressive strengths of concrete.

It is reported in the literature that the concentrations of Ca, K, Na help to increase the rate of hydration reaction which facilitated the early increment of compressive strength, but later, a reduction is witnessed due to their excessive quantities [49]. A high concentration of Mg also causes the deterioration of concrete [50]. In this study the Mg concentration in greywater was 20 mg/L which was more than three times higher than that of tap water. Like magnesium, a high concentration of calcium can also lead to destructive crystal growth in concrete. Calcium also helps to form complex salts composed of CaCl_2 , Ca(OH)_2 and CaCO_3 [51,52]. In this study, the concentrations of Ca, K and Na in greywater were found higher around six times, three times and seven times, respectively. These might be the reasons for reducing the compressive strength of the concrete.

It has been found that oxygen plays a significant role in the chemical reactions during concrete manufacturing. The DO concentrations were 5.06 mg/l and 0.61 mg/l in tap water and greywater respectively. This substantial lower amount of oxygen could have affected the hydration process that might have reduced the strength as well.

In the case of pH value, it is reported that the ideal pH range in mixing water for concrete is slightly basic i.e., between 7.2 and 7.6 [29]. In this study, the pH of tap water was 6.58 and that of greywater was 5.59. More acidic conditions of greywater rather than tap water could have influenced the reduction of the compressive strength and this phenomenon also agrees with the literature [53].

Significantly high concentrations of biologically and chemically degradable organic contents (BOD, COD) could be another reason for such a strength-reduction phenomenon, although no standard limits were found for the organic contents in any codes and specifications (Table 3).

4. Conclusions

The effects of using raw greywater on compressive strength of concrete were investigated targeting to save freshwater. Greywater was used during the casting phase, curing phase and casting-curing phases of concrete production. The following conclusions could be drawn:

1. In terms of pollution load, raw greywater could be characterized as “weak to medium.” However, its physico-chemical properties met the limits set by the relevant codes and specifications for using water in concrete production.
2. Compressive strength reduced about 20 % with the use of greywater instead of fresh (tap) water in the casting-curing phase with brick chips. Negligible variations in compressive strengths were observed with stone chips instead of brick chips.
3. Compressive strength decreased by 10.5 % when greywater was used in the casting phase only with brick chips. This reduction was lower (3.8 %) with stone chips as coarse aggregate.
4. Compressive strength decreased by 10 % when greywater was used in the curing phase only with brick chips. This reduction was found much higher (up to 18.5 %) with stone chips as coarse aggregate. Although in these compared cases greywater was used in the casting phase rather than freshwater.
5. Regardless of the water sources, the compressive strength of concrete increased with an increase in curing age.
6. An almost similar trend like compressive strengths, i.e., reduction in densities was also found in all phases.
7. Excessive concentrations of solids, turbidity, organic contents, nutrients, calcium, sodium, potassium and magnesium and a substantially lower amount of dissolved oxygen might be the affecting factors on compressive strength and density.
8. Raw greywater could be used in concrete for some specified structures considering its lower strengths as found in this study. But in such cases, the impact of the greywater on other important characteristics of concrete and the consequent changes in the phase-structural parameters of the material also need to be clarified through further research.

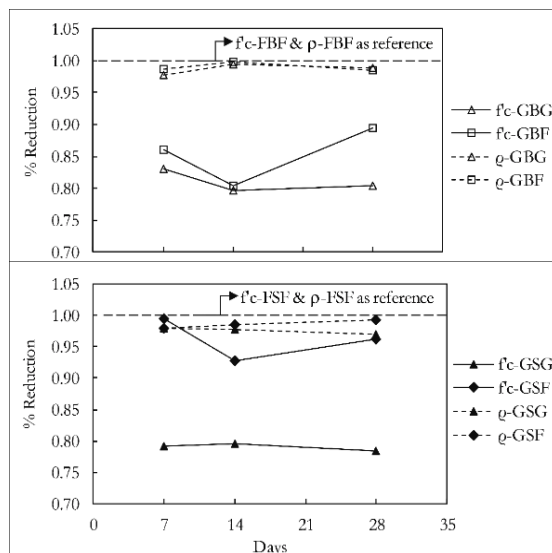


Figure 5. Reduction of compressive strengths of concrete a) brick chips as coarse aggregate b) stone chips as coarse aggregate.



Figure 6. Specimen fracture pattern after compressive strength test.

5. Acknowledgment

The authors acknowledge funding and facilities provided by the Department of Civil Engineering, University of Asia Pacific (UAP). The authors would also like to express their gratitude to Mr. Shahadat Hossain, Technical Assistant of Environmental Engineering and Chemistry Laboratory and Mr. Md. Homaun

Kabir, Laboratory Attendant of Engineering Materials Laboratory, Department of Civil Engineering, University of Asia Pacific, Dhaka, Bangladesh.

References

- Hasan, M.M., Shafiquzzaman, M., Azam, M.S., Nakajima, J. Application of a simple ceramic filter to membrane bioreactor. *Desalination*. 2011. 276(1–3). Pp. 272–277. <https://doi.org/10.1016/j.desal.2011.03.062>
- Mahasneh, B.Z. Assessment of replacing wastewater and treated water with tap water in making the concrete mix. *Electronic Journal of Geotechnical Engineering*. 2014. 19(K). Pp. 2379–2386. DOI: 10.35940/ijitee.K1709.0981119
- Li, F., Wichmann, K., Otterpohl, R. Review of the technological approaches for greywater treatment and reuses. *Science of Total Environment*. 2009. 407. Pp. 3439–3449. DOI: 10.1016/j.scitotenv.2009.02.004
- Liu, S., Butler, D., Memon, F.A., Makropoulos, C., Avery, L., Jefferson, B. Impacts of residence time during shortage on potential of water saving for greywater recycling systems. *Water Research*. 2010. 44. Pp. 267–277. DOI: 10.1016/j.watres.2009.09.023
- Pidou, M., Avery, L., Stephenson, T., Jeffrey, P., Parsons, S.A., Liu, S., Memon F.A., Jefferson, B. Chemical solutions for greywater recycling. *Chemosphere*. 2008. 71. Pp. 147–155. DOI:10.18178/ijesd.2017.8.6.990
- Kujawa, K., Zeeman, G. Anaerobic treatment in decentralized and source-separation-based sanitation concepts. *Environmental Science and Biotechnology*. 2006. 5. Pp. 115–139. DOI: 10.1007/s11157-005-5789-9
- Lu, W., Leung, A.Y.T. A preliminary study on potential of developing shower/laundry wastewater reclamation and reuse system. *Chemosphere*. 2003. 52. Pp. 1452–1459. DOI: 10.1016/S0045-6535(03)00482-X
- Friedler, E., Hadari, M. Economic feasibility of on-site greywater reuse in multi-story buildings. *Desalination*. 2006. 190(1–3). Pp. 221–234. DOI: 10.1016/j.desal.2005.10.007
- Hernandez, L., Zeeman, G., Temmink, H., Buisman, C.J.N. Characterization and biological treatment of greywater. *Water Science and Technology*. 2007. 56. Pp. 193–200. <https://doi.org/10.3390/w2010101>
- Jabornig, S., Favero, E. Single household greywater treatment with a moving bed biofilm membrane reactor (MBBMR). *Journal Membrane Science*. 2013. 446. Pp. 277–285. DOI: 10.1016/j.memsci.2013.06.049
- Paulo, P.L., Azevedo, C., Begosso, L., Galbiati, A.F., Boncz, M.A. Natural systems treating greywater and blackwater on-site: Integrating treatment, reuse and landscaping. *Ecological Engineering*. 2013. 50. Pp. 95–100. DOI: 10.1016/j.ecoleng.2012.03.022
- Santasmasas, C., Rovira, M., Clarens F., Valderrama, C. Grey water reclamation by decentralized MBR prototype. *Resources, Conservation & Recycling*. 2013. 72. Pp. 102–107. DOI: 10.1016/j.resconrec.2013.01.004
- Hiremath, P.N., Yaragal, S.C. Influence of mixing method, speed and duration on the fresh and hardened properties of Reactive Powder Concrete. 2017. *Construction and Building Materials*. 2017. 141. Pp. 271–288. DOI: 10.1016/j.conbuildmat.2017.03.009
- Asselanis, J.G., Aitcin, P.C., Mehta, P.K. Effect of curing conditions on the compressive strength and elastic modulus of very high-strength concrete. *Cement and Concrete Association, London*. 1989. 2 (1). Pp. 80–83. <https://doi.org/10.1520/CCA10106J>
- Ayodeji, Y.K. Effect of High Mixing Temperature 38°C on the Compressive Strength of Concrete made with Bama Gravel of Mix Proportion liVi'A and Water-Cement Ratio w/c (0.5, 0.55, 0.65). Final Year Project. 1999. Department of Civil and Water Resources Engineering, University of Maiduguri, Nigeria.
- Barry, R. *The Construction of Buildings*. 1998. Blackwell Science Limited, United Kingdom.
- Meyer, C. Sustainable development and the concrete industry. *CIB Bulletin*. 2004. <http://www.columbia.edu/cu/civileng/meyer/publications/publications/80%20sustainable%20development.pdf> (12 January 2020)
- Silva, M., Naik, R.T., Sustainable Use of Resources – Recycling of Sewage Treatment Plant Water in Concrete. 2nd International Conference on Sustainable Construction Materials and Technologies. 2010. Italy.
- Sandrolini, F., Franzoni, E. Waste wash water recycling in ready-mixed concrete plants. *Cement and Concrete Research*. 2001. 31. Pp. 485–489. DOI: 10.1016/S0008-8846(00)00468-3
- Su, N., Miao B., Liu, Fu-S. Effect of wash water and underground water on properties of concrete. *Cement and Concrete Research*. 2002. 32. Pp. 777–782. DOI: 10.1016/S0008-8846(01)00762-1
- Chatveera, B., Lertwattanakul, P., Makul, N. Effect of sludge water from a ready-mixed concrete plant on properties and durability of concrete. *Cement and Concrete Composites*. 2006. 28. Pp. 441–450. DOI: 10.1016/j.cemconcomp.2006.01.001
- Asadollahfardi, G., Asadi, M., Jafari, H., Moradi, Asadollahfardi, A.R. Experimental and statistical studies of using wash water from ready-mix concrete trucks and a batching plant in the production of fresh concrete. *Construction and Building Materials*. 2015. 98. Pp. 305–314. DOI: 10.1002/suco.201700255
- Noruzman, A.H., Muhammad, B., Ismail, M., Majid, A.Z. Characteristics of treated effluents and their potential applications for producing concrete. *Journal of Environmental Management*. 2012. 110. Pp. 27–32. DOI: 10.1016/j.jenvman.2012.05.019
- Neville, A.M. Water--Cinderella ingredient of concrete. *Concrete International*. 2000. 22 (9). Pp. 66–71. <https://doi.org/10.1016/j.matpr.2017.11.216>
- Neville, A.M. *Properties of concrete*. 5th edition. 2011. Pearson Education Limited, England. ISBN: 978-0-273-75580-7.
- Lee, O.S., Salim, M.R., Ismail, M., Ali, M.I. Reusing treated effluent in concrete technology. *Journal of Technology*. 2001. 34(F). Pp 1–10. DOI: 10.1051/mateconf/20178701018
- Cebeci, O.Z., Saatci, I.S. Domestic sewage as mixing water in concrete. *ACI Material Journal*. 1989. 86. Pp. 503–506.
- Kosmatka, S.H., Panarese, W.C. Mixing water for concrete, design and control of concrete mixtures. 6th Canadian Portland Cement Association. 1995. Pp. 32–35.
- Babu, G.R., Reddy, B.M., Ramana, N.V. Quality of mixing water in cement concrete: A review. *Materials Today: Proceedings*. 2018. 5. Pp. 1313–1320. <https://doi.org/10.1016/j.matpr.2017.11.216>
- Abrams, D.A. Tests of impure waters for mixing concrete. *Proceedings of The American Concrete Institute*. 1924. 20. Pp. 442–486.
- Emmanuel, A.O., Oladipo, F.A., Olabode, E.O. Investigation of salinity effect on compressive strength of reinforced concrete. *Journal of Sustainable Development*. 2012. 5(6). Pp. 74–82. DOI:10.5539/jsd.v5n6p74
- Ekinci, C.E., Kelesoglu, O. A study on occupancy and compressive strength of concrete with produced injection method. *Advances in Materials Science and Engineering*. 2014, Article ID 241613. DOI: 10.1155/2014/241613
- Pescod, M. Wastewater treatment and use in agriculture. 1992. FAO Irrigation and Drainage Paper. Pp. 47.

34. Tay, J.H., Yip, W. K. Use of reclaimed water for cement mixing. *Journal of Environmental Engineering*. 1987. 113(5). Pp. 1156–1160. [https://doi.org/10.1061/\(ASCE\)0733-9372\(1987\)113:5\(1156\)](https://doi.org/10.1061/(ASCE)0733-9372(1987)113:5(1156))
35. White, G.R. *Concrete technology*. Von Nostrand Reinhold. 1977. New York.
36. AS 1379. *Specification and supply of concrete standards*, Australia. 2007.
37. NZS 3121. *Specification for water and aggregate for concrete*, New Zealand Standards. 2002.
38. IS 456. *Code of practice for plain and reinforced concrete*. 3rd revision. 2000. Bureau of Indian Standards. New Delhi. India.
39. Neville, A.M. *Properties of concrete*. 4th and Final edition. 1995. Addison Wesley Longman, London.
40. BS 3148. *British Standard Institute*. 1980. *Water for making concrete*, London.
41. ASTM C94. *Standard specification for ready mix concrete*. 1992. American Society for Testing and Materials.
42. Steinour, H.H. Concrete mix water- How impure it can be? *J. PCA Res. and Dev. Lab*. 1960. 2(3). Pp. 32–50.
43. CIRIA. *Guide to concrete construction in the Gulf region*. 1984. Construction Industry Research and Information Association (CIRIA), London.
44. Mindness, S., Young, J.F. *Concrete*. 1981. Prentice Hall, Inc. Englewood Cliffs. New Jersey.
45. SANS 51008. *Mixing water for concrete*. 2006. South African National Standards.
46. BS EN 1008. *Mixing water for concrete: Specifications for sampling, testing and assessing the suitability of water, including water recovered from the process in the concrete industry, as mixing water in concrete*. 2002. British Standards Institute, London.
47. Kong, F.K., Evans, R.H. *Properties of structural concrete*. In: *Reinforced and Prestressed Concrete*. Springer, Boston, MA. 1987. DOI https://doi.org/10.1007/978-1-4899-7134-0_2
48. Soroka, I. *Portland cement paste and concrete*. 2nd edition. 1979. MacMillan Press, England. DOI <https://doi.org/10.1007/978-1-349-03994-4>
49. Lawrence, O.E. Empirical Investigation of the Effects of Water Quality on Concrete Compressive Strength. *International Journal of Constructive Research in Civil Engineering*. 2016. 2(5). Pp. 30–35. <http://dx.doi.org/10.20431/2454-8693.0205006>
50. Cody, R.D., Spry, P.G., Cody, A.M., Gan, -Liang, *The Role of Magnesium in Concrete Deterioration*. Iowa DOT HR-355, Project Development Division, The Iowa Department of Transportation and The Iowa Highway Research Board. 1994.
51. Chatterji, S. Mechanism of the CaCl₂ Attack on Portland Cement Concrete. *Cement and Concrete Research*. 1978. 8(4). Pp. 461–467.
52. Berntsson, L., S. Chandra. Damage of Concrete Sleepers by Calcium Chloride. *Cement and Concrete Research*. 1982. 12(1). Pp. 87–92.
53. Hama, S.M., Mawloodb, I.A., Hilal, N.N. Influence of Mix Water Quality on Compressive Strength of Making Concrete. *Iraqi Journal of Civil Engineering*. 2019. 013–001. Pp. 19–22.

Contacts:

Md Mahmudul Hasan, drhasan@uap-bd.edu

Md Asaduzzaman Pial, mapialbd@gmail.com

M Shahriar Arafat, arafat.shahriar121@gmail.com

Md Jihad Miah, jihad.miah@uap-bd.edu

M Shamim Miah, mmshamim@iubat.edu

© Hasan, M.M., Pial, M.A., Arafat, M.S., Miah, M.J., Miah, M.S., 2020



DOI: 10.18720/MCE.100.11

Temperature and moisture in highways in different climatic regions

B.B. Teltayev^{1a}, G. Loprencipe^b, G. Bonin^c, E.A. Suppes^a, K. Tileu^a

^a *Kazakhstan Highway Research Institute, Almaty, Republic of Kazakhstan*

^b *Sapienza University of Rome, Rome, Italy,*

^c *SPT Studi e Pianificazione del Territorio S.r.l., Rome, Italy*

* *E-mail: bagdatbt@yahoo.com*

Keywords: Pavement, subgrade, sensors, temperature, moisture, cyclic freezing and thawing

Abstract. The article represents the results of experimental research for temperature and moisture variations in pavements and subgrade of highways located in five different climatic regions, an analysis of cyclic freezing and thawing of a pavement. To measure temperature and moisture in pavements and subgrade the sensors have been used which allow making measurement of these characteristics simultaneously in the points of interest. The peculiarities of variation were analyzed for air temperature, temperature in pavements and subgrade in different regions in warm and cold 24 hours. The differences were established in distribution of temperature and moisture in pavements and subgrade in warm and cold 24 hours. To analyze cyclic freezing and thawing (FT) of a pavement the air temperature values have been used during twenty sequential winter seasons in six geographical points of Kazakhstan. The dependences were established for the number of FT cycles on duration and minimal temperature of the cycles.

1. Introduction

A highway during its service life is subject to the impact of mechanical and climatic factors [1–3]. Out of climatic factors the most dynamic (non-stationary) one is a temperature which is varied both in the annual cycles and in 24-hour ones [4–14]. The temperature impacts greatly on an asphalt concrete and a cement concrete pavements [15–20] and on subgrade [4–9, 20–23].

At designing of pavements [24–28] the deformation and strength characteristics of the asphalt concretes and other materials containing organic binders are determined depending on calculated temperature values. Deformation characteristics of soils (especially of clay soils) depend greatly on moisture. Therefore, deformation properties of soils at designing of pavements are determined depending on a type of soil and moisture.

It is known that at low temperatures part of water contained in soil pores transforms into a solid condition (ice) [7–9, 21–23]. Mechanical properties of frozen soils differ greatly from those of ordinary (non-frozen) ones [29–32]. Unfortunately, frozen condition of soils of subgrade is not taken into account at designing of pavements in Kazakhstan [27, 28], Russia [26] and other countries of former Soviet Union.

The abovementioned shows practical importance of information about temperature and moisture variation in a pavement and subgrade of a highway.

This article is a continuation of the authors' works for the research of temperature and moisture in pavements and subgrade of highways. It contains the results of experimental research for temperature and moisture variation in pavements and subgrade of highways located in five regions of Kazakhstan, and the analysis of cyclic freezing and thawing of a pavement.

As the selected test sections are located in different geographical regions of a large territory of Kazakhstan (the 9th position in the world) their climatic conditions differ greatly. As it is seen from Table 1, the average multiyear air temperature of January in Shymkent is equal to -21.7°C, and in Oskemen it is equal to -49°C; the number of days per year with average daily air temperature higher than 0°C in Petropavlovsk and



Shymkent is equal to 194 and 304 respectively; the largest thickness of snow cover in Petropavlovsk and Turkestan is 124 cm and 34 cm respectively, i.e. the difference can be up to 4 times; frost penetration depth of a highway in Petropavlovsk and Shymkent is 241.1 cm and 69.3 respectively, i.e. the difference is 3.5 times.

Such a big difference in climatic characteristics of the geographical regions where the test sections are located can provide essential variations in temperature and moisture values in pavement and subgrade layers.

Experimental results, included into the article, are of high value at designing of pavements and operation of highways not only in Kazakhstan, but also in many countries of the world, for example in Russia, the USA, China, Canada, Mexico, Brasilia, India, in European countries and other countries, as they have the climatic conditions close to those ones which are considered in the article.

Table 1. Climatic characteristics and geographical coordinates.

Characteristic	City						
	Petro-pavlovsk	Almaty	Nur-Sultan	Turkestan	Oskemen	Atyrau	Shymkent
Average multiyear minimal air temperature in January, °C	-42.5	-22.1	-39.4	-26.4	-49.0	-35.9	-21.7
Average multiyear maximal air temperature in July, °C	35.7	37.8	39.2	44.2	43.0	41.0	41.7
Number of days with average daily air temperature ≥ 0 °C	194	254	198	279	211	240	304
The largest thickness of snow cover, cm	124	43	42	34	104	42	62
Average quantity of precipitation per year, mm	345	450	318	448	441	169	493
Average annual wind velocity, m/s	2.4	0.7	2.9	2.0	2.4	2.8	1.8
Frost penetration depth of a highway, cm	241.1	101.2	222.1	91.3	231.8	131.7	69.3
Geographical coordinates:							
- latitude (n.l.):	54°52'00"	43°15'24"	51°10'48"	43°17'50"	49°58'17"	47°07'00"	42°17'57"
- longitude (e.l.):	69°09'00"	76°55'42"	71°26'45"	68°15'06"	82°36'21"	51°52'59"	69°35'59"
Altitude above sea level, m	142	787	358	214	287	-25	513

2. Methods

2.1. Test sections

For the purpose of long-term monitoring realization for temperature and moisture variation in points of pavements and subgrade of highways the test sections have been selected which are located in different climatic regions of Kazakhstan (Fig. 1) and temperature and moisture sensors have been installed. Sensors for the test section of "Nur-Sultan-Burabai" highway (km 76+30) were installed in 2009, and for the test sections of "Almaty-Bishkek" (km 58+895), "Atyrau-Astrakhan" (km 598+50), "Kyzylorda-Shymkent" (km 2097+00) and

“Oskemen-Zyryanovsk” (km 0+75) the sensors were installed in 2013. Geographical coordinates for the cities located close to the selected test sections are given in Table 1.

Materials and thickness of pavements layers and soils with their characteristics are represented in Tables 2 and 3 respectively.



Figure 1. Locations of the test sections of the highways.

Table 2. Pavement structures on the test sections.

Layer number	Pavement material and thickness, cm				
	Almaty-Bishkek	Atyrau-Astrakhan	Kyzylorda-Shymkent	Nur-Sultan-Burabai	Oskemen-Zyryanovsk
1	Fine-grained dense asphalt concrete, 5	Fine-grained dense asphalt concrete, 8	Stone mastic asphalt concrete, 5	Stone mastic asphalt concrete, 6	Fine-grained dense asphalt concrete, 3
2	Coarse-grained porous asphalt concrete, 10	Fine-grained dense asphalt concrete, 6	Coarse-grained porous asphalt concrete, 10	Coarse-grained porous asphalt concrete, 9	Coarse-grained cold asphalt concrete, 10
3	Fine-grained dense asphalt concrete, 7	Coarse-grained porous asphalt concrete, 11	Coarse-grained high porous asphalt concrete, 13	Stone treated with bitumen, 12	Sand and gravel mix, 10
4	Coarse-grained cold asphalt concrete, 15	Stone treated with bitumen, 5	Sand and gravel mix, 42	Stone and sand mix treated with Portland cement (7%), 18	–
5	Fine sand and gravel mix, 25	Gravel and sand mix, 60	Dusty sand, 20	Stone and sand mix, 15	–
6	Coarse sand and gravel mix, 35	–	–	Sand, 20	–
Total thickness of pavement, cm	97	90	90	80	23

Table 3. Type and characteristics of soils on the test sections.

Test section	Type of soil	Liquidity limit W_L , %	Plasticity limit W_{PL} , %	Plasticity number I_p
Almaty-Bishkek	Heavy sandy clay loam	26.6	13.4	13.2
Atyrau-Astrakhan	Heavy silt clay loam	25.3	12.4	12.9
Kyzylorda-Shymkent	Silt sand	22.0	-	Not plastic
Nur-Sultan-Burabai	Heavy sandy clay loam	34.8	18.7	16.1
Oskemen-Zyryanovsk	Heavy sandy clay loam	26.8	13.5	13.3

2.2. Temperature and moisture sensors

Company “Interpribor” (Chelyabinsk, Russia) produced temperature and moisture sensors on the order of Kazakhstan Highway Research Institute (KazdorNII). Each sensor, produced in the form of a metal capsule, contains an element for measurement of temperature based on the effect of thermal resistance and an element for measurement of moisture through diamagnetic permeability (Fig. 2). Such design concept allows performing simultaneously the measurement of temperature and moisture in points of a pavement and a subgrade.

Temperature elements of sensors were calibrated by the producer and moisture elements were calibrated in the laboratory of KazdorNII. The calibration of the sensors was performed with the use of soils, selected from the location of their installation.

Installation of the sensors into the pavement and the subgrade layers of the highways was performed by the specialists of KazdorNII. Measurement ends of the sensors were put on the surface of the highways and collected in measurement chambers of land system of the set (Fig. 3).



Figure 2. General view of one set of the temperature and moisture sensors.



Figure 3. View of surface part of the temperature and moisture automatic measurement system on the highway “Almaty-Bishkek”.

The depths for temperature and moisture sensors locations on test sections are given in Table 4. As an example, the scheme of sensors locations in pavement and subgrade of “Almaty-Bishkek” highway is shown in Fig. 4.

Table 4. The depths for temperature and moisture sensors locations on the test sections.

Sensor number	Depth for sensor location, cm				
	Almaty-Bishkek	Atyrau-Astrakhan	Kyzylorda-Shymkent	Nur-Sultan-Burabai	Oskemen-Zyryanovsk
1	2	2	2	6	2
2	5	10	10	15	12
3	15	20	15	45	23
4	21	30	30	80	35
5	38	90	70	115	70
6	65	115	90	150	105
7	100	140	120	185	140
8	135	165	150	220	175
9	170	190	180	-	210
10	205	215	210	-	245
11	240	240	240	-	280

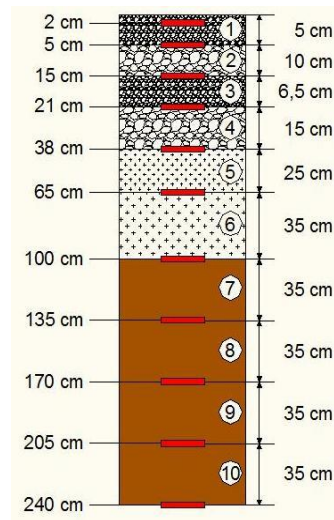


Figure 4. Pavement structure and scheme of sensors location on the highway “Almaty-Bishkek” – a sensor of temperature and moisture.

Complete procedure for installation of the sensors was performed in the following consecutive sequence:

1. A well was developed with diameter of 16 cm and depth 280 cm from the pavement surface by a machine drilling.
2. Soil was carefully removed from the well, then it was stored in separate portions in a row, and measures were taken for observance of its initial moisture content without change.
3. The sensor, installation of which was provided in the depth of 280 cm, was laid on the bottom of the well.
4. A portion of soil was excavated from the subgrade in the depth of 280 cm and filled above the sensor.
5. The soil was compacted physically up to the designed level.

All other sensors were installed by similar way. Portions of soil, excavated from the well, were filled in reversed order and compacted up to the designed level.

3. Results and Discussion

3.1. Air temperature

Comparison of air temperature variations in the cities of Oskemen (eastern region of the country) and Shymkent (southern region of the country) shows that they differ considerably between each other (Fig. 5). The temperature is considerably higher (higher than +40 °C) in the south of the country in a summer season than in the east of it. And the minimal temperature is considerably lower (it reaches -40 °C) in the east of the country in a winter season than in the south of it.

Fig. 6 and 7 represent the graphs for an air temperature variation for warm and cold 24 hours on the test sections of highways located in different regions of Kazakhstan. The graphs have been constructed according to the temperature values measured by the sensors. As it is seen from Fig. 6, the air temperature of warm 24 hours is varied quasi-harmonically practically in all considered regions. Meanwhile, as a rule, the highest temperatures occur between 3 p.m. and 6 p.m., and the least ones occur between 3 a.m. and 6 a.m. As one should expect, the highest temperature value equal to 37.5 °C has been obtained on “Kyzylorda-Shymkent” highway (in the south of the country), and the least temperature value equal to 15.5 °C has been measured on “Nur-Sultan-Burabai” highway (in the north of a country). Daily amplitude of the temperature for warm 24 hours of northern part of the country was 16.8 °C, and in the southern part of the country it was equal to 15 °C.

Behavior of air temperature variation for cold 24 hours in the regions is greatly different from that one of warm 24 hours (Fig. 7). Practically for all the considered highways (except for “Almaty-Bishkek” highway) the air temperature for the considered 24 hours has been little varied: daily temperature variation was 2.5 °C, 2.0 °C and 3.8 °C for the highways “Nur-Sultan-Burabai”, Kyzylorda-Shymkent” and “Oskemen-Zyryanovsk” respectively. And for “Almaty-Bishkek” highway the temperature increase for 6 °C from -5.5 °C to 0.5 °C occurred from 11 a.m. to 4 p.m. and further the temperature was varied within the limits of -3.5 °C and 1.0 °C.

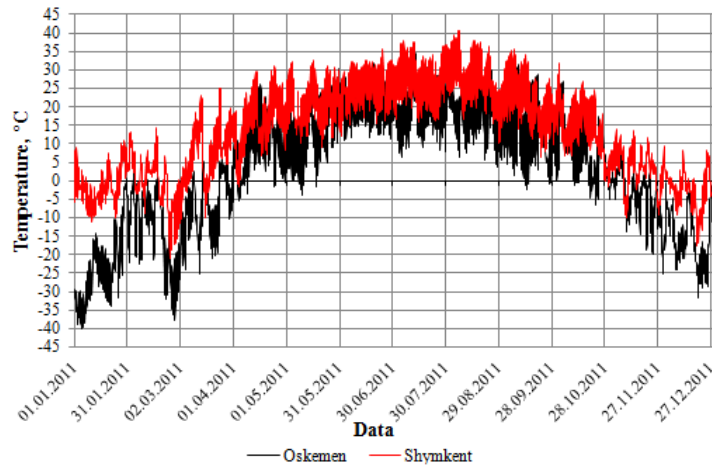


Figure 5. Graphs of an air temperature variation in the cities of Oskemen and Shymkent in 2011.

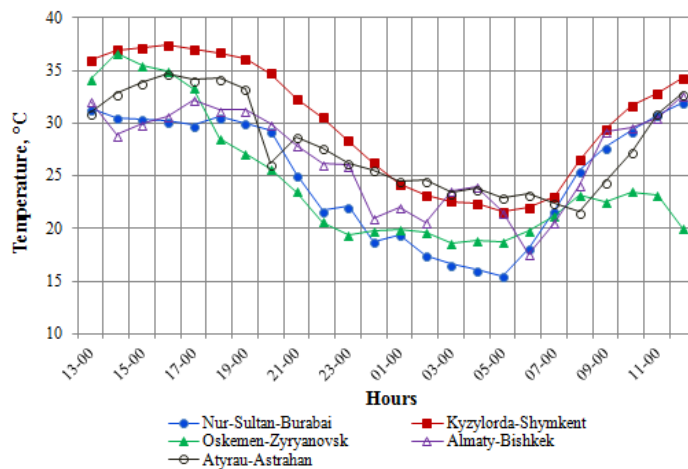


Figure 6. Air temperature variation for warm 24 hours.

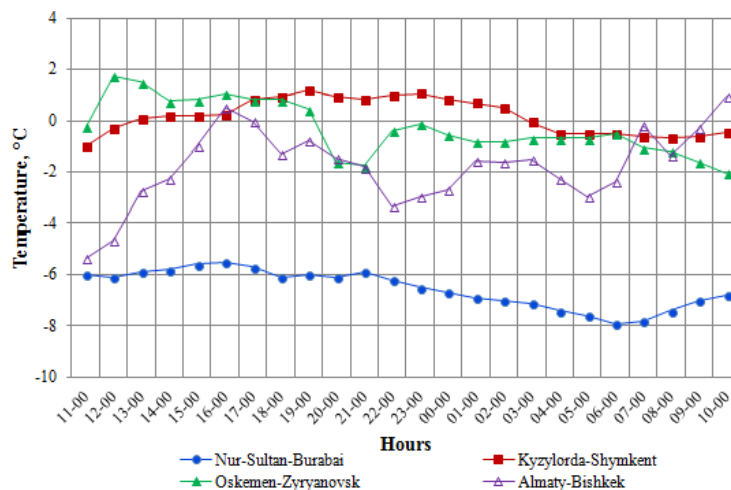


Figure 7. Air temperature variation for cold 24 hours.

3.2. Temperature in pavement and subgrade

Daily temperature variations in points of the pavement (in the depths of 10 cm, 30 cm and 80 cm) for cold and warm 24 hours are shown in Fig. 8-11. It is clearly seen that for warm 24 hours (Fig. 8) a temperature variation in the depth of 10 cm (on the bottom part of asphalt concrete layers) has a clear harmonicity. A temperature in this depth is higher than an air temperature. And for cold 24 hours (Fig. 10) the harmonicity for the temperature variation is interrupted. An amplitude for daily temperature variation is decreased with the depth increase (faster in winter): the temperature is not practically varied for warm (Fig. 9) and cold (Fig. 11) 24 hours in the depths of 80 cm and 30 cm respectively.

Fig. 12 and 13 represent the graphs for a temperature distribution in the depth of pavement and subgrade on test sections for warm and cold 24 hours. The graphs show that the temperature is decreased in the depth in summer season and it is increased in the depth in winter season. The temperatures in the depth of 100 cm of “Nur-Sultan-Burabai” and “Kyzylorda-Shymkent” highways were: 21 °C and 37 °C respectively for summer 24 hours; -4.0 °C and 4.2 °C respectively for winter 24 hours. It is clearly seen (Fig. 18) that for the considered 24 hours (14 January 2015) the freezing depth for “Atyrau-Astrakhan”, “Almaty-Bishkek”, “Oskemen-Zyryanovsk” and “Nur-Sultan” highways was 101 cm, 112 cm, 140 cm and 174 cm respectively.

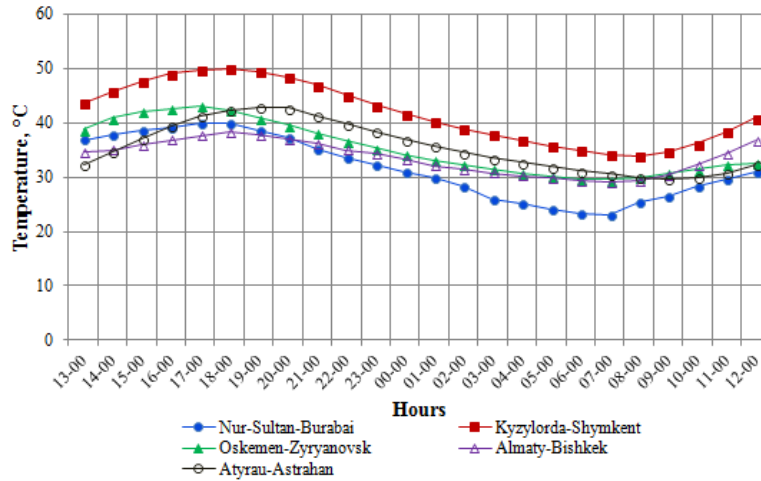


Figure 8. Temperature variation for warm 24 hours in the depth of 10 cm.

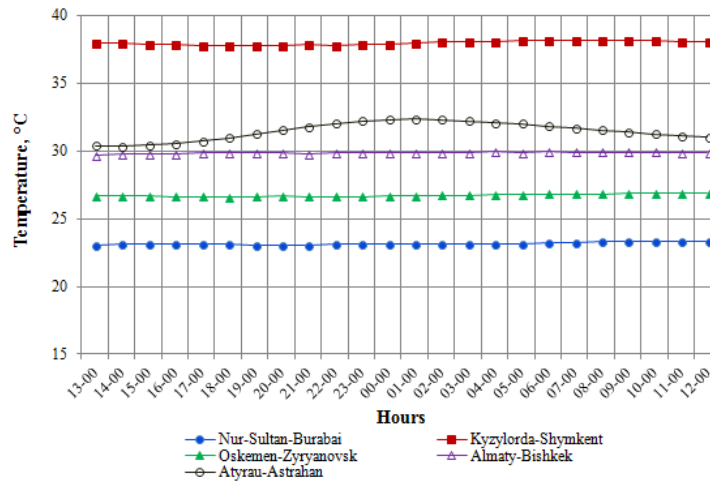


Figure 9. Temperature variation for warm 24 hours in the depth of 80 cm.

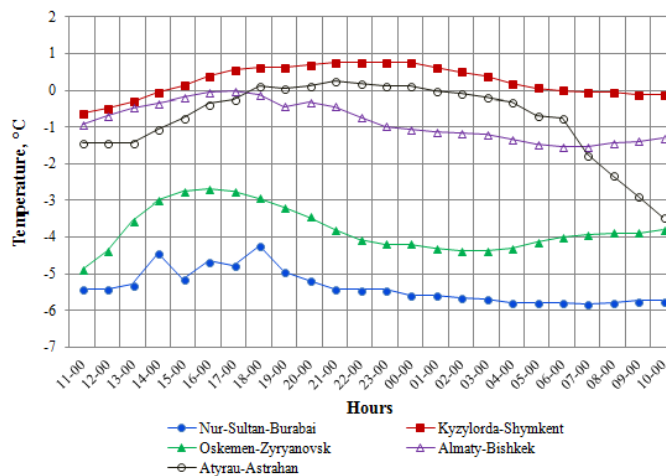


Figure 10. Temperature variation for cold 24 hours in the depth of 10 cm.

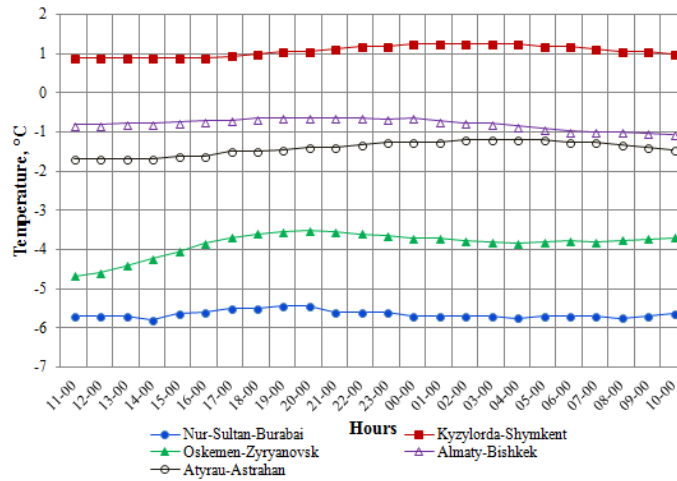


Figure 11. Temperature variation for cold 24 hours in the depth of 30 cm.

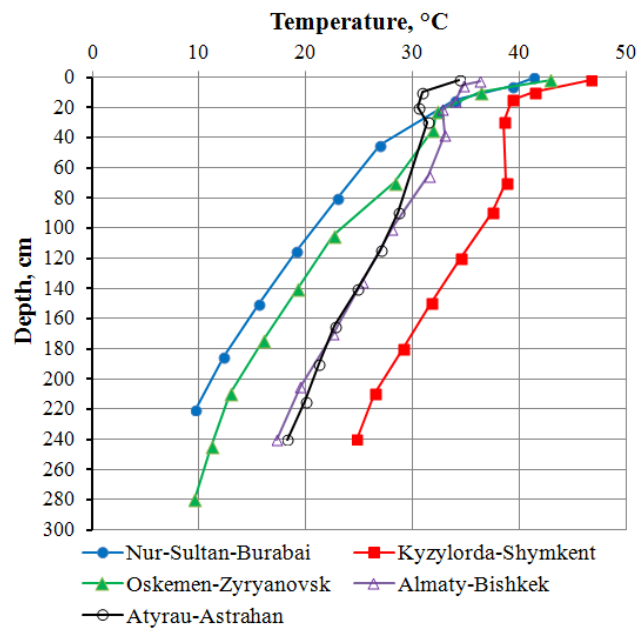


Figure 12. Temperature distribution in the depth of pavement and subgrade for warm 24 hours.

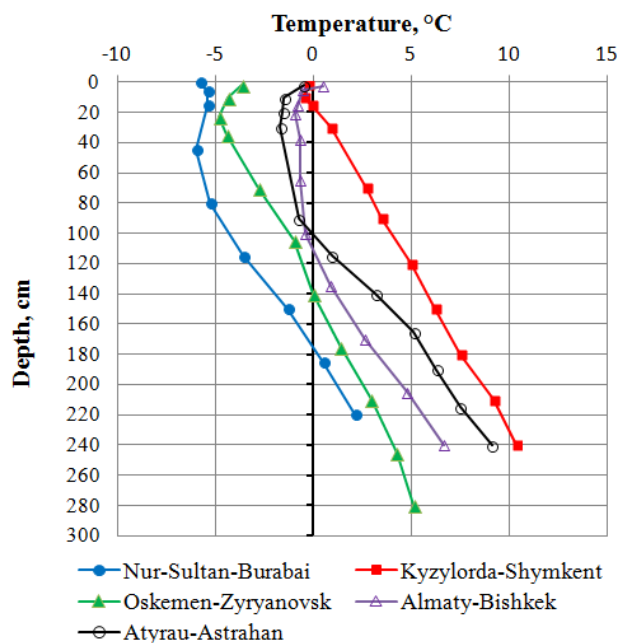


Figure 13. Temperature distribution in the depth of pavement and subgrade for cold 24 hours.

3.3. Moisture in pavement and subgrade

Moisture distribution in the depth of pavements and subgrade on test sections for warm and cold 24 hours is represented in Fig. 14 and 15. These graphs show that moisture distribution in the depth of pavements and subgrade (up to 240–280 cm) is of complex nature for all the considered test sections. Moisture values in pavement layers and points of subgrade of “Almaty-Bishkek”, “Atyrau-Astrakhan” and “Kyzylorda-Shymkent” highways are between the limits of 2 % and 10 % for warm and cold 24 hours. An exception is only the “Oskemen-Zyryanovsk” highway. Moisture in this highway is varied between wider limits: 2 % and 17.5 %.

Part of moisture transforms into solid state (ice) at negative temperatures in winter season. This phenomenon reduces the content of liquid moisture in points of a pavement and subgrade which is clearly seen in Fig. 16 and 17.

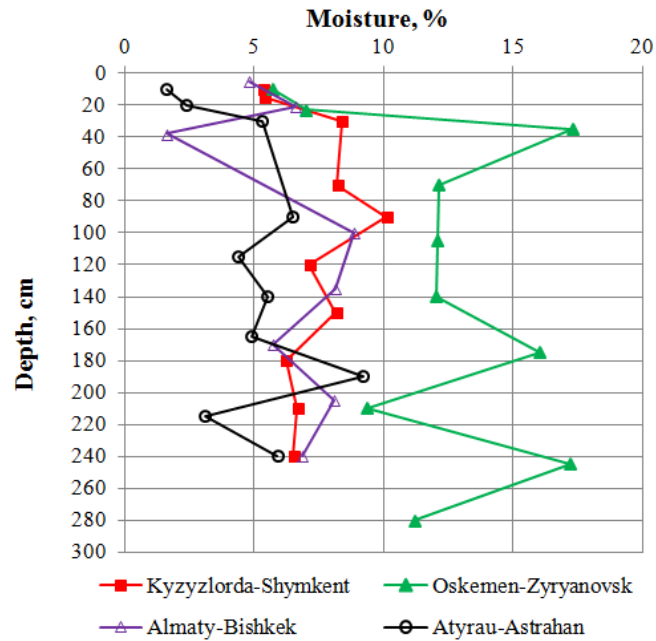


Figure 14. Moisture distribution in the depth of pavement and subgrade for warm 24 hours.

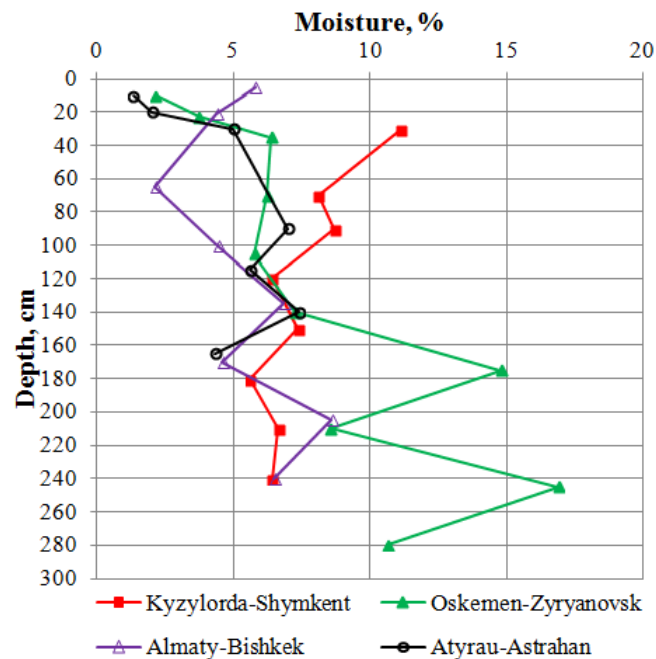


Figure 15. Moisture distribution in the depth of pavement and subgrade for cold 24 hours.

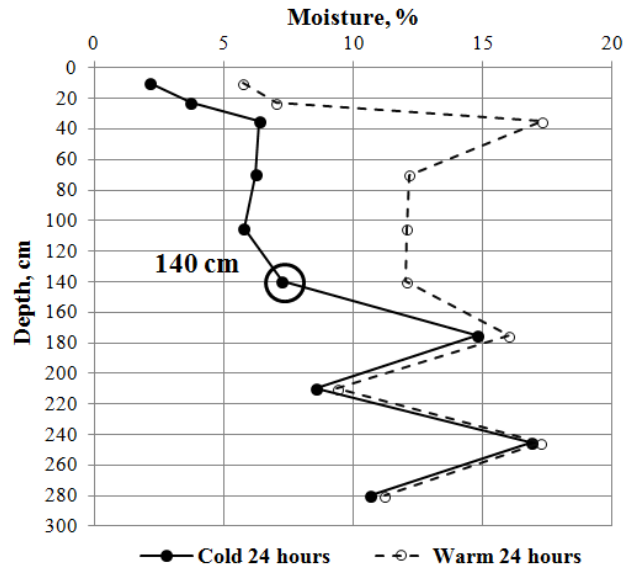


Figure 16. Temperature distribution in the depth of pavement and subgrade for warm and cold 24 hours on “Oskemen-Zyryanovsk” highway: ○ is a frost bound.

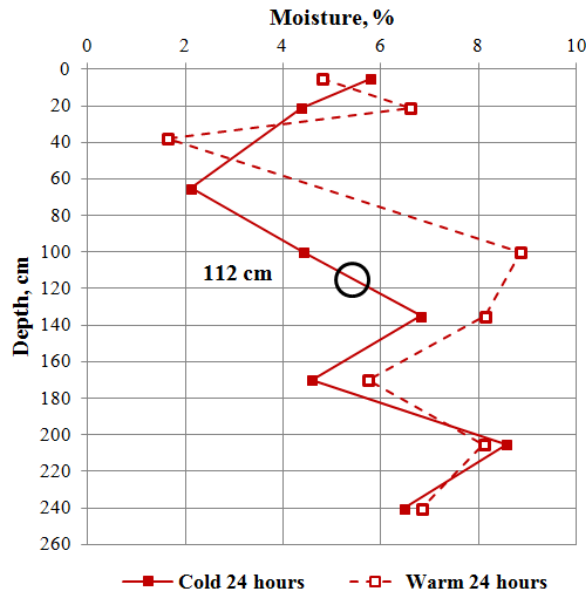


Figure 17. Temperature distribution in the depth of pavement and subgrade for warm and cold 24 hours on “Almaty-Bishkek” highway: ○ is a frost bound.

3.4. Cyclic freezing and thawing

To analyze cyclic freezing and thawing (CFT) of a highway pavement the air temperature values have been used during twenty consecutive winter seasons (from the 1st of January 1992 to the 31st of December 2011) at six geographical points (in the cities of Nur-Sultan, Almaty, Shymkent, Oskemen, Petropavlovsk and Zhanybek village) located in various regions of Kazakhstan. Geographical coordinates and climatic characteristics of these communities are given in Table 1. The temperature values have been measured in the specialized meteorological stations of RSE “KAZHYDROMET” [33].

Fig. 18 and 19 represent the histograms showing visually a dependence between the number of cycles for freezing and thawing (FT) and cycle duration. It is found out that the number of FT cycles is sharply decreased with the cycle duration increase. For example, 88–97 % of all FT cycles have a duration up to 100 hours. Meanwhile, the duration for 72–80 % of all FT cycles is up to 200 hours. It should be also mentioned that the duration of FT cycles is considerably lower in warm regions than in the cold ones. For example, the largest duration of cycles in Almaty and Shymkent reaches up to 700 hours, in Oskemen it reaches up to 2600 hours, and in Petropavlovsk it reaches up to 3400 hours.

As it is shown in Fig. 20 and 21, there is a reliable correlation relationship between the number of FT cycles and cycle duration. This correlation relationship for all the considered communities is approximated with a high accuracy by the following power function:

$$N_{cycles} = a \cdot t_{cycle}^{-b}, \tag{1}$$

where N_{cycles} is the number of FT cycles;

t_{cycle} is a cycle duration, hour:

a, b are coefficients.

Coefficient b shows for how many orders the number of FT cycles is decreased at the cycle duration increase for one order.

It is found out that there is also a dependence between the number of FT cycles and minimal temperature of the cycle (Fig. 22): the number of FT cycles is decreased with the minimal temperature decrease; as one should expect, an absolute value of a minimal temperature in southern region is less (in Almaty and Shymkent it is above -27 °C), and in the northern and eastern regions it is more (in Petropavlovsk it is below -42 °C, in Oskemen it is below -45 °C); 80–89 % of all FT cycles have a minimal temperature within the limits of -0.1 °C and -9 °C.

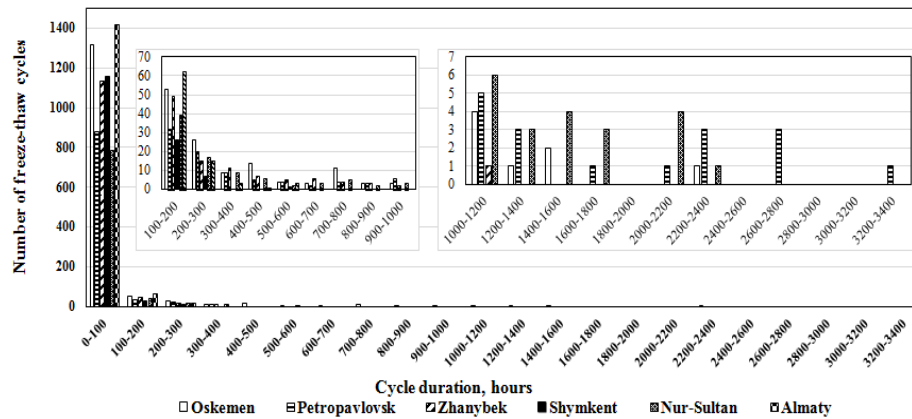


Figure 18. Dependence of the number of freeze-thaw cycles on cycle duration (cycle duration up to 3400 hours).

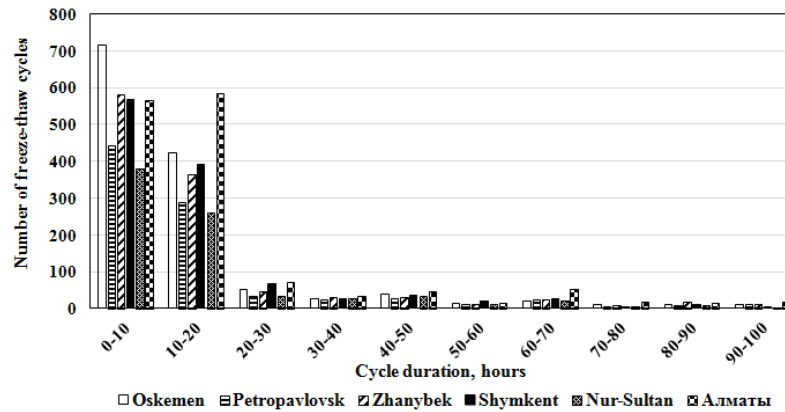


Figure 19. Dependence of the number of freeze-thaw cycles on cycle duration (cycle duration up to 100 hours).

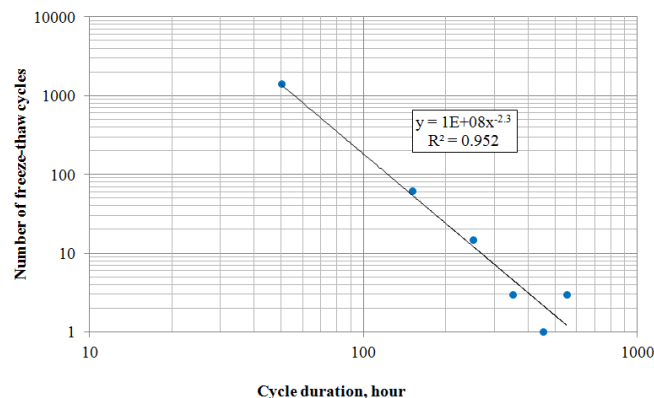


Figure 20. Dependence of the number of freeze-thaw cycles on cycle duration for Almaty.

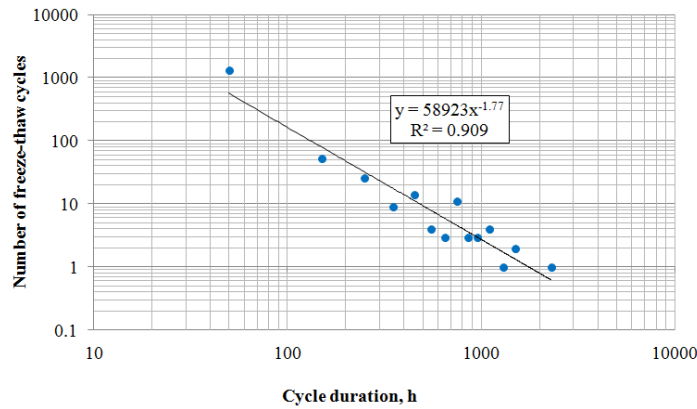


Figure 21. Dependence of the number of freeze-thaw cycles on cycle duration for Oskemen.

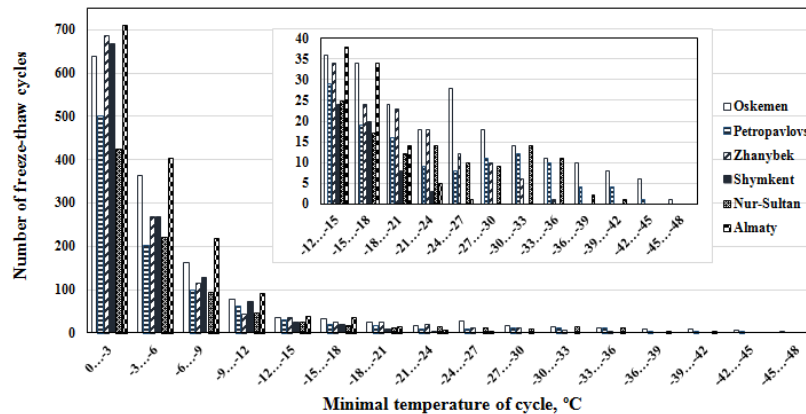


Figure 22. Dependence of the number of freeze-thaw cycles on minimal temperature of cycle.

4. Conclusion

The results of the experimental research for temperature and moisture variation in pavements and subgrade of the highways located in different regions of Kazakhstan and the analysis of cyclic freezing and thawing of a pavement, which are of high value at designing of pavements and operation of highways in many countries of the world, allowed drawing the following conclusions:

1. An air temperature of the upper part of a pavement is considerably varied. In the south the air temperature is considerably higher (above +40°C) than it is in the north and in the east; in winter season a minimal air temperature in the north and in the east is considerably lower (it reaches -40 °C) than in the south.

The air temperature of upper part of a pavement is varied quasi-harmonically in warm 24 hours in all regions. The highest temperatures occur between 3 o'clock and 6 o'clock in the afternoon, and the lowest ones occur between 3 o'clock and 6 o'clock in the morning.

The behavior of the air temperature is considerably different in upper part of a pavement in cold 24 hours than that of warm 24 hours: its quasi-harmonic behavior is interrupted.

The temperature of the upper part of an asphalt concrete pavement in warm 24 hours is higher than the air temperature.

The temperature of a pavement and subgrade is decreased in the depth in summer season, and it is increased in the depth in winter season.

Amplitude of daily temperature variation in the pavement and subgrade is decreased with the depth increase: the temperature is not practically varied in a daily cycle in warm and cold 24 hours in the depths of 80 cm and 30 cm respectively.

2. Moisture distribution in the depth of a pavement and subgrade has complicated behavior. The minimal moisture value is 2 %. The maximal moisture value reaches 10 % in the south, in the north and in the west, and it reaches 17.5 % in the east.

3. The number of cycles is sharply reduced with increase of FT cycles duration. 88–97 % of all FT cycles have duration up to 100 hours and 72–80 % of all FT cycles have duration up to 200 hours.

The duration of FT cycles is considerably lower in warm regions than that of cold regions: the highest duration of cycles reaches 700 hours in warm regions and it is up to 3400 hours in cold regions.

The number of FT cycles is decreased with the minimal temperature in cycles decrease. An absolute value of a minimal temperature in cycles is higher in warm regions and it is lower in cold regions. 80–89 % of all FT cycles have a minimal temperature within the limits of $-0.1\text{ }^{\circ}\text{C}$ and $-9\text{ }^{\circ}\text{C}$.

References

1. Yoder, E.J., Witczak, M.W. Principles of pavement design. John Wiley & Sons Inc. New Jersey, 1975. 711 p.
2. Huang, Y.H. Pavement analysis and design. Pearson Education Inc. New Jersey, 2004. 792 p.
3. Papagiannakis, A.T., Masad, E.A. Pavement design and materials. John Wiley & Sons Inc. New Jersey, 2008. 544 p.
4. Teltayev, B., Aitbayev, K. Modeling of transient temperature distribution in multilayer asphalt pavement. *Geomechanical Engineering*. 2015. 8(2). Pp. 133–152. DOI: 10.12989/2015.8.2.133
5. Teltayev, B., Aitbayev, K. Modeling of temperature field in flexible pavement. *Indian Geotechnical Journal*. 2015. 45(4). Pp. 371–377. DOI: 10.1007/s40098-014-0122-6
6. Teltayev, B.B., Suppes, E.A. Regularities for temperature variation in subgrade of highway. *Geomechanical Engineering*. 2017. 13(5). Pp. 793–807. DOI: 10.12989/gae.2017.13.5.793
7. Teltayev, B.B., Suppes, E.A. Temperature in pavement and subgrade and its effect on moisture. *Case Studies and Thermal Engineering*. 2019. No. 13. (100363). Pp. 1–11. DOI: 10.1016/j.csite.2018.11.014
8. Teltayev, B.B., Suppes, E.A. Temperature and moisture in a highway in the south of Kazakhstan, *Transportation and Geotechnics*. 2019. 21. Pp. 1–11. DOI: 10.1016/j.trgeo.2019.100292
9. Teltayev, B.B., Suppes, E.A. Temperature and moisture distribution in a highway in south-eastern Kazakhstan. *MATEC Web of Conferences*. 2019. Pp. 02005. DOI: 10.1051/mateconf/201926502005
10. Aliawdin, P., Marcinowski, J., Wilk, P. Theoretical and experimental analysis of heat transfer in the layers of road pavement. *Civil Environmental Engineering Report*. 2005. No. 1. Pp. 7–18.
11. Kim, B. Laboratory calibration of time-domain reflectometry and analysis of soil water content in Korea LTPP sections. *KSCE Journal of Civil Engineering*. 2010. 14(4). Pp. 503–511. DOI: 10.1007/s12205-010-0503-z
12. Wen, Z., Zhang, M., Ma, W., Wu, Q., Niu, F., Yu, Q., Fan, Z., Sun, Z. Thermal-moisture dynamics of embankments with asphalt pavement in permafrost regions of Central Tibetan Plateau. *European Journal of Environmental Civil Engineering*. 2015. Vol.19 (4). Pp. 387–399. DOI: 10.1080/19648189.2014.945043
13. Lee, J., Son, D., Kwon, S., Ryu, S.W. Evaluation of methods of prevent soil on a box culvert from freezing-heaving. *KSCE Journal of Civil Engineering*. 2016. Pp. 1–6. DOI: 10.1007/s12205-016-0772-2
14. Yao, Y.-S., Zheng, J.-L., Zhang, J.-H., Li, Y. Field measurements on numerical simulation of temperature and moisture in highway engineering using a frequency domain reflectometry sensor. *Sensors*. 2016. No. 16. Pp. 1–18. DOI: 10.3390/s16060857
15. Teltayev, B. Evaluation of low temperature cracking indicators of hot mix asphalt pavement. *International Journal of Pavement Research and Technologies*. 2014. No. 5. Pp. 343–351. DOI: 10.6135/ijprt.org.tw/2014.7(5).343
16. Teltayev, B., Radovskiy, B. Low temperature cracking problem for asphalt pavements in Kazakhstan. *Proceedings of 8 RILEM International Conference on Mechanisms of Cracking and Debonding in Pavements*. Nantes, 2016. Vol.1. Pp. 139–145. DOI: 10.1007/978-94-024-0867-6_20
17. Teltayev, B., Radovskiy, B. Predicting thermal cracking of asphalt pavements from bitumen and mix properties. *Road Materials and Pavement Design*. 2018. 19(8). Pp. 1–6. DOI: 10.1080/14680629.2017.1350598
18. Radovskiy, B., Teltayev, B. Viscoelastic Properties of Asphalts Based on Penetration and Softening Point. *Springer International*. Cham, 2018. 115 p. DOI: 10.1007/978-3-319-67214-4
19. Teltayev, B.B., Amirbayev, E.D., Radovskiy, B.S. Viscoelastic characteristics of blown bitumen at low temperatures. *Construction and Building Materials*. 2018. No. 189. Pp. 54–61. DOI: 10.1016/j.conbuildmat.2018.08.200
20. Teltayev, B.B. Influence of mechanical indices for soil basement on strength of road structure, *Proceedings of the 18 International Conference on Soil Mechanics and Geotechnical Engineering "Challenges and Innovations in Geotechnics"*. Paris, 2013. Vol. 2. Pp. 1365–1368.
21. Teltayev, B., Baibatayrov, A., Suppes, E. Characteristics of highway subgrade frost penetration in regions of the Kazakhstan. *15 Asian Regional Conference on Soil Mechanics and Geotechnical Engineering*. Fukuoka, 2015. Pp. 1664–1668. DOI: 10.3208/jgssp.KAZ-08
22. Teltayev, B., Suppes, E. Impact of freezing of subgrade on pavement deformation, *Proceedings of the 19th International Conference on Soil Mechanics and Geotechnical Engineering*. Seoul, 2017. Pp. 1–4.
23. Teltayev, B., Suppes, E. Freezing characteristics of a highway subgrade. *Science in Cold and Arid Regions*. 2017. 9(3). Pp. 325–330.
24. Guide for mechanics-empirical design of new and rehabilitated pavement structures, Final report, NCHRP Project 1-37 A. ARA. Inc., ERES Consultants Division, Transportation Research Board of the National Academies, Washington, D.C. 2004.
25. VSN 46-83. Instruksiya po proektirovaniyu nezhestkoi dorozhnoi odezhdyy [Guide to flexible pavement design]. Moscow: Transport, 1985. 157 p. (rus)
26. ODN 218.046-01. Proektirovanie nezhestkoi dorozhnoi odezhdyy [Design of flexible pavement]. Moscow: Transport, 2001. 145 p. (rus)
27. SN RK 3.03-19-2006. Proektirovanie nezhestkoi dorozhnoi odezhdyy [Design of flexible pavements]. Astana, 2007. 86 p. (rus)
28. SN RK 3.03-34-2006. Instruksiya po proektirovaniyu zhestkoi dorozhnoi odezhdyy [Guide to rigid pavement design]. Astana, 2007. 88 p. (rus)
29. Wang, T.L., Ma, C., Yan, H., Liu, J.K. Influence of repeated freeze-thaw on dynamic modulus and damping ratio properties of silty sand. *Science in Cold and Arid Regions*. 2013. 5(5). Pp. 0572–0576. DOI: 10.3724/sp.j.1226.2013.00572
30. Huang, X., Li, D.Q., Ming, F., Fang, J.H. An experimental study on the relationship between acoustic parameters and mechanical properties of frozen silty clay. *Science in Cold and Arid Regions*. 2013. 5(5). Pp. 0596–0602. DOI: 10.3724/SP.J.1226.2013.00596
31. Shin, E.C., Ryu, B.H., Hwang, S.G., Park, J.Y. Frost heaving characteristics of subgrade soil by laboratory test. *Proceedings of 5 International Geotechnical Symposium*. Incheon, 2013. Pp. 576–579.

32. Liu, W., He, P., Zhang, Z. A calculation method of thermal conductivity of soils. Journal of Glaciology and Geocryology. 2002. 24(6). Pp. 770–773.
33. <https://kazhydromet.kz>

Contacts:

Bagdat Teltayev, bagdatbt@yahoo.com

Giuseppe Loprencipe, giuseppe.loprencipe@uniroma1.it

Guido Bonin, guido.bonin@gmail.com

Elena Suppes, suppes08@mail.ru

Kurmangazy Tileu, tileu.kurmangazy@gmail.com

© Teltayev, B.B., Loprencipe, G., Bonin, G., Suppes, E.A., Tileu, K., 2020



DOI: 10.18720/MCE.100.12

Mechanical properties of sustainable wooden structures reinforced with Basalt Fiber Reinforced Polymer

K.G. Kozinets^a, T. Kärki^b, Yu.G. Barabanshchikov^a, V. Lahtela^b, D.K. Zotov^{*a}

^a Peter the Great St. Petersburg Polytechnic University, St. Petersburg, Russia,

^b Lappeenranta University of Technology, Lappeenranta, Finland,

*E-mail: zotovdk@gmail.com

Keywords: timber, basalt fiber, sustainable materials, FEM, wooden structures

Abstract. The long-lasting materials are sustainable goal for future, which were improved with various material combination, such as wood and basalt fibers. When materials with various nature were combined, properties might be altered and those must be evaluated. This study investigates the effect of basalt fibers on the wooden structure. Test materials were three various wood frames; pure, reinforced, and basalt fiber reinforced frames. The materials were analyzed by mechanical tests and elements were modelled with software package. In mechanical test, the strength value of pure and reinforced wooden structures ranging from 5.2 to 11.2 kN with a 19–25 mm deformation. The strength and deformation of basalt reinforced frames varied between 12.0–18.6 kN and 4–6 mm, correspondingly. Finite element modeling supported to the achieved results in the mechanical tests. It is concluded that basalt fiber reinforced wooden structures are more sustainable material from the viewpoint of material features.

1. Introduction

Sustainable practices in materials science have received increasing attention last time, such as light-weight, reduced emission and waste amounts, as well as improved material properties. The circular economy is a model that contributing the principle of sustainability. One strategy of circular economy is to extend what is made [1]. Therefore, it is essential to improve material, which life cycle is so long-lasting as possible, such as wooden structures. Wood is a popular material in construction and the market share of wooden multistory apartments were grown remarkable in the Nordic countries during last decade [2]. The wooden structures are environmentally less impactful compared to the concrete structures [3], but it still must be remembered that wood in products should have a design life span that matches timber rotation periods that might be 35 years and more [4]. Therefore, the improvement of material properties must be studied with care, such as advanced mechanical properties.

Currently, a large number of lightly loaded structures are being constructed from metal, for example, summer houses, pavilions, short pedestrian bridges [5]. The loads acting on these structures are noticeably lower than critical for metal, which has a significant for these structures own weight. For such structures, metal can be replaced by wooden structures [6]. Wood is barely light, tensile and ecologic material. But now days, it is not very distributed due its poor strength characteristics in comparison with steel and concrete as civil engineering material. By reinforcement, it can be made tougher [7]. For example, one way is to reinforce it by using basalt fiber reinforced polymer [8], like the way wood is repaired using epoxy [9]. Basalt fiber is a sustainable alternative for reinforcement, due to unlimited reserves and simple manufacturing process, for instance [10]. One approach is to reinforce by combining wood and basalt fiber reinforced polymer. To obtain a strong contact, the reinforcement of basalt fiber is made directly on wood [11]–[14]. At the same time, wood receives new properties, such as increased tensile strength [15]. Another approach, is to use basalt fabric reinforcement [16]–[19]. It can be used as lamination material on wood, or other construction material. At the same time, mass, volume and geometric characteristics remain unchanged. Assessing these changes is difficult due to the orthotropy of wood and the isotropy of basalt fiber reinforced polymer [29–32]. One of the most relevant methods is mechanical strength testing. But due

Kozinets, K.G., Kaarki, T., Barabanshchikov, Yu.G., Lahtela, V., Zotov, D.K. Mechanical properties of sustainable wooden structures reinforced with Basalt Fiber Reinforced Polymer. Magazine of Civil Engineering. 2020. 100(8). Article No. 10012. DOI: 10.18720/MCE.100.12



This work is licensed under a CC BY-NC 4.0

to the limited size of the test benches, it is possible to test only small parts. For testing finished products and taking into account the maximum number of influencing factors, in any case, the use of finite element modeling [20]–[25] ensure with strong results validation.

OBJECTIVES

In this study we assessed the maximum possible designs to obtain the relevant results. The objective of this study was to demonstrate that the functionality of wooden structures that can be improved with the presence of basalt fiber. The functionality of wooden structures was evaluated by mechanical strength test and modelling of element with software package. This study offers a contribution to the available knowledge of basalt fibers' effects, and an initial basis for further research.

2. Materials and Methods

2.1. Sources of materials and mechanical properties

Three various wooden frames were tested with the following parameters; T1, T2, T3 are pure wood frames, T1A, T3A – are reinforced T1 and T3 frames, and T1L7, T2L4, T3L3 are different type of frames – they are reinforced with basalt fiber lamination. The wood used is coniferous, in this case, first class pine, with a minimum number of knots, exclusively in the center of the canvas. They are shown on Fig. 1.

Pine wood has density from 487 to 520 kg/m³. Pine belongs to the genus of conifers. A total of about one hundred and thirty species of pine are known. Pine is an evergreen tree containing a large amount of resin. The most common species in Russia is ordinary pine. Pine is the most used type of wood in Russia. About 30% of all types of wood used in Russia is pine. Pine wood is not afraid of the effects of fungi, insect pests, putrefactive damage due to increased resinity. According to this indicator, pine varieties are divided into the first type (with a high resin content) and the second type (reduced resin content). Resin pine is not recommended for use in carpentry, since the resin makes it difficult to saw and plan, sticking to tools. When heated, the varnish coating may rise. High resin content pine wood must be treated before processing. For this, solvents, acetone, gasoline, alkali solutions, and alcohol substances are used. Also, pine lumber is divided into grades by the presence of defects (in particular, knots). For class 1 lumber, up to 40 mm thick, no more than 3 knots per linear meter are allowed, no more than 1/4 of the size of the lumber.

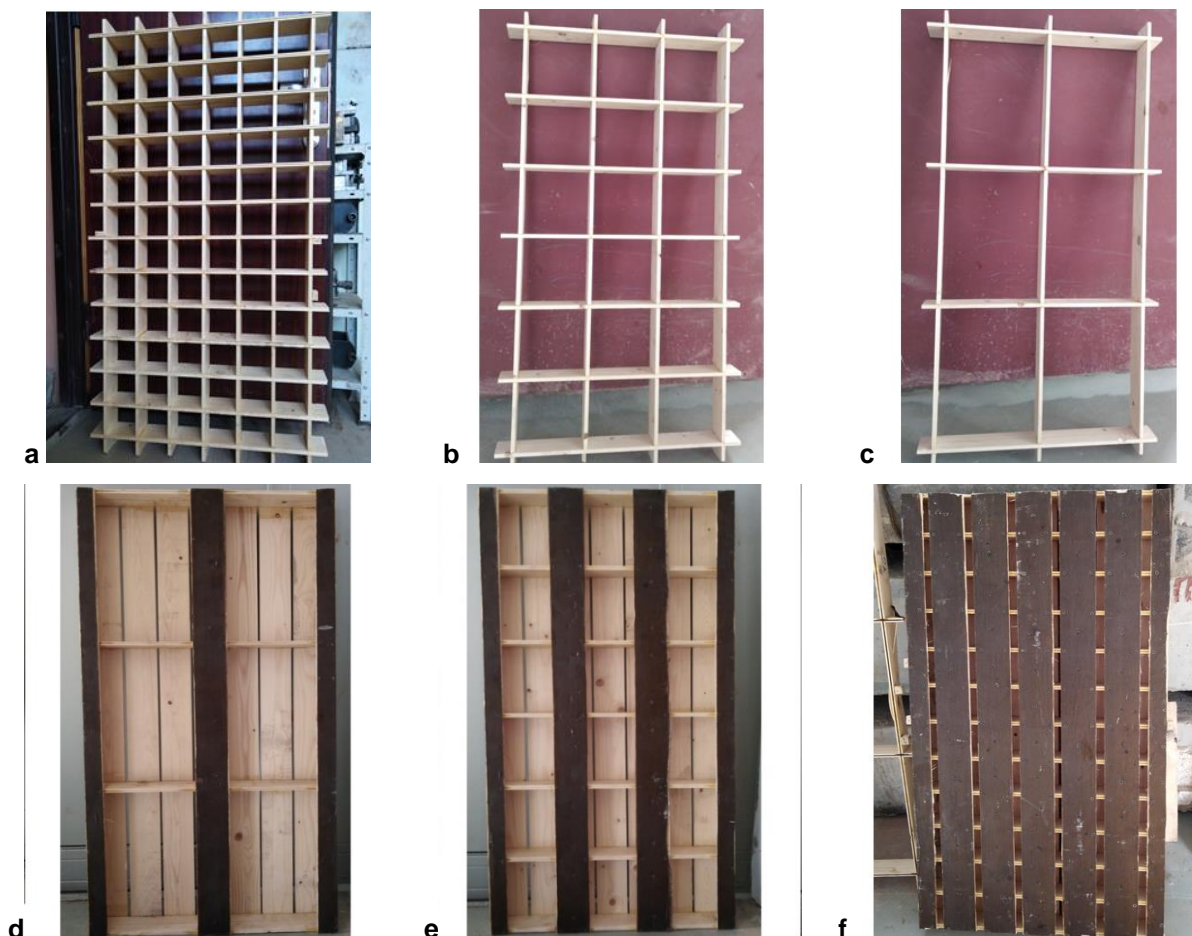


Figure 1. Frame types. (a) T1, T1A; (b) T2; (c) T3, T3A; (d) T1L7; (e) T2L4; (f) T3L3.

The reinforcement material for frames T1, T2, T3, T1A, T3A is basalt-fiber rowing reinforced with epoxy-diane resin (Epoxy ED-20).

2.2. Mix design

Density of ED-20 is 1166 kg/m^3 in uncured state. Dynamic viscosity, $13\text{--}20 \text{ Pa} \cdot \text{sec}$, at $(25 \pm 0.1) \text{ }^\circ\text{C}$. It consists of epoxy groups (20.0–22.5%), chlorine ion (0.001 %), saponified chlorine (0.3 %), hydroxyl groups (1.7 %). Of the distinguishing features of the ED-20, excellent adhesion to wood and does not cause corrosion of materials in contact with them. As a hardener was used Polyethylenepolyamine. Its density is $0.956\text{--}1.011 \text{ g/cm}^3$. Bulk prp mixing with epoxy is 10%.

Basalt roving with a fiber thickness of 10 microns and a linear density of 4800 mg/m , Specific density 2.67 g/cm^3 . Breaking load is $500\text{--}650 \text{ mN/Tex}$.

The result of reinforcement is shown in Fig. 2. And the reinforcement material for frames T1L7, T2L4, T3L3 is reinforced with basalt fabric, by lamination. The result of reinforcement is shown in Fig. 2. Blueprints of both types of reinforcements are shown on Fig. 3.

As basalt fabric, was used Basalt fabric TBK-100. The width of the original canvas 1000 mm . The surface density of $190\text{--}230 \text{ g/m}^2$. Number of threads $9\text{--}11 / \text{cm}$. Breaking load of 780 N . Thickness 0.19 mm .

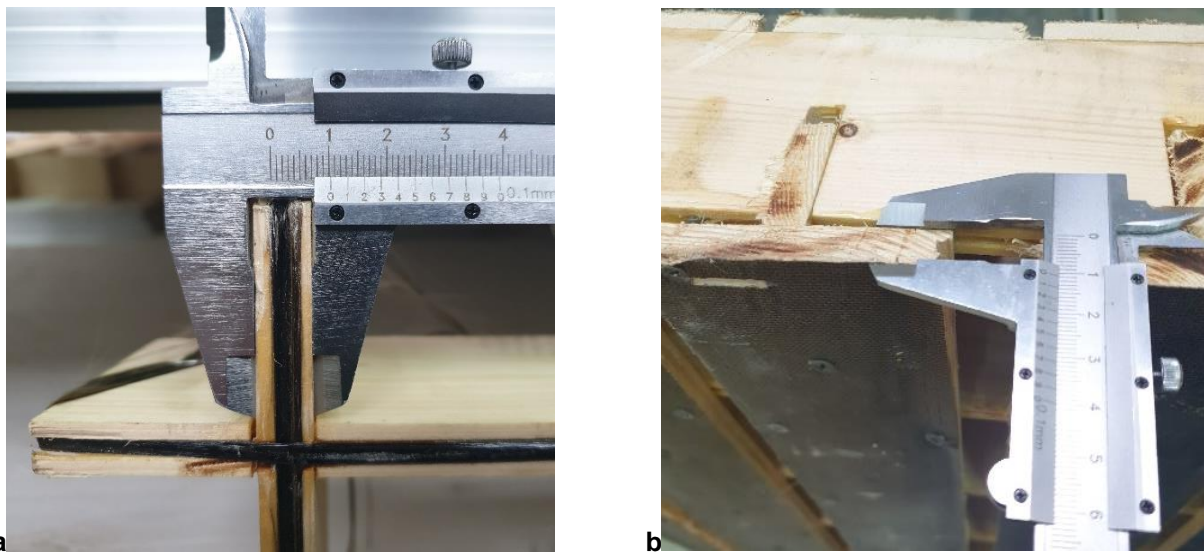


Figure 2. The result of basalt fiber reinforcement (a) and the result of basalt fabric reinforcement (b).

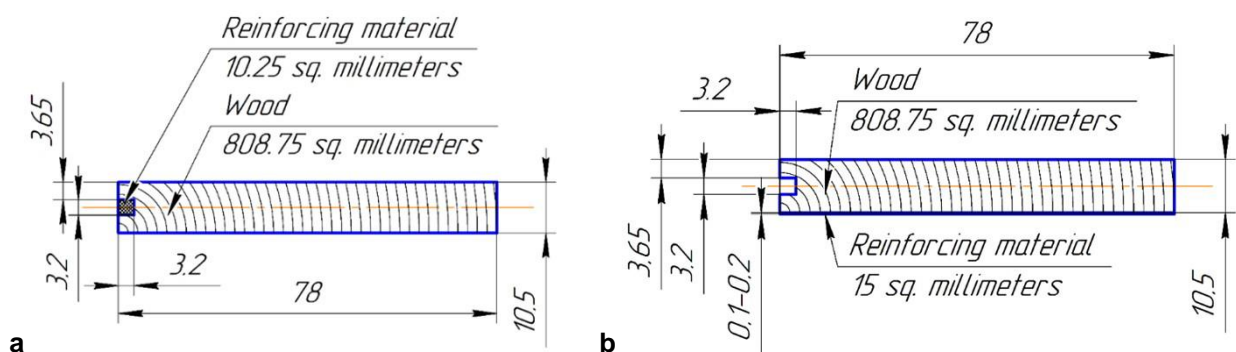


Figure 3. The blueprint of basalt fiber reinforcement (a) and the blueprint of basalt fabric reinforcement (b).

2.3. Method of research

The research methodology is shown in Fig. 4. First of all, the most suitable designs for mechanical testing were developed. Minimization of cost was chosen as the main criterion, and therefore, ease of manufacture. The most attractive shapes would be octagons, hexagons, or a 45-degree square. But these shapes are quite laborious to manufacture and reinforce, so the shape of a rectangle with edges located at an angle of 90 degrees was chosen in the form of a frame. The groove for the reinforcing material is performed in a standard operation for woodworking - by sawing in the form of a groove (it is used in the manufacture of lumber of the "lining" brand, which has similar dimensions, which is why the production of

these strips is very cheap) As the materials, as described above, the most the timber available in the north is pine. It does not have outstanding mechanical properties, but is inexpensive, readily available and has few knots. Basalt roving was chosen as a reinforcing material, initially it was planned to use a cord, but it is much worse impregnated with epoxy resin, as well as basalt sheet (for type 2). To fix the basalt roving in the groove of the wood, it was decided to use the epoxy resin described above. The main requirement for the resin is high mobility in the liquid state, for a more uniform impregnation of the roving, and an increase in the area of adhesion to the wood. Due to the large area of adhesion to the wood, the epoxy resin formed a monolithic structure, which added additional strength to the reinforced frames. For frame sizes, normal sizes were used to facilitate the manufacturing process, this is a series of numbers 400, 300, 200, 100. Then structures were created, representing the frames of various types described earlier, as well as digital 3D models, taking into account the materials used. For the wood-to-wood connection and for the epoxy resin-wood connection, the bonded type was used because these surfaces are firmly bonded. Then mechanical tests were carried out, as well as calculation by the finite element method with preliminary tabular characteristics of materials. After that, comparisons and optimization of the coefficients for the calculation model were carried out, and the final design was calculated.

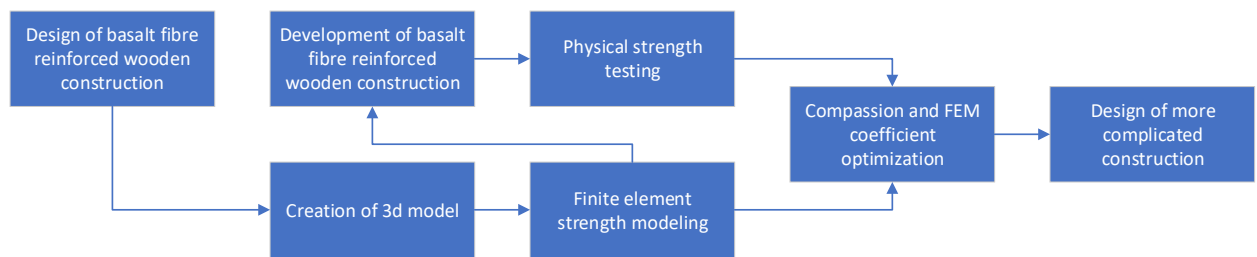


Figure 4. Research methodology.

2.4. Mechanical testing

The loading was carried out continuously with a hydraulic jack at a speed of 1 kN/min. The load was measured by an electronic force meter, deflections were measured using dial indicator. Deflections were measured in the middle of the span at three points across the width of the model. Indications were recorded by a camera. The scheme of testing is shown in Fig. 5. and camera record of unloaded and loaded frames are shown in Fig. 6.

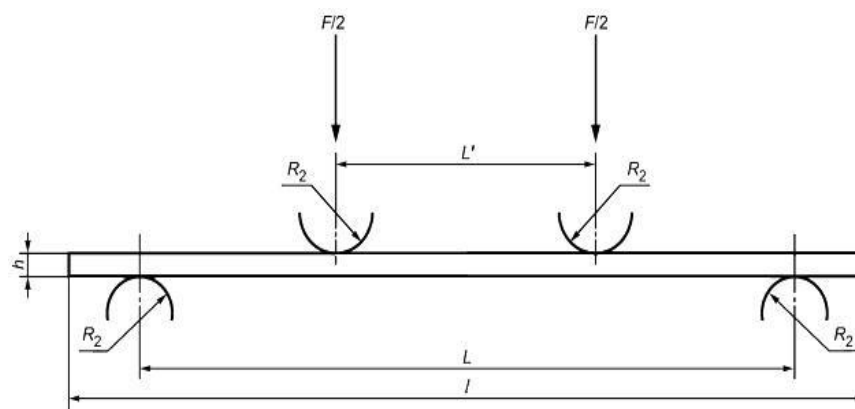


Figure 5. Load scheme ($L=1000$ mm; $L'=333$ mm; $R_2=50$ mm; $h=78$ mm).

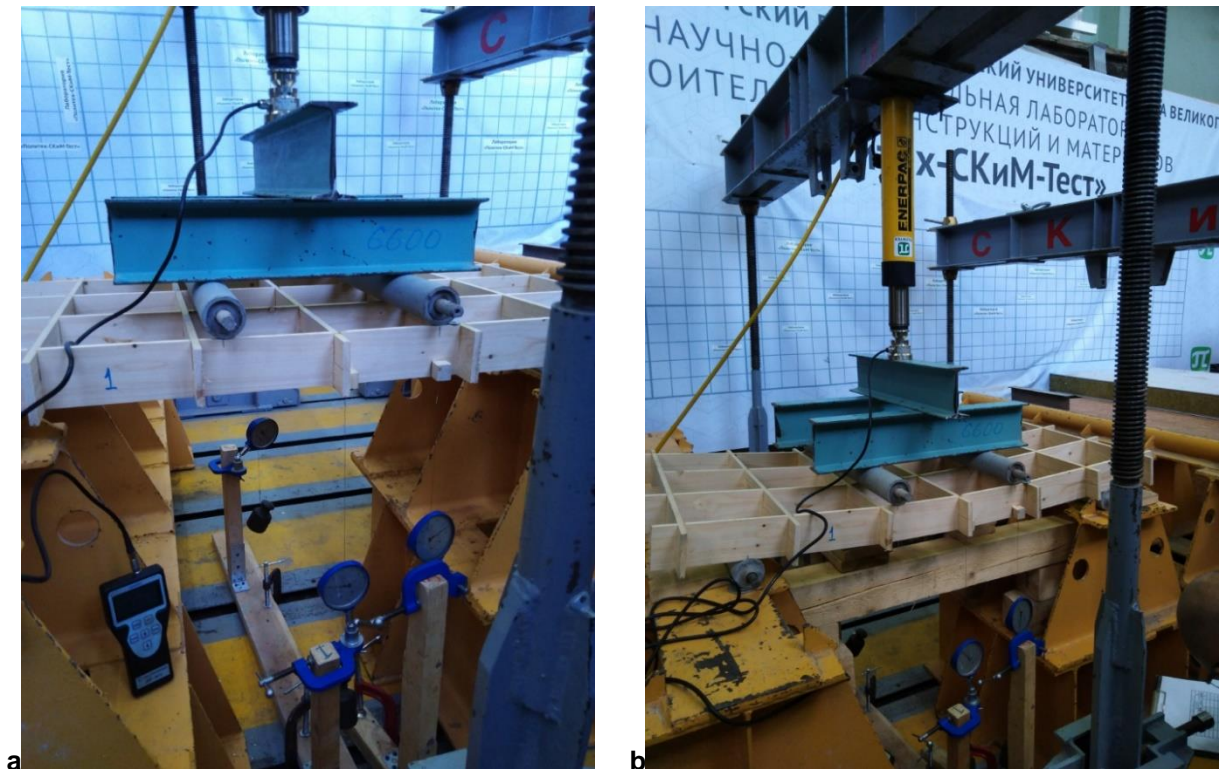


Figure 6. Unloaded frame (a) and loaded frame (b).

2.5. Finite element testing

Element modeling was carried out in the Ansys software package, and in the calculation module - static structural. The design scheme is shown in Fig. 7. The loads were set in accordance with the loads on the test bench.

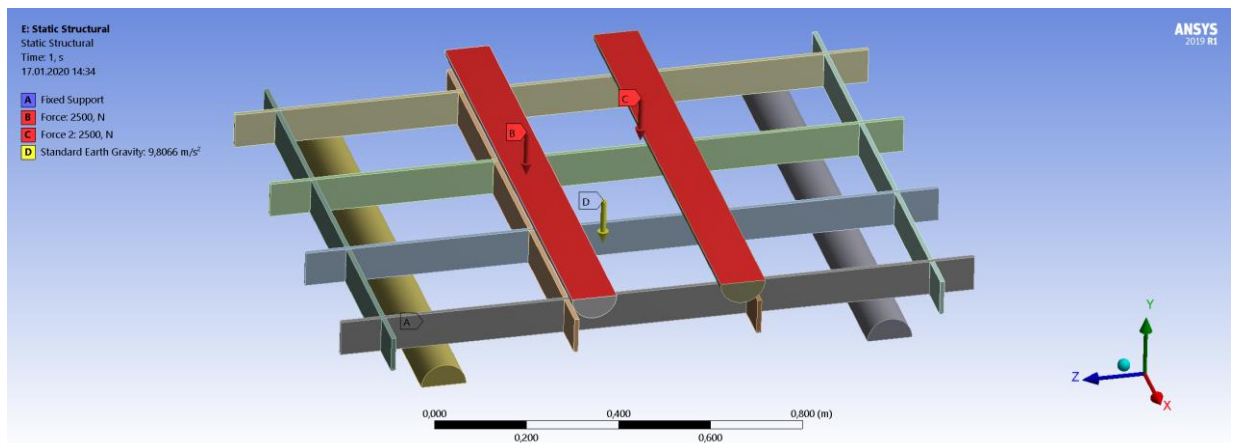


Figure 7. Design scheme and loads for T3A frame.

3. Results and Discussions

3.1. Testing results

The result of mechanical testing of first type of frames (T1,T3,T1A,T3A) are provided in Fig. 8. Results of T2 does not provided, because, there was not T2A frame. The destruction of the T3 sample occurs at a load of 5.2 kilonewton, with a deformation of 19 mm, while the destruction of the T3A sample occurs at a load of 6.4 kilonewton and a deformation of 24 mm. The destruction of the T1 specimen occurs at a load of 6.8 kilonewton, with a deformation of 22 mm, while the destruction of the T1A specimen occurs at a load of 11.2 kilonewton and a deformation of 25 mm.

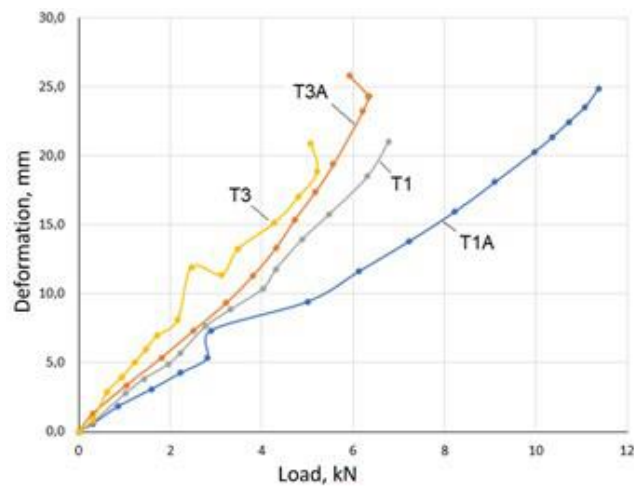


Figure 8. Results of mechanical testing of frames T1, T3, T1A, T3A.

The destruction of the reinforcement wooden frame occurs immediately after the tear of the reinforcing fiber. Samples of destruction are shown in Fig. 9.

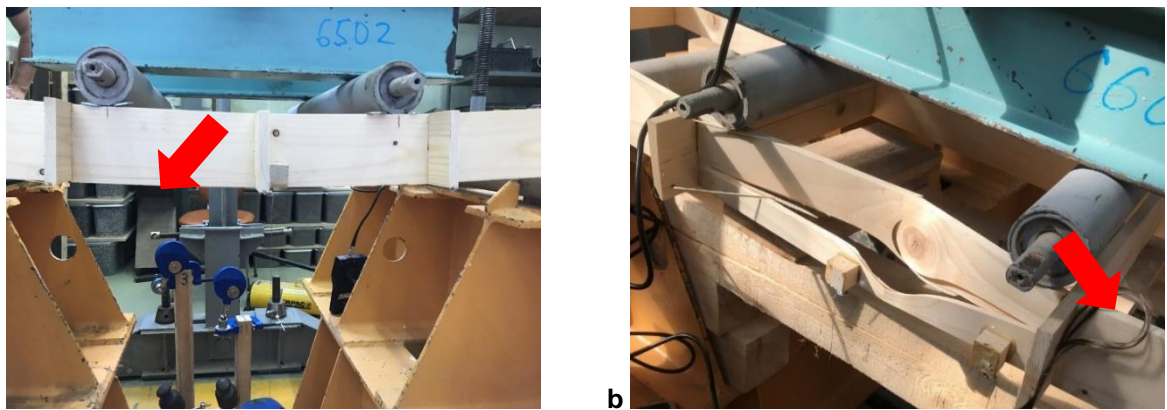


Figure 9. Crack in the bottom of frame (a), and teared reinforcement material (b), demonstrated by red arrow.

The result of mechanical testing of second type of frames (T1L7, T2L4, T3L3) are provided in Fig. 10. The destruction of the T1L7 sample occurs at a load of 16.2 kilonewtons, with a deformation of 4 mm, the destruction of the T2L4 sample occurs at a load of 18.6 kilonewtons and a deformation of 6 mm, the destruction of the T3L3 specimen at a load of 12.0 kilonewtons and a deformation of 4.2 mm

Previously, it has found that the strength of basalt reinforced timber increased by 10–15 %, and deflection was reduced 16 %, in the case of glulam [26]. In our case with wooden structures, the properties were improved even more significant. Stiffness or elastic modulus have received a relatively low value with basalt fibre-reinforced polymer [27], [28], addressing to need for further enhancement.

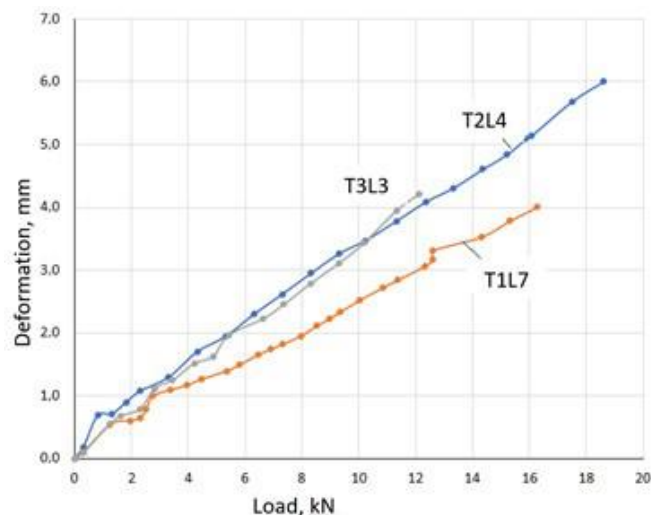


Figure 10. Results of mechanical testing of frames T1L7, T2L4, T3L3.

3.2. FEM

Finite element modeling of samples T3 (Fig. 11) and T3A (Fig. 12) were carried out with the corresponding materials. The maximum deformations are detectable approximately correspond to those obtained during mechanical tests. Deformations 19 and 19.8 mm for specimen T3, and 17 and 17.1 mm for specimen T3A at a load of 5 kilonewtons. This corresponds to approximately a tensile yield strength of 20 MPa in the base material (wood).

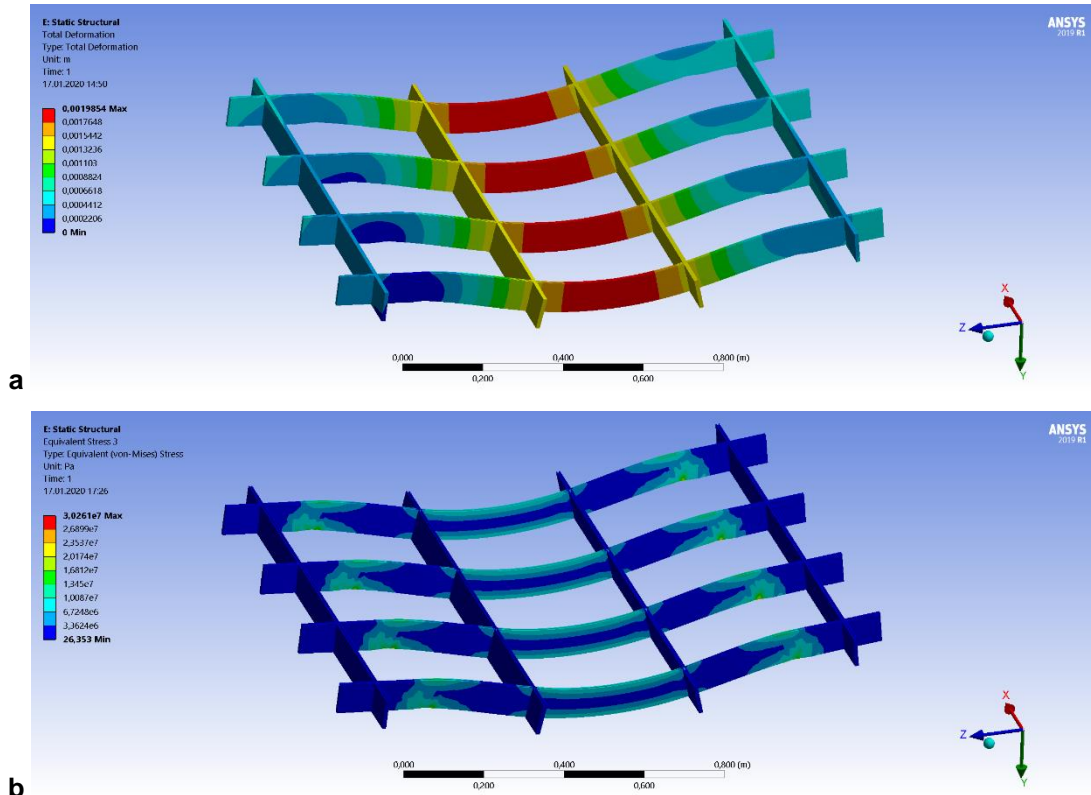


Figure 11. Deformations (a) and von-mises Stress (b) of pure wood frame T3.

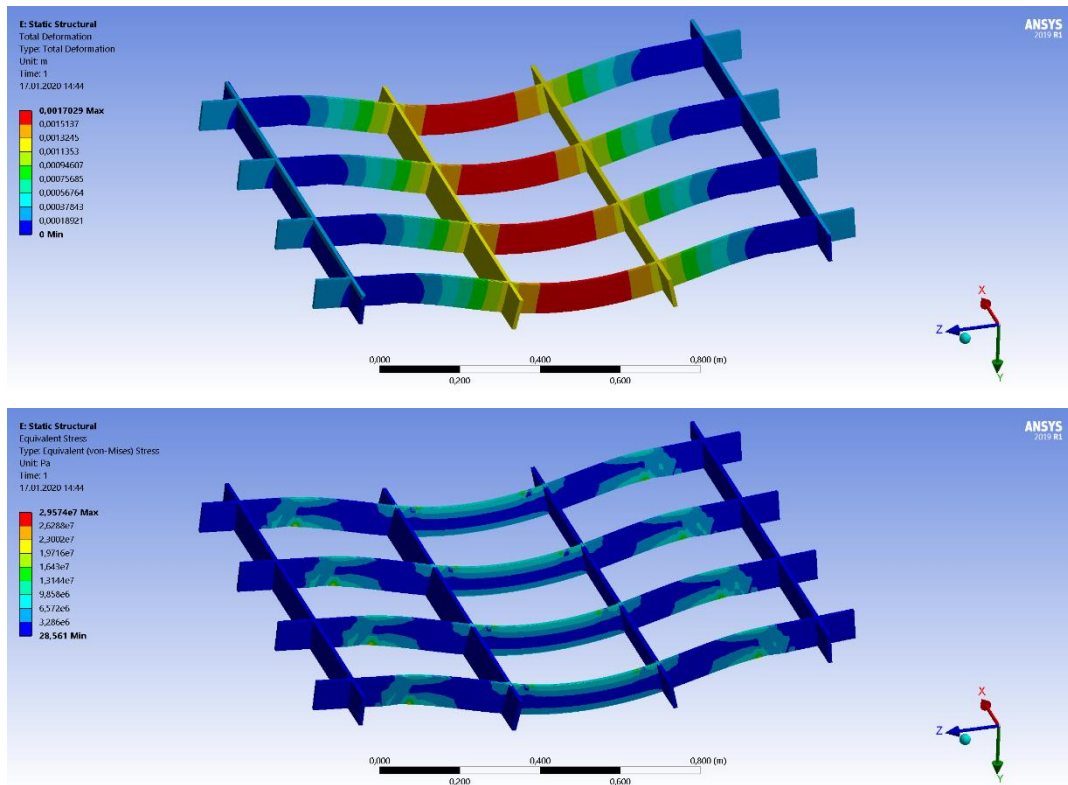


Figure 12. Deformations (a) and von-mises Stress (b) of pure wood frame T3A.

3.3. Material Consumption

Table 1. Property information of studied materials and the features of material from mechanical tests.

No	Frame name	Frame cell size, mm	Bottom roving reinforcement	Lower laminated planks	Wood Mass, kilograms	Reinforcing material Mass, kilograms	Maximum load, kN	Tensile yield strength, %	Tensile yield Strength per mass
1	T1	100x100	no	no	6.55	0	6.6	100	1.01
2	T2	200x200	no	no	3.64	0	5.6	100	1.54
3	T3	300x400	no	no	2.43	0	5.2	100	2.14
4	T1A	100x100	yes	no	6.55	0.22	11.2	170	1.65
5	T3A	300x400	yes	no	2.43	0.08	6.2	119	2.47
6	T1L7	100x100	no	7	13.34	0.17	16.2	245	1.20
7	T2L4	200x200	no	4	8.98	0.10	18.4	329	2.03
8	T3L3	300x400	no	3	7.28	0.07	12	231	1.63

The studied materials, are listed in Table 1, including also the results of mechanical strength test by different parameters. The information in Table 1 show that the studied materials were quite heterogenous, indicating that several aspects will be accounted in this study, which again increase the reliability of done work. The ability of wooden frame to carry load will increase when frame was reinforced, but naturally, the density of materials influences the strength, as “strength per mass” demonstrated.

4. Conclusion

In this article, the results of mathematical and physical modeling of structures using combined materials (wood, basalt roving, basalt canvas, epoxy) were presented. The research results showed that structures made of combined materials show increased strength on the influence of external factors. And thus, we can conclude that the applicability of these materials and structures for the construction of wooden structures.

With a minimum amount of wood and a minimum reinforcement (sample T3A), an increase in strength of 19 % is achieved, with a minimum cost of reinforcing material, and destruction occurs at a load of 6.4 kilonewtons with a deformation of 24 mm, in contrast to the original sample T3, the destruction of which occurs under load at 5.2 kilonewtons and deformation of 19mm, which makes it, with a weight of 2.43 kg, almost equal in strength to the sample T1, weighing 6.55 kg. For specimen T1A, the reinforcement leads to an increase in strength by 70%, and fracture occurs at a load of 11.2 kilonewtons with a deformation of 25 mm, in contrast to the original specimen T1, which fractures at a load of 6.8 kilonewtons and a deformation of 22 mm.

Laminated samples show even more impressive results, The destruction of the T1L7 sample occurs at a load of 16.2 kilonewtons, with a deformation of 4 mm, the destruction of the T2L4 sample occurs at a load of 18.6 kilonewtons and a deformation of 6 mm, the destruction of the T3L3 specimen at a load of 12.0 kilonewtons and a deformation of 4.2 mm. But at the same time, these samples are much more material-intensive and heavy: 7.28 kg for sample T3L3, 8.98 kg for sample T2L4 and 13.34 kg for sample T1L7.

In the light of the results, the improved properties of materials encourage researchers to continue studies in this field and for example, various material amounts and those combination should be studied more exactly in future. Also, other mechanical tests could describe the nature of material wider, such as impact strength that describing a momentary strain for material or stiffness that implies the momentary maximum force whereof deformations will return after the load is removed. In addition, the whole effect of treatments on the environment could be analyzed, such as life cycle assessment.

References

1. Morseletto, P. Targets for a circular economy. Resources, Conservation and Recycling. 2020. 153. Pp. 104553. DOI: 10.1016/j.resconrec.2019.104553. URL: <http://www.sciencedirect.com/science/article/pii/S0921344919304598>.
2. Toppinen, A., Röhr, A., Pätäri, S., Lähtinen, K., Toivonen, R. The future of wooden multistory construction in the forest bioeconomy – A Delphi study from Finland and Sweden. Journal of Forest Economics. 2018. 31(1). Pp. 3–10. DOI: 10.1016/j.jfe.2017.05.001.
3. Guardigli, L., Monari, F., Bragadin, M.A. Assessing Environmental Impact of Green Buildings through LCA Methods: A comparison between Reinforced Concrete and Wood Structures in the European Context. Procedia Engineering. 2011. 21. Pp. 1199–1206. DOI: 10.1016/j.proeng.2011.11.2131. URL: <http://www.sciencedirect.com/science/article/pii/S1877705811049654>.

4. Ramage, M.H., Burrige, H., Busse-Wicher, M., Fereday, G., Reynolds, T., Shah, D.U., Wu, G., Yu, L., Fleming, P., Densley-Tingley, D., Allwood, J., Dupree, P., Linden, P.F., Scherman, O. The wood from the trees: The use of timber in construction. *Renewable and Sustainable Energy Reviews*. 2017. 68. Pp. 333–359. DOI: <https://doi.org/10.1016/j.rser.2016.09.107>.
5. Fleming, P., Smith, S., Ramage, M. Measuring-up in timber: a critical perspective on mid-and high-rise timber building design. *arq: Architectural Research Quarterly*. 2014. 18(1). Pp. 20–30.
6. Mallo, M.F.L., Espinoza, O. Cross-Laminated Timber vs. Concrete/steel: Cost comparison using a case study. *WCTE 2016–World Conference on Timber Engineering*. 2016.
7. Meier, U. Strengthening of structures using carbon fibre/epoxy composites. *Construction and Building Materials*. 1995. 9(6). Pp. 341–351.
8. Wang, J., Yang, Y., Hu, L., Zhuang, R. Experimental study on bond-slip behavior between bfrp and wood [J]. *Fiber Reinforced Plastics/Composites*. 2009. 3.
9. Richard Avent, R. Decay, weathering and epoxy repair of timber. *Journal of Structural Engineering*. 1985. 111(2). Pp. 328–342.
10. Chen, Z., Huang, Y. Mechanical and interfacial properties of bare basalt fiber. *Journal of Adhesion Science and Technology*. 2016. 30(20). Pp. 2175–2187. DOI:10.1080/01694243.2016.1174510.
11. Borri, A., Corradi, M., Speranzini, E. Reinforcement of wood with natural fibers. *Composites Part B: Engineering*. 2013. 53. Pp. 1–8.
12. de la Rosa García, P., Escamilla, A.C., García, M.N.G. Bending reinforcement of timber beams with composite carbon fiber and basalt fiber materials. *Composites Part B: Engineering*. 2013. 55. Pp. 528–536.
13. Raftery, G.M., Kelly, F. Basalt FRP rods for reinforcement and repair of timber. *Composites Part B: Engineering*. 2015. 70. Pp. 9–19.
14. Righetti, L., Corradi, M., Borri, A. Basalt FRP spike repairing of wood beams. *Fibers*. 2015. 3(3). Pp. 323–337.
15. Chen, W., Pham, T.M., Sichebe, H., Chen, L., Hao, H. Experimental study of flexural behaviour of RC beams strengthened by longitudinal and U-shaped basalt FRP sheet. *Composites Part B: Engineering*. 2018. 134. Pp. 114–126.
16. Guojun, L.U., Weihong, W., Shijie, S. Mechanical properties of wood flour reinforced high density polyethylene composites with basalt fibers. *Materials Science*. 2014. 20(4). Pp. 464–467.
17. Sarasini, F., Tirillò, J., Valente, M., Ferrante, L., Cioffi, S., Iannace, S., Sorrentino, L. Hybrid composites based on aramid and basalt woven fabrics: Impact damage modes and residual flexural properties. *Materials & Design*. 2013. 49. Pp. 290–302.
18. Dhand, V., Mittal, G., Rhee, K.Y., Park, S.-J., Hui, D. A short review on basalt fiber reinforced polymer composites. *Composites Part B: Engineering*. 2015. 73. Pp. 166–180.
19. de la Rosa García, P., Escamilla, A.C., García, M.N.G. Analysis of the flexural stiffness of timber beams reinforced with carbon and basalt composite materials. *Composites Part B: Engineering*. 2016. 86. Pp. 152–159.
20. Bodig, J., Jayne, B.A. *Mechanics of wood and wood composites*. 712. Van Nostrand Reinhold New York, 1982.
21. Fragiacomio, M., Ceccotti, A. Long-term behavior of timber–concrete composite beams. I: Finite element modeling and validation. *Journal of structural engineering*. 2006. 132(1). Pp. 13–22.
22. Dias, A., Van de Kuilen, J.W., Lopes, S., Cruz, H. A non-linear 3D FEM model to simulate timber–concrete joints. *Advances in Engineering Software*. 2007. 38(8–9). Pp. 522–530.
23. Oudjene, M., Meghlat, E.M., Ait-Aider, H., Lardeur, P., Khelifa, M., Batoz, J.L. Finite element modelling of the nonlinear load-slip behaviour of full-scale timber-to-concrete composite T-shaped beams. *Composite Structures*. 2018. 196. Pp. 117–126.
24. Hassanieh, A., Valipour, H.R., Bradford, M.A., Sandhaas, C. Modelling of steel-timber composite connections: Validation of finite element model and parametric study. *Engineering Structures*. 2017. 138. Pp. 35–49.
25. Kozinec, G.L. Generalization of the Methodology of Studying the Durability of Segmental Gates. *Power Technology and Engineering*. 2018. 52(4). Pp. 395–399.
26. Zhang, P., Shen, S. Strengthening mechanical properties of glulam with basalt fiber. *Advances in Natural Science*. 2011. 4(2). Pp. 130–133.
27. McConnell, E., McPolin, D., Taylor, S. Post-tensioning glulam timber beams with basalt FRP tendons. *Proceedings of the Institution of Civil Engineers-Construction Materials*. 2015. 168(5). Pp. 232–240.
28. Lopresto, V., Leone, C., De Iorio, I. Mechanical characterisation of basalt fibre reinforced plastic. *Composites Part B: Engineering*. 2011. 42(4). Pp. 717–723. DOI: <https://doi.org/10.1016/j.compositesb.2011.01.030>.
29. Klyuev, S.V., Klyuev, A.V., Khezhev, T.A., Pukhareno, Y. High-strength fine-grained fiber concrete with combined reinforcement by fiber. *Journal of Engineering and Applied Sciences*. 2018. 13. Pp. 6407–6412.
30. Fediuk, R.S., Lesovik, V.S., Liseitsev, Yu.L., Timokhin, R.A., Bituyev, A.V., Zaiakhanov, M.Ye., Mochalov, A.V. Composite binders for concretes with improved shock resistance. *Magazine of Civil Engineering*. 2019. 85(1). Pp. 28–38. DOI: 10.18720/MCE.85.3.
31. A D Tolstoy; V S Lesovik; E S Glagolev; A I Krymova. Synergetics of hardening construction systems. *IOP Conference Series: Materials Science and Engineering*. 2018. 327(3). 032056. doi: 10.1088/1757-899X/327/3/032056
32. Badenko, V., Fedotov, A., Zotov, D., Lytkin, S., Volgin, D., Garg, R.D., Min, L. Scan-to-bim methodology adapted for different application. *International Archives of the Photogrammetry, Remote Sensing and Spatial Information Sciences - ISPRS Archives*. 2019. 42(5/W2). Pp. 1–7.

Contacts:

Galina Kozinetc, galina4410@yandex.ru

Timo Kaarki, Timo.Karki@lut.fi

Yuriy Barabanshchikov, ugb@mail.ru

Ville Lahtela, Ville.Lahtela@lut.fi

Dmitry Zotov, zotovdk@gmail.com

© Kozinetc K.G.,Kaarki T.,Barabanshchikov Yu.G.,Lahtela V.,Zotov D. K., 2020



ПОЛИТЕХ
Санкт-Петербургский
политехнический университет
Петра Великого

Инженерно-строительный институт
Центр дополнительных профессиональных программ

195251, г. Санкт-Петербург, Политехническая ул., 29,
тел/факс: 552-94-60, www.stroikursi.spbstu.ru,
stroikursi@mail.ru

Приглашает специалистов проектных и строительных организаций,
не имеющих базового профильного высшего образования
на курсы профессиональной переподготовки (от 500 часов)
по направлению «Строительство» по программам:

П-01 «Промышленное и гражданское строительство»

Программа включает учебные разделы:

- Основы строительного дела
- Инженерное оборудование зданий и сооружений
- Технология и контроль качества строительства
- Основы проектирования зданий и сооружений
- Автоматизация проектных работ с использованием AutoCAD
- Автоматизация сметного дела в строительстве
- Управление строительной организацией
- Управление инвестиционно-строительными проектами. Выполнение функций технического заказчика

П-02 «Экономика и управление в строительстве»

Программа включает учебные разделы:

- Основы строительного дела
- Инженерное оборудование зданий и сооружений
- Технология и контроль качества строительства
- Управление инвестиционно-строительными проектами. Выполнение функций технического заказчика и генерального подрядчика
- Управление строительной организацией
- Экономика и ценообразование в строительстве
- Управление строительной организацией
- Организация, управление и планирование в строительстве
- Автоматизация сметного дела в строительстве

П-03 «Инженерные системы зданий и сооружений»

Программа включает учебные разделы:

- Основы механики жидкости и газа
- Инженерное оборудование зданий и сооружений
- Проектирование, монтаж и эксплуатация систем вентиляции и кондиционирования
- Проектирование, монтаж и эксплуатация систем отопления и теплоснабжения
- Проектирование, монтаж и эксплуатация систем водоснабжения и водоотведения
- Автоматизация проектных работ с использованием AutoCAD
- Электроснабжение и электрооборудование объектов

П-04 «Проектирование и конструирование зданий и сооружений»

Программа включает учебные разделы:

- Основы сопротивления материалов и механики стержневых систем
- Проектирование и расчет оснований и фундаментов зданий и сооружений
- Проектирование и расчет железобетонных конструкций
- Проектирование и расчет металлических конструкций
- Проектирование зданий и сооружений с использованием AutoCAD
- Расчет строительных конструкций с использованием SCAD Office

П-05 «Контроль качества строительства»

Программа включает учебные разделы:

- Основы строительного дела
- Инженерное оборудование зданий и сооружений
- Технология и контроль качества строительства
- Проектирование и расчет железобетонных конструкций
- Проектирование и расчет металлических конструкций
- Обследование строительных конструкций зданий и сооружений
- Выполнение функций технического заказчика и генерального подрядчика

По окончании курса слушателю выдается диплом о профессиональной переподготовке
установленного образца, дающий право на ведение профессиональной деятельности

